Technische Universität München

TUM School of Engineering and Design

Parametric Modeling of Battery Electric Vehicles in the Early Development Phase

Lorenzo Nicoletti, M.Sc.

Vollständiger Abdruck der von der TUM School of Engineering and Design der Technischen Universität München zur Erlangung des akademischen Grades eines

Doktors der Ingenieurwissenschaften

genehmigten Dissertation.

Vorsitz:	Prof. Dr.-Ing. Johannes Fottner
Prüfer*innen der Dissertation:	1. Prof. Dr.-Ing. Markus Lienkamp
	2. Prof. Dr.-Ing. Thomas Vietor

Die Dissertation wurde am 03.03.2022 bei der Technischen Universität München eingereicht und durch die TUM School of Engineering and Design am 14.06.2022 angenommen.

Acknowledgment

This work was carried out in the years 2019 to 2022, during my occupation as a research assistant at the Institute of Automotive Technology of the Technical University of Munich and in cooperation with the Audi AG. For the trust, support, and freedom of decision I thank first of all my supervisor Prof. Dr.-Ing. Markus Lienkamp. I am grateful to him not only for his professional supervision, but also for his personal support and for motivating me during all phases of my thesis. I would also like to thank Prof. Dr.-Ing. Thomas Vietor as my second supervisor.

For the unforgettable time at the Institute for Automotive Technology, I want to express my gratitude to my former colleagues from the Vehicle Concepts Research Group. I would like to especially thank my colleagues and friends Adrian König, Ferdinand Schockenhoff, Matthias Brönner, and Benedikt Danquah for the scientific discussions and for proofreading this thesis. A special thanks also goes to the colleagues Nikolaos Wassiliadis, Julian Kreibich, and Matthias Steinsträter who were always good companions during the Dokkoloqs. In addition, I want to thank my students Andrea Romano, Peter Köhler, Gabriele Ranocchia, and Michael Spreng who supported this thesis with their bachelor, semester, and master theses.

My gratitude also goes to the colleagues of the Audi AG and especially to my supervisor Maximilian Heinrich. The multitude of meetings in which we discussed my research were a fundamental contribution to this thesis. I am also grateful to the colleagues Dr.-Ing. Hendrik Gronau and Martin Abersmeier, who supported me during the thesis.

Most of the models presented in this thesis were generated with the vehicle data of the A2mac1 benchmarking database. Therefore, I am thankful for the access to this database granted by Pir Ivedi.

I also want to express my deepest gratitude to my parents Mariapaola and Stefano as well as my sister Irene who supported me during my first arrival in Munich and during my master's studies at the Technical University of Munich. Without their support, I would not have been able to start a doctorate at the Institute of Automotive Technology.

Finally, I want to thank my girlfriend Katarina, who was by my side during the entire doctorate and motivated me during my ups and downs. Without her support, this work would not have been possible.

Garching, February 2022

Lorenzo Nicoletti

Contents

List of Abbreviations

AC	Alternating Current
ADAC	Allgemeiner Deutscher Automobil Club
AHP	Acceleration Heel Point
AWD	All-Wheel Drive
BEV	Battery Electric Vehicle
BIW	Body in White
BMS	Battery Management System
BOF	Ball of Foot
C2B	Cell to Body
COG	Center of Gravity
DC	Direct Current
ETRTO	European Tyre and Rim Technical Organization
FRP	Floor Reference Point
HEV	Hybrid Electric Vehicle
HV	High Voltage
HVAC	Heating Ventilation and Air Conditioning
ICEV	Internal Combustion Engine Vehicle
IM	Induction Machine
LDS	Longitudinal Dynamic Simulation
LDT	Light Duty Truck
LR	Long Range
LV	Low Voltage
MAE	Mean Absolute Error
NEDC	New European Driving Cycle
nMAE	Normalized Mean Absolute Error
PHEV	Plug-in Hybrid Electric Vehicle
PMSM	Permanent Magnet Synchronous Machine
SAE	Society of Automotive Engineers
SgRP	Seating Reference Point
SOP	Start of Production
SQL	Structured Query Language
SR	Standard Range
STP	Shortened Test Procedure
SUV	Sport Utility Vehicle
VW	Volkswagen AG
WLTC	Worldwide Light Vehicles Test Cycle
WLTP	Worldwide Harmonized Light Vehicles Test Procedure

Formula Symbols

In this thesis, the internal and external vehicle dimensions are described with the nomenclature proposed by the Society of Automotive Engineers (SAE). An overview of the considered SAE dimensions is documented in Table A.1 and A.2.

Formula Symbols	Unit	Description
C_{cycle}	$\mathrm{W\,h\,km^{-1}}$	Vehicle consumption in a given driving cycle
c_{d}	-	Aerodynamic drag coefficient
$C_{\text{DS,WLTC}}$	$\mathrm{W\,h\,km^{-1}}$	Weighted consumption in the dynamic segments of the WLTC
c_{r}	-	Rolling resistance coefficient
$C_{\text{WLTP,comb}}$	$\mathrm{W\,h\,km^{-1}}$	Combined vehicle consumption in the WLTP
$C_{\text{WLTC1–2}}$	$\mathrm{W\,h\,km^{-1}}$	Measured vehicle consumption in the WLTP dynamic segments
D_{brake}	mm	Outer diameter of the brake disc
$d_{\text{clear,axle,z}}$	mm	Ground clearance at the axle
$d_{\text{clear,batt,f/r,x}}$	mm	Clearance between the front/rear drive unit and the battery
$d_{\text{clear,batt,z}}$	mm	Clearance between the module and the battery top cover
$d_{\text{clear,gear}}$	mm	Clearance between the differential wheel and the gearbox housing
$d_{\text{clear,man,y}}$	mm	Clearance between the manikin and the door
$d_{\text{clear,ub,z}}$	mm	Ground clearance at the underbody
$d_{\text{COG,veh,x}}$	mm	Distance between the vehicle's center of gravity and the front axle
$d_{\text{critic,f/r,x}}$	mm	Critical length of the front/rear drive unit, expressing the portion of drive unit that limits the battery space
$d_{\text{FRP,AHP,z}}$	mm	Distance between the FRP and the AHP
$d_{\text{FRP,axle,x}}$	mm	Distance between the FRP and the front axle
$d_{\text{FRP,batt,z}}$	mm	Distance between the FRP and the battery
$d_{\text{gb,shafts,12/23}}$	mm	Distance between the gearbox shafts
D_{mach}	mm	Outer diameter of the electric machine
$D_{\text{mach,stat/rot}}$	mm	Outer diameter of the electric machine's stator/rotor
$d_{\text{mach,stat,y}}$	mm	Difference between the stator length and the electric machine length
D_{rim}	mm	Outer diameter of the rim
$D_{\text{rim,inch}}$	inch	Outer diameter of the rim in inches

$d_{\mathrm{SgRP2,batt,z}}$	mm	Distance between the SgRP-2 and the battery upper cover
$d_{\mathrm{SgRP2,lug,x}}$	mm	Distance between the SgRP-2 and the luggage compartment
D_{tire}	mm	Outer diameter of the tire
$d_{\mathrm{veh,lug,x}}$	mm	Distance between the luggage compartment and the vehicle's rear-end
$d_{\mathrm{wa,batt,y}}$	mm	Clearance between the wheel arch and the battery
E_{AC}	Wh	Required energy to refill the battery after the WLTP shorted test procedure
$E_{\mathrm{batt,is}}$	kWh	Installable battery gross energy in the vehicle
$E_{\mathrm{batt,req}}$	kWh	Required battery gross energy to reach a given range
$E_{\mathrm{cell,grav}}$	$\mathrm{Wh\,kg^{-1}}$	Gravimetric energy density at the cell level
$E_{\mathrm{cell,vol}}$	$\mathrm{Wh\,l^{-1}}$	Volumetric energy density at the cell level
E_{STP}	Wh	Consumed battery energy during the shorted test procedure of the WLTP
$F_{\mathrm{axle,f/r}}$	N	Occurring static load at the front/rear axle
F_{G}	N	Weight force of the empty vehicle (no passengers and no luggage)
F_{lug}	N	Weight force of the luggage load
$F_{\mathrm{pass,f/r}}$	N	Weight force of the passengers at the front/rear row of seats
i_{gb}	-	Transmission ratio of the gearbox
K_{cell2mod}	-	Ratio between the module mass and the cell mass
$K_{\mathrm{gross2net}}$	-	Ratio between the net and the gross battery energy
$K_{\mathrm{pack,x/y}}$	-	Battery package factors
$K_{\mathrm{rep,f/r}}$	%	Mass distribution at the front/rear axle
K_{SP}	-	Secondary to primary mass ratio
K_{stat}	-	Ratio between the stator length and the stator diameter
K_{tire}	%	Aspect ratio of the tire
L_{cycle}	km	Distance of a driving cycle
$m_{\mathrm{axle,f}}$	kg	Mass of the front axle, springs, and shock absorbers
$m_{\mathrm{batt,cells}}$	kg	Mass of the cells
$m_{\mathrm{batt,hous}}$	kg	Mass of the battery housing
$m_{\mathrm{batt,mod}}$	kg	Mass of the cells, module housings, and inner module cables
m_{BIW}	kg	Mass of the body in white
$m_{\mathrm{brakes,f/r}}$	kg	Mass of the front/rear brake system
$M_{\mathrm{cell/pack}}$	mm	Matrix storing the cell/pack dimensions of the simulated cells
m_{console}	kg	Mass of the interior console
$m_{\mathrm{frame,other}}$	kg	Mass of the sound insulation, frame reinforcements, cross members, aerodynamic shields, and rock panel covers
$m_{\mathrm{doors,f/r}}$	kg	Mass of the front/rear doors

$m_{\mathrm{gross,n}}$	kg	Calculated vehicle gross mass at the n_{th} iteration
m_{hood}	kg	Mass of the hood
$m_{\mathrm{load,axle,f/r}}$	kg	Occurring maximum load at the front/rear axle
$m_{\mathrm{load,tire}}$	kg	Required tire load
m_{n}	kg	Calculated vehicle empty mass at the n_{th} iteration
m_{PMC}	kg	Primary mass change
m_{rim}	kg	Mass of one rim
$m_{\mathrm{seat,f}}$	kg	Mass of the front seat with frame, cushion, and adjustment mechanism
m_{SMC}	kg	Secondary mass change
m_{trim}	kg	Mass of the interior trim parts
m_{trunk}	kg	Mass of the trunk
m_{wheel}	kg	Mass of one wheel (includes both tire and rim mass)
$N_{\mathrm{cell,serial}}$	-	Number of the serial cells
$N_{\mathrm{cell,tot}}$	-	Number of cells fitting in the available battery space
$N_{\mathrm{serial,max/min}}$	-	Maximum/minimum allowed number of serial cells
$n_{\mathrm{mach,max}}$	min^{-1}	Maximum rotational speed of the electric machine
P_{aux}	kW	Auxiliaries power
$P_{\mathrm{mach,max}}$	kW	Maximum power of one machine
$P_{\mathrm{machs,max}}$	kW	Maximum installed machine power in the vehicle
R_{veh}	km	Vehicle range
$R_{\mathrm{WLTP,comb}}$	km	Combined range in the WLTP
$s_{\mathrm{av,f,y}}$	mm	Available installation space at the vehicle's front-end
$s_{\mathrm{batt,cool,z}}$	mm	Thickness of the battery cooling plate
$s_{\mathrm{batt,cover,z}}$	mm	Thickness of the battery cover
$s_{\mathrm{batt,lowp,z}}$	mm	Thickness of the battery lower protection
$s_{\mathrm{cell,av,z}}$	mm	Available cell space along the vertical direction
$s_{\mathrm{cell,x/y/z}}$	mm	Dimensions of the cells
$s_{\mathrm{gb,flg}}$	mm	Thickness of the gearbox housing including its flanges
$s_{\mathrm{gb,gears,y}}$	mm	Width of the gearbox wheels
$s_{\mathrm{gb,pklk,x}}$	mm	Required installation space for the gearbox parking lock wheel
$s_{\mathrm{gb,seal,y}}$	mm	Required installation space for the gearbox sealing ring
$s_{\mathrm{gb,x/y/z}}$	mm	Dimensions of the gearbox
$s_{\mathrm{lb,y}}$	mm	Width of the longitudinal beam
$s_{\mathrm{lug,x}}$	mm	Length of the luggage compartment
$s_{\mathrm{mach,hous,x}}$	mm	Thickness of the electric machine's housing

$s_{\mathrm{mach,rib,x}}$	mm	Thickness of the electric machine's ribs
$s_{\mathrm{mach,stat,y}}$	mm	Length of the electric machine's stator
$s_{\mathrm{mach,y}}$	mm	Length of the electric machine
$s_{\mathrm{man,hr,z}}$	mm	Headroom of the driver's manikin
$s_{\mathrm{man,leg}}$	mm	Length of the manikin's lower leg
$s_{\mathrm{man,thigh}}$	mm	Length of the manikin's thigh
$s_{\mathrm{man,tot,z}}$	mm	Required vertical space for the driver's manikin
$s_{\mathrm{man,upb,z}}$	mm	Height of the manikin's upper body
$s_{\mathrm{man,y}}$	mm	Width of the manikin's upper body
$s_{\mathrm{pack,x/y}}$	mm	Pack dimensions of the cell
$s_{\mathrm{roof,z}}$	mm	Thickness of the vehicle's roof
$s_{\mathrm{sl,x/y/z}}$	mm	Available battery space in the second level
$s_{\mathrm{tire,y}}$	mm	Width of the tire
$s_{\mathrm{tun,x/y/z}}$	mm	Available battery space in the tunnel
$s_{\mathrm{ub,x/y/z}}$	mm	Available battery space in the underbody
$s_{\mathrm{wa,f/r,y}}$	mm	Width of the front/rear wheel arch
t_{0-100}	s	Acceleration time from 0 to 100 $\mathrm{km\,h^{-1}}$
$T_{\mathrm{mach,max}}$	N m	Maximum torque of the electric machine
$U_{\mathrm{batt,nom}}$	V	Nominal voltage of the battery
$U_{\mathrm{batt,max/min}}$	V	Maximum/minimum allowed battery voltage
$U_{\mathrm{cell,nom}}$	V	Nominal voltage of the cell
V_{batt}	l	Volume of the battery
V_{cell}	l	Volume of the cell
$V_{\mathrm{mach,stat}}$	l	Volume of the electric machine's stator
$V_{\mathrm{tire,min}}$	$\mathrm{mm^3}$	Required tire volume to carry a given tire load $m_{\mathrm{load,tire}}$
$v_{\mathrm{veh,max}}$	$\mathrm{km\,h^{-1}}$	Maximum vehicle speed
$V_{\mathrm{veh,s}}$	$\mathrm{m^3}$	Vehicle substitute volume
$\alpha_{12/23}$	°	Inclination angles of the gearbox shafts
α	°	Inclination angle of the manikin's lower leg
δ	°	Steering angle at the front wheel
ρ_{Alu}	%	Percentage of aluminum in the body in white

1 Introduction

Over the last years, there has been a global effort to reduce human-induced CO_2 emissions [1, 2] and to slow down the side effects of global warming. This effort also concerns the automotive sector, where the industry's focus has shifted towards sustainable mobility. In particular, one of the current challenges is reducing CO_2 fleet emissions [3], which is further enhanced by European regulations [4] aimed at decreasing greenhouse gas emissions of the automotive sector [5].

One way for car manufacturers to reduce local CO_2 emissions is to electrify the powertrain [6]. Vehicles with electrified powertrains (electrified vehicles) are categorized into Hybrid Electric Vehicles (HEVs), Plug-in Hybrid Electric Vehicles (PHEVs), and Battery Electric Vehicles (BEVs) [7, pp. 157-159]. Unlike Internal Combustion Engine Vehicles (ICEVs), electrified vehicles are partially or fully powered by a battery that, in the case of BEVs, can zero out local CO_2 emissions. The absence of local CO_2 emissions makes BEVs particularly promising in the long term to meet progressively stricter regulations.

The reduction in local CO_2 emissions offered by electrified vehicles is transforming the passenger car sector. For example, China started a decade-long subsidy program in 2009 [8] with the goal of electrified vehicles reaching a share of $25\,\%$ of all passenger car sales by 2025 [9, 10]. These policies led to rapid growth of the Chinese BEV market and the emergence of new Chinese manufacturers such as NIO, BYD, and Geely [11]. European manufacturers are also increasing their investments in research and development of BEVs. For example, Volkswagen AG (VW) announced a plan to provide around 70 different BEV models by 2025 [12], while the PSA group unveiled two new platforms (the Common Modular Platform and the Efficient Modular Platform) that can integrate any powertrain (ICEVs, HEVs, BEVs, and PHEVs) [13]. Meanwhile, Tesla has been further increasing its share and production capabilities reaching almost half a million deliveries in 2020 [14].

1.1 Research Motivation

The development of BEVs is still a challenge for both new players and already established manufacturers. BEVs require the usage of new technologies and components such as electric machines, power electronics, and traction battery, all of which have completely different characteristics compared to ICEV components. Due to these new components, BEVs have two main disadvantages when compared to ICEVs: lower range and higher mass.

Most German buyers see the lower range compared to ICEVs [15] combined with a still inadequate charging network and the long charging times as the main criteria against purchasing a BEV [16]. The German neologism *Reichweitenangst* (range anxiety) sums up this problem and denotes: "The fear of not reaching the destination or a charging station with an electrically

powered vehicle due to the limited range of the available battery and of coming to a standstill on the route" [17]. Paradoxically, the ranges offered by current BEVs suffice to cover the vast majority of average customer trips [18, pp. 173-175, 19]. Yet, on rare occasions such as long business or vacation trips, range anxiety is still a major problem.

The second major difference between BEVs and ICEVs is vehicle mass. Current BEVs have higher masses than comparable ICEVs. The main cause for this difference lies in the traction battery [20, p. 9]. Over the last years, energy densities of lithium-ion batteries have been rapidly improving [21]. Nevertheless, their current energy densities are still a fraction of the values achieved by gasoline and diesel. While lithium-ion batteries reach pack-level densities between $150\,\mathrm{W\,h\,kg^{-1}}$ and $175\,\mathrm{W\,h\,kg^{-1}}$ [15], gasoline and diesel fuels have values around $12\,800\,\mathrm{W\,h\,kg^{-1}}$ and $11\,800\,\mathrm{W\,h\,kg^{-1}}$, respectively [22, p. 34]. The same applies to the volumetric level, where the lithium-ion batteries' pack-density (approx. $250\,\mathrm{W\,h\,l^{-1}}$ [21]) is below gasoline (approx. $9000\,\mathrm{W\,h\,l^{-1}}$ [23, p. 73]) and diesel (approx. $10\,000\,\mathrm{W\,h\,l^{-1}}$ [24, p. 6]).

The low energy densities of lithium-ion batteries are partially balanced by the higher powertrain efficiency of BEVs. While ICEVs attain peak tank-to-wheel efficiencies between $30\,\%$ (gasoline engines) and $40\,\%$ (diesel engines), BEVs can achieve values of approx. $85\,\%$ [25]. However, the higher efficiency of BEV powertrains is not enough to compensate for their low energy density. This renders the battery one of the heaviest and largest components in a BEV. On the one hand, the high mass of the battery increases vehicle consumption. On the other hand, its large dimensions complicate its integration into the vehicle. The combination of these effects affects the maximum achievable range of BEVs. For an improvement of current BEVs, a detailed analysis of the battery and its impact on the vehicle concept design is required.

1.2 Research Objective

At the start of developing a new BEV, concept engineers need to define several design parameters [26]. Examples include acceleration time, maximum speed, and target range. These design parameters form the vehicle portfolio that is the basis for the vehicle concept design [27]. A crucial design parameter is vehicle mass, as it affects consumption and determines the required battery energy to cover a certain range. Due to limited experience with BEVs, concept engineers have difficulties estimating the mass during the vehicle concept design phase. As a result, BEV development is an iterative process, in which the vehicle's mass is gradually corrected as the BEV is detailed. At each new mass iteration step, the required battery energy must be adjusted to maintain the target range. Due to low energy densities of lithium-ion batteries, adjustments of a few $\mathrm{kW\,h}$ have a considerable impact on the battery's volume and mass [28].

The vehicle mass fluctuations occurring during the vehicle concept design phase do not exclusively impact the battery, but also involve other mass-dependent components such as wheels, electric machines, and gearboxes [27]. The dimensions of these components in turn influence the available battery space, which ultimately defines the installable energy in the vehicle. Therefore, a correct estimation of the available battery space requires the modeling of several other components. Since the concept engineer cannot model the entire package of the vehicle, this inevitably leads to further errors in estimating the installable battery energy.

Ensuring that target ranges are achieved requires a consideration of mass and volume fluctuations occurring on the battery and other components. For this scope, a tool-based approach is developed that is able to model both mass and package. This tool must estimate occurring

mass fluctuations during the vehicle concept design phase, describe their effects on the vehicle components (in particular the battery), and estimate their impact on the available battery space. By fulfilling these requirements, it is ultimately possible to estimate the installable battery energy and determine the maximum feasible range of future BEVs.

1.3 Position in the Vehicle Concept Research Group

This chapter discusses the relation of this thesis with respect to other running theses at the Institute for Automotive Technology at the Technical University of Munich. This thesis is developed in collaboration with the colleagues König [29], Koch [30], and Schockenhoff [31] of the Vehicle Concept Research Group. Figure 1.1 presents the theses based on two main research foci. The first research focus distinguishes between electric (level 1 to level 3 vehicles as defined in [32]), autonomous (level 3 to level 5 vehicles as defined in [32]), and shared (for different shared-mobility scenarios) vehicles. Regarding the second research focus, a distinction is made between modeling package and components, modeling software (driving strategies and trajectory planning), and improving the structure of the current development process.

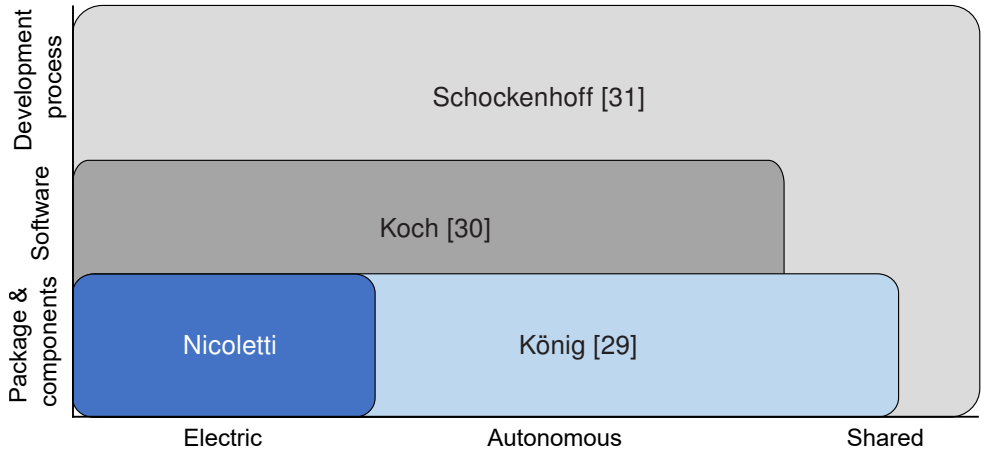

Figure 1.1: Positioning of this thesis in the Vehicle Concept Research Group [33].

In contrast to the current thesis, which focuses on non-autonomous BEVs, König et al. [34] extend the methodology to describe how the vehicle concept design can be adapted to derive optimal autonomous vehicles. To answer this question, König et al. focus on features such as non-conventional passenger compartments and seat layouts [35] or the influence of auxiliary consumers on the vehicle concept [34, 36]. Since König also focuses on vehicle package and vehicle consumption, many component sizing models, as well as the longitudinal simulation used in the current thesis, are developed in collaboration with him.

Koch focuses on the vehicle driving strategy. Through detailed modeling of the longitudinal dynamics and an optimization approach, he identifies the most efficient driving profile (eco-driving) for different powertrain topologies [37, 38]. Hereby, he describes the potential that can be obtained with an optimal eco-driving powertrain. He does not consider the vehicle package, but includes some of the mass and inertia models developed in this thesis to describe the inertial losses of the vehicle. The current thesis relies on several efficiency maps (for electric machines and gearboxes), which are developed in collaboration with him.

Schockenhoff [31] questions the current concept development process in the context of electric, autonomous, and shared vehicles. He develops a method that derives vehicle concepts based on user needs of electric, autonomous, and shared mobility. For this purpose, he considers vehicle properties that conventional vehicle concepts also possess (such as driving dynamics) and novel properties (such as driving styles and quality of automation). He models the vehicle package by extending König's tool with additional aspects, such as driving style-related speed profiles instead of conventional driving cycles.

1.4 Thesis Structure

This thesis is divided into seven chapters (Figure 1.2). Chapter 1 presents the research motivation and highlights the importance of a tool-based approach to support BEV development. Chapter 2 begins with the description of the main features of a BEV architecture (Section 2.2). Subsequently, the effects of mass fluctuations on vehicle mass and package are explained (Section 2.3). Based on these notions, the existing methods for modeling BEVs are evaluated (Section 2.4) and the research gap is identified (Section 2.5).

Chapter 3 presents the structure of the developed tool. Section 3.1 lists the input parameters of the tool. Subsequently, the developed database system that enables an automatic update of the models, is described (Section 3.2). Section 3.3 presents the implemented longitudinal simulation. Then, the models used to size the volumes (Section 3.4) and masses (Section 3.5) of the vehicle components are described. Section 3.6 summarizes the tool's capabilities.

Chapter 4 performs a validation of the longitudinal simulation (Section 4.1). Then, the models used for the sizing of volumes (Section 4.2) and masses (Section 4.3) of the vehicle components are validated. Section 4.4 applies the tool to simulate a set of existing BEVs. Finally, Section 4.5 summarizes the main findings of the validation.

Chapter 5 assesses the impact of different electrification strategies on future BEVs. Section 5.1 simulates the influence of different cell types, while Section 5.2 assesses the potential of a novel (not yet on the market) battery integration principle. Subsequently, Section 5.3 performs an optimization of three reference BEVs to identify which cell types and integration principles offer the greatest potential for future BEVs. The chapter closes with a summary of the main findings of the thesis (Section 5.4).

Chapter 6 questions the methodological procedure this thesis follows, discusses its results, and outlines room for improvement. Finally, Chapter 7 provides a summary of the thesis.

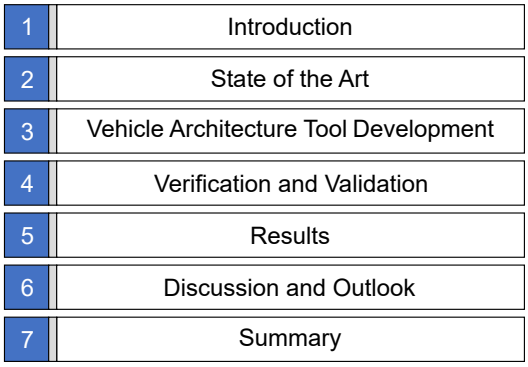

Figure 1.2: Structure of the current thesis.

2 State of the Art

This chapter begins with positioning the current thesis in the vehicle development process (Section 2.1). Subsequently, Section 2.2 defines the main features of BEV architectures. Afterward, Section 2.3 categorizes the secondary effects that occur when developing a new vehicle architecture and outlines the problems they cause. Based on these notions, the existing methods for modeling vehicle architectures are compared (Section 2.4). Finally, as a result of this comparison, the research gap is identified (Section 2.5).

2.1 Position in the Vehicle Development Process

The vehicle development process (Figure 2.1) describes the steps beginning with the product idea until the Start of Production (SOP) [39, p. 7]. It can be divided into four phases: planning, definition, realization, and production [40].

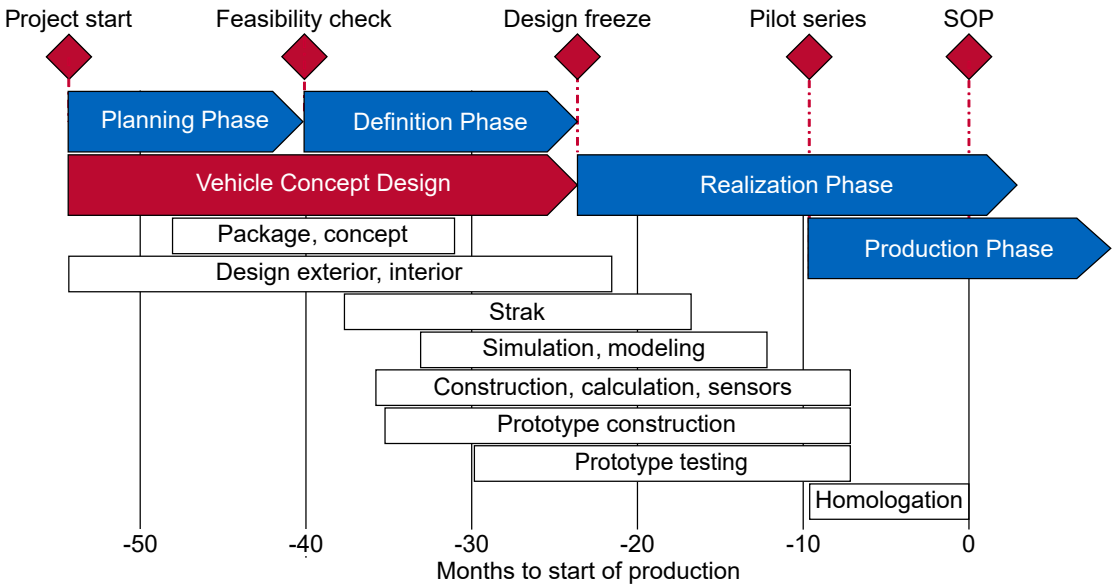

Figure 2.1: Vehicle development process based on [40]. The process is divided into phases (blue arrows) and milestones (red rhombuses). The specifications occurring during each phase are marked as white rectangles and the position of this thesis is denoted with a red arrow.

The planning phase starts approx. 55 months before the SOP with a product idea, which is the result of a scenario analysis of the customer needs [41, p. 9]. During the planning phase, the product idea is detailed and a vehicle property portfolio is outlined. Subsequently, target values for the vehicle properties are defined [42, p. 10]. The planning phase concludes with a feasibility check of vehicle properties, production costs, and capacities [43, pp. 1040-1043].

The definition phase starts approx. 40 months before SOP. The vehicle concept derived in the previous phase is further detailed until it is ready to be forwarded to the realization phase [44, p. 5]. The design freeze initiates the handover to the realization phase [39, p. 7], which concludes the specification of the vehicle design [45, p. 17].

In the realization phase, vehicle prototypes are constructed and tested. The end of the prototype testing overlaps with the beginning of the production phase, which begins with the launch of a pilot series [39, p. 7]. Knowledge gained from the pilot series is used for the actual series production. While the realization phase is concluded with the SOP, the production phase continues over the vehicle's entire lifetime by performing tasks such as customer care and quality control.

This thesis focuses on vehicle concept design, more precisely on the planning phase and the first steps of the definition phase. This part of the development process plays a central role since it defines the vehicle architecture, which is the foundation for any further development. Errors and conflicts not identified during the vehicle concept design have expensive consequences since the cost of changes exponentially increases in the following development steps [46, p. 159].

2.2 Vehicle Architecture

In the current literature, there are several definitions of vehicle architecture [39, pp. 10-11, 44, p. 13, 47, pp. 6-7, 48]. This thesis employs the definition presented in a previous publication of the author [11], according to which a vehicle architecture is described based on its four main features (Figure 2.2): dimensional concept (Subsection 2.2.1), drive topology (Subsection 2.2.2), component models (Subsection 2.2.3), and dimensional chains (Subsection 2.2.4).

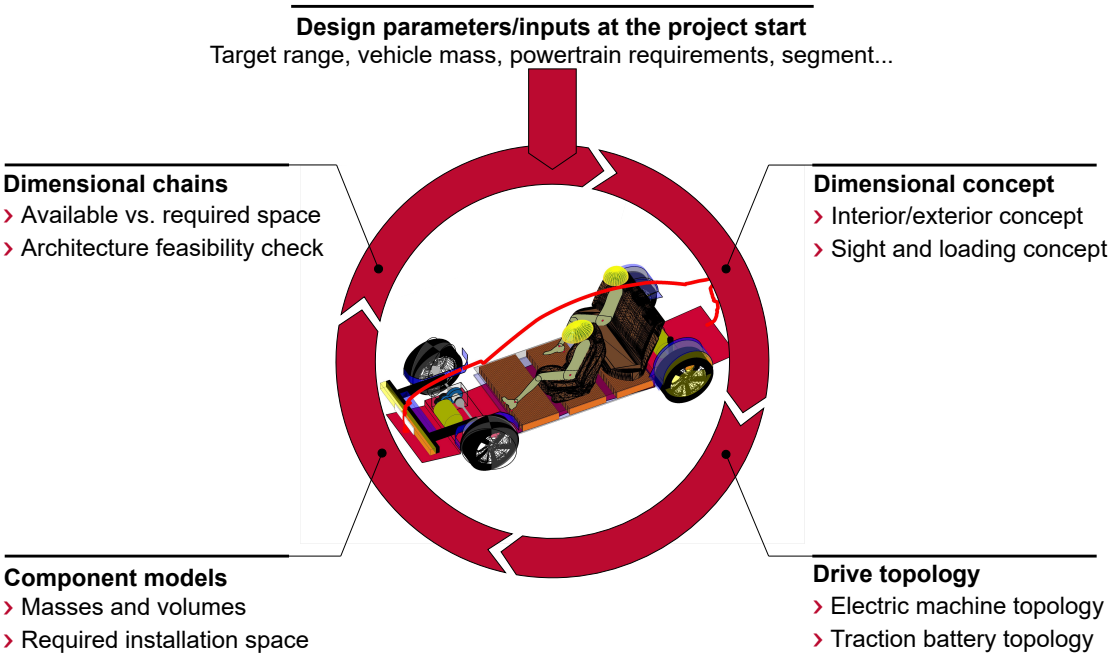

Figure 2.2: Architectural features. Based on [11].

Modeling the vehicle architecture begins with the design parameters available at the project start (Figure 2.2) and is based on the four architectural features that are detailed in the planning and definition phases. The next sections detail these architectural features.

2.2.1 Dimensional Concept

Within the framework of the dimensional concept, engineers and designers define the vehicle proportions. Since the dimensional concept describes the external and internal dimensions of the vehicle, it influences the available installation space inside the vehicle [49]. According to [11, 50, p. 5], this architectural feature is divided into exterior concept, interior concept, sight concept, and entrance/exit/loading concept. The following subsections explain these four tasks in detail. Subsequently, the existing design strategies for the derivation of BEV architectures are presented.

Exterior Concept

The exterior concept defines the vehicle's external dimensions and assigns it to a specific segment and body type. The standards defined by the SAE are commonly used for defining the external dimensions. SAE standard J1100 [51] specifies a set of dimensions that form the basis for defining the exterior concept and enable a comparison with competitor products (Figure 2.3). Some of the most widely used external dimensions are the vehicle overhangs (L104, L105), its wheelbase (L101), its length (L103), and its height (H100). When designing the exterior concept, different legal requirements need to be considered. An example is the vehicle ground clearance $d_{\mathrm{clear,ub,z}}$ [52, pp. 62-63, 53]. Table A.1 specifies an overview of the exterior concept dimensions considered in this thesis.

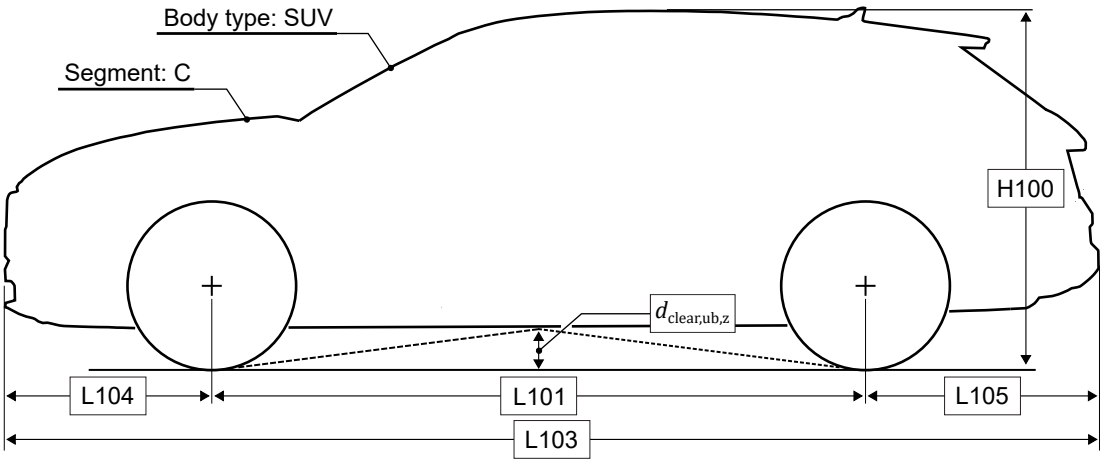

Figure 2.3: Exterior concept dimensions, segment, and body style.

Several standards specify a vehicle segmentation [44, p. 12, 54, 55]. For this scope, the vehicles are divided into classes based on features such as external dimensions, number of passengers, or interior volume. In addition to the external dimensions and segment, another distinguishing feature is the vehicle body type [47, p. 9], which is categorized into different variants [7, p. 146, 56]. However, this categorization is not static, but rather subject to changes over time, e.g. due to the increasing number of crossover concepts such as the combination between van and coupé or coupé and limousine [7, p. 170].

This thesis follows the segment denomination from A00 to E described by J. Fuchs [44, p. 12], since this method is used by most car manufacturers. Regarding body type, the seven variants proposed by Achleitner et al. [7, p. 146] are reduced to three basic categories: Sport Utility Vehicle (SUV), sedan (or limousine), and hatchback. Finally, this thesis follows the nomenclature laid out by the SAE when referring to the internal and external vehicle dimensions.

Interior Concept

The interior concept defines various ergonomic aspects, such as the positioning of the steering wheel and the seat layout. Table A.2 gives an overview of the interior concept dimensions considered in this thesis. When defining an interior concept, the driver's anthropometry plays a major role [45, p. 14]. To describe the dimensions of the driver (and the other occupants), the concept engineers use standardized manikins that categorize the population in different percentile groups. Usually, the concept engineers employ the 95th male manikin and the 5th female manikin [57, p. 182]. The former specifies the maximum required space in the vehicle while the latter ensures that also occupants with smaller body sizes can reach pedals and steering wheel. Basing the interior concept design on these manikins ensures that the passenger compartment is comfortable for 95 % of the male and female population [58].

A specific manikin can be positioned in the vehicle using reference points. Important reference points to mark the driver's position are the Seating Reference Point (SgRP), the Acceleration Heel Point (AHP), and the Ball of Foot (BOF). The SgRP (①, Figure 2.4) describes the manufacturer's intended position for the driver's hip [59, p. 6], while the AHP (②, Figure 2.4) defines the location of his heel [51, p. 25]. The BOF (③, Figure 2.4) describes the contact point between foot and pedal. The manikins of the second row have a hip point (the SgRP-2, ④ in Figure 2.4) and a heel point (⑤, Figure 2.4), which is denoted as Floor Reference Point (FRP).

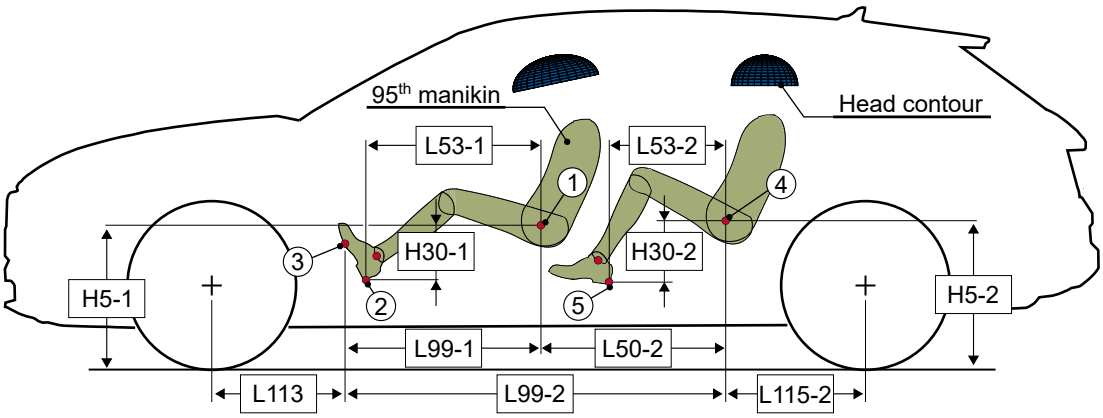

Figure 2.4: Interior concept dimensions and reference points SgRP ①, AHP ②, BOF ③, SgRP-2 ④, and FRP ⑤. Although the L113 and L115-2 belong to the exterior concept, they are shown in this figure since they couple exterior and interior concepts.

Most of the interior concept dimensions are defined by the reference points. For example, the vertical distance between AHP and SgRP, the H30-1, quantifies the driver's seating height, while the longitudinal distance between BOF and SgRP (L99-1) quantifies his legroom. More information regarding the internal dimensions is specified in the SAE standards [59–63].

While the passengers' feet, legs, and upper bodies are described with standardized manikins, the SAE proposes using head contours to model the head. The head contours are described with ellipsoids and defined in the SAE standard J1052 [64]. They represent the passenger's head location and are expressed in percentiles. For example, if the 95th percentile head contour is tangent to the interior compartment roof, this means that 5 % of the population would be in contact with the roof while sitting in the vehicle.

Sight, Entrance/Exit, and Loading Concept

Since the majority of the information required for driving is received visually [65, p. 21], the purpose of the sight concept is to ensure the driver visibility. For this scope, the driver's field of view is described using surfaces that are positioned according to the position of the driver's eyes. The SAE standard J941 describes the driver's eye position with an eye ellipse [66] (red ellipse, Figure 2.5), while the field of view can be modeled as a surface according to [67] (light blue surface, Figure 2.5). To ensure adequate visibility, no part (with the only exception of the A-pillars) shall collide with the field of view surface [67, pp. 42-43].

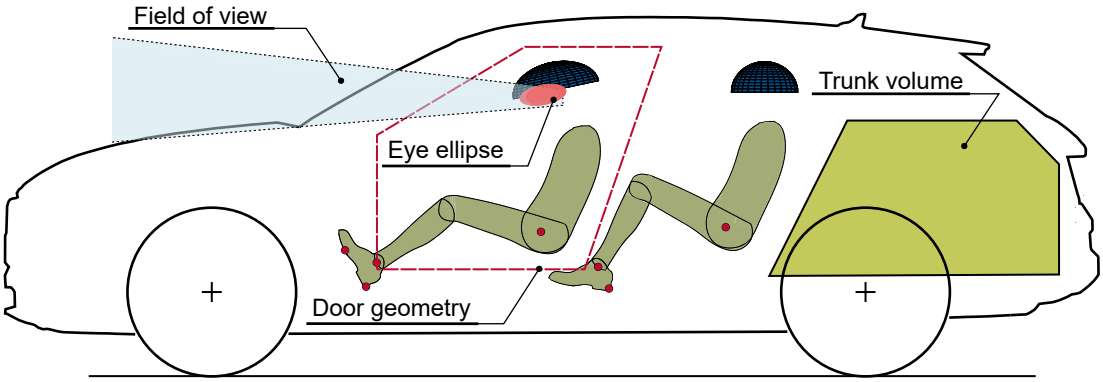

Figure 2.5: Sight, entrance/exit, and loading concept.

The entrance and exit concept must ensure comfortable access into the vehicle and define the position and geometry of the doors (dashed red line, Figure 2.5). On the one hand, the upper and lower edges of the door geometry depend on exterior concept characteristics, such as the roof and underbody position. On the other hand, front and rear edges are defined by the seating position [68, p. 65].

The loading and unloading concept defines the position and volume of the trunk compartment (green surface, Figure 2.5). The trunk volume has a high influence on the everyday usability of the vehicle [69, p. iv, 70] and is affected by external dimensions [42, p. 82], the position of the last row of seats, and the drive topology [71, pp. 8-9]. Standards such as the ISO 3832 [72] detail an approach to defining trunk volume.

With the set of dimensions shown in Figure 2.3 - 2.5, it is possible to define the dimensional concept of the vehicle. However, due to the electric powertrain, the dimensional concept needs to be adapted depending on the applied design strategy. The following section, therefore, outlines existing design strategies for BEVs.

Design Strategies

When defining a dimensional concept, the design strategy determines whether the same rules and proportions suitable for ICEVs can be employed or whether adaptation is required to integrate the electric powertrain. The former case is defined as conversion design, while the latter is commonly known as purpose design.

Conversion design is an adaptation strategy where vehicles originally intended as ICEVs are equipped with an electrified powertrain [73, pp. 140-141]. On the one hand, this strategy allows reusing existing production facilities [41, p. 4], thus saving time and costs. On the other hand, the resulting vehicle architecture has to be derived under the constraints imposed by the ICEV architecture [6].

Purpose design is not restricted by these constraints, since it defines a vehicle architecture exclusively for BEVs [6]. The result is an architecture where the vehicle is designed considering the specific requirements of the electric powertrain, thus reaching an optimal solution from the technical point of view [41, p. 4]. However, these advantages come with higher costs and development time than the conversion design strategy.

A third case, which is a combination of purpose and conversion design, is the multi-traction strategy. It consists of deriving a vehicle architecture suitable for all powertrains [74]. Examples are the PSA group's platforms that can be used for ICEVs, BEVs, and PHEV [13]. Although the multi-traction approach offers a better integration than conversion design, since it considers the battery already at the start of vehicle architecture development, it is still constrained by the requirements of the ICEV and PHEV powertrains.

To fully understand the potential of different design strategies an analysis of their influence on the powertrain components, i.e. on the drive topology of the vehicle, is required. For this scope, the following section outlines the characteristics of BEV drive topologies.

2.2.2 Drive Topology

Drive topology defines the choice, dimensioning, and location of the powertrain components [49, p. 23, 58]. These components are traction battery, power electronics, electric machines, and gearboxes (including driveshafts and, if required, differentials) [6, 75, p. 5].

The traction battery supplies the powertrain components with energy. It consists of several cells arranged in interconnected modules [76, p. 180]. The current technology for the cells is the lithium-ion chemistry [77, p. 18].

The power electronics includes the inverter, the DC-DC converter, and the charger. The inverter commutes the Direct Current (DC) of the battery, into Alternating Current (AC) for the electric machines [78, p. 3]. In the recuperation phase, it carries out the reverse transformation [6]. The inverter is normally integrated into a compact unit with the electric machine [41, p. 45] thus reducing complexity and cutting costs, e.g. due to the shorter wiring path [22, p. 42]. The DC-DC converter supplies the Low Voltage (LV) components by converting the battery's High Voltage (HV) into LV. The last component is the charger, which converts the current from the charger plug to meet the current and voltage requirement of the battery [6]. The charger is typically positioned so that the wiring path to the battery is minimized [79, p. 82].

The electric machines transform the electrical power into mechanical power [6]. The two leading technologies at the moment are Induction Machine (IM) and Permanent Magnet Synchronous Machine (PMSM) [80, p. 67]. Electric machines can provide the maximum torque at low rotational speeds and do not require a clutch system. Furthermore, the speed range of electric machines covers the entire speed range required by the vehicle and omits the need for a transmission with several reduction stages (as used in ICEVs) [80, p. 68-69]. For this reason, single-speed gearboxes are the current solution for most BEVs to transfer the torque from the electric machine to the wheels [26].

Due to the above-cited constraints and depending on the position of the electric machine and traction battery, the location of both power electronics and charger can be estimated. For this reason, it will be further distinguished between electric machine topology (position and number) and battery topology (position and shape).

Electric Machine Topology

Electric machines have compact dimensions and can be placed with a high degree of freedom, enabling machine layouts that would otherwise be impossible for ICEVs, such as one machine on each axle or two machines on the same axle [6]. There are three main electric machine topologies [75, pp. 6-8]: central machine (Figure 2.6a and 2.6b), machine near-the-wheel (Figure 2.6c), and wheel hub machine (Figure 2.6d).

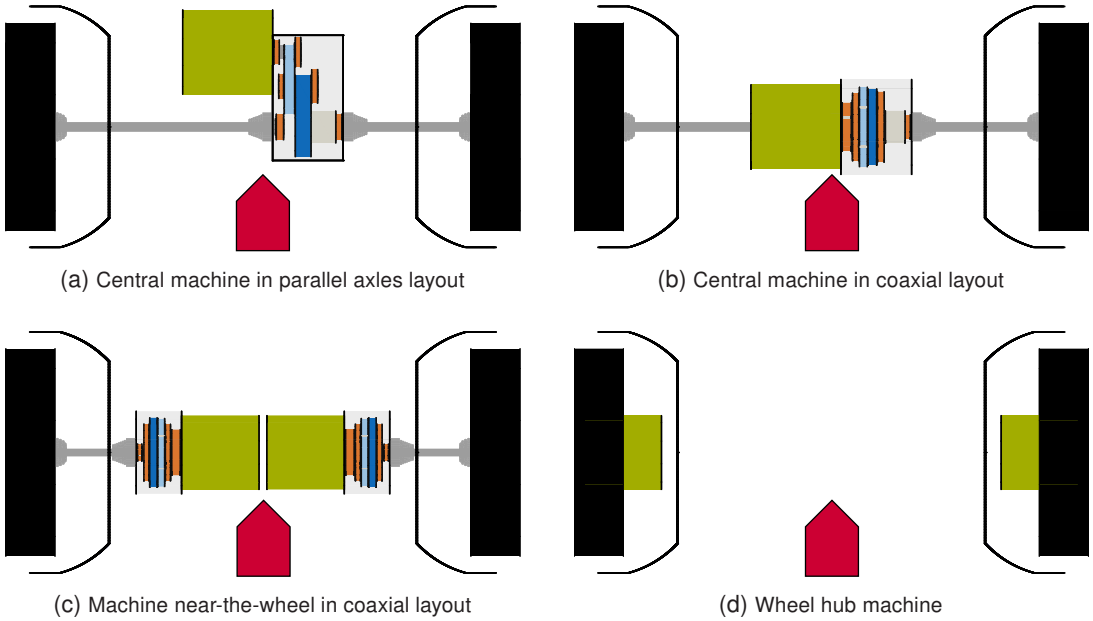

(a) Central machine in parallel axles layout

(b) Central machine in coaxial layout

(c) Machine near-the-wheel in coaxial layout

(d) Wheel hub machine

Figure 2.6: Electric machine topologies and their components: electric machine (green), bearings (orange), gears (light blue and blue), differential cage (light gray), driveshafts (dark gray), and tires (black). The red arrow points toward the driving direction.

The central machine topology has a maximum of one electric machine per axle. The machine can be coupled with a parallel axles gearbox (Figure 2.6a) or a planetary gearbox (Figure 2.6b). The former is commonly installed in small BEVs such as the VW e-Up! and the VW e-Golf [81]. The latter can be found in vehicles of a higher price bracket, such as the Jaguar I-Pace [82] and the Audi e-tron 55 [83]. Independent of the layout, the gearbox is coupled with a differential that splits the torque to the wheels. For BEVs, the differential is usually integrated into the gearbox housing, thus building a compact transmission unit.

The second topology (Figure 2.6c) has two machines. This configuration does not require a differential [84], since there is one machine per wheel. An example of a series vehicle with a near-the-wheel topology is the Audi e-tron S [85].

The wheel hub machine topology (Figure 2.6d) is equipped with two machines integrated directly into the wheels. For this topology, neither the differential nor the driveshafts are required. This results in lower rotating masses, fewer components, and a compact unit. The main drawback is the high undamped mass of the driving unit, which impacts driving dynamics [23, p. 199].

Another possible variant is the direct drive [75, p. 7]. Since electric machines can provide high power over a wide speed range [23, p. 103], direct coupling with the wheels (without a gearbox) is also possible [86]. Although this configuration does not require a gearbox unit, due to the missing transmission ratio of the gearbox, the required torque at the machine increases and, since the machine dimensions are proportional to its torque [77, p. 312], leads to larger and heavier machines.

This thesis considers the topologies with central machines and machines near-the-wheel. Technical solutions for wheel hub machines have been around for years [87, 88] and are still being developed [89–91]. Nevertheless, wheel hub machines are still not technically mature, they are expensive, and cause an increase of the unsprung masses [7, p. 158]. For this reason, this topology will not be considered. The same applies to the direct drive variant. An overview of the considered electric machine topologies is documented in Section B.1.

Battery Topology

Due to the large variety of battery shapes and positions, a categorization of the existing cases is required. In the scope of this thesis, battery topology is described in terms of two features: its integration principle and its battery shape [6]. The integration principle describes the position of the battery and how it impacts the dimensional concept. Based on the categorization proposed by J. Fuchs [44, p. 13], it is possible to distinguish between three integration principles: highfloor, mixedfloor, and lowfloor (Figure 2.7).

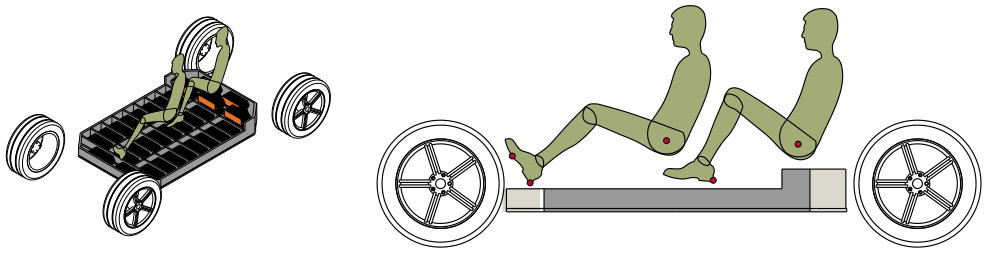

(a) Highfloor principle with second level of cells

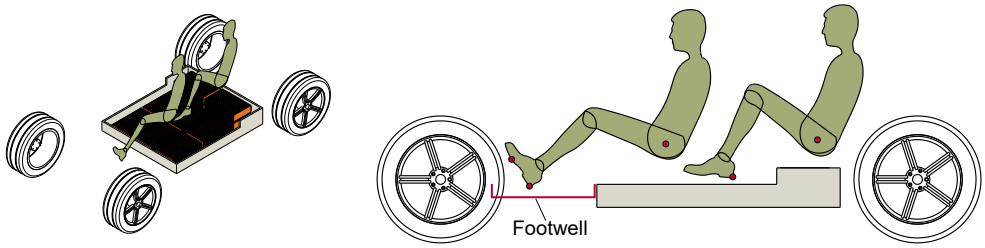

(b) Mixedfloor principle, with second level of cells

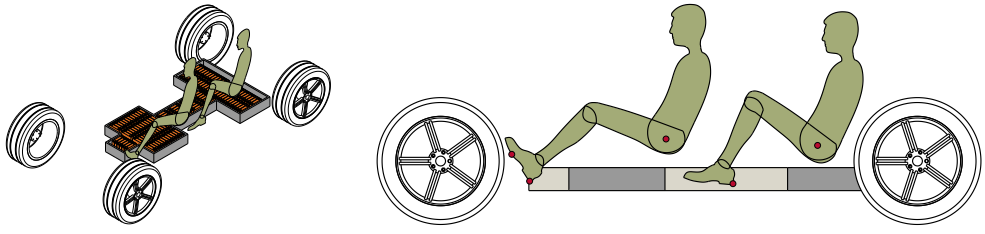

(c) Lowfloor principle

Figure 2.7: Existing integration principles. Based on [6].

The highfloor principle (Figure 2.7a) is suitable only for purpose design vehicles such as the BMW i3. The battery is placed in the underbody to maximize usage of space comprised between the front and rear axles. To free up space required for the battery, all the reference points of the vehicle occupants (and thus the entire passenger compartment, Subsection 2.2.1) have to be shifted vertically [11]. Therefore, vehicles with a highfloor principle have a greater H100 and frontal area [44, p. 14], which increases drag losses and raises vehicle consumption.

The mixedfloor principle (Figure 2.7b) is employed for purpose design vehicles, such as the Nissan Leaf [92, pp. 145-146], and conversion design vehicles, such as the VW e-Up! [93, p. 38]. For these vehicles, the battery length is limited along the longitudinal direction by the driver's foot. This concept can be imagined by cutting off battery space in proximity of the driver's foot, thus creating a *footwell*. In some cases, such as the Porsche Taycan [94] or the Audi e-tron GT [95], the footwell is located at the second seating row. With this integration strategy, the battery does not impact all the reference points of the passengers. For example, in the configuration shown in Figure 2.7b, the driver's AHP does not have to be shifted (as it is the case for Figure 2.7a). On the one hand, the footwell causes a loss of space, since it reduces the usable battery length. On the other hand, this loss can be compensated by building an additional level of cells underneath the second row of seats.

The lowfloor principle (Figure 2.7c) is typically found in conversion design vehicles, such as the VW e-Golf, and multi-split vehicles, such as the Peugeot e-208. This integration principle fits the battery in the tunnel and below the first and second seating rows. This way, none of the passengers' reference points are affected by the electric powertrain. Although this strategy does not increase H100 (as is the case with the other two integration principles), the usable battery space is strongly limited.

The second feature to describe battery topology is battery shape. As the name suggests, this feature describes the form of the battery. BEV manufacturers have adopted differing strategies, leading to a high variability of shapes. Nevertheless, every battery can be described using a combination of basic shapes. For this scope, based on a previous publication of the author [6], three basic shapes are defined: rectangular, drop and T-shape (Figure 2.8).

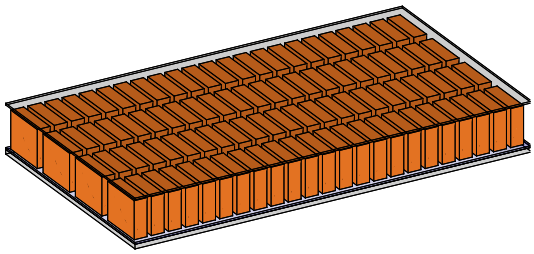

(a) Rectangular shape, e.g. BMW i3

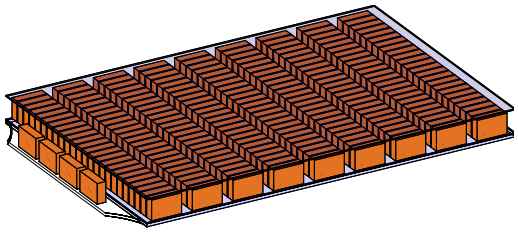

(b) Drop shape, e.g. Jaguar I-Pace

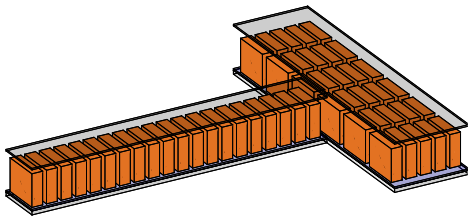

(c) T-shape, e.g. GM EV1

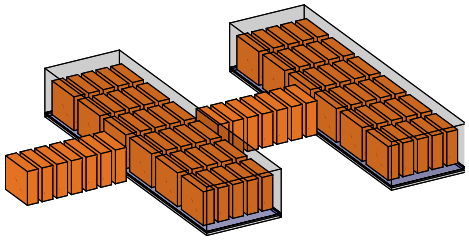

(d) T-shape with extra compartment underneath the first row of seats, e.g. Opel Corsa-e

Figure 2.8: Existing basic battery shapes. Based on [6].

The rectangular shape (Figure 2.8a) is used in highfloor and mixedfloor vehicles. Due to its simple form, it is not possible to maximize the space usage in the vehicle. This disadvantage is overcome by the drop shape (Figure 2.8b). The drop shape can be found only in highfloor integration strategies and is therefore suitable only for purpose design vehicles. The corners at the front (and sometimes also at the rear) edge of the battery are cut off, which enables placing the battery closer to the wheels. This leads to optimal usage of the space between the front and

rear axles, yielding high installable battery energy. Nevertheless, the higher energy comes with the price of a more complicated housing shape.

The last basic shape, the T-shape (Figure 2.8c), was employed in one of the first series BEVs: the General Motors EV1 [96]. At the time, this shape was chosen due to limited knowledge about BEV architectures, as it offered an easy integration into the vehicle. Today, it is employed coupled with a lowfloor integration principle for conversion and multi-split vehicles. The battery is fitted in the spaces resulting from the removal of the ICEV powertrain, i.e. in the tunnel and below the second seating row. To further increase the installed energy (for example for the VW e-Golf [97, p. 60] and the Opel Corsa-e [98]), the T-shape is extended with a further cell pack placed underneath the first row of seats (Figure 2.8d).

Not every BEV has a basic battery shape, nevertheless, the shape of every battery can be described by combining the basic shapes. For example, the Audi e-tron has a battery with two levels: the first is placed in the vehicle underbody and is shaped like a drop shape. The second level is fitted below the second seating row and has a drop shape as well. In the case of the Audi e-tron, the second level fits five extra modules and increases the installed gross energy by $13.2\,\mathrm{kWh}$ [83]. Section B.2 specifies a detailed overview of existing battery shapes.

The combination of battery shapes and integration principles generates a high number of possibilities. To show which configurations offer the best integration, a potential assessment is conducted [6]. A set of existing BEVs is analyzed, and for each vehicle the integration principle and basic battery shape are identified. The integration potential is then evaluated by dividing the gross energy of the battery by the empty mass of the vehicle, and the dimensions of the passenger compartment. This calculation yields the total gravimetric energy density (how many Wh are comprised in $1\,\mathrm{kg}$ of the vehicle), and the total volumetric energy density (how many Wh are comprised in $1\,\mathrm{l}$ of passenger compartment). Since the usual installation space for the battery is below the passenger compartment, its volume and not the volume of the whole vehicle is accounted for the total volumetric energy density. Figure 2.9 shows the results.

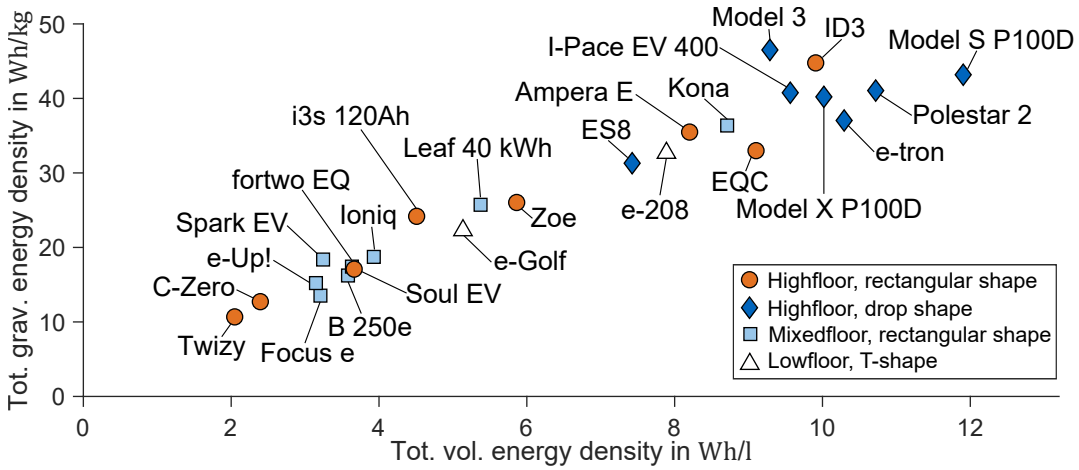

Figure 2.9: Total vol. energy density (ratio between battery energy and passenger compartment volume) vs. total grav. energy density (ratio between battery energy and vehicle mass). Based on [6].

The vehicles in the upper right corner of Figure 2.9 are the ones with the highest integration potential both gravimetric and volumetric. They usually mount a drop or rectangular shape combined with a highfloor integration principle (and they are mostly purpose design vehicles). The mixedfloor integration principle appears to be always coupled with a base rectangular shape and does not yield an integration potential as high as the highfloor option. The same applies to

the lowfloor principle. Since this thesis focuses on purpose design vehicles, the highfloor and mixedfloor principles will be further considered. Although the lowfloor option is a strategy that is still in use today, it is not investigated further in this work due to its low potential. Consequently, batteries with a T-shape are also neglected, as they are exclusively paired with a lowfloor integration principle.

2.2.3 Component Models

To derive the vehicle architecture and its package, the required space for the vehicle components needs to be estimated. The component models fulfill this task [49] by estimating the volume and mass of the components. For this scope, three model types can be employed [99, pp. 28-29]:

- Physical models: Mathematical models derived from physical laws.
- Semi-physical models: Incorporate physical equations and information that can be obtained from measured data.
- Empirical models: Statistical models derived by evaluating measured data.

Physical models provide an accurate representation of the system they describe. However, their creation requires detailed knowledge of the system being modeled. Consequently, physical models often need inputs that are not available during the vehicle concept design phase [39, p. 37]. Since the aim of this thesis is to model vehicle architectures during the vehicle concept design phase, only semi-physical and empirical models are suitable.

An example of a semi-physical model is the BEV gearbox model developed in the theses of Köhler [100, 101], which applies physical correlations and empirical factors to model gear dimensions and mass. Examples of empirical models are linear regressions and constant values. The former method is suitable if a correlation between the to-be-modeled component dimension and other variables can be observed. If no statistically significant regression can be derived, the dimension can be modeled with a constant value (as mean value or median), which means that its value is independent of other variables [102]. Figure 2.10 shows a linear regression for estimating the mass of a rim from its outer diameter.

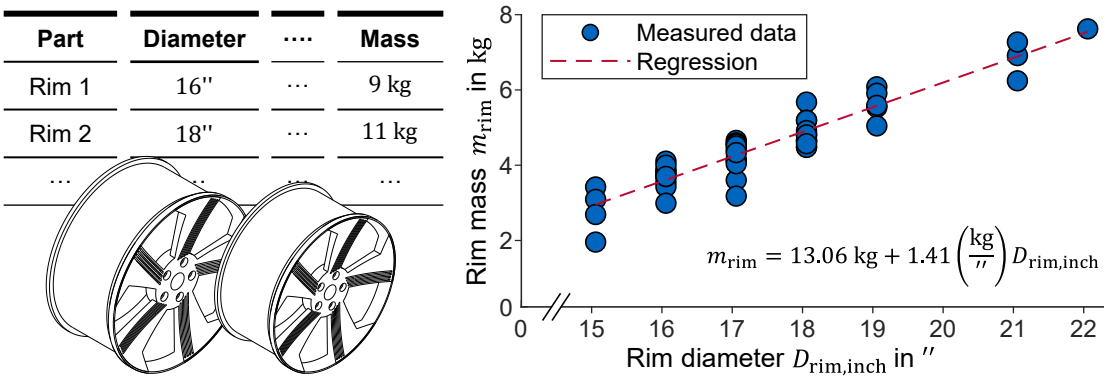

Figure 2.10: An exemplary procedure for the creation of an empirical model. Based on [103].

The first step in defining an empirical model is creating a component database of existing rims (left-hand side of Figure 2.10). The component database contains the to-be-modeled variable (in this case the mass of the rim), and the variables used for modeling (in this case the rim diameter). Subsequently, the data is evaluated following the approach described by Felgenhauer [102], thus deriving an empirical regression model (right-hand side of Figure 2.10) or a constant value.

The quality of the model approximation is further estimated using statistical units such as the coefficient of determination (R^2), the Mean Absolute Error (MAE), and the Normalized Mean Absolute Error (nMAE) [104, pp. 16-18].

Empirical models offer an advantage in the planning and definition phases since they require a limited amount of input. One drawback is that, for modeling each component, a corresponding component database has to be created and evaluated. This results in dozens of tables (one for each component), all of which have to be stored separately and cause data dispersion. A further disadvantage is *data aging*, i.e. the data used for deriving empirical models becomes outdated over time. As a result, the derived empirical models are no longer valid. To counter this problem, new data has to be collected and the empirical models used for the vehicle architecture derivation have to be updated manually.

A possible solution to address the above-cited disadvantages is to store the component databases in a Structured Query Language (SQL) database. Furthermore, it is possible to implement the SQL database so that all the models can be automatically updated when new data is added [11].

2.2.4 Dimensional Chains

The last step of architecture derivation is to verify the feasibility of the vehicle package. This task is achieved with dimensional chains which are used to estimate the available space in the vehicle, position the components, and ensure that no collision occurs [105]. As shown in Figure 2.11, a dimensional chain consists of the sum of component sizes and the distances between adjacent components projected along a defined coordinate direction [39, p. 11]. By combining dimensional chains with the component models, the package layout of the vehicle architecture is derived.

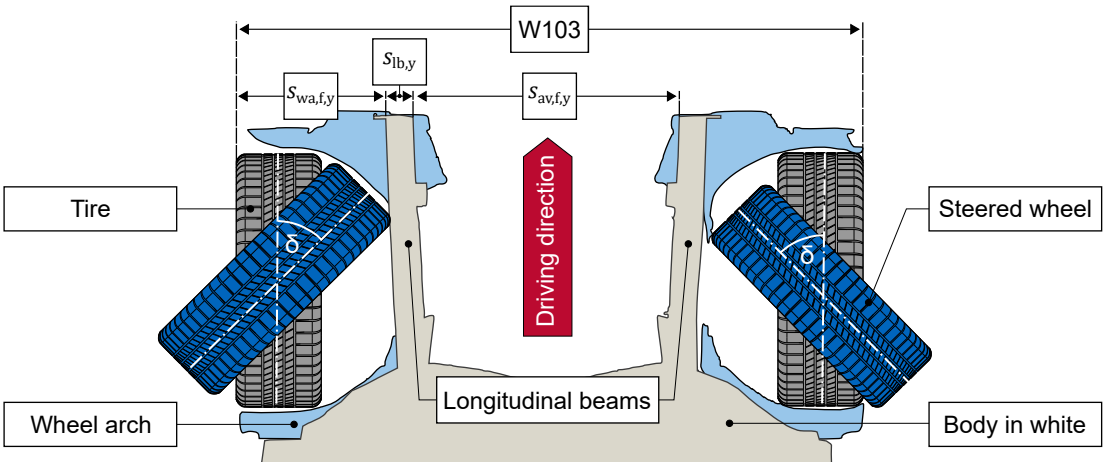

Figure 2.11: Dimensional chain to estimate the available installation space at the vehicle's front-end.

Equation (2.1) summarizes the dimensional chain in Figure 2.11. The chain estimates the available space for the powertrain components $s_{av,f,y}$ based on the vehicle width (W103), the wheel arch width $s_{wa,f,y}$, and the longitudinal beam width $s_{lb,y}$.

$$s_{av,f,y} = W103 - 2\,s_{wa,f,y} - 2\,s_{lb,y} \tag{2.1}$$

The wheel arch width is derived from the tire size and the maximum steering angle δ. The former can be estimated based on the tire load (Subsection 3.4.1). The latter depends on the

vehicle's external dimensions [42, p. 82]. Finally, the longitudinal beam width $s_{\mathrm{lb,y}}$ can be modeled empirically with a constant value. In this way, it is possible to derive the available space at the front-end of the vehicle $s_{\mathrm{av,f,y}}$.

2.3 Secondary Effects

Regardless of the powertrain type, vehicle mass increases are frequent during the vehicle concept design and can either be corrected through targeted measures or must be accepted [7, pp. 158-159]. For BEVs, a further parameter plays a major role: range. Range is an essential selling point [106] and is usually selected at the start of the planning phase according to the vehicle segment and the targeted customer group [27]. Given a target range and vehicle mass, consumption and required battery energy are estimated. However, the vehicle mass can only be roughly estimated at this stage of development. Such an estimate is prone to error and leads to further inaccuracies in the quantification of vehicle consumption and battery energy. Consequently, the battery energy must be iteratively adjusted, which causes additional mass fluctuations. These fluctuations trigger secondary effects that complicate architecture derivation and can be associated with changes in mass of the components (secondary mass effects) or in their volume (secondary volume effects).

If a new component is added or an already existing component becomes larger, this results in mass fluctuation, defined as primary mass increase [107, p. 9]. The primary mass increase affects the vehicle's consumption and its performance (such as acceleration time and maximum speed). In order to maintain the original performance requirements, the vehicle components need to be adjusted. This sets off a mass spiral as shown in Figure 2.12.

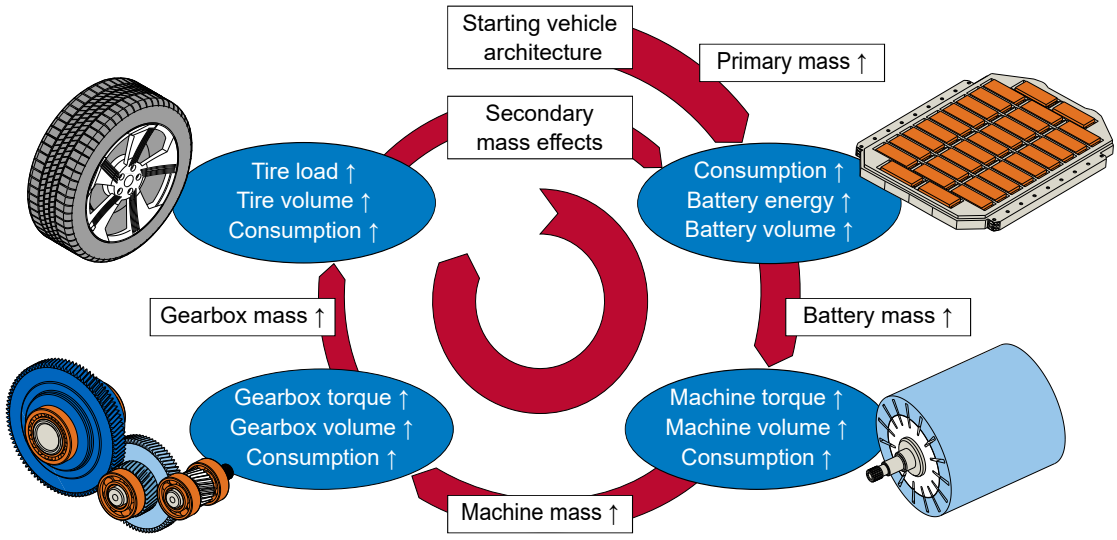

Figure 2.12: Mass spiral with resulting secondary effects.

Since a primary mass increase raises the vehicle's consumption, it may require additional battery energy to maintain the targeted range. Due to the low energy density of lithium-ion batteries (Section 1.1), small energy adjustments may lead to considerable mass increases and affect further components [103]. Figure 2.12 shows how the primary mass increase can impact electric machines, gearboxes, and tires. The sum of the mass increases of the affected components is the secondary mass change. The secondary mass change triggers in turn a further loop in the

spiral. Consequently, the spiral has to be repeated until no further mass increase results. In the case of a primary mass reduction, the spiral works in the opposite direction and the secondary effects allow for additional mass savings [108, p. 43].

The secondary to primary ratio K_{SP} is a possible measure to quantify the mass variation initiated by a primary mass change [107, pp. 9-10]. It expresses the ratio between the secondary mass change m_{SMC} and the primary mass change m_{PMC} that caused it (Equation (2.2)). For example, a K_{SP} of 0.5 means that given a primary mass reduction of $100\,\mathrm{kg}$, further $50\,\mathrm{kg}$ can be saved due to secondary mass effects.

$$K_{\mathrm{SP}} = \frac{m_{\mathrm{SMC}}}{m_{\mathrm{PMC}}} \tag{2.2}$$

Table 2.1 provides an overview of the authors who quantify the K_{SP} [28]. All authors follow a similar approach by dividing the vehicle into modules and estimating the mass of each module separately. If a mass reduction (or increase) is introduced, each module is recalculated and the secondary mass change estimated. The values show a high variability since the authors consider vehicles with different model years and dimensions.

Table 2.1: Typical K_{SP} values according to the reviewed literature.

Author	K_{SP}	Employed database
Malen et. al [109]	0.8-1.5	32 ICEVs (model years between 2002 and 2007)
Göbbels et al. [110, pp. 141-145]	0.3-0.46	Opel Corsa C (first value) and VW Golf V (second value)
Göbbels et al. [110, p. 145]	0.5-0.58	Derived from literature research including approx. 1300 sources. Only ICEVs considered.
Alonso et al. [111]	0.49	Analysis from 77 ICEVs (model years between 2007 and 2009)
S. Fuchs et al. [107, 112]	0.32-0.45	24 ICEVs and BEVs (model years between 2007 and 2012). The K_{SP} is calculated for a two-seater BEV with $150\,\mathrm{km}$ range.

Except for S. Fuchs [107, 112], the authors focus exclusively on ICEVs and their results are not relevant to the scope of this thesis. The research of S. Fuchs shows that, in the case of BEVs, the K_{SP} is strongly influenced by cell energy density, battery size, and range [112]. Nevertheless, the estimate of S. Fuchs relies on a limited number of vehicles produced between 2007 and 2012 [107, p. 34] and is therefore not up-to-date.

A primary mass change can also impact component volumes. For example, a primary mass increase may raise the axle load and may require resizing the tires. This leads to an increase in tire volume (secondary volume effect), which in turn triggers a secondary mass effect. In other words, a secondary mass effect is usually caused by a component resizing, i.e. a secondary volume effect. Figure 2.13 shows an example of secondary volume effect based on the dimensional chain presented in Subsection 2.2.4.

If a primary mass increase occurs, the tires have to be resized since they must carry a higher load. This causes an increase in their diameter, width, or both. Concurrently, to guarantee the same agility to the vehicle, the steering angle δ cannot change. Therefore, the longitudinal beam is moved towards the vehicle center to accommodate the larger tire, thereby causing a reduction in the available space at the vehicle's front-end $s_{\mathrm{av,f,y}}$. In this case, there are two distinct secondary effects: the first is the resizing of the tire caused by the primary mass increase that in turn leads to a reduction of $s_{\mathrm{av,f,y}}$, i.e. a secondary volume effect (Figure 2.13). In a previous publication [103], it was estimated that this specific secondary volume effect can cause an

available space loss between 4 % and 12 %, following a primary mass increase between 75 kg and 130 kg. If the space loss causes an unfeasibility of the package, a countermeasure is increasing the vehicle width. By inverting Equation (2.1), the larger wheel arch width can be compensated with a greater W103. However, the increase in W103 raises the Body in White (BIW) mass and causes secondary mass effects in other vehicle modules [103].

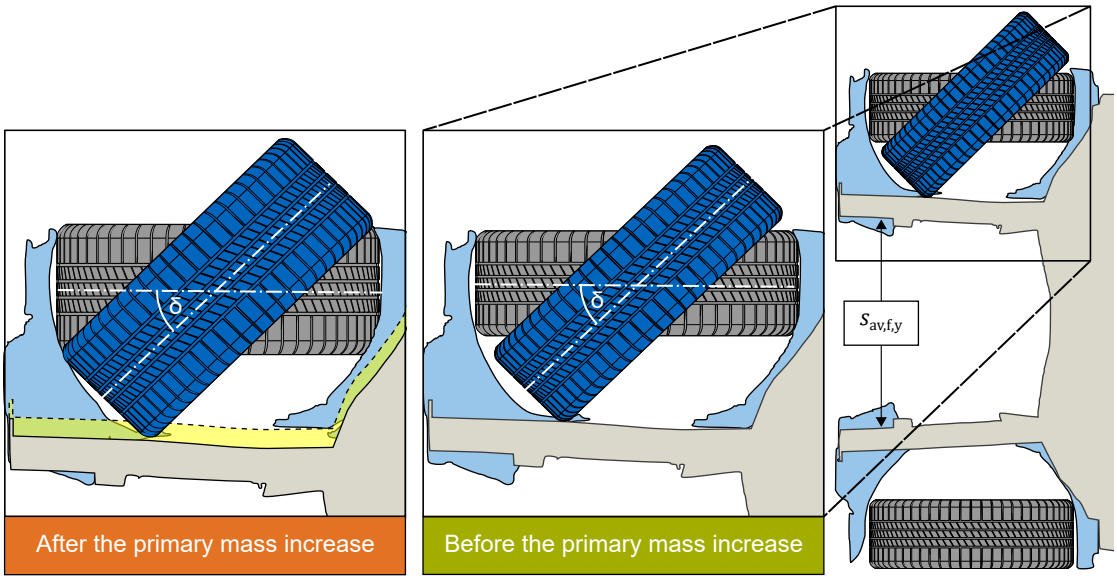

Figure 2.13: Impact of a primary mass increase on the tire dimensions and the available space at the vehicle's front-end $s_{av,f,y}$. Based on [69, 103].

The tires do not exclusively impact the available space at the vehicle's front-end, but also other components such as the battery. Therefore, secondary volume effects in the tires may also impact the installable battery energy. As a result, it can be concluded that secondary volume effects can compromise the feasibility of the vehicle architecture. However, apart from previous publications of the author on this topic [27, 103], no further quantification of secondary volume effects was found in the reviewed literature (Section 2.4).

2.4 Existing Methods

To identify the existing methods for modeling BEV architectures, a literature review was conducted [26, 113, 114]. The methods are evaluated according to the degree of detail of modeling the architectural features. Table 2.3 summarizes the existing methods and their degree of detail.

Angerer [75] develops a multi-criteria optimization algorithm to model the longitudinal and lateral dynamics of BEVs. He models masses, volumes, and costs of the powertrain components with empirical and semi-physical models. To model vehicle mass, Angerer applies the model of S. Fuchs [107]. Although he models the powertrain components and all feasible topologies in detail, the dimensional concept is neglected, dimensional chains are barely used, and a feasibility check of the vehicle architecture is not conducted. The modeled components are not documented in a database and an automatic update of the models is not possible.

Felgenhauer [39] implements an algorithm for the automated derivation of ICEV, HEV, and BEV platforms. The author focuses exclusively on the front-end of the vehicle. Consequently, the modeling of dimensional concept, drive topology, and dimensional chains is incomplete.

Furthermore, he does not consider the traction battery, since it is not usually placed at the vehicle's front. The remaining components are described with semi-physical and empirical models. He estimates vehicle mass with a simplified linear empirical regression [115] and neglects secondary mass effects. Although the regressions and constant values required for the empirical modeling are stored in a centralized Excel table, an automatic update of the empirical model is not implemented.

S. Fuchs [107] creates a parametric model for estimating mass and CO_2 life-cycle emissions of ICEVs and BEVs. He divides the vehicle into modules that are in turn subdivided into components. The single components are described with empirical models and the vehicle mass is estimated by summing up the components' masses. His parametric model estimates the secondary mass effects, but cannot derive a vehicle package. Accordingly, neither a dimensional concept nor dimensional chains are considered. Although mass estimation is largely based on empirical models, no centralized database is implemented, which precludes an automatic update of the models, thus making them sensitive to data aging.

Matz [41] develops a multi-criteria optimization algorithm to identify optimal BEV architectures while considering customer and mobility requirements. Given a set of customer requirements (including also the desired route), the algorithm identifies whether the optimal solution requires the purchase of a vehicle (and suggests a vehicle fulfilling the customer needs) or if the customer can be satisfied with the available public transportation systems. Vehicle topology is not fully modeled, since All-Wheel Drive (AWD) topologies are not considered. Most of the component models are selected from a component database, and are therefore not scalable, which hinders modeling secondary volume effects. For mass estimation, Matz uses the model of S. Fuchs [41, p. 51]. Although the component database is theoretically extendable, it does not allow an automatic update of the empirical models.

Hahn [45] describes a procedure for vehicle conception in the planning and definition phase. The methodology derives a rough dimensional concept and visualizes it as a 2.5-D model. For modeling, various relationships between the vehicle dimensions are identified and expressed as dimensional chains, empirical models, or physical equations. She focuses on the derivation of internal and external dimensions without considering the powertrain components. Secondary mass and volume effects are not considered. She mentions a database containing the data used for the empirical models, clearly stating that the model update is not automatic [45, p. 96].

Kuchenbuch [47] couples a vehicle architecture model with the NSGA-II [116] multi-criteria optimization algorithm. His model derives BEV architectures based on different optimization targets. The algorithm varies the seat layout (considering also layouts where not all passengers face the driving direction) and the battery's position to identify the optimal solution. The vehicle's main components are selected from a component database and positioned using dimensional chains. Modeling the vehicle's mass employs an empirical regression for ICEVs derived by Yanni et al. [117]. An estimation of secondary effects is not possible.

Raabe [118] develops a parametric tool for modeling and visualizing dimensional concepts. The tool considers more than 100 internal and external dimensions. For the calculation of the dimensional concept, he employs a set of dimensional chains and empirical models. Only the components relevant to the dimensional concept (wheels, steering wheel, and pedals) are considered. The tool enables a comparison between the calculated dimensional concept and the dimensional concepts of existing vehicles, which are stored in a database. For this scope, the tool is coupled with a centralized and structured database system. However, no mention is made regarding the automatic update of the empirical models.

Ried [119] develops a tool for PHEV architectures. The main objectives of the tool are to calculate available component spaces, component costs, and vehicle consumption. The author only focuses on PHEVs and does not consider BEV topologies. Nevertheless, the components of the electric powertrain are modeled with a particular focus on the traction battery. For this scope, Ried models the dimensional concept and uses a set of dimensional chains to derive the available installation space for the battery. Although the mass of the powertrain components and their secondary effects are considered for the vehicle consumption estimation, no mention is made about secondary volume effects.

Stefaniak et al. [120, 121] focus on estimating the available battery space. The authors develop a tool capable of deriving the installation space based on a simplified dimensional concept. The calculated space is subsequently filled with cells using the NSGA II optimization algorithm. The electric machine and gearbox dimensions are modeled to account for their impact on battery space. However, no clear statement is made about modeling the vehicle and component masses (except the electric machines and the battery).

Wiedemann [42] describes a model for the requirement-based generation of BEV architectures. The inputs are vehicle properties such as longitudinal or transversal dynamic that are expressed as target values on a scale from 5 to 10. Subsequently, the tool derives the required physical properties and component dimensions according to the given target values. To derive the available battery space, Wiedemann [42] implements a simplified dimensional concept model and employs several dimensional chains. All possible BEV topologies are considered and both mass and volume of the powertrain components are included. Nevertheless, the remaining components (such as wheels and axles) are only marginally considered. The tool can estimate secondary mass effects but only for powertrain components.

Table 2.3: Existing methods for modeling BEV architectures during the vehicle concept design [26].

Degree of fulfillment ● Completely modeled ◕ Consistently modeled ◑ Partially modeled ◔ Mentioned ○ Not present	ANGERER [75]	FELGENHAUER [39]	FUCHS [107]	MATZ [41]	HAHN [45]	KUCHENBUCH [47]	RAABE [118]	RIED [119]	STEFANIAK et al. [120, 121]	WIEDEMANN [42]
Modeling of architectural features										
Dimensional concept	○	◑	○	◕	◑	◕	●	●	◕	◑
Drive topology	●	◑	●	◑	○	●	○	◑	◑	●
Component models	◕	◕	◑	◑	○	◑	◔	◑	◑	◑
Dimensional chains	◔	◑	○	◕	◑	●	◕	◑	◑	◑
Further modeling requirements										
Modeling of secondary mass effects	●	○	●	●	○	○	○	○	○	◑
Modeling of secondary volume effects	○	◑	○	◔	○	○	○	○	○	◑
Database and automatic model update	○	◑	○	◑	◑	◑	◕	◑	◑	◑

2.5 Research Gap

Secondary mass and volume effects have a high influence on BEV architectures and must be considered already in the planning phase to avoid time-consuming errors in the following development steps. None of the authors listed in Table 2.3 consider the influence of secondary mass and volume effects at the same time. S. Fuchs [107] is the first author to fully model secondary mass effects and his approach is later applied by other authors [41, 75]. Nevertheless, the model of S. Fuchs cannot be used in this thesis since its empirical correlations are based on vehicle data from 2007-2012 and are therefore outdated. Secondary volume effects could be quantified by some of the existing models, however, none of the authors focus on this topic. Consequently, it was not possible to identify an approach that simultaneously models vehicle package, vehicle mass, and the coupling between these two features.

Most of the reviewed approaches employ empirical models, however, none of the authors address the problem of data aging nor do they consider the possibility of storing the data in a centralized SQL database. In most cases, data are stored in Excel tables, which do not allow an automatic update of the models. Correspondingly, the presented methods are destined to be outdated within a few years and most already are. Furthermore, the authors in Table 2.3 do not consider all relevant architectural features, but rather focus on one or two features, while neglecting others. However, without modeling each architectural feature, the derivation of the BEV architecture is incomplete. Consequently, no method for the derivation of BEV architectures exists that considers the main architectural features, the secondary effects, and can be updated automatically.

The aim of this thesis is to develop a vehicle architecture tool with the following requirements:

- **Secondary effects:** The tool must consider secondary mass and volume effects and describe their impact on the vehicle architecture. This requires modeling vehicle package, vehicle mass, and the coupling between these two features.
- **Always up-to-date:** The tool must address the problem of data aging by allowing an automatic update of the empirical models.
- **Architectural features:** The tool must consider all four architectural features.
- **Suitability for early development design:** The tool must have a low number of inputs for usability during the vehicle concept design.

Based on these requirements, a vehicle architecture tool to support concept engineers during the vehicle concept design is implemented in Chapter 3. The result is a tool capable of identifying conflicts and weaknesses of soon-to-be-developed BEVs already in the planning phase. The tool can be further coupled with an optimization algorithm to derive optimal BEV architectures and gain a better understanding of the limits of current and future BEVs. For this scope, NSGA-II appears as a suitable optimizer, since it has been used by several of the reviewed authors [41, 47, 75, 121].

3 Vehicle Architecture Tool Development

Based on the research gap (Section 2.5), this chapter outlines an approach for the automated derivation of BEV architectures. The approach considers different drive topologies and models the main vehicle components as well as the dimensional concept. Furthermore, it quantifies both secondary mass and secondary volume effects. These features are bundled in a tool (implemented in MATLAB [122], Figure 3.1), which addresses the data aging problem by providing a transparent and updatable model structure.

This chapter is organized according to the six tool steps: Input Initialization (Section 3.1), Component Database (Section 3.2), Longitudinal Dynamic Simulation (Section 3.3), Volumetric Component Modeling (Section 3.4), Gravimetric Component Modeling (Section 3.5), and Output of a Feasible Architecture (Section 3.6).

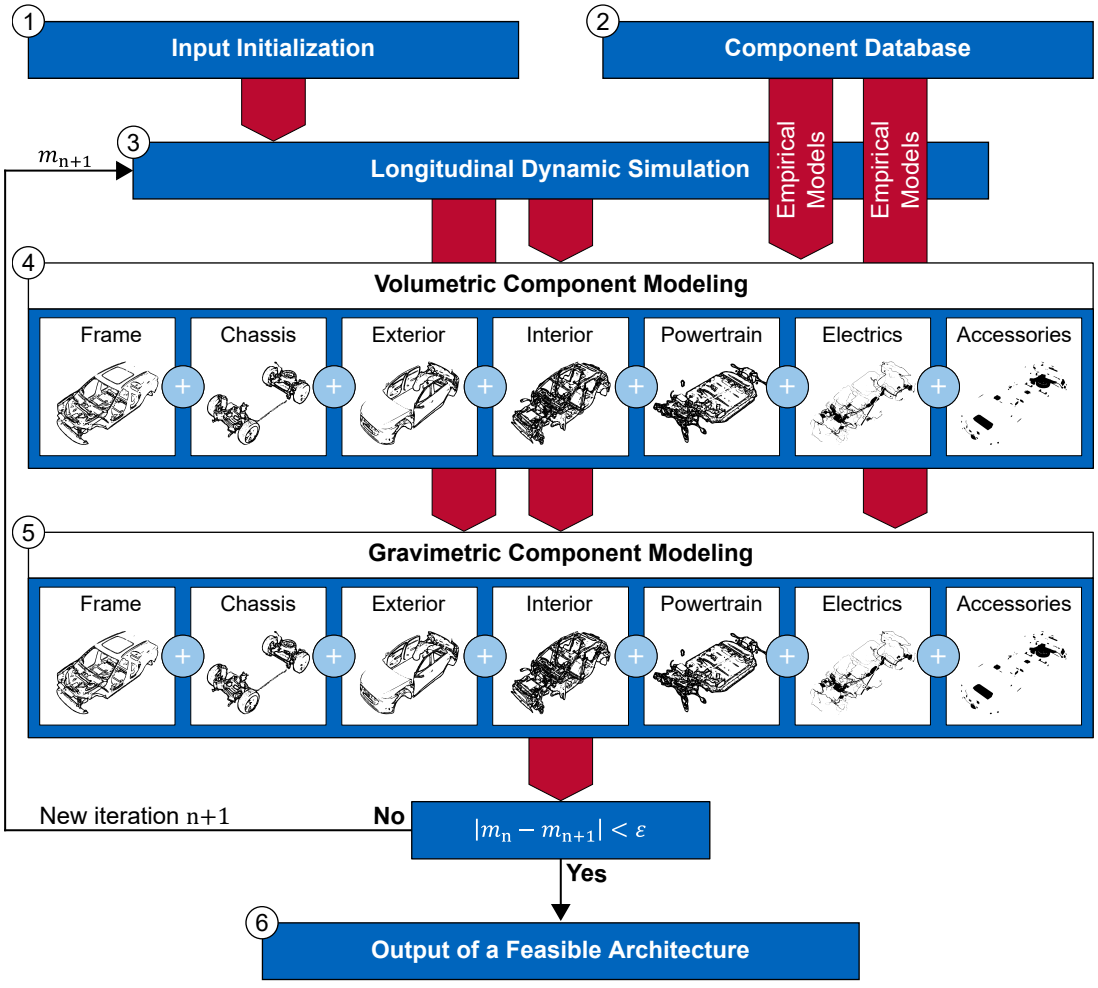

Figure 3.1: Structure of the vehicle architecture tool. Based on [27].

For the tool to be usable during the vehicle concept design, the number of inputs must be kept low (Section 2.5). For this reason, a literature review is carried out to identify the most important design parameters that are available during the planning phase (Section 3.1). The identified parameters are implemented as tool inputs. Examples are the vehicle maximum speed, the target range, and the required acceleration time.

Apart from the inputs, empirical models are employed to size the vehicle components. These models are derived from component data, which is stored in a component database (Section 3.2). Every time new data is added to the database, an automatic update is performed. The updated empirical models are then stored for further use during volumetric and gravimetric component modeling.

In the following step, a Longitudinal Dynamic Simulation (LDS) simulates the dynamics of the vehicle to derive further design parameters, such as the required drive unit power and battery energy (Section 3.3).

Subsequently, the tool inputs are combined with the LDS results to size the vehicle components and calculate their volumes (Section 3.4). For this scope, the vehicle is divided into modules. The main components of each module are estimated using semi-physical and empirical models as well as dimensional chains. At the end of this step, the components are placed in the vehicle using dimensional chains. Finally, the vehicle package is derived.

Given the volumes and dimensions of the components, their masses are calculated (Section 3.5). The masses of the vehicle modules are estimated using empirical models. A new vehicle empty mass $m_{\mathrm{n+1}}$ is obtained by summing up the contributions of each module. The corresponding gross mass $m_{\mathrm{gross,n+1}}$ is calculated by adding the vehicle's payload to $m_{\mathrm{n+1}}$. If the difference between the new vehicle mass and m_{n} lies below a certain tolerance ε, the tool visualizes the resulting vehicle architecture. Otherwise, another iteration is carried out by plugging $m_{\mathrm{n+1}}$ back into the LDS. Since the mass has changed, the simulation will compute different power and battery energy requirements, thus influencing the battery size and causing secondary mass and volume changes. Once the iterative calculation is concluded, the resulting vehicle architecture is visualized (Section 3.6).

3.1 Input Initialization

To implement the architecture tool, certain design parameters have to be identified that are available in the planning phase and can be used as tool inputs. A literature review identifies the publications dealing with architecture modeling for vehicle concept design [26]. Subsequently, each of the identified authors is analyzed and the design parameters that he considers as relevant are collected. Table 3.1 summarizes the design parameters with the highest number of citations.

The literature review confirms the relevance of vehicle range and mass. Therefore, a target range R_{veh} and an initial vehicle mass m_0 (latter is needed as the start value for the iterative mass calculation) are chosen as model inputs. Furthermore, several authors base their powertrain sizing on maximum vehicle speed $v_{\mathrm{veh,max}}$ and acceleration time t_{0-100}. Therefore, these two performance requirements are added to the tool inputs. It is also possible to size the powertrain based on maximum torque and speed of the electric machine. However, for inexperienced tool users, acceleration time and maximum speed are more intuitive inputs, as they are characteristics that can be directly perceived while driving.

Table 3.1: Most cited vehicle characteristics and dimensional concept parameters for vehicle concept design. Based on [26].

Vehicle characteristics	
Design parameter	**Sources**
Initial vehicle mass in kg	[123], [124], [125, 126], [39, p. 27, 115], [44, p. 41], [107, p. 1], [45, p. 47], [127, p. 101], [47, p. 58], [41, p. 51], [128], [129, p. 70], [130, p. 71], [131, 132], [42, p. 56]
Target range in km	[123], [44, p. 53], [107, p. 36], [45, p. 47], [47, p. 54, 133], [128], [134, p. XXV], [129, p. 70], [18], [130, p. 67], [135, p. 176], [136], [42, p. 56, 106]
Maximum speed in $\mathrm{km\,h^{-1}}$	[123], [125, 126], [39, p. 27], [44, p. 53], [45, p. 47], [47, p. 54], [128], [129, p. 70], [130, p. 67], [135, p. 176], [136], [42, p. 56]
Acceleration time 0 to $100\,\mathrm{km\,h^{-1}}$ in s	[126], [39, p. 27, 115], [44, p. 53], [107, p. 36], [47, p. 54], [128], [129, p. 70], [130, p. 67], [136] [42, p. 56]
Drag coefficient	[123], [39, p. 34], [125], [45, p. 47], [47, p. 58], [41, p. 50], [129, p. 70], [130, p. 69], [131, 132]
Dimensional concept	
Design parameter	**Sources**
Length (L101), wheelbase (L103) or overhangs (L104, L105) in mm	[123], [124], [105], [39, p. 26], [44, p. 41] [107, p. 36], [45, p. 47], [41, p. 56], [129, p. 70], [130, p. 76], [118, 137, p. 79], [42, p. 56], [138]
Height (H100) in mm	[123], [124], [105], [44, p. 41], [107, p. 36], [45, p. 47], [139], [41, p. 56], [130, p. 76], [118, 137, p. 79], [42, p. 63-64], [138]
Width (W103) in mm	[123], [124], [105], [39, p. 26], [44, p. 41], [107, p. 36], [45, p. 47], [41, p. 56], [130, p. 76], [118, 137, p. 85], [138]
Vehicle segment	[123], [124, 140], [39, p. 27], [44, p. 41], [139], [128], [130, p. 72]
Ground clearance	[44, p. 70], [45, p. 47], [41, p. 55], [130, p. 76], [118, p. 82], [42, p. 56], [119, p. 110]
Headroom	[140], [45, p. 47], [47, p. 54], [41, p. 43-44], [130, p. 74], [118, p. 83, 137], [42, p. 56]
Legroom	[140], [45, p. 47], [41, p. 43-44], [130, p. 74], [118, p. 92], [42, p. 56]

Apart from the vehicle characteristics listed in Table 3.1, further relevant parameters are identified for each of the four architectural features (dimensional concept, topology, component model, and dimensional chains). Table 3.1 also lists the dimensional concept parameters with the highest number of citations. The remaining architectural features are documented in [26, 113].

Table 3.1 highlights the importance of the vehicle's external dimensions (length, wheelbase, width, and height) for the definition of the dimensional concept. Since the external dimensions depend on the vehicle segment, which is in turn defined at the beginning of the vehicle concept design (Subsection 2.2.1), they are implemented as model inputs. Furthermore, ground clearance assumes an important role for BEVs due to its influence on the available battery space. Nevertheless, it is not necessary to implement it as an input, since it can be estimated from the external dimensions (Subsection 3.4.2).

Regarding the interior concept, the reviewed authors use different methods to model headroom and legroom, which are key features for defining the passenger compartment. In the scope of this thesis, to minimize the number of inputs, the passenger compartment sizing is based on H30-1 and H30-2, while the other internal dimensions are derived using empirical and geometrical models (Subsection 3.4.3).

This literature review allows to identify suitable inputs for the architecture tool (Table 3.2). In the next sections, the vehicle architecture is further detailed and developed using the inputs listed in Table 3.2.

Table 3.2: The minimum set of inputs required by the vehicle architecture tool. Further optional inputs (such as drag coefficient, battery energy density, and internal dimensions) can be added to the input set, otherwise they are modeled with empirically derived default values.

Exterior and interior concept	**Powertrain requirements (for LDS)**
Vehicle width (W103) in mm	Initial vehicle mass m_0 in kg
Vehicle height (H100) in mm	Payload in kg
Wheelbase (L101) in mm	Acceleration time t_{0-100} in s
Overhangs (L104, L105) in mm	Maximum vehicle speed $v_{\mathrm{veh,max}}$ in $\mathrm{km\,h^{-1}}$
Body type (SUV/hatchback/sedan)	Required range R_{veh} in km
Ground clearance class	Gearbox transmission ratio i_{gb}
Number of seats	Driving cycle (WLTC/NEDC/...)
Passengers position (H30-1, H30-2, L113) in mm	
Topology	**Component models**
Machine number and type (IM/PMSM)	Tire type (standard load/extra load)
Machine position (coaxial/in front/behind the axle)	Tire diameter D_{tire} in mm
Gearbox type (coaxial/parallel axes/planetary)	Rim diameter D_{rim} in mm
Integration principle (highfloor/mixedfloor)	Axle type (five link/sword arm link/...)
	Cell type (pouch/prismatic/cylindrical)

3.2 Component Database

The vehicle components included in this thesis are described in part or entirely through empirical models. Therefore, according to Figure 2.10, for modeling each component, a dataset of existing components is created through benchmark analysis. The single datasets are bundled in a centralized component database (step 2, Figure 3.1). This chapter briefly explains the structure and workflow of the component database (Figure 3.2), detailed information is documented in [11, 141].

The established language to store, manipulate, and query data from a database is SQL, which was first developed by IBM in the 1970's [142, p. 35] and later became a standardized programming language [143]. There are several SQL database engines on the market, such as MySQL [144], PostgreSQL [145], SQLite [146], and Microsoft Access [147]. For this thesis, SQLite is chosen due to its simplicity and the possibility to connect it with MATLAB via the MathWorks add-in Database Toolbox [148]. Figure 3.2 gives an overview of the component database. To clarify its structure, four tables are presented: model series, model, dimensional concept, and battery.

The model series table is the backbone of the database, because it organizes and connects the other tables. Every component data stored in the database refers to a specific vehicle and is linked to a row (i.e. a model series) of the model series table. For filling the table, the author uses the categorization defined by the Allgemeiner Deutscher Automobil Club (ADAC) [149]. The ADAC provides an up-to-date overview of current and discontinued model series that are (or

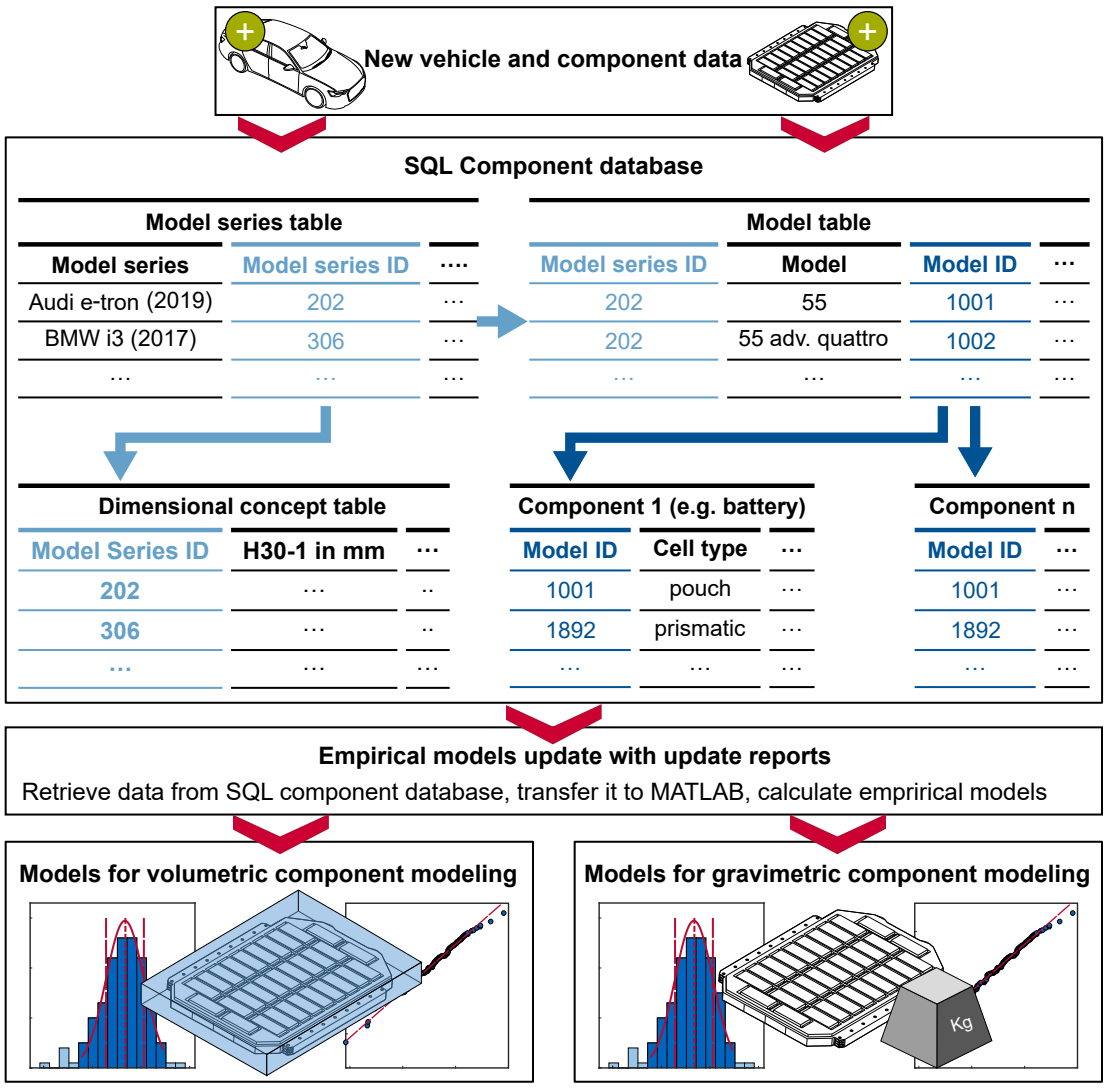

Figure 3.2: Structure of the SQL database. New vehicle data is stored in the database by populating the model, model series, and component tables. Every time new data is added, MATLAB automatically updates the volumetric and gravimetric component models.

were) available on the German market. When a new model series is launched, it can be added to the model series table by copying its data from the ADAC web page. The model series table stores information such as the manufacturer (e.g. Audi), the model series name (e.g. e-tron), its external dimensions, and its production year (e.g. 2019). Furthermore, to avoid inconsistencies, each model series has a unique numeric identifier (Model series ID, Figure 3.2).

A model series groups several models (or variants) with different characteristics (such as vehicle mass, installed power, and costs). For example, the model series Audi e-tron includes the variants 50 quattro, 50 advanced quattro, 55 quattro, 55 advanced quattro, etc. The model table lists the corresponding models and the model-dependent characteristics for each Model Series ID. Once again, the categorization defined by the ADAC is used and each model has a unique identifier (Model ID, Figure 3.2).

The model and model series tables both organize the vehicle and component data. For example, the dimensional concept table lists internal and external dimensions (such as H30-1, H30-2, L113-1). Each row of this table refers to a specific model series and is linked to a Model series ID. The empirical models derived from this data are used to size the interior and exterior modules

(Subsection 3.4.2 and 3.4.3). Another element of the database is the battery table that stores information such as cell type, battery dimensions, and battery mass for each Model ID. The empirical models derived from this data are used to size the powertrain (Subsection 3.4.6).

To enable an automated empirical model generation, an update report is integrated into the database. Using the update report, a MATLAB script retrieves the component and vehicle data from the database and derives linear regressions and constant values. For their calculation, the statistical tool developed by Marksteiner [150] and Schneider [151] is extended by Ranocchia [141]. Finally, once the models are computed, they are stored in a MATLAB structure for further use in volumetric and gravimetric component modeling.

When new vehicles enter the market, they can be added to the model and model series tables. Subsequently, their component data can be stored in the corresponding tables and linked to Model and Model series IDs. For the next model update, MATLAB retrieves the empirical data, while also considering the newly added vehicles and derives updated empirical models. Inversely, old vehicles can be filtered out by deleting the corresponding model series and models from the database. This implementation solves the problem of data aging, resulting in an always up-to-date set of empirical models.

3.3 Longitudinal Dynamic Simulation

The LDS (step 3, Figure 3.1) translates the tool inputs into requirements for the powertrain components. For implementation, two approaches are possible: a quasi-static and a dynamic approach [152, pp. 37-42]. Examples for quasi-static LDSs are documented in [39, 44, 75, 134, 153], while the dynamic approach is adopted by authors like Matz [41] and Pesce [129].

Since a high number of variants have to be tested when deriving a vehicle architecture, the LDS has to be implemented in a manner that minimizes computational effort. Therefore, the quasi-static approach was chosen because of its low computational time [152, p. 39]. This chapter briefly presents the structure of the LDS (Figure 3.3); detailed information is documented in [154–156] and the LDS code is available open-source at [157].

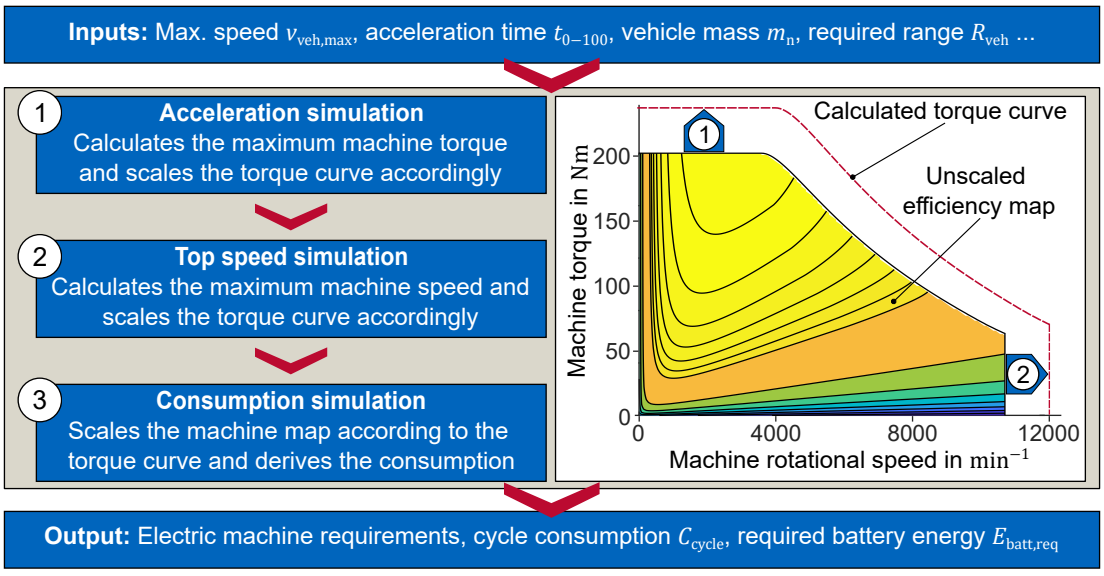

Figure 3.3: Structure of the LDS. The LDS consists of an acceleration simulation ①, a maximum speed simulation ②, and a consumption simulation ③. Based on [154].

The LDS inputs constitute a subgroup of the tool inputs (Table 3.2) and include performance requirements (maximum vehicle speed, acceleration time t_{0-100}, target range R_{veh}, and transmission ratio), parameters for estimating vehicle losses (external dimensions and vehicle mass of the current iteration m_{n}), and topology specifications (number, type, and position of the electric machines). Furthermore, for estimating the vehicle range, a driving cycle must be selected. It is possible to choose among several driving cycles such as the New European Driving Cycle (NEDC) and the Worldwide Harmonized Light Vehicles Test Procedure (WLTP). The former was the standard cycle for type approval in Europe until the European Commission stated its inadequacy to reflect real-world emissions and substituted it with the Worldwide Light Vehicles Test Cycle (WLTC) [158, pp. 1-2]. Therefore, when referring to vehicle consumption, the author always refers to the WLTC consumption measured according to the WLTP. More information regarding this test procedure is specified in Appendix C.

In step ①, the machine torque is iteratively scaled until the desired t_{0-100} is reached. The simulation also derives the torque curve, which depicts the profile of the maximum torque as a function of the machine rotational speed. Subsequently, a top speed simulation (②, Figure 3.3) is employed to select the maximum machine rotational speed depending on a given transmission ratio and vehicle speed [156, p. 20, 155, p. xvii]. If the previously calculated torque curve does not extend up to the required rotational speed, the algorithm scales the curve accordingly.

In step ③, the energy consumption in the selected cycle is calculated while considering all relevant losses. For the machine losses, an efficiency map database is created. The database contains several electric machine efficiency maps (with different torque and rotational speed levels) generated through the design software developed by Kalt et al. [159]. The simulation selects the efficiency map from the database that best approximates the torque curve derived in steps ① and ②, and scales it to perfectly match the torque curve. The gearbox losses are also considered using efficiency maps, which are calculated with the method described by Moller [160]. The remaining losses, such as battery and power electronics losses, are modeled with constant efficiencies. The main output of step ③ is the energy consumption in the cycle C_{cycle}, based on which the required battery gross energy $E_{\mathrm{batt,req}}$ is calculated according to Equation (3.1).

$$E_{\mathrm{batt,req}} = \left(\frac{C_{\mathrm{cycle}}}{L_{\mathrm{cycle}}}\right) R_{\mathrm{veh}} \left(K_{\mathrm{gross2net}}\right)^{-1} \tag{3.1}$$

Where L_{cycle} is the distance of test cycle in km. $K_{\mathrm{gross2net}}$ is the ratio between net and gross battery energy. The gross battery energy represents the energy installed in the vehicle, while the net battery energy represents the energy that can effectively be used. Manufactures typically limit the usable energy to increase the battery lifetime [161]. König [21], proposes a $K_{\mathrm{gross2net}}$ value of $93\,\%$.

In conclusion, the procedure shown in Figure 3.3 yields the electric machine requirements (maximum torque $T_{\mathrm{mach,max}}$ and rotational speed $n_{\mathrm{mach,max}}$) and the required battery energy $E_{\mathrm{batt,req}}$ for the current iteration n of the architecture tool. These results are used in the following steps to estimate the masses and dimensions of the powertrain components.

3.4 Volumetric Component Modeling

During volumetric component modeling (step 4, Figure 3.1), the components of the architecture are sized and the vehicle package is derived. For this scope, the vehicle is divided into modules

that are used for both volumetric and gravimetric modeling. In total, seven modules are defined: frame, chassis, exterior, interior, powertrain, electrics, and accessories. Figure 3.4 gives an overview of the modules and their subsystems.

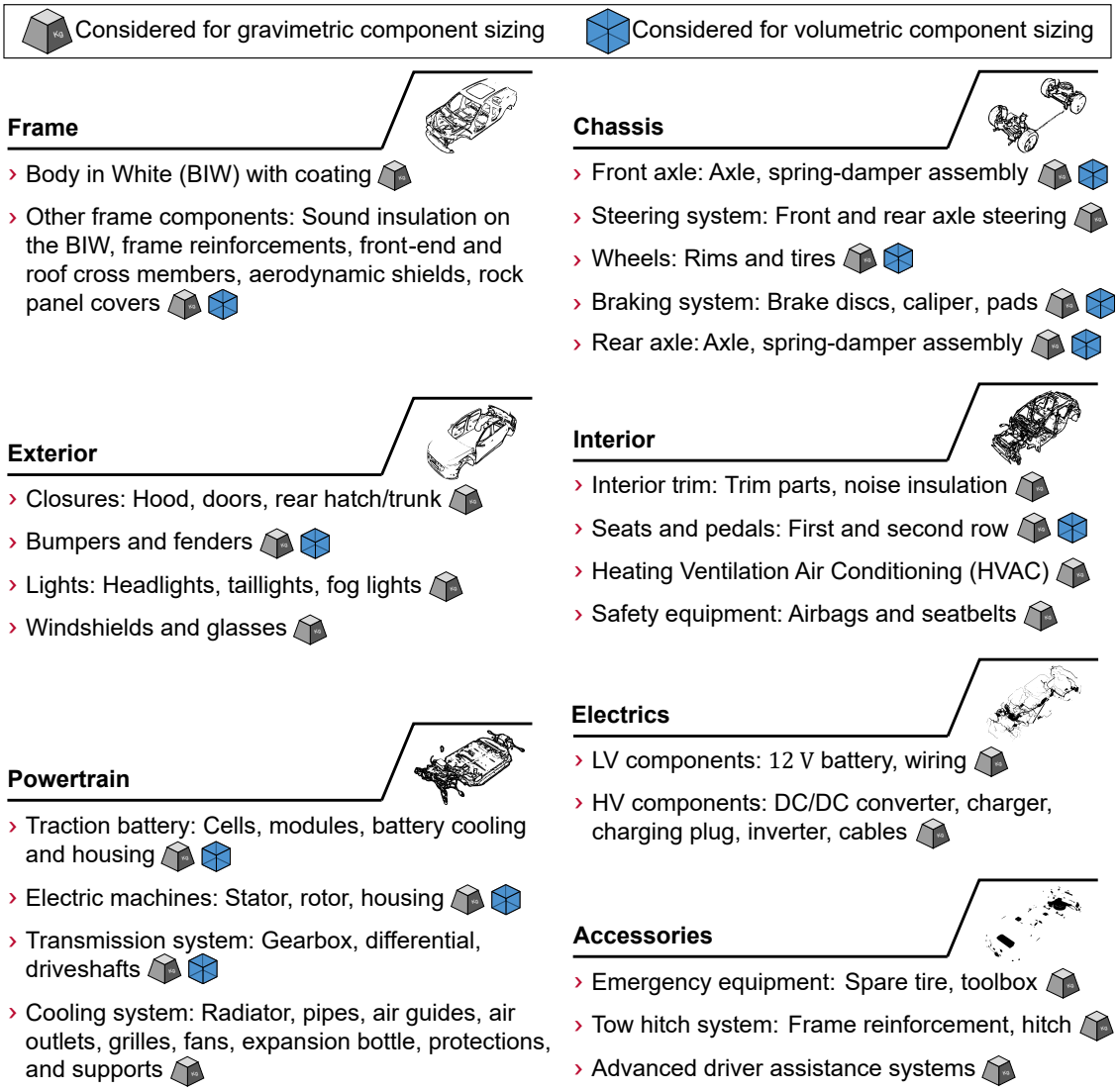

Figure 3.4: Defined modules and their sub-components for volumetric and gravimetric component modeling. For the module definition, the categorization introduced by S. Fuchs [107, p. 37] is improved by Romano [162].

A mix of empirical and semi-physical models as well as geometrical relationships is used for volumetric sizing. These models are generated based on several benchmark studies. The main source for these studies is the automotive benchmarking database A2mac1 [163]. A2mac1 documents more than 700 vehicles from over 50 automotive manufacturers. These vehicles include ICEVs, HEVs, and BEVs with various model years and destination markets.

For each vehicle in the A2mac1 database, masses and dimensions of every single component are documented including a list of materials and various pictures. In some cases, the vehicle data includes an extensive analysis of the internal dimensions (documented in accordance with SAE standards), which is the foundation for modeling the interior module (Subsection 3.4.3). Additionally, for a selected number of vehicles, a 3D scan is available. These vehicles can be visualized in a 3D editor, where it is possible to display and hide specific components, insert sections, and measure distances between components as well as within the component itself.

For up-to-date modeling, only vehicles from 2010 to 2021 are employed for volumetric component sizing. For the empirical modeling of the powertrain components, a dataset containing exclusively BEVs is used, while ICEVs and HEVs are also included for components such as seats and wheels. In the following sections, four modules are exemplarily detailed. First, the chassis sizing is explained (Subsection 3.4.1). Subsequently, Subsection 3.4.2 and 3.4.3 describe the modules exterior and interior. Finally, the powertrain module and its subsystems, the drive unit (Subsection 3.4.4) and the battery (Subsection 3.4.5 and 3.4.6) are presented.

The models for volumetric sizing are included in the iterative loop of the architecture tool (Figure 3.1). Therefore, at each new iteration n, every module is resized and a new vehicle package is calculated according to the mass of the current iteration m_{n}.

3.4.1 Chassis Module

The chassis module includes the front and rear axles, steering system, wheels, and braking system. This chapter briefly presents the modeling approach developed for the wheels (an extensive description is documented in [103, 164]). The wheels generate a coupling between mass and package, since their dimensions are influenced by the vehicle mass, and in turn impact the available space for the drive unit and battery (Subsection 3.4.5). For modeling purposes, the wheel is divided into three sub-components: brake disc, rim, and tire (Figure 3.5).

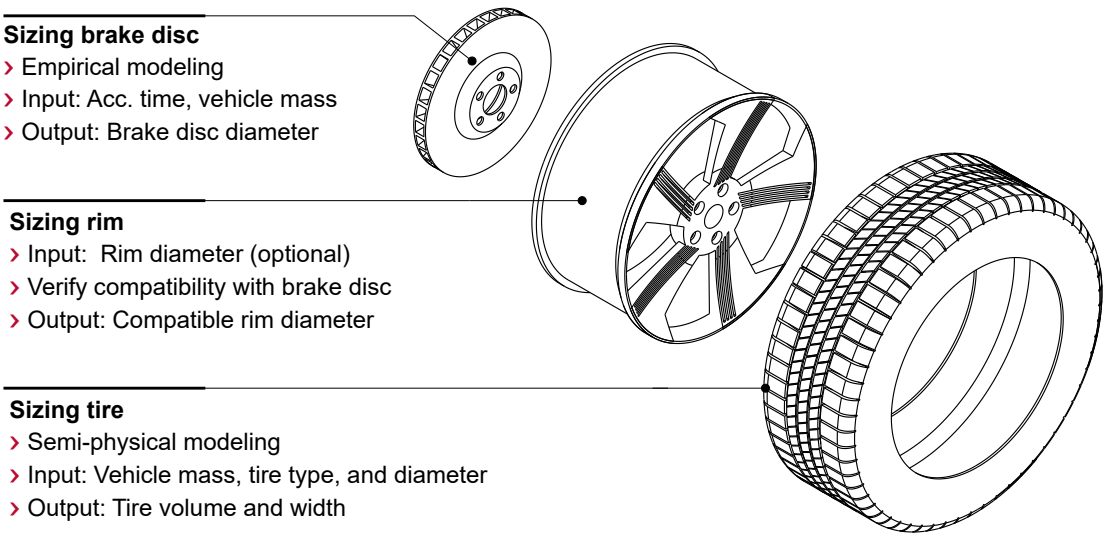

Figure 3.5: Structure of the wheel volumetric modeling.

Regarding the brake system, most vehicles use disc brakes at the front axle and (in the smaller segments) occasionally drum brakes at the rear axle. With increasing vehicle mass and higher speeds, drum brakes are not able to meet thermal requirements [165, p. 64]. Therefore, this thesis only considers disc brakes. Unlike ICEVs, BEVs can cover decelerations of about $0{,}3\mathrm{g}$ with regenerative braking, which reduces the usage of friction brakes [166]. However, there are scenarios (e.g. when the battery is fully charged) where regenerative braking is not possible. Consequently, when testing the brake system of a BEV, recuperative braking is switched off, and the component is sized following the same criteria used for ICEVs [166]. Therefore, in this thesis, recuperation is not considered as an influencing factor for dimensioning the brake system.

The brake disc is sized using an empirical correlation between the vehicle acceleration time t_{0-100} and its gross mass $m_{\mathrm{gross,n}}$ in the current iteration. On the one side, if the acceleration time

decreases, the available time to cool down the brakes between two consecutive decelerations decreases, which requires a greater thermal mass of the brake (i.e. a greater disc diameter [167, p. 71-72]). On the other side, if the vehicle mass increases, the kinetic energy of the vehicle increases as well, raising the amount of energy converted into heat while braking [166]. As a result, the brake disc diameter must be increased once again. To describe the interdependency between brake disc diameter D_{brake}, vehicle gross mass $m_{\mathrm{gross,n}}$, and acceleration time t_{0-100}, a database containing over 60 vehicles (the complete list given in a previous publication [103]) is created from the A2mac1 database [163]. Based on these vehicles, the empirical correlation shown in Equation (3.2) is derived.

$$D_{\mathrm{brake}} = 238.345\,\mathrm{mm} + (0.053\,\mathrm{mm\,kg^{-1}})\, m_{\mathrm{gross,n}} - (5.361\,\mathrm{mm\,s^{-1}})\, t_{0-100} \tag{3.2}$$

The rim is the second sub-component of the wheel. It is a major design element and its dimensions depend on the specific design strategy of the manufacturer. For this reason, the rim diameter D_{rim} is set as an optional user input, meaning that, if the vehicle architecture requires a certain rim size for design reasons, this can be assigned as an input. If, on the other hand, no rim diameter is specified or it is not compatible with the previously calculated brake disc diameter, the tool derives the smallest possible rim size that can accommodate the brake disc.

The third and last sub-component is the tire. For its modeling, the guidelines prescribed by the European Tyre and Rim Technical Organization (ETRTO) are employed. The ETRTO standardizes rim and tire sizes, defining an unambiguous sizing method, which is documented in the ETRTO manual [168]. The most important tire dimensions are the outer diameter D_{tire}, nominal aspect ratio K_{tire}, and section width $s_{\mathrm{tire,y}}$. The tire internal diameter is equivalent to the rim diameter D_{rim}. The rim and tire diameters influence the vehicle proportions and aesthetics [169]. Since design and aesthetic strategies differ between manufacturers, they cannot be modeled empirically. Therefore, the outer tire diameter is selected as a model input (Table 3.2). The remaining tire dimensions are interdependent as shown in Equation (3.3).

$$D_{\mathrm{tire}} = D_{\mathrm{rim}} + \frac{(2\, s_{\mathrm{tire,y}}\, K_{\mathrm{tire}})}{100} \tag{3.3}$$

For the tire modeling, a database containing over 600 tires (which will be denoted as *tire dataset*) with different aspect ratios and section widths is created from the ETRTO manual. While the section width ranges between $125\,\mathrm{mm}$ and $325\,\mathrm{mm}$, the aspect ratio is between $20\,\%$ and $80\,\%$. Furthermore, the value of $s_{\mathrm{tire,y}}$ is restricted to multiples of ten, while K_{tire} is always expressed as a multiple of five. According to these ranges and with respect to Equation (3.3), given an input D_{rim} and D_{tire}, a finite number of geometrically compatible tires is selected from the database [103]. To choose a suitable tire among the compatible ones, two further inputs are needed: the vehicle mass of the current iteration m_{n} and the tire type.

The m_{n} is needed to estimate the tire load $m_{\mathrm{load,tire}}$ (in kg), which is calculated by simulating different vehicle loading scenarios (Section D.1). Regarding the tire type, there are two main categories: standard and extra load tires. As the name suggests, extra load tires are designed for higher pressures than the standard ones [168, p. G10].

The tire type and the vehicle mass influence the required tire volume $V_{\mathrm{tire,min}}$. The higher the mass, the higher the tire load, the greater its volume. To describe this interdependency, the standard and extra load tires of the tire dataset are analyzed and a correlation between load and volume is derived. Equation (3.4) shows the resulting linear regression between $m_{\mathrm{load,tire}}$ and

$V_{\text{tire,min}}$ for a standard load tire [103].

$$V_{\text{tire,min}} = -11113407\,\text{mm}^3 + (84925\,\text{mm}^3\,\text{kg}^{-1})\,m_{\text{load,tire}} \tag{3.4}$$

With Equation (3.4), the required $V_{\text{tire,min}}$ is estimated, and the solution is selected from the set of geometrically compatible tires, that has the closest value to $V_{\text{tire,min}}$. Following this step, all the wheel dimensions (width, tire diameter, tire volume, and rim diameter) are defined.

3.4.2 Exterior Module

The main task of this module is to calculate the vehicle's ground clearance. In the case of BEVs the ground clearance plays a key role, as it limits the available battery space along the vertical direction. For defining the ground clearance, the vehicle is divided into sections with different clearance requirements. These are expressed as angles such as approach (A106-1), departure (A106-2), and ramp angle (A117), or minimum offsets such as ground clearance at the axles $d_{\text{clear,axle,z}}$ and ground clearance at the underbody $d_{\text{clear,ub,z}}$. Table 3.3 summarizes the requirements for different ground clearance classes.

The classes M1G (valid for vehicles in the European Union) and Light Duty Truck (LDT) are usually employed for off-road vehicles and SUVs. For the remaining vehicle types (such as sedans and hatchbacks) it is possible to use country-dependent requirements (such as the clearance classes for Korea and Australia) or the set proposed by the SAE. The exterior model includes all the classes listed in Table 3.3. Figure 3.6 exemplarily shows the clearance surface for the SAE class. Since this class does not specify any $d_{\text{clear,ub,z}}$, the clearance at the underbody corresponds to the vertical offset required by the ramp angle requirement.

Table 3.3: Different ground clearance classes and their requirements.

Class/Standard/Region	A106-1	$d_{\text{clear,axle,z}}$	A117	$d_{\text{clear,ub,z}}$	A106-2
M1G[1] [52, p. 63]	25°	180 mm	20°	200 mm	20°
LDT[1] [53, p. 85]	28°	180 mm	14°	200 mm	20°
Korea [170, p. 6]	n.a.	100 mm	n.a.	100 mm	n.a.
Australia[3] [171, p. 6]	n.a.	100 mm	n.a.	$(33.33\,\text{mm}\,\text{m}^{-1})$ L101	n.a.
SAE[2] [172, p. 3]	16°	203 mm	12°	n.a.	13°

[1] Only four of the five requirements have to be fulfilled
[2] Minimum advised values by the SAE
[3] In the formula for $d_{\text{clear,ub,z}}$ L101 is expressed in m

Besides the specifications listed in Table 3.3, the vehicle wheelbase and the tire diameter are required for the clearance surface shown in Figure 3.6. On the one hand, if the tire size remains constant and the wheelbase increases, $d_{\text{clear,ub,z}}$ must also be increased to guarantee the same ramp angle. On the other hand, the reference surfaces for the ramp, approach, and departure angles are positioned tangent to the outer diameter of the tire. Consequently, a modification of the tire size also affects their orientation and position.

These relationships create a geometrical coupling between the external dimensions and the available battery space along the vertical direction (Figure 3.6). For example, an increase of the wheelbase leads to more available battery space along the longitudinal direction, but may also require a higher $d_{\text{clear,ub,z}}$, thus reducing battery space along the vertical direction. Based on the battery dimensions, the energy gain obtained with the increased wheelbase may be

compensated by the space loss along the vertical direction. Therefore, a measure intended to increase the available battery space could result in the opposite effect.

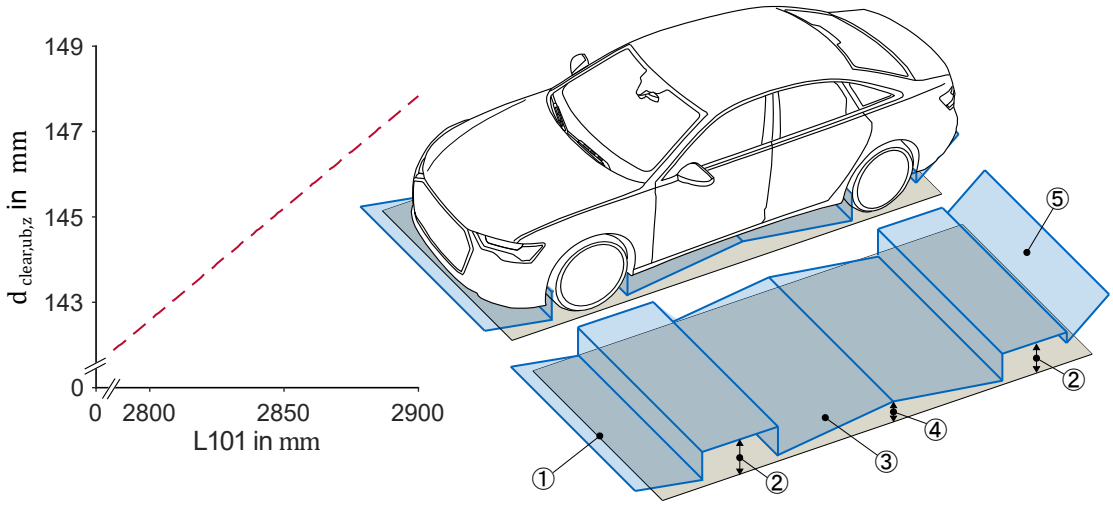

Figure 3.6: SAE class requirements: A106-1 ①, clearance at the axle $d_{\text{clear,axle,z}}$ ②, A117 ③ and resulting clearance at the underbody $d_{\text{clear,ub,z}}$ ④, A106-2 ⑤.

3.4.3 Interior Module

The interior module includes the subsystems interior trim, seats, pedals, as well as Heating Ventilation and Air Conditioning (HVAC). While these components are modeled singularly for gravimetric modeling, the task of the interior module in the volumetric modeling is to derive the seating layout and position of the passengers. This chapter presents some of the models used to describe the first (Figure 3.7) and the second (Figure 3.8) row of seats. Based on these models, the position of the interior floor (Figure 3.8), which is an important constraint on available battery space, is identified. More information in this regard is documented in the theses of Mirti [173], Elagamy [71], and in a previous publication of the author [58].

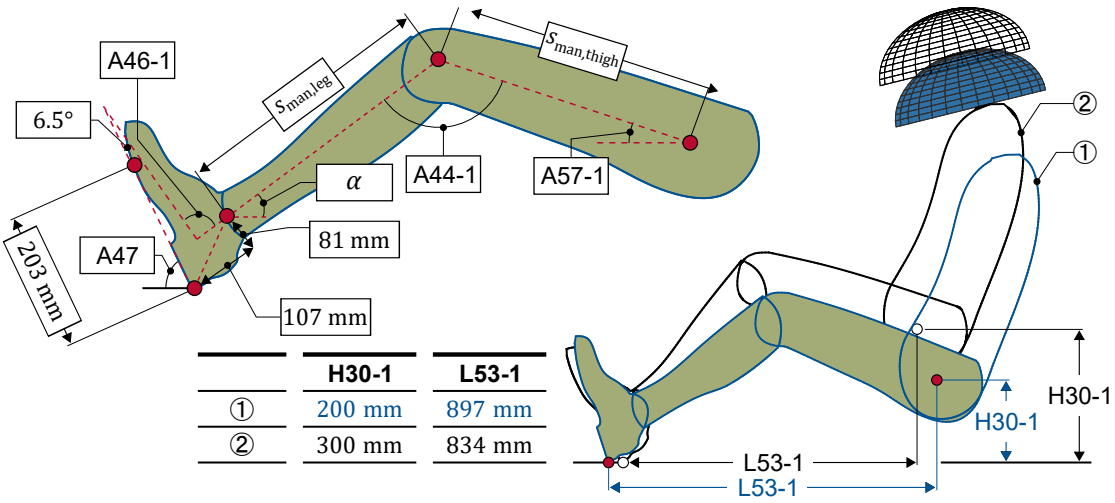

Figure 3.7: Main dimensions and angles of the driver's leg and influence of different H30-1 values on seating position and legroom (L53-1).

The interior model combines trigonometrical relationships, dimensional chains, and empirical models. The empirical models are derived from a selected dataset from A2mac1 [163], which

will be denoted as *interior dataset*. The interior dataset documents the SAE dimensions of over 150 vehicles from 2010 to 2021 and includes BEVs, ICEVs, and HEVs. ICEVs and HEVs are considered based on the assumption that the same passenger space has to be offered to the customer regardless of the powertrain type. A complete list of vehicles contained in the interior dataset is specified in [71].

The model for the first row of seats derives the required driver's legroom from the H30-1 (input of the tool, Table 3.2). The legroom calculation is based on trigonometrical correlations between the dimensions in Figure 3.7. First, the shoe plane angle (A47) is estimated from the H30-1 using the cubic correlation proposed in the SAE J4004 [63, p. 11]. Subsequently, combining A47, the bare foot flesh line angle (6.5°, SAE J1100 [51, p. 26]), and ankle angle A46-1 (set to 87° as proposed by Mau et al. [174]), the inclination of the driver's lower leg (α, Figure 3.7) is calculated according to Equation (3.5).

$$\alpha = 180° - A46\text{-}1 + A47 + 6.5° \tag{3.5}$$

To uniquely define the position of the manikin, the thigh angle A57-1 is estimated using the lengths of the thigh $s_{\mathrm{man,thigh}}$ and lower leg $s_{\mathrm{man,leg}}$, as shown in Equation (3.6).

$$A57\text{-}1 = asin\left(\frac{s_{\mathrm{man,leg}} sin(\alpha) + (\sqrt{107^2 + 81^2}) sin(180 - A47 - atan(107/81)) - H30\text{-}1}{s_{\mathrm{man,thigh}}}\right) \tag{3.6}$$

$s_{\mathrm{man,thigh}}$ and $s_{\mathrm{man,leg}}$ depend on the employed manikin percentile [60, p. 9]. Finally, with the previously calculated dimensions, the driver legroom L53-1 is derived through Equation (3.7).

$$L53\text{-}1 = (\sqrt{107^2 + 81^2}) cos(180 - A47 - atan(107/81)) + s_{\mathrm{man,leg}} cos(\alpha) + s_{\mathrm{man,thigh}} cos(A57\text{-}1) \tag{3.7}$$

The trigonometric relationships in Equation (3.5) - (3.7) create a coupling between H30-1 and L53-1: an increase of H30-1 triggers a decrease of the driver's legroom and vice versa (Figure 3.7). The L53-1, in turn, affects legroom and the position of the second row of seats. The distance between first and second rows is influenced by different factors such as vehicle segment and comfort requirements. Equation (3.8) and Figure 3.8 present the empirical correlation (derived from the interior dataset) between SgRP position (L114) and FRP location ($d_{\mathrm{FRP,axle,x}}$).

$$d_{\mathrm{FRP,axle,x}} = 267\,\mathrm{mm} + 1.011\,L114 = 267\,\mathrm{mm} + 1.011\,[L53\text{-}1 + (203\,\mathrm{mm})\,cos(A47) + L113] \tag{3.8}$$

All parameters required for estimating L114 have been previously calculated or are inputs of the tool. To complete the positioning of the second row of seats, a further dimensional chain is required to couple the heights of the first and second row of seats (Figure 3.8).

Once L53-1 and H30-1 are known, the driver's seating position and his head contour are derived. This calculation step yields the driver's upper body height $s_{\mathrm{man,upb,z}}$. An analysis of the interior dataset showed that most manufacturers add an additional clearance $s_{\mathrm{man,hr,z}}$ between the head contour and the interior compartment's roof. To include this clearance in the total driver height $s_{\mathrm{man,tot,z}}$, an empirical regression model is derived [71, p. 74] as shown in Equation (3.9).

$$s_{\mathrm{man,tot,z}} = s_{\mathrm{man,upb,z}} + s_{\mathrm{man,hr,z}} + H30\text{-}1 = 1.085\,(s_{\mathrm{man,upb,z}} + H30\text{-}1) - 24.6\,\mathrm{mm} \tag{3.9}$$

Given $s_{\mathrm{man,tot,z}}$ the driver is positioned based on the vehicle height H100 and the roof thickness $s_{\mathrm{roof,z}}$. At the end of this step, the positions of AHP and SgRP are fully defined. For the second row, a similar method is applied. The interior roof at the second row is (depending on the

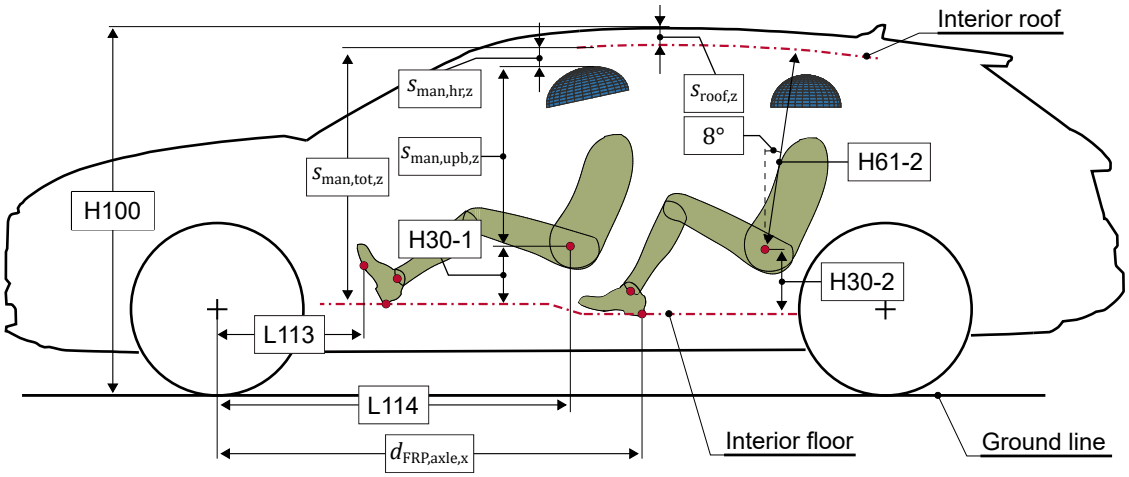

Figure 3.8: Dimensional chain coupling first and second row of seats. Based on the vehicle height, the chain determines the positions of SgRP, SgRP-2, AHP, and FRP.

body type) usually lower. To consider this difference, an empirical offset is derived from the interior dataset [71, pp. 75-76]. Given the interior roof position at the second row, the SgRP-2 is calculated using the SAE dimension H61-2. An empirical analysis of the interior dataset did not yield any strong correlation between the H61-2 and other internal dimensions. The H61-2 is strongly influenced by the shape of the vehicle's rear-end, which in turn varies depending on the body type and the manufacturer's design strategy. Therefore, to model this element, three body-type-dependent H61-2 values are derived and listed in Section D.2. By combining H61-2 and H30-2, the vertical position of FRP and SgRP-2 is calculated. With these steps, the heights of AHP and FRP are determined. The point with the lowest position defines the available battery space along the vertical direction. In the case shown in Figure 3.8, the lowest point is the FRP.

To further increase the tool's flexibility, it is also possible to import an already existing interior concept (which requires assigning further inputs, marked with an asterisk in Table A.1 and A.2). In this case, the models presented in this chapter are not used and the architecture tool sizes the interior according to the imported interior concept.

3.4.4 Powertrain Module: Drive Unit

The powertrain module includes the transmission system (gearbox and driveshafts), electric machines, and the traction battery. This section focuses on the developed volumetric models for the drive unit. The models calculate the volume of electric machines and gearboxes based on power and torque requirements.

To adapt the torque and speed of the electric machine to the traction force required by the wheels, gearboxes are usually placed between the machine and wheels [23, p. 199]. Current BEVs are usually equipped with single-speed gearboxes [6]. Two exceptions are the Porsche Taycan [175] and the Rimac Concept Two [176], which have two-speed gearboxes. This solution increases the performance of the powertrain, since it is possible to size the first transmission ratio according to the acceleration requirement, and the second transmission ratio based on the top speed [177]. However, two-speed gearboxes require a higher number of components [178], which ultimately results in larger dimensions, mass, and costs. Currently, two-speed gearboxes are only used in high-performance vehicles and are therefore neglected in this thesis.

For single-speed gearboxes with transmission ratios below 6, one reduction stage is sufficient [179, p. 89]. Nevertheless, with ratios over 6, the gear's mass drastically increases if only one reduction stage is used. Since the typical transmission ratios for BEVs range between 6 and 14 [21], series BEVs usually have two reduction stages (Figure 3.9). Therefore, only cases with two reduction stages are considered.

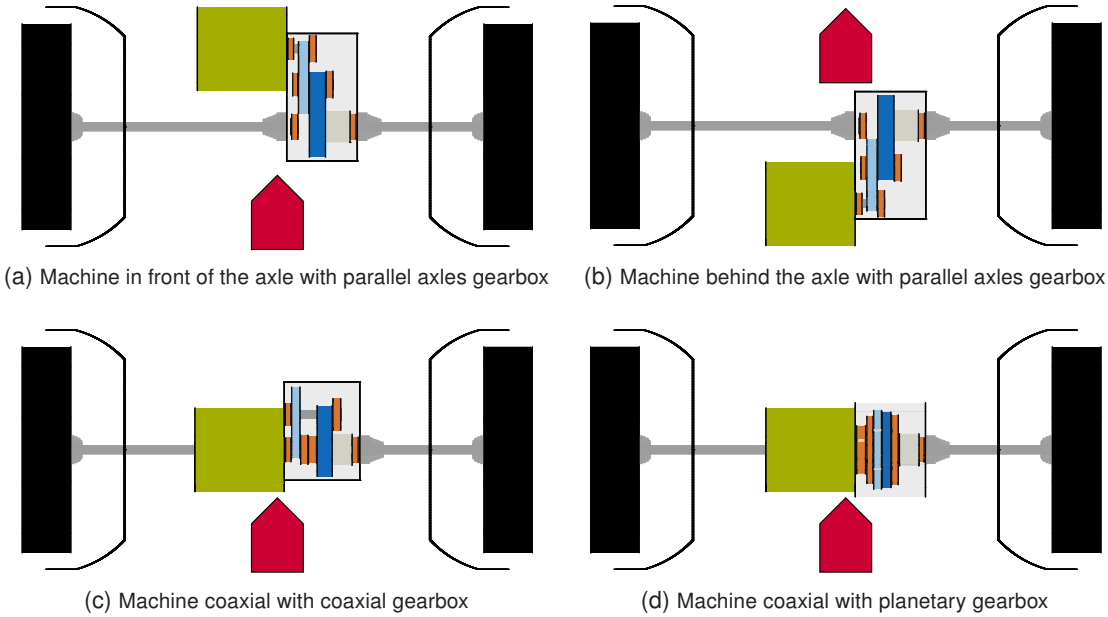

(a) Machine in front of the axle with parallel axles gearbox

(b) Machine behind the axle with parallel axles gearbox

(c) Machine coaxial with coaxial gearbox

(d) Machine coaxial with planetary gearbox

Figure 3.9: Possible drive unit configurations. The figures show the following components: electric machine (green), bearings (orange), first stage of gears (light blue), second stage of gears (dark blue), differential cage (light gray), driveshafts (dark gray), and tires (black). The red arrow points towards the driving direction.

BEV gearboxes are divided into two categories based on the shaft layout: coaxial and parallel axes. In the first category, coaxial gearboxes, the input shaft (the shaft connected to the electric machine), is coaxial with the output shaft (the shaft connected to the differential). In the second category (parallel axles gearboxes), input and output shafts are parallel instead of coaxial. These two gearbox types can be combined with the electric machine topologies presented in Subsubsection 2.2.2, generating different drive unit configurations. Figure 3.9 depicts the four possible drive unit configurations for a central machine mounted at the front axle.

Figure 3.9a shows a parallel machine layout (positioned in front of the axle) with a parallel axle gearbox. This is the most common layout for BEVs and is composed of three shafts: an input shaft from the electric machine, an intermediate shaft, and an output shaft where the differential is mounted. A two-shaft layout (where the first stage consists of a planetary gear) is also possible and is built on the front axle of the Audi e-tron [83]. Due to its high complexity and the rare usage, the two-shaft variant is not modeled in this thesis. In the drive unit shown in Figure 3.9b, the gearbox has the same characteristics as in Figure 3.9a but the electric machine is placed behind the front axle, thus reducing the available space for the traction battery. An example of this drive unit configuration is the Tesla Model 3. Figure 3.9c shows a coaxial machine coupled with a coaxial gearbox. This configuration is more compact than Figure 3.9a and 3.9b. Nevertheless, since both stages are mounted on the same shafts, the axle distance of the first (light blue) and the second stage (dark blue) has to be the same. This imposes further constraints on gearbox sizing since the gear diameters and the number of teeth of the two stages become interdependent. An example for this drive unit configuration is the Opel Ampera [23, p. 581].

The last possible configuration is the coaxial machine layout coupled with a planetary gearbox (Figure 3.9d). This solution offers a compact unit and is used in vehicles such as the Jaguar I-Pace [82] and the rear axle of the Audi e-tron [83].

The architecture tool models all drive units presented in Figure 3.9, including the corresponding variants with two machines on the axle (in this case, the differential is not modeled, since it is not required). The drive unit modeling is divided into three parts: gearbox sizing, machine sizing, and calculation of drive unit dimensions. For this scope, two inputs of the vehicle architecture tool (Table 3.2) are required: the machine position (in front, behind, or coaxial) and the gearbox type (parallel axles, coaxial, or planetary gearbox).

For gearbox sizing, a benchmark analysis is conducted, and a dataset of existing BEV gearboxes (further referred to as *gearbox dataset*) is created. A complete list of the vehicles contained in the gearbox dataset is specified in [101, p. xvii]. Based on the knowledge gained from the gearbox dataset, three separate models are developed for coaxial, planetary, and parallel axles gearboxes. With the machine requirements (maximum torque and rotational speed, calculated by the LDS), the model derives the gears and bearing loads. Based on these loads, shafts and gears are iteratively detailed and suitable bearings are chosen from a bearing catalog [180]. Finally, the gears are disposed according to the gearbox type and the resulting gearbox housing dimensions are derived. For this scope, a set of dimensional chains (which are displayed in Section D.3) is employed. More information regarding the gearbox model is documented in [27, 100, 101].

For electric machine sizing, the inputs are the machine type as well as its torque and rotational speed requirements. Regarding the machine type, only IMs and PMSMs are considered, since they are state of the art technologies [6]. A benchmark analysis is conducted and a dataset of existing electric machines (further referred to as *machine dataset* and documented in [101, p. xv]) created. For modeling, the machine (including its housing) is simplified as a cylinder. Subsequently, its dimensions (diameter and length) are estimated using empirical correlations derived from the machine dataset. These correlations are documented in Section D.4.

Finally, the gearbox and electric machine are assembled according to the chosen electric machine position and the drive unit dimensions are derived. The hereby calculated drive unit dimensions are required in the next steps of the architecture tool, to estimate the available battery space (Subsection 3.4.5).

3.4.5 Powertrain Module: Available Battery Space Estimation

The traction battery stores the energy required for propelling the vehicle. It includes cell modules, the cell cooling system, the Battery Management System (BMS), and the battery housing [77, p. 58]. Due to the high complexity of this component, its modeling is discussed in two separate chapters. This section presents the dimensional chains implemented to estimate the maximum allowable battery size. In the following chapter (Subsection 3.4.6), the derived battery dimensions are filled with cells.

The battery dimensions are the result of a compromise between conflicting objectives. On the one hand, to guarantee its safety (for instance in a side crash scenario [181]), small dimensions are preferable, since this allows placing the battery into the area of low crash loads, located close to the center of the vehicle [182]. On the other hand, to increase the vehicle range, bigger battery packs are required. Since this thesis focuses on the early development phase, it is not possible to implement crash simulations for battery sizing. To address this problem, a benchmark

analysis of over 20 BEVs of the A2mac1 database [163] is conducted. The result of the analysis is a dataset that will further be referred to as *battery dataset*, containing detailed information about battery, module, and cell dimensions. The list of BEVs contained in the battery dataset is documented in the thesis of Köhler [101, p. xix]. From the battery dataset, a set of dimensional chains defining the available space for the battery is derived. These chains are divided into three groups, to represent different constraints on the battery dimensions:

- Constraints imposed by the drive unit.
- Constraints imposed by front and rear wheels.
- Constraints imposed by the passenger compartment.

The following sections detail these constraints and their characteristics.

Drive Unit Constraints

The drive unit impacts the battery space along the x-direction (i.e. the driving direction) as shown in Figure 3.10. To consider this limitation, the drive unit is sized as described in Subsection 3.4.4. Subsequently, from the drive unit dimensions, the critical lengths $d_{\mathrm{critic,f,x}}$ and $d_{\mathrm{critic,r,x}}$ are derived. These two variables are defined as the portion of drive unit, which limits the battery dimensions. For example, if the machine is placed on the front axle, the critical length $d_{\mathrm{critic,f,x}}$ corresponds to the distance between the point of the driving unit that is closest to the battery and the front axle. $d_{\mathrm{critic,r,x}}$ is defined in the same way, but refers to the rear axle.

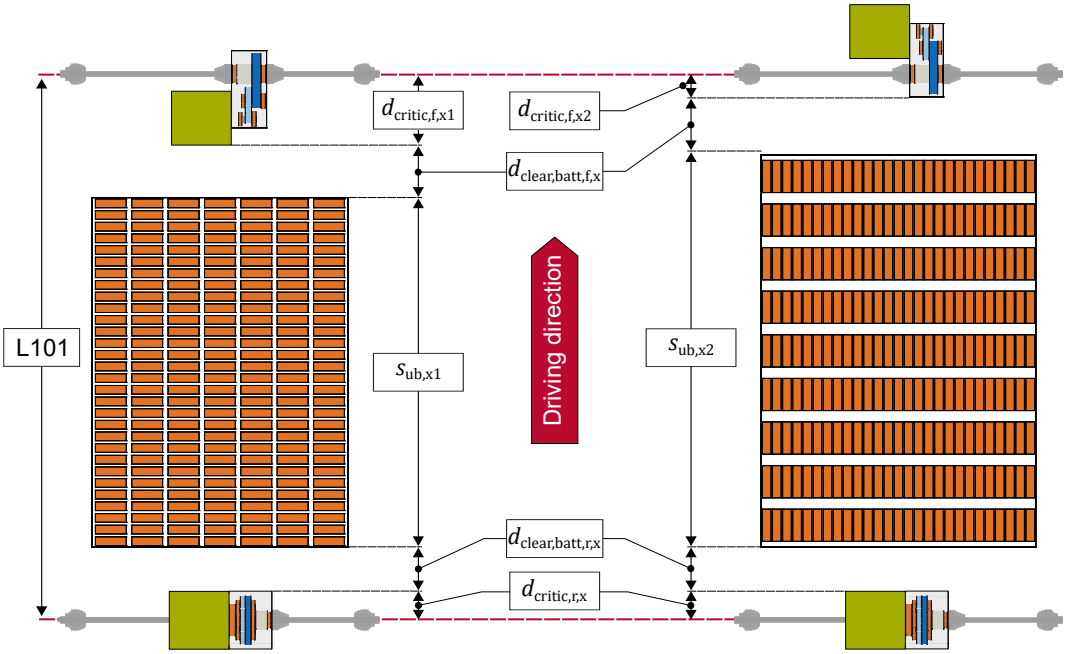

Figure 3.10: Two drive topologies simulated on a C-segment SUV (similar to the Audi e-tron). The topology on the right has, due to its different positioning of the front machine, approx. 7 kW h more than the option on the left.

To ensure the safety of the battery in the event of a collision, such as the New Car Assessment Program frontal crash test [183], a clearance must be maintained between battery and drive unit. If a drive unit is mounted at the front axle, it will be displaced towards the battery in a frontal crash scenario, which might lead to a collision between the two components. This collision could damage the cells and cause a thermal runaway. A properly chosen clearance ensures that most

of the crash energy is absorbed before the drive unit collides with the battery. To model this feature, typical values for the clearance at front $d_{\mathrm{clear,batt,f,x}}$ and rear axle $d_{\mathrm{clear,batt,r,x}}$ (Figure 3.10) are derived from the battery dataset. Based on these dimensions, the dimensional chain shown in Equation (3.10) is implemented in the tool to estimate the length of the underbody battery $s_{\mathrm{ub,x}}$.

$$s_{\mathrm{ub,x}} = L101 - d_{\mathrm{critic,f,x}} - d_{\mathrm{clear,batt,f,x}} - d_{\mathrm{clear,batt,r,x}} - d_{\mathrm{critic,r,x}} \tag{3.10}$$

The dimensional chain in Equation (3.10), creates a geometrical coupling between the battery and drive unit dimensions. The drive unit dimensions are calculated depending on the input performance requirements (such as acceleration time and maximum speed) and the mass of the current tool iteration m_{n}. If in the following iteration $n+1$ the vehicle mass changes, this leads to resizing the drive unit. As a consequence of Equation (3.10), every drive unit resizing induces a proportional change (i.e. a secondary volume effect) on the battery dimensions.

Wheel Constraints

The vehicle wheels are another crucial component in case of a frontal crash. A particularly critical scenario is the small overlap frontal test specified by the Insurance Institute for Highway Safety [184]. During the test, the vehicle is accelerated toward a rigid barrier. Since the barrier is placed on one side of the vehicle and covers $25\,\%$ of the vehicle surface, only one side of the crash structure can absorb the impact energy. When colliding with the barrier, the tires, brake discs, rims, and axle links are displaced and may crash into the battery. In order to avoid cell damage, BEVs with batteries close to the front axle are usually equipped with a minimum clearance between battery and wheels. To account for the geometrical coupling between these two components, a minimum value for the wheel clearance is derived from the battery dataset.

Figure 3.11 visualizes the modeling approach for the wheel clearance. At each new tool iteration, the tire dimensions are calculated (Subsection 3.4.1). Subsequently, the wheel arch dimensions are derived from tire size and steering angle δ (Figure 2.11). Combining the wheel arch with the empirically derived minimum clearance, a limit curve denoting the safe area to install the battery (limit small overlap, left-hand side of Figure 3.11) is derived. Finally, depending on its width and shape, the battery is placed on the limit curve.

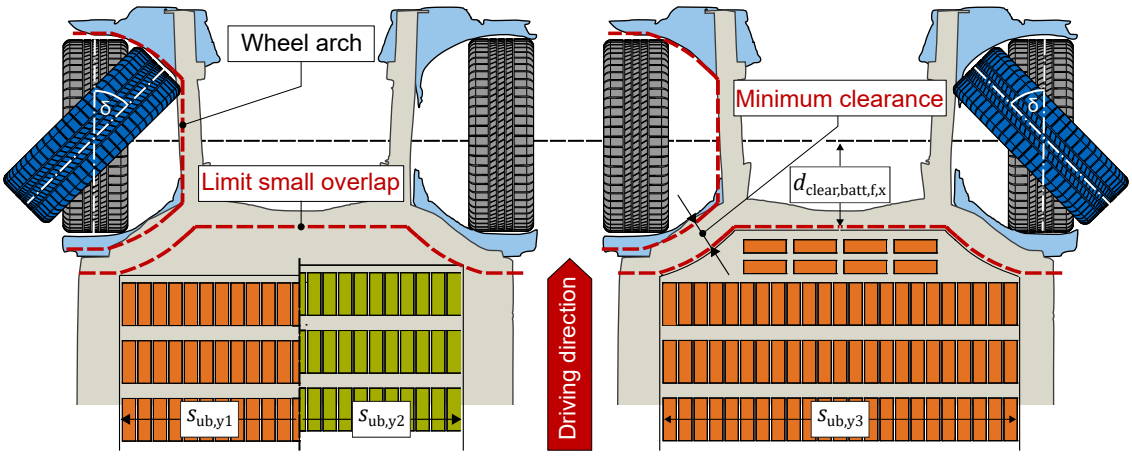

Figure 3.11: Rectangular (left-hand side) vs. drop shape (right-hand side). For the rectangular shape, the battery is positioned depending on its width. The orange battery ($s_{\mathrm{ub,y1}}$) is wider than the green battery ($s_{\mathrm{ub,y2}}$) and must be therefore positioned further away from the front axle. On the other hand, the drop shape on the right-hand side optimally uses the available space.

As shown on the left-hand side of Figure 3.11 decreasing the battery width enables placing the battery closer to the axle while fulfilling crash safety requirements. A solution to maximize the battery energy is the drop shape employed on the right-hand side of Figure 3.11, where the battery housing is shaped to optimally fit the area enclosed by the small overlap limit curve. Examples of drop shape batteries are the Audi e-tron (Figure B.2a), the Jaguar I-Pace (Figure B.2b), and the Tesla Model 3 (Figure B.3a).

The dimensional chain depicted in Figure 3.11 creates a coupling between tires and battery. Therefore, resizing the tires (for example due to a higher vehicle mass) does not only generate secondary volume effects on the drive unit available space (Figure 2.13) but also impacts the battery position and its dimensions.

Positioning the battery on the small overlap limit requires the battery width $s_{\mathrm{ub,y}}$. An analysis of the battery database shows that in most cases the battery width correlates with the available space comprised between the rear wheel arches (Figure 3.12). This trend has two main causes: on the one side, this space offers an acceptable level of safety for the case of a side crash impact. On the other side, to make use of all the available space along the longitudinal direction, also the area comprised between the rear wheels is employed. Therefore, the rear wheels and wheel arches represent a further constraint that must be included in the tool.

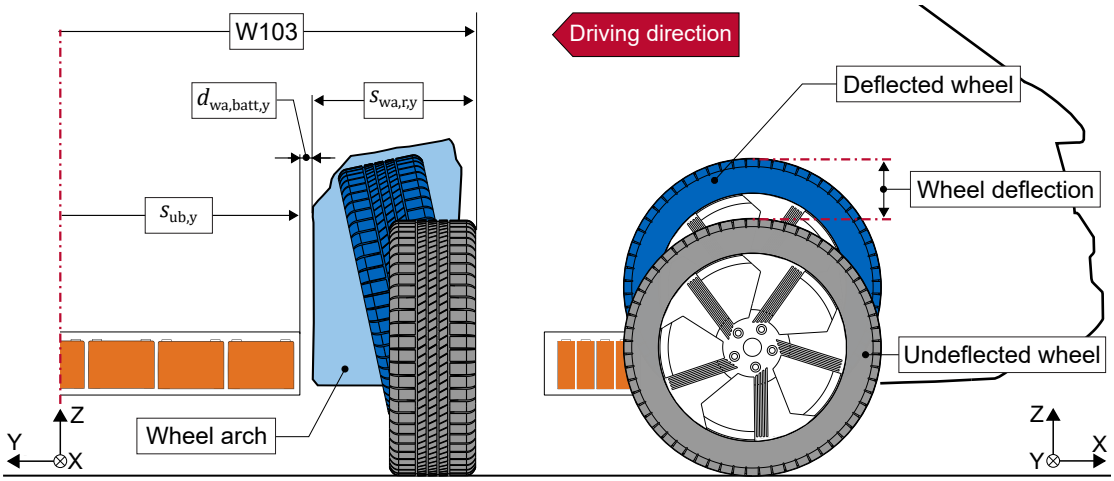

Figure 3.12: Kinematic of the wheel at the rear axle. The maximum deflected wheel (marked as blue) defines the required wheel arch width $s_{\mathrm{wa,r,y}}$.

Unlike the front wheel arches, the rear ones are not affected by the steering angle, as current vehicles are generally not equipped with rear axle steering. Exceptions can be found in vehicles with a particular long wheelbase, such as the Audi A8, which is equipped with an all-wheel steering to reduce its turning radius [185]. In such cases, nevertheless, the rear steering angle is small (the Audi A8 reaches a maximum value of $5°$ [186]) and barely impacts the wheel arch dimensions. The width of the rear wheel arch $s_{\mathrm{wa,r,y}}$ is mostly influenced by the axle vertical kinematics. To overcome obstacles such as irregularities in the road surface, the axle must allow the tires to have a certain vertical deflection. The value of this deflection depends on the axle kinematics.

To model the axle kinematics, an analysis of different axle types is conducted. In the analysis over 100 vehicles from the A2mac1 database [163] are measured and categorized according to their axle type. The result is a semi-physical axle model documented in the thesis of Spreng [187]. The axle model estimates the position of the maximum deflected tire based on the axle type. Given the position of the maximum deflected wheel, the dimensions of the wheel arch are

derived. Finally, a minimum clearance $d_{\mathrm{wa,batt,y}}$ between the rear wheel arch and the battery is derived through an empirical analysis. With these results and the vehicle width (W103), the dimensional chain shown in Equation (3.11) is implemented in the tool.

$$s_{\mathrm{ub,y}} = W103 - 2\left(s_{\mathrm{wa,r,y}} + d_{\mathrm{wa,batt,y}}\right) \tag{3.11}$$

The dimensional chain in Equation (3.11) creates a geometrical coupling between the rear tire dimensions and the battery width. With increasing tire width (for example due to a higher vehicle mass), the width of the wheel arch also raises, triggering secondary volume effects on the battery.

Passenger Compartment Constraints

To increase battery energy, the tunnel and the space below the second row of seats (second level) can also be filled with modules (similarly to the Polestar 2, Figure B.3b). These spaces are influenced, through their position, by the passenger compartment (Figure 3.13).

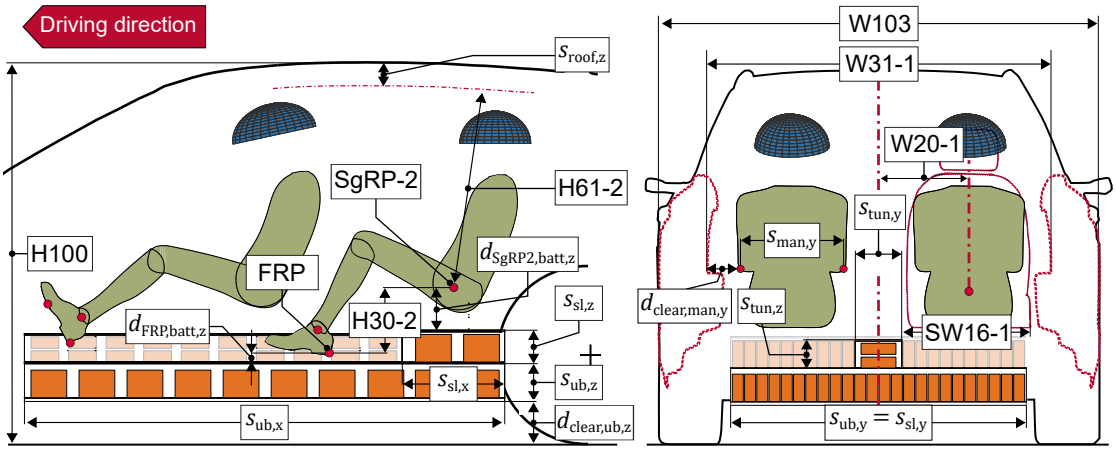

Figure 3.13: Dimensional chains for underbody, tunnel, and second level.

The second level dimensions depend on the passenger compartment and the size of the underbody battery. The underbody length $s_{\mathrm{ub,x}}$ and width $s_{\mathrm{ub,y}}$ are calculated with Equation (3.10) and Equation (3.11). The underbody height $s_{\mathrm{ub,z}}$ is derived from the interior concept dimensions (Subsection 3.4.3) and the ground clearance $d_{\mathrm{clear,ub,z}}$ (Subsection 3.4.2) following the relationship in Equation (3.12).

$$s_{\mathrm{ub,z}} = H100 - s_{\mathrm{roof,z}} - H61\text{-}2\,cos(8) - H30\text{-}2 - d_{\mathrm{FRP,batt,z}} - d_{\mathrm{clear,ub,z}} \tag{3.12}$$

Where $d_{\mathrm{FRP,batt,z}}$ takes into account the thickness of acoustic and damping materials, BIW, and the clearance between battery and BIW. For the estimation of $d_{\mathrm{FRP,batt,z}}$, the minimum vertical distance between FRP and the top of the underbody battery is measured for the vehicles contained in the battery dataset. Given the underbody battery dimensions, the second level is defined. While its width $s_{\mathrm{sl,y}}$ is equal to $s_{\mathrm{ub,y}}$, its length $s_{\mathrm{sl,x}}$ depends on $s_{\mathrm{ub,x}}$ and the position of the FRP. Finally, the height $s_{\mathrm{sl,z}}$ is derived following Equation (3.13).

$$s_{\mathrm{sl,z}} = H100 - s_{\mathrm{roof,z}} - H61\text{-}2\,cos(8) - d_{\mathrm{SgRP2,batt,z}} - s_{\mathrm{ub,z}} - d_{\mathrm{clear,ub,z}} \tag{3.13}$$

Where $d_{\mathrm{SgRP2,batt,z}}$ accounts for the thickness of seats, insulation, BIW, and the clearance between battery and BIW. Its value is derived from the same dataset used for $d_{\mathrm{FRP,batt,z}}$. The second level

is not always filled with cells: in vehicles such as the Tesla Model 3 or the Jaguar I-Pace, it is used to install the BMS and the battery relays. In other vehicles, such as the VW ID3, it remains unused.

Given the vehicle width W103 (input of the tool, Table 3.2), the width of the interior compartment at the first row, W31-1, is derived with an empirical correlation [71, p. 72]. Then, the transversal distance between SgRP and vehicle center (W20-1) is estimated in Equation (3.14).

$$W20\text{-}1 = \left(\frac{W31\text{-}1}{2}\right) - d_{\text{clear,man,y}} - \left(\frac{s_{\text{man,y}}}{2}\right) \tag{3.14}$$

Where $d_{\text{clear,man,y}}$ is an empirically derived value (vehicle segment-dependent) which describes the clearance between the passenger's elbow and the inner side of the door [71, p. 70]. For modeling the manikin width $s_{\text{man,y}}$, the value proposed by [188] is used. Finally, the width of the tunnel $s_{\text{tun,y}}$ is derived from the driver's seat cushion width SW16-1, which is modeled with empirical values (vehicle segment-dependent) [71, p. 70].

$$s_{\text{tun,y}} = 2\left[W20\text{-}1 - \left(\frac{SW16\text{-}1}{2}\right)\right] \tag{3.15}$$

The tunnel length $s_{\text{tun,x}}$ (not shown in Figure 3.13) is calculated from the difference between underbody $s_{\text{ub,x}}$ and second level length $s_{\text{sl,x}}$ and the tunnel height by multiplying the H30-1 with an empirically derived conversion factor. The tunnel is not always filled with cells and can also be used to install the BMS and the relays (e.g. for the Audi e-tron). Other manufacturers, like VW for the ID.3, choose a battery integration that minimizes the tunnel height. In this case, the tunnel is only used to lead high voltage cables.

With the approach presented in this chapter, the battery dimensions for underbody, tunnel, and second level are derived. These dimensions are influenced by the wheel and the drive unit size, which in turn depend on the performance requirements and the vehicle mass. At every new tool iteration n, the battery space is recalculated. Subsequently, the battery space is filled with cells and the maximum installable energy is derived. Subsection 3.4.6 presents the developed battery filling algorithm.

3.4.6 Powertrain Module: Installable Battery Energy Estimation

In the previous sections, a set of dimensional chains for the estimation of the battery dimensions has been presented. This section focuses on the estimation of the maximum installable energy. For this scope, a battery filling algorithm is developed (Figure 3.14).

The filling algorithm inputs are cell type (Table 3.2), required battery energy (calculated by the LDS, Section 3.3), dimensional concept (Subsection 3.4.2 and 3.4.3), and dimension and position of the drive units (Subsection 3.4.4). Regarding the cell type, there are three possibilities: pouch, cylindrical, and prismatic [189, p. 324, 190, p. 105]. Currently, there is no standardized cell, since all the available types are used by various automotive manufacturers [15]. For example, the BMW i3 (both the 2014 and the 2017 model series) has prismatic cells [191], the Audi e-tron features pouch cells [83], while the Tesla products usually have cylindrical cells [191]. For the scope of this thesis, all three cell types are considered.

Similar to the main tool (Figure 3.1), the battery filling model is also based on an iterative process. In the first loop, the model calculates the maximum available space (①, Figure 3.14) independently from the required battery energy $E_{\text{batt,req}}$. This calculation follows the approach presented

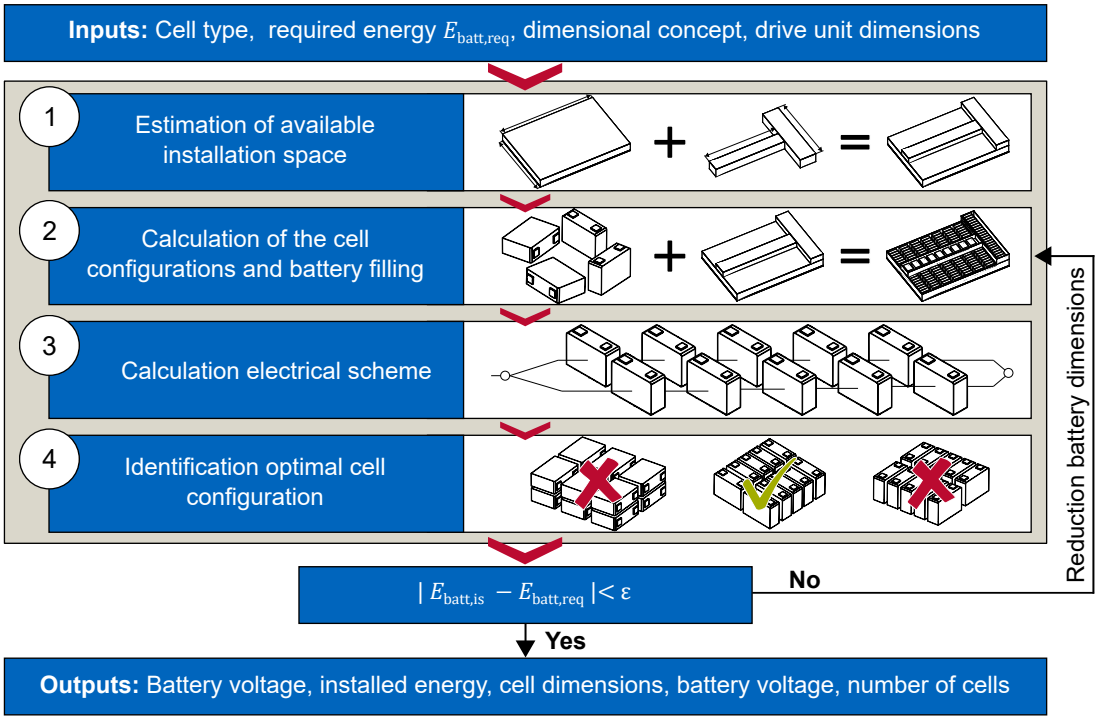

Figure 3.14: Structure of the battery model. The model consists of four steps: Estimation of available installation space ①, calculation of possible cell configurations and battery filling ②, calculation of electrical scheme ③, and identification of configuration with the highest installed energy $E_{batt,is}$ ④.

in Subsection 3.4.5 and yields the maximum allowable battery dimensions. Subsequently, the battery space is filled with cells (②, Figure 3.14). While filling the battery, minimal variations of cell length or width may radically change the number of cells that fit in the available space. Therefore, the filling algorithm simulates thousands of different cell sizes and orientations to identify the one with the highest energy potential.

Depending on cell type, different dimensions and proportions are possible [76, pp. 174-175, 192, 193]. For example, although the Tesla Model S and Model 3 have both cylindrical cells, the former has 18600 cells ($18\,\mathrm{mm}$ diameter and $60\,\mathrm{mm}$ height) [194], while the latter has 21700 cells ($21\,\mathrm{mm}$ diameter and $70\,\mathrm{mm}$ height). To model this variability, an empirical analysis is performed to estimate the typical ranges for width, height, and length of different cell types (Section F.3). Depending on the type (pouch, prismatic or cylindrical), all possible sizes are generated by varying the cell width, height, and length in the derived empirical ranges (Figure 3.15).

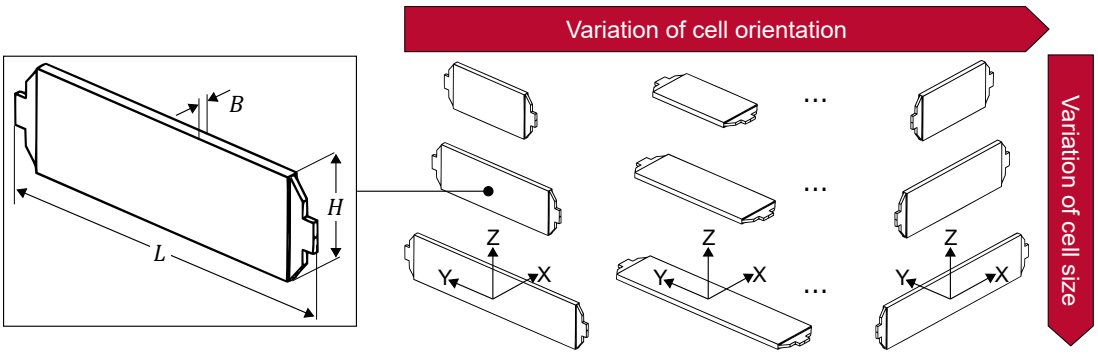

Figure 3.15: Using empirical ranges, all possible cell sizes are calculated by varying width, height, and length. Subsequently, for each cell size, all possible orientations are derived.

A cell with a defined size can be placed in the battery with different orientations. Depending on the orientation, different numbers of the same cell can be fitted in a given space. To consider this effect all existing orientations are calculated for each previously derived cell size (Figure 3.15). If necessary, it is also possible to exclude certain orientations.

The cell sizes and their respective orientations are stored in the matrix M_{cell} as shown in Equation (3.16). Each row of M_{cell} describes the orientation and size of a different cell by storing its dimensions in the x-, y-, and z-directions. The number of rows (denoted as m) corresponds to the number of simulated cells and depends on the step size used to vary the cell dimensions (by default $1\,\text{mm}$) and the allowed orientations (for each cell size, there are six possible orientations in space if no orientation is excluded).

$$M_{\text{cell}} = \begin{bmatrix} s_{\text{cell-1,x}} & s_{\text{cell-1,y}} & s_{\text{cell-1,z}} \\ .. & ... & ... \\ s_{\text{cell-m,x}} & s_{\text{cell-m,y}} & s_{\text{cell-m,z}} \end{bmatrix} \tag{3.16}$$

Besides the cells, other components occupy installation space in the battery. Examples are the battery cooling, the cell module housings, and the battery inner cables [58]. To consider their space requirements, empirical package factors ($K_{\text{pack,x}}$, $K_{\text{pack,y}}$) and dimensional chains are employed. The package factors express the percentage of space along the considered direction, which is filled with cells. They can assume a value between 1 ($100\,\%$ filling) and 0 (no cell fitting). For example, a $K_{\text{pack,x}}$ of 0.8 means, that $80\,\%$ of the battery space along the x-direction is filled with cells. Correspondingly, the remaining $20\,\%$ is occupied by module casings, cables, and side reinforcements. Typical values for the package factors as well as their calculation approach are documented in Section D.5. The space occupied by the inactive components along the x- and y-directions is added to the cell dimensions according to Equation (3.17). Since for the z-direction no package factor is required, it is set to 1.

$$M_{\text{pack}} = \begin{bmatrix} s_{\text{pack-1,x}} & s_{\text{pack-1,y}} & s_{\text{cell-1,z}} \\ ... & ... & ... \\ s_{\text{pack-m,x}} & s_{\text{pack-m,y}} & s_{\text{cell-m,z}} \end{bmatrix} = M_{\text{cell}} \begin{bmatrix} K_{\text{pack,x}}^{-1} & 0 & 0 \\ 0 & K_{\text{pack,y}}^{-1} & 0 \\ 0 & 0 & 1 \end{bmatrix} \tag{3.17}$$

Equation (3.17) yields the pack matrix M_{pack}, which stores the pack dimensions of each cell configuration in M_{cell}. For the z-direction, instead of using package factors, a dimensional chain is derived (Equation (D.12)) that models the internal components of the battery (covers, cooling plate, module housings, see Figure D.8) and derives the available space for the cells along the z-direction $s_{\text{cell,av,z}}$.

Combining the pack matrix M_{pack} and the dimensional chain in Equation (D.12), the available installation space is filled with cells as shown in Figure 3.16. For example, Equation (3.18) calculates the number of cells fitting in the underbody for the i_{th} element of M_{pack}.

$$N_{\text{cell-i,x,ub}} = \frac{s_{\text{ub,x}}}{s_{\text{pack-i,x}}} \qquad N_{\text{cell-i,y,ub}} = \frac{s_{\text{ub,y}}}{s_{\text{pack-i,y}}} \qquad N_{\text{cell-i,z,ub}} = \frac{s_{\text{cell-i,av,z,ub}}}{s_{\text{cell-i,z}}} \tag{3.18}$$

The same approach is used for deriving the number of cells in the tunnel and the second level. The total number of cells is calculated by multiplying the contributions on the x-, y-, and z-directions. Equation (3.19) exemplarily shows how to calculate the number of cells fitting in the underbody for the i_{th} element of M_{pack}. Furthermore, for the battery dimensions shown in

Figure 3.16, the total amount of cells $N_{\text{cell-i,tot}}$ must also consider the contributions of the tunnel and the second level according to Equation (3.20).

$$N_{\text{cell-i,tot,ub}} = N_{\text{cell-i,x,ub}}\, N_{\text{cell-i,y,ub}}\, N_{\text{cell-i,z,ub}} \tag{3.19}$$

$$N_{\text{cell-i,tot}} = N_{\text{cell-i,tot,ub}} + N_{\text{cell-i,tot,sl}} + N_{\text{cell-i,tot,tun}} \tag{3.20}$$

As shown in Figure 3.16, the cell orientation does not necessarily have to be the same in the different spaces (tunnel, underbody, second level), nevertheless, the cell dimensions are imposed to be the same. This prevents the battery from being filled with cells of different dimensions.

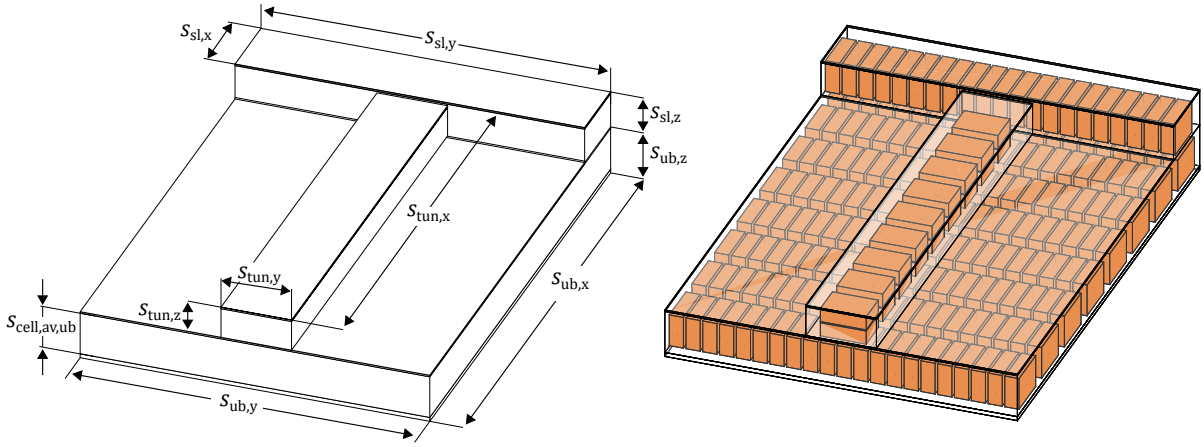

Figure 3.16: Comparison between empty and filled battery space.

The calculations shown in Equation (3.18) - (3.20) are performed for each row (i.e. each cell orientation and size) of M_{pack}. This yields the vector $N_{\text{cell,tot}}$ which stores how many cells fit in the available battery space for each element of M_{pack}. However, this filling step does not ensure that the installed number of cells yields an acceptable battery voltage. To test the voltage requirements, the electrical scheme of each element of M_{pack} must be calculated (③, Figure 3.14).

The battery voltage depends on the cell chemistry, i.e. on the coupled positive and negative electrode materials [190, p. 104, 195]. Current chemistries in the automotive sector are Lithium Nickel Cobalt Manganese Oxide, Lithium Nickel Cobalt Aluminum Oxides, Lithium Manganese Oxide, Lithium Cobalt Oxide, and Lithium Iron Phosphate [196]. Latter is at the moment mostly employed in the Chinese market by manufacturers such as BYD [196, 197], while the other chemistries are more common among European manufacturers. For these chemistries, the cell nominal voltage $U_{\text{cell,nom}}$ ranges between $3.6\,\text{V}$ and $3.7\,\text{V}$ [191]. Therefore, a default value of $3.65\,\text{V}$ is implemented in the battery model. This value can be optionally changed to model alternative chemistries. Given $U_{\text{cell,nom}}$, the voltage at the battery level $U_{\text{batt,nom}}$ is calculated by multiplying $U_{\text{cell,nom}}$ with the number of serial cells $N_{\text{cell,serial}}$ according to Equation (3.21).

$$U_{\text{batt,nom}} = U_{\text{cell,nom}}\, N_{\text{cell,serial}} \tag{3.21}$$

Following the approach of Wiedemann [42, p. 64], instead of imposing a specific voltage requirement, a feasible voltage range is implemented. The minimum allowed value $U_{\text{batt,min}}$ is set to $350\,\text{V}$ while the maximum allowed value $U_{\text{batt,max}}$ is set to $450\,\text{V}$. Nevertheless, in order to model high-performance cars (which usually have higher values [161]), the voltage limits can be

optionally changed. Due to the imposed battery voltage range, the number of serial cells must be higher than a minimum value $N_{\text{serial,min}}$ and cannot exceed a maximum value $N_{\text{serial,max}}$. This generates a range of feasible numbers of serial cells as depicted in Equation (3.22).

$$\frac{U_{\text{batt,min}}}{U_{\text{cell,nom}}} = N_{\text{serial,min}} \leq N_{\text{cell,serial}} \leq N_{\text{serial,max}} = \frac{U_{\text{batt,max}}}{U_{\text{cell,nom}}} \tag{3.22}$$

With the range defined in Equation (3.22), the electrical scheme can be further analyzed. Figure 3.17 shows the possible electrical schemes and the corresponding battery energies for an Audi e-tron cell. The cell has an energy of $220\,\text{Wh}$ and a $U_{\text{cell,nom}}$ of $3.67\,\text{V}$ (estimated from [83]). For this reason, in order to reach the minimum voltage requirement of $350\,\text{V}$, at least 96 serial cells are required, which corresponds to a battery energy of approx. $21\,\text{kWh}$. By increasing the number of serial cells, the battery energy is further raised, before reaching the limit value of 122 cells. Exceeding this limit would mean achieving a voltage higher than $450\,\text{V}$ and is therefore not compatible with the imposed range. To achieve a further energy increase, the cells must be set in a parallel configuration (Figure 3.17).

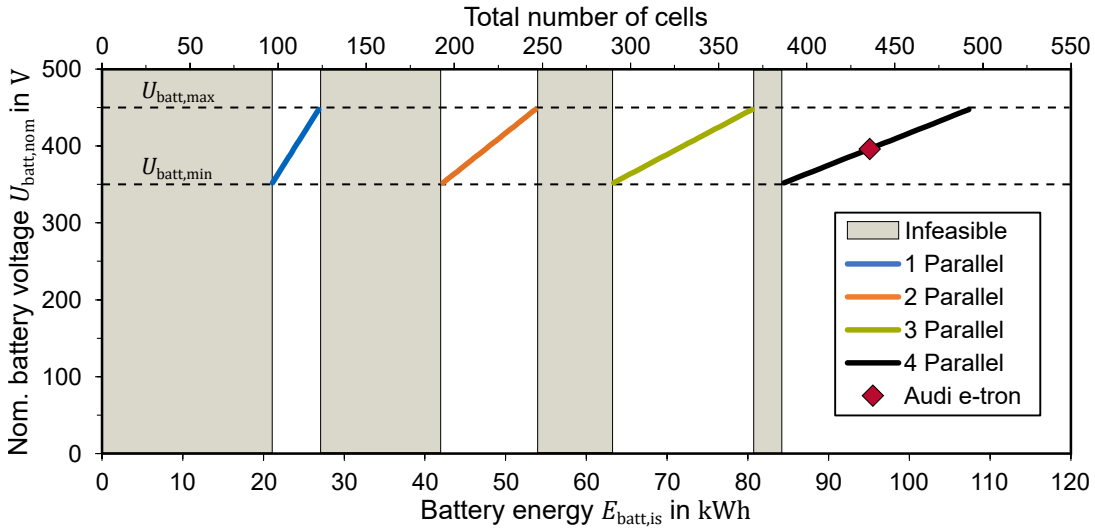

Figure 3.17: Possible electrical scheme with an Audi e-tron cell. In the case of the Audi e-tron, the $95\,\text{kWh}$ battery energy requires four parallel strands with 108 cells each.

The constraints imposed by the voltage requirements render certain battery energies (and a certain number of cells) infeasible. The infeasible combinations are marked as gray areas (their size and position depend on the cell energy) in Figure 3.17. The battery model tests if the number of installed cells is a multiple of at least one of the values comprised between $N_{\text{serial,min}}$ and $N_{\text{serial,max}}$ for each row of $N_{\text{cell,tot}}$. If this is the case, the configuration can attain a battery voltage within the given limits. Otherwise, the configuration lies in one of the infeasible areas and the number of cells is iteratively reduced until $U_{\text{batt,nom}}$ is within the allowed range. Following the electric scheme sizing, the $N_{\text{cell,tot}}$ vector has been corrected. In some cases, cell orientations capable of fitting a high number of cells may have been reduced in number due to the voltage requirements.

In the last step (④, Figure 3.14), the optimal size and orientation, i.e. the cell that maximizes the installable battery energy, is identified. For this scope, the vector $E_{\text{batt,is}}$ that stores the battery energy for each element of $N_{\text{cell,tot}}$, is derived according to Equation (3.23).

$$E_{\text{batt,is}} = N_{\text{cell,tot}}\, V_{\text{cell}}\, E_{\text{cell,vol}} \tag{3.23}$$

Where V_{cell} is the vector containing the volume of each element of M_{cell} and $E_{\text{cell,vol}}$ is the volumetric energy density (in $\mathrm{Wh\,l^{-1}}$) at the cell level. For modeling $E_{\text{cell,vol}}$, typical energy densities for different cell types are derived through an extensive literature research [21]. The optimal cell is the one that maximizes the vector $E_{\text{batt,is}}$.

At the end of this step, the maximum installable battery energy $E_{\text{batt,is}}$ is derived. If $E_{\text{batt,is}}$ is higher than $E_{\text{batt,req}}$, the battery length and width are iteratively reduced to avoid an overfilling of the energy requirement. Otherwise, the model exits the iterative loop and its outputs are saved in the architecture tool. These outputs are the dimensions, energy, and orientation of the optimal cell, the battery voltage, and the number of parallel and serial cells. These results are further required for the gravimetric component modeling, which is described in the next section.

3.5 Gravimetric Component Modeling

The fifth step of the architecture tool (Figure 3.1) estimates the new vehicle mass $m_{\text{n+1}}$ for each iteration n (Figure 3.18). $m_{\text{n+1}}$ is in turn required for the following iteration. The mass calculation uses the same modules shown in Figure 3.4 and models over 110 components. Each component is described with empirical models, documented in Appendix E.

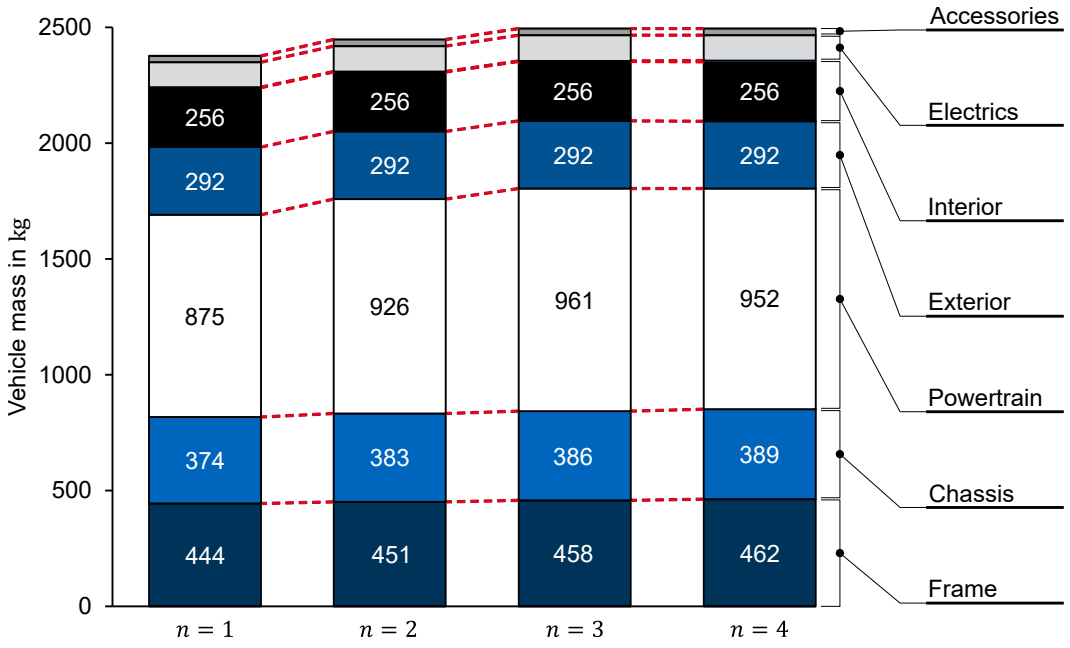

Figure 3.18: Mass calculation for an SUV similar to the Audi e-tron with 400 km range. The model iterates four times before reaching convergence. The increase in powertrain, chassis, and frame masses between iterations is caused by secondary mass effects.

The dataset used for the calculation of the empirical models contains over 200 vehicles from the A2mac1 database [163] including ICEVs, HEVs, PHEVs, and BEVs. In the following sections, this dataset will be referred to as *mass dataset* (the complete list is available in [28]). ICEVs, HEVs, and PHEVs are included to model components that are used in both electric and combustion vehicles, such as subsystems of chassis, frame, exterior, and interior. Most of the vehicles in the mass dataset are newer than 2015, but to increase modeling accuracy of some components for which limited data were available, older vehicles are included.

The mass estimate is obtained by combining the set of inputs shown in Table 3.2, the results of the LDS (Section 3.3), and the results from the volumetric component models (Section 3.4). In addition, it is possible to define a set of optional inputs (Table E.1) to further increase the estimate's accuracy. Examples include the material type for the exterior components or the presence of extra accessories such as lane-keeping support or park assistant. If the set of optional inputs is not assigned, default values are used instead. Figure 3.18 shows an exemplary output of the mass model.

In Figure 3.18 the simulation starts with an initial vehicle mass m_0 of $2000\,\mathrm{kg}$ (not shown in the figure) and outputs a mass m_1 of $2377\,\mathrm{kg}$ after the first iteration. As the difference between m_1 and m_0 is higher than the default tolerance (which is set to $10\,\mathrm{kg}$), a second loop is performed by inserting m_1 into the LDS. Since m_1 is higher than m_0, the vehicle consumption increases, which requires resizing the battery and generates secondary mass effects. The model iterates four times before reaching convergence at a mass of $2501\,\mathrm{kg}$.

In the following sections, the modules frame, chassis, exterior, interior, and powertrain are presented. Detailed information regarding the other modules is specified in the thesis of Romano [162] and in a previous publication [28].

3.5.1 Frame Module

The frame module is divided into two subsystems: BIW and other frame components (sound insulation, frame reinforcements, front-end and roof cross members, aerodynamic shields, and rock panel covers).

In ICEVs, the BIW accounts on average for almost $30\,\%$ of the vehicle mass [198]. Although this value changes when BEVs with a heavy traction battery are considered, the BIW still remains one of the heaviest components [199]. An important role for mass savings in the BIW is played by the materials used. For example, an aluminum frame has a mass reduction potential between $30\,\%$ and $40\,\%$ compared to standard steel frames [200]. Carbon fiber, which is around $50\,\%$ lighter than steel [201], has an even higher reduction potential. However, the main obstacle to using carbon fibers in series production is the higher process and manufacturing costs compared to steel [202, p. 436]. For this reason, only a few series vehicles with a carbon fiber BIW (regarding BEVs an example is the BMW i3 [202, p. 435]) can be found up-to-date. This lack of data impedes empirical modeling of carbon fiber BIWs. Therefore, only aluminum and steel BIWs are considered.

For applicability in the early development phase, the BIW is modeled using only top-level parameters such as the vehicle's external dimensions and the body type (SUV, sedan, and hatchback). A further model input is the vehicle gross mass $m_{\mathrm{gross,n}}$. If the vehicle mass or the payload increases, the frame load also increases and the BIW must be resized to meet crash requirements and ensure the passengers' safety. Finally, the percentage of aluminum in the BIW ρ_{Alu} is implemented as optional input. It can assume values between $0\,\%$ (full steel frame) and $100\,\%$ (full aluminum frame). If not assigned, ρ_{Alu} is set to zero.

The first step for the mass estimation is the calculation of a vehicle substitute volume $V_{\mathrm{veh,s}}$ (Figure 3.19). For this scope, the vehicle volume is modeled with the external dimensions using the method introduced by S. Fuchs [107, p. 39]. To consider the influence of the body type on the vehicle volume $V_{\mathrm{veh,s}}$, S. Fuchs derives two formulas, one for sedans (Equation (3.24)) and

one for hatchback and SUVs (Equation (3.25)).

$$V_{\text{veh,s,sedan}} = \left(\frac{L104}{2} + L101 + \frac{2\,L105}{3} \right) W103\; H100 \tag{3.24}$$

$$V_{\text{veh,s,SUV}} = V_{\text{veh,s,hatchback}} = \left(\frac{L104}{2} + L101 + \frac{3\,L105}{4} \right) W103\; H100 \tag{3.25}$$

In the following step, an empirical correlation is derived between the substitute volume $V_{\text{veh,s}}$, the aluminum percentage ρ_{Alu}, the corresponding steel percentage $(1-\rho_{\text{Alu}})$, and the vehicle gross mass $m_{\text{gross,n}}$. To account for the influence of material density on the BIW's mass, an interaction between the terms $V_{\text{veh,s}}$, ρ_{Alu}, $(1-\rho_{\text{Alu}})$ is introduced. Equation (3.26) shows the empirical regression derived from the mass dataset.

$$m_{\text{BIW}} = 4.575\,\text{kg} + (5.911\,\text{kg m}^{-3}) V_{\text{veh,s}}\,\rho_{\text{Alu}} + (13.203\,\text{kg m}^{-3})\,V_{\text{veh,s}}(1-\rho_{\text{Alu}}) + 0.080\,m_{\text{gross,n}} \tag{3.26}$$

The second term in the equation represents the empirically derived BIW density of aluminum. The empirical density of the steel is $13.2\,\text{kg m}^{-3}$, more than twice that of aluminum. The last term of the equation models the influence of the gross mass on m_{BIW}. According to its value, an increase in gross mass of $100\,\text{kg}$ (for example due to an increase of the required vehicle payload) would induce $8\,\text{kg}$ secondary mass changes just for the BIW.

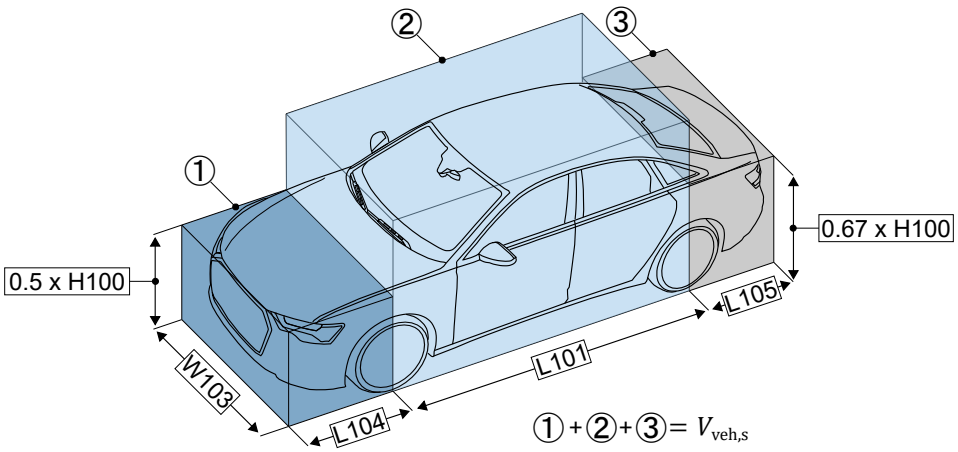

Figure 3.19: Vehicle substitute volume $V_{\text{veh,s}}$ for a sedan.

Regarding the other frame components' mass $m_{\text{frame,other}}$, the statistical analysis did not show any correlation with the gross vehicle mass nor the aluminum percentage. Therefore, $m_{\text{frame,other}}$ is modeled based only on the vehicle substitute volume $V_{\text{veh,s}}$ as shown in Equation (3.27).

$$m_{\text{frame,other}} = -18.270\,\text{kg} + (4.090\,\text{kg m}^{-3})\,V_{\text{veh,s}} \tag{3.27}$$

3.5.2 Chassis Module

In ICEVs, the chassis module accounts on average for approx. $25\,\%$ of vehicle mass [203]. Although this value decreases for BEVs due to the heavy electric powertrain, the chassis remains one of the heaviest modules [199]. This section presents the models for the brake system, axles, and wheels. A complete overview of the chassis components is specified in Table E.4.

For modeling the front brake system (two brake discs, four brake calipers, and four brake pads), its mass is correlated with the vehicle gross mass. This yields the regression model presented in Figure 3.20a. The mass of the rear brake system is derived from the mass of the front brake system as shown in (Figure 3.20b).

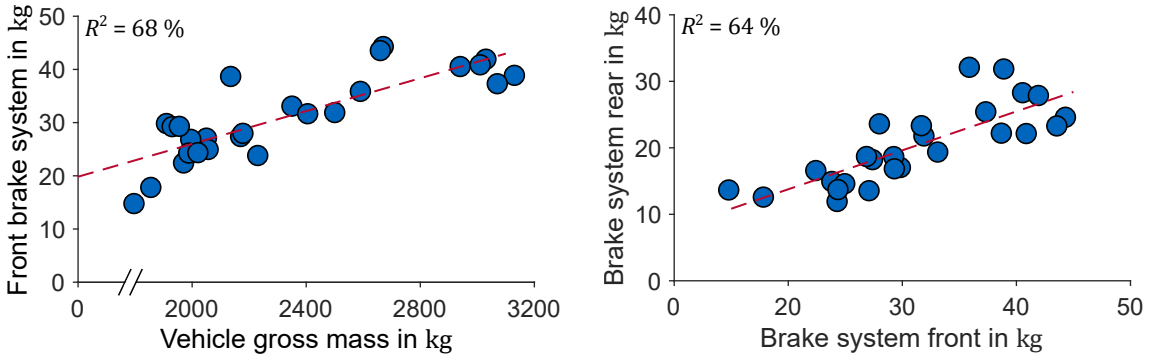

(a) Model for the mass estimation of the front brake system (b) Model for the mass estimation of the rear brake system

Figure 3.20: Empirical regressions for the brake system mass (two brake discs with corresponding pads and calipers) at the front and the rear axle (the formulas are listed in Table E.4).

One of the most important design variables for the axles and their sub-components (springs and shock absorbers) is the axle load $m_{\mathrm{load,axle}}$, which depends on the vehicle gross mass $m_{\mathrm{gross,n}}$. To account for this effect, the occurring maximum loads at the front $m_{\mathrm{load,axle,f}}$ and rear $m_{\mathrm{load,axle,r}}$ axles are estimated as described in Section D.1 for the vehicles of the mass dataset. Subsequently, an empirical correlation is derived between the axle load and its mass. Equation (3.28) shows the derived regression for the front axle $m_{\mathrm{axle,f}}$. The precision of the estimation is increased by introducing the width of the vehicle (W103) as further model input.

$$m_{\mathrm{axle,f}} = -83.262\,\mathrm{kg} + 0.028\,m_{\mathrm{load,axle,f}} + (0.053\,\mathrm{kg\,mm^{-1}})\,W103 \tag{3.28}$$

While W103 is an input of the architecture tool (Table 3.2) and can therefore be directly used in Equation (3.28), the axle load $m_{\mathrm{load,axle}}$ needs to be calculated. For this scope, an empirical analysis is conducted for the BEVs documented in the mass dataset. Hereby, typical mass distributions are derived for front-wheel drive (56/44), rear-wheel drive (46/54), and AWD BEVs (50/50). Based on these values, the architecture tool calculates the axle loads from the vehicle gross mass at each new iteration n. These loads are further used to estimate the axle mass as presented in Equation (3.28).

To estimate the wheel's mass, two regressions are derived from the mass dataset for rims and tires. Equation (3.29) shows the correlation between the rim diameter and its mass. A distinction according to rim material (steel or aluminum) did not show any statistical relevance, therefore, all rims are modeled together regardless of their material.

$$m_{\mathrm{rim}} = -13.063\,\mathrm{kg} + (1.405\,\mathrm{kg\,inch^{-1}})\,D_{\mathrm{rim,inch}} \tag{3.29}$$

For the tires, no distinction is required between extra and standard load tires, since they have similar masses. The tire mass is estimated from its width $s_{\mathrm{tire,y}}$ and outer diameter D_{tire} (which are derived during volumetric component modeling, Subsection 3.4.1) as shown in Equation (3.30).

$$m_{\mathrm{tire}} = -16.890\,\mathrm{kg} + (0.023\,\mathrm{kg\,mm^{-1}})\,D_{\mathrm{tire}} + (0.054\,\mathrm{kg\,mm^{-1}})\,s_{\mathrm{tire,y}} \tag{3.30}$$

The tire width is in turn influenced by the vehicle mass m_{n} of the current iteration n (Subsection 3.4.1). Finally, combining Equation (3.29) and (3.30) yields the wheel mass m_{wheel}.

3.5.3 Exterior Module

The exterior module includes closures, bumpers, fenders, lights, windshields, and windows. To calculate the exterior mass, these components are modeled separately. This section presents the models developed for doors, hood, and trunk. A complete overview of the exterior components is specified in Table E.5.

The doors are one of the heaviest components of the exterior module and include door frames, hinges, interior trims, window mechanisms, and rearview mirrors. Atypical designs such as the dual hinged door patented by Tesla [204] are not considered in this thesis. For modeling, a distinction between two- and four-door vehicles is made, as this feature strongly affects the shape and mass of the doors. For four-door vehicles, regressions are derived for the front $m_{\mathrm{doors,f}}$ and rear doors $m_{\mathrm{doors,r}}$. Furthermore, a distinction is introduced according to the door material (aluminum or steel). Equation (3.31) shows the resulting regression for a four-door vehicle with steel doors.

$$m_{\mathrm{doors,f,steel}} = 2\left[-23.602\,\mathrm{kg} + (0.015\,\mathrm{kg\,mm^{-1}})\,L101 + (0.011\,\mathrm{kg\,mm^{-1}})\,H100\right] \tag{3.31}$$

The hood's mass m_{hood} is estimated through the vehicle width (W103) and the hood material (two separate regressions are derived for steel and aluminum hoods). Using the front overhang (L104) as a modeling variable did not improve accuracy. Equation (3.32) shows the resulting correlation for a steel hood.

$$m_{\mathrm{hood,steel}} = 78.901\,\mathrm{kg} + (0.054\,\mathrm{kg\,mm^{-1}})\,W103 \tag{3.32}$$

For the vehicle trunk, two distinctions are introduced: the first is based on the trunk material (aluminum or steel) and the second on the body type (sedans or SUVs and hatchbacks). Sedans usually have a small trunk without rear glass (referred to as "trunk lid", Figure 3.21a) and the rear glass remains fixed when the lid is open. On the other hand, SUVs and hatchbacks have a rear glass integrated within the trunk frame (Figure 3.21b).

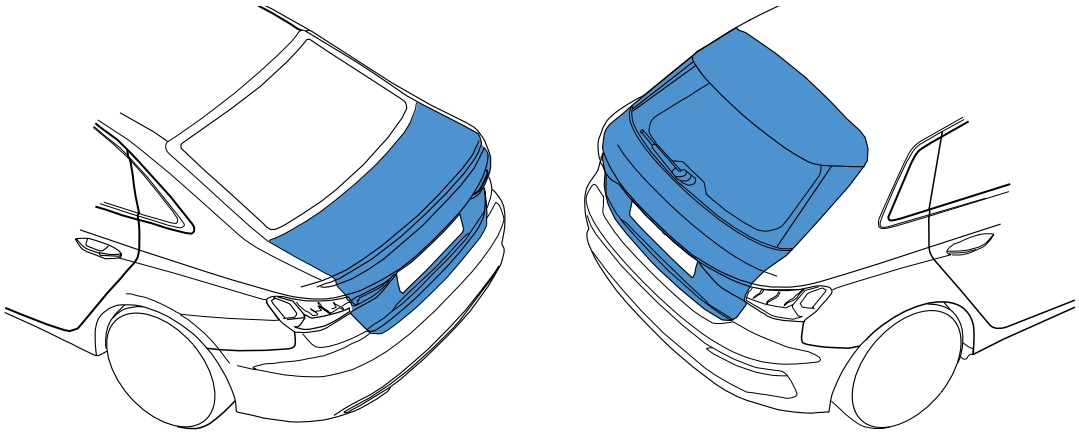

(a) Trunk lid (marked as blue) for a sedan (b) Trunk (marked as blue) for a hatchback

Figure 3.21: Comparison between a sedan and a hatchback hatch.

The analysis of the trunk lid did not show any correlation with the external dimensions of the vehicle. Therefore, the trunk lid mass is modeled with two constant values, one for aluminum and one for steel lids (Table E.5). For SUVs and hatchbacks, a correlation is identified based on the vehicle's height, its width, and the trunk material. Equation (3.33) shows the linear regression derived for a steel trunk.

$$m_{\text{trunk,steel}} = 103.041\,\text{kg} + (0.056\,\text{kg}\,\text{mm}^{-1})\,W103 + (0.019\,\text{kg}\,\text{mm}^{-1})\,H100 \tag{3.33}$$

The remaining subsystems of the exterior are described similarly to the components presented in this section (Table E.5). The statistical analysis of the data showed no dependency between the vehicle mass and the mass of the exterior components. This is primarily because the vehicle mass is not the main design variable for doors, hatch, lights, etc. Thus, since the components are only modeled based on the vehicle dimensions, this module does not result in any secondary mass effects.

3.5.4 Interior Module

The interior module exhibits a high variability in mass, depending on the manufacturer's design strategy. In this chapter, the models for the two subsystems interior trim and seats are further detailed. A complete overview of the interior components is specified in Table E.6.

The interior trim comprises the instrument panel (dashboard, cross-car beam, glove box, etc.), center console, trim parts, and noise insulation. The components of the instrument panel are all modeled with constant values (Table E.6) since their mass does not show any correlation with the vehicle dimensions.

Regarding the center console, the relevant variable for defining a regression model is the vehicle wheelbase (L101). Based on L101, the mass of the center console is estimated with an R^2 of $50\,\%$, which is not particularly high (Equation (3.34)). This problem was addressed by S. Fuchs [107] by introducing a *comfort factor* to consider that vehicles belonging to more luxurious segments also have heavier consoles. In this thesis, the author wants to avoid introducing subjective factors that are difficult to assess for an inexperienced user of the architecture tool. While this choice renders the tool more user-friendly, it also leads to lower accuracy of the mass estimation for some interior components.

$$m_{\text{console}} = -25.461\,\text{kg} + (0.012\,\text{kg}\,\text{mm}^{-1})\,L101 \tag{3.34}$$

The mass of the trim parts and noise insulation is influenced by the passenger compartment dimensions, the vehicle segment, as well as the noise vibration and harshness requirements. BEVs have a different sound impression than ICEVs [205]. First, the noise sources from the electric powertrain are different, e.g. due to strong harmonics and potential whining noise. In addition, other noise sources (such as the tires) that are normally masked by the combustion engine, become predominant [206]. This leads to new requirements in terms of noise vibration and harshness. Therefore, for modeling the trim parts and noise insulation, only the BEVs of the mass dataset are considered. The derived model is shown in Equation (3.35).

$$m_{\text{trim}} = -260.280\,\text{kg} + (0.009\,\text{kg}\,\text{mm}^{-1})\,L103 + (0.139\,\text{kg}\,\text{mm}^{-1})\,W103 \tag{3.35}$$

The seat mass comprises the seat frame, cushion, and adjustment mechanism. Since larger vehicles are usually equipped with larger seats [162, p. 43], this component is described in

dependency of vehicle width (W103) and wheelbase (L101). Equation (3.36) exemplarily shows the calculated correlation for the driver's seat mass $m_{\mathrm{seat,f}}$.

$$m_{\mathrm{seat,f}} = -44.081\,\mathrm{kg} + (0.026\,\mathrm{kg\,mm^{-1}})\,W103 + (0.007\,\mathrm{kg\,mm^{-1}})\,L101 \tag{3.36}$$

The remaining components are listed in Table E.6. Once again and similar to former findings, none of the component masses shows a dependency on the vehicle mass. Therefore, this module does not generate secondary mass effects.

3.5.5 Powertrain Module

This chapter presents the models developed for the electric machines, transmission system (gearbox and driveshafts), and traction battery. For calculating these subsystems, the results from the volumetric modeling (Subsection 3.4.4 and 3.4.6) are required.

The machine mass is strongly influenced by its maximum torque $T_{\mathrm{mach,max}}$. For modeling the machine mass, two separate regressions are derived for IMs and PMSMs based on the machine dataset (Table E.7).

For the mass calculation, the transmission system is divided into gears, shafts, bearings, gearbox housing, and driveshafts. The volume of shafts and gears is estimated during the volumetric sizing based on the torque and rotational speed requirements (Subsection 3.4.4). For these components, the assumed material is steel of the type 16MnCr5 [27]. Their mass is estimated by multiplying their volume with the density of the material. The estimation for bearings is simpler since they are selected from a catalog [180] that documents the corresponding mass for each bearing type. Based on the dimensions of shafts, gears, and bearings, the volume of the gearbox housing is derived with the dimensional chains shown in Section D.3. The housing mass is estimated by assuming that the housing is composed entirely of the alloy AlSi9Cu3 [27]. Finally, for the estimation of the driveshafts, an empirical correlation (based on the output torque of the gearbox) is derived from the gearbox dataset [100, p. 68].

The battery is divided into three main sub-components: cell modules, battery housing, and battery electrics (cables, BMS, relays, etc.). The volumetric modeling described in Subsection 3.4.6 yields the installed battery gross energy $E_{\mathrm{batt,is}}$ at every tool iteration. The cells' mass $m_{\mathrm{batt,cells}}$ is estimated by multiplying $E_{\mathrm{batt,is}}$ for the gravimetric energy density at the cell level $E_{\mathrm{cell,grav}}$. Subsequently, the mass of the cell modules $m_{\mathrm{batt,mod}}$ (including cells, module housings, and module cables) is estimated by multiplying the conversion factor K_{cell2mod} as shown in Equation (3.37).

$$m_{\mathrm{batt,mod}} = K_{\mathrm{cell2mod}}\, m_{\mathrm{batt,cells}} = K_{\mathrm{cell2mod}} \left(\frac{E_{\mathrm{batt,is}}}{E_{\mathrm{cell,grav}}} \right) \tag{3.37}$$

$E_{\mathrm{cell,grav}}$ (in $\mathrm{W\,h\,kg^{-1}}$) depends on the cell type and is modeled according to the values proposed by König et al. [21]. Over the next years, further improvements in cell energy density are expected [207, 208], which will impact the battery and vehicle mass. Therefore, to assess the influence of cell improvements on the vehicle architecture, $E_{\mathrm{cell,grav}}$ is chosen as an optional mass model input (Table E.1). The factor K_{cell2mod} describes the mass increase caused by the module housings. Köhler [100] identifies three distinct K_{cell2mod} from an analysis of the BEVs in the mass dataset: 1.23 for pouch, 1.14 for cylindrical, and 1.12 for prismatic cells. Unlike prismatic and cylindrical cells, pouch cells do not have a hard case [76, pp. 174-175]. Therefore, due to their lower mechanical stability, they require a robust module structure [209, p. 225, 210, p. 27], which explains the higher K_{cell2mod} compared to prismatic and cylindrical cells.

For estimating the battery housing mass, the previously calculated battery dimensions (Subsection 3.4.5) are used to calculate the battery volume V_{batt}. Subsequently, the battery housing mass is expressed as a function of its volume as shown in Equation (3.38).

$$m_{\mathrm{batt,hous}} = 1.790\,\mathrm{kg} + (0.033\,\mathrm{kg\,l^{-1}})\,V_{\mathrm{batt}} \tag{3.38}$$

Regression-based modeling of the battery electrics did not yield statistically significant results. Therefore, this sub-component is modeled with two constant values: one for vehicles with AWD and one for vehicles without AWD (Table E.7). For AWD vehicles, the inner battery cables have to be wired at both front and rear axle, which increases the battery electrics mass.

3.6 Output of a Feasible Architecture

The tool presented in the previous chapters fulfills all requirements defined in Section 2.5. Once the tool reaches convergence, the resulting vehicle architecture can be visualized (Figure 3.22) and further analyzed. Some of the most important outputs of the tool are:

- LDS results: Required machine power, torque and rotational speed, vehicle consumption, attainable range, and required battery energy.
- Interior concept: Headroom, legroom, shoulder room, and resulting passenger compartment dimensions.
- Exterior concept: Ground clearance requirements and turning radius.
- Tire dimensions: Tire width, aspect ratio, and maximum load.
- Drive unit dimensions: Size of gearbox (gear diameters, width, number of teeth, etc.) and electric machine (diameter and length).
- Battery: Required and installed battery energy, cell dimensions and orientation as well as the resulting battery voltage.
- Masses and inertia: Empty and gross mass of the vehicle, its modules, and their sub-components. The LDS also calculates the inertia of electric machines, gearboxes, and wheels.

By simultaneously considering both vehicle mass and package, it is possible to couple these two features, thus describing the impact of mass on package and vice versa. To demonstrate how the tool supports the vehicle concept design, the following list presents possible case studies:

- Cell type impact: Given a vehicle architecture, the tool can calculate the available battery space and estimate the installable battery energy. This process can be repeated for different cell types, which yields different installable battery energies, vehicle consumptions, and ranges. This enables a comparison between cell types and a quantification of their impact on the vehicle architecture.
- Vehicle dimensions impact: The tool can describe the impact of external (or internal) dimensions on the vehicle architecture. For example, it is possible to quantify how a change in the wheelbase affects mass, consumption, installed battery energy, and vehicle range. Furthermore, the tool also considers secondary volume and mass effects induced by the wheelbase change.

- Mass and volume saving impact: The tool can also quantify the impact of mass savings (e.g. due to lightweight measures) and space saving (e.g. due to an improved integration of the battery in the vehicle) on the BEV architecture. Again, the impact of these measures can be expressed through the change in mass, consumption, and range that they produce.
- Identification of design boundaries: The tool can also be coupled with an optimization algorithm (such as the NSGA-II) to identify the design boundaries of BEV architectures. For this scope, a set of design variables (for example the external dimensions of the vehicle) can be varied by the optimization algorithm to identify the combination that yields the maximum range. Such a study provides a perspective on current and future physical limits of BEVs.

These case studies are faced regularly by the concept engineer during the early development phase. However, they have not yet been thoroughly analyzed, since this requires simultaneous modeling of vehicle dynamics, components masses, and component volumes, which is beyond the capabilities of the concept engineer. The vehicle architecture tool offers a solution to this problem as will be shown in Chapter 5.

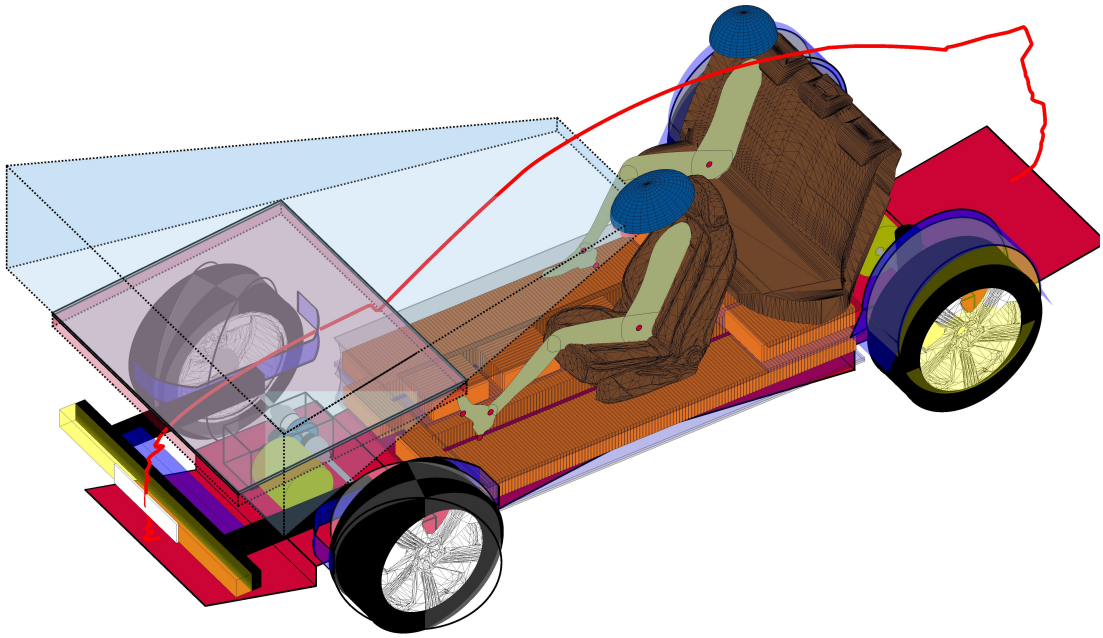

Figure 3.22: An exemplary output of the vehicle architecture tool.

4 Verification and Validation

This chapter verifies and validates the vehicle architecture tool and its subsystems. Verification, on the one hand, ensures that the models are implemented correctly. Validation, on the other hand, ensures that the models correctly replicate the reality. In the first section (Section 4.1), the acceleration and consumption simulations implemented in the LDS are validated and verified. In the following step (Section 4.2), the most important volumetric models are analyzed. Subsequently, the gravimetric component modeling is validated based on a database of existing vehicles (Section 4.3). In Section 4.4, the entire architecture tool is applied to simulate a set of BEVs. Finally, Section 4.5 summarizes the outcomes of the validation.

4.1 Longitudinal Dynamic Simulation Validation

The results of the LDS form the basis for sizing the powertrain. Therefore, a validation of its main modules (acceleration and consumption simulation) is required. Since the aim of this section is to validate the LDS, only the modules presented in Figure 3.3 are used.

The goal of the acceleration simulation is to derive the machine torque curve (Figure 3.3) based on a given acceleration time. To ensure that the torque curve is implemented correctly, a series of acceleration tests is performed on an e-Golf (model year 2014) [154]. During the tests, the vehicle is accelerated from $0\,\mathrm{km\,h^{-1}}$ to $100\,\mathrm{km\,h^{-1}}$ while its speed and acceleration are tracked with three different mobile devices (an iPhone 11, an iPhone 5, and an iPad 6) using the mobile app *Phypox* [211]. With this method, it is not possible to track the machine torque curve, however, the measurements can be represented as an acceleration profile (Figure 4.1a), which is equivalent to the torque curve.

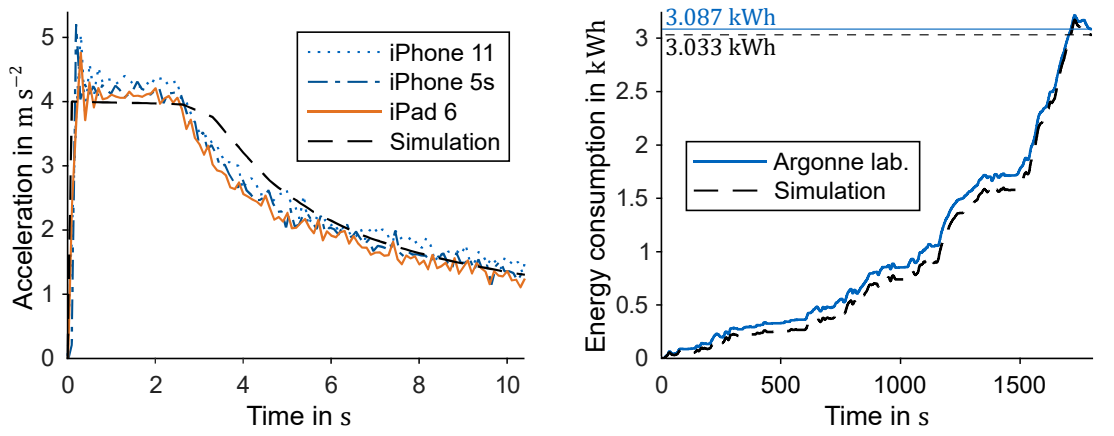

(a) Measured vs. simulated acceleration profile from $0\,\mathrm{km\,h^{-1}}$ to $100\,\mathrm{km\,h^{-1}}$

(b) Measured vs. simulated consumption in a class 3b WLTC

Figure 4.1: Simulated vs. measured acceleration and consumption of an e-Golf. Based on [154].

Subsequently, the main characteristics of the e-Golf (acceleration time, empty mass, maximum speed, etc.) are parametrized in the LDS. The LDS iteratively scales the torque until the desired acceleration time is reached. Finally, the resulting torque curve is converted into an acceleration profile (black dashed line, Figure 4.1a) and compared to the measured one.

During the first few seconds, both simulated and measured acceleration profiles have a value of approx. $4\,\mathrm{m\,s^{-2}}$. Once the electric machine reaches its nominal rotational speed, the torque (and therefore also the acceleration) sinks following a hyperbolic profile. These two parts are visible in both measured and simulated profiles. The simulation overestimates the nominal rotational speed of the machine, leading to a deviation from the measured profile in the range from $2\,s$ to $6\,s$. Due to this overestimation, the simulated hyperbolic profile starts at slightly higher rotational speeds. However, this deviation is compensated after a few seconds. More information on this validation step is documented in the publication of König et al. [154] and in the thesis of Moller [155].

For the validation of the consumption simulation, a comparison with real WLTP measurements is required. The WLTP consumption declared by the manufacturers also includes battery charging losses (Appendix C). However, since the LDS does not model battery charging losses, the validation measurements should only include the losses occurring during the cycle. The dynamometer dataset of the Argonne laboratory [212] fulfills these requirements. The Argonne dataset contains consumption measurements for ten BEVs (model years between 2012 and 2015) performed on different driving cycles (including the WLTC). Besides recording the vehicle consumption (without charging losses), the Argonne laboratory also provides the measured resistance forces and the driven speed profile. Four of the ten BEVs (including the e-Golf that was used for the acceleration simulation) are chosen and simulated in the LDS. Figure 4.1b compares the simulated consumption profile (black dashed line) with the profile measured by the Argonne laboratory (blue continuous line) for the e-Golf.

The main drawback of the Argonne dataset is that it does not include vehicles newer than 2015. For validation with current BEVs, a VW ID.3 Pro Performance 1st Max [213] is measured with a roller dynamometer, property of the Institute of Automotive Technology [214]. More information on the roller dynamometer is specified in the publication of Danquah [215]. The ID.3 is positioned on the dynamometer and tested several times on a WLTC. Each time, the driven speed profile, occurring resistance forces, and energy consumption are measured. The hereby measured consumption does not include battery charging losses. Due to the complex calibration of the roller dynamometer, it is not possible to exactly match the given speed profile at each repetition. Therefore, the measured consumption is represented as an area (blue surface in Figure 4.2) containing all the driven WLTCs.

Subsequently, the ID.3 is parameterized as documented in Table F.1 and simulated. Since the mass model is deactivated, the vehicle mass measured during the dynamometer test is assigned as input (Table F.1). The LDS selects a suitable machine from the efficiency map database and calculates vehicle consumption, which is depicted as an orange dashed line in Figure 4.2. The simulated WLTC consumption is overestimated with a deviation of $24\,\%$ compared to the highest value measured on the roller dynamometer. Such a deviation undermines the applicability of the vehicle architecture tool during the early development phase. After verification of the LDS, no errors were found in the code nor the parameter set in Table F.1. Repeating the simulation with other maps from the database also showed deviations in the order of $20\,\%$.

These results show that there are differences between the ID.3 efficiency map and the PMSM maps contained in the database (Section 3.3). To test this assumption, the LDS needs to be

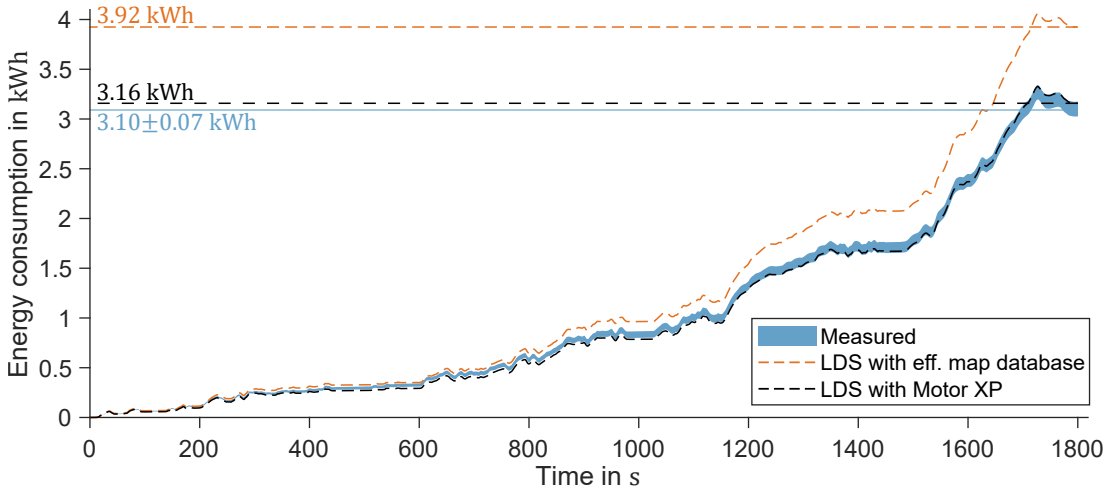

Figure 4.2: Comparison between measured WLTC consumption, simulated WLTC consumption with the efficiency map database, and simulated WLTC consumption with the Motor XP map.

simulated with a different efficiency map. For this purpose, the machine design tool *Motor XP* [216, 217] is used. Motor XP is a software for PMSM sizing which offers a pre-calculated PMSM efficiency map. This map is integrated into the LDS and the simulation is repeated (black dashed line in Figure 4.2). The Motor XP map has a considerably higher efficiency than the maps in the database. Consequently, vehicle consumption decreases. A considerable improvement of the estimation can be observed, and the profile simulated with the Motor XP map always remains within the values recorded on the roller dynamometer.

It appears that the set of PMSM maps implemented in the database is adequate to model older vehicles (Figure 4.1b). Nevertheless, for newer vehicles, these maps underestimate the machine efficiency, leading to an overestimation of vehicle consumption. A similar validation for IM maps is not possible for two main reasons. Firstly, there are no vehicles equipped with this machine technology at the Institute of Automotive Technology. Secondly, Motor XP does not include (for the moment) IMs.

In conclusion, for validating the entire architecture tool (Section 4.4), the Motor XP map (and not the ones contained in the efficiency map database) will be used. For the (rare) cases where vehicles equipped with IMs are simulated (Section 4.4), the maps contained in the database are used due to the lack of alternative solutions.

4.2 Volumetric Component Modeling Validation

This section validates three volumetric component models: wheels (Subsection 4.2.1), gearbox (Subsection 4.2.3), and traction battery (Subsection 4.2.2). The remaining components are validated in the theses of Elagamy [71], Köhler [100, 101], Romano [164, 162], and Spreng [187].

4.2.1 Wheels

Wheels and tires have a high influence on secondary mass effects of the chassis and generate secondary volume effects on electric machines, gearboxes, and the battery. This section assesses the correctness of tire sizing using the vehicles documented in Table F.2. Since the focus is on tire sizing, only the modeling approach presented in Subsection 3.4.1 and D.1 is used while

the remaining parts of the architecture tool are deactivated. For the vehicles in Table F.2, empty mass, mass distribution, tire diameter, rim size, interior, and exterior concept dimensions are collected. With these inputs, the maximum occurring axle loads are estimated for each validation vehicle as described in Section D.1. Subsequently, the occurring tire loads are derived and the required tire volumes estimated (Equation (3.4)). Finally, a suitable tire is chosen from the tire dataset. Figure 4.3 compares the real and calculated tire dimensions and shows the average deviations, which are expressed as MAE and nMAE.

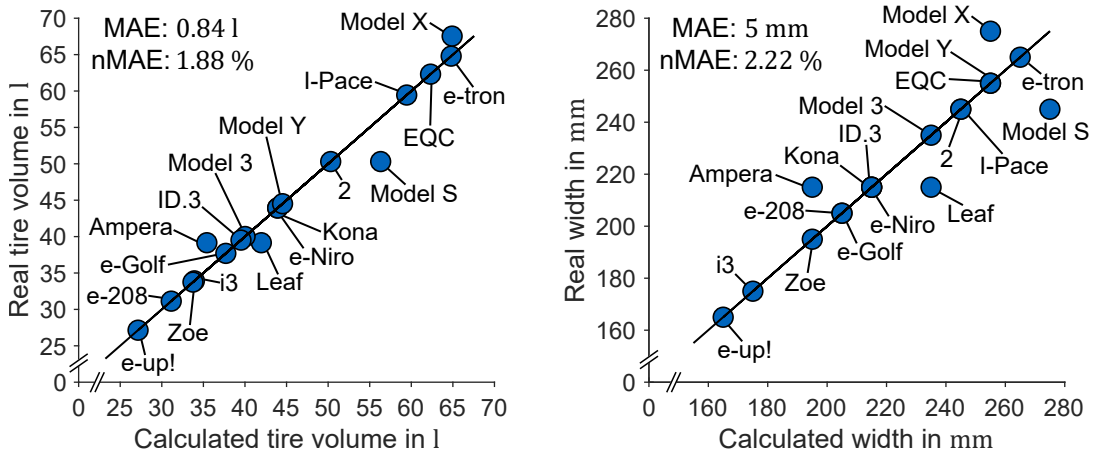

(a) Calculated vs. real tire volume

(b) Calculated vs. real tire width

Figure 4.3: Calculated vs. real tire dimensions for the vehicles listed in Table F.2.

Figure 4.3a compares the calculated tire volumes with the real ones. Most of the vehicles are estimated correctly. One exception is the Tesla Model S, for which the A2mac1 archives [163] are incomplete and the exact mass distribution and internal dimensions are unknown. The missing values are estimated from the Tesla Model X, which nevertheless introduces a certain degree of uncertainty into the model. Figure 4.3b shows the comparison between calculated and real tire width. Since the tire width and volume are interdependent, the same vehicles that deviate in Figure 4.3a also deviate in Figure 4.3b. For the few cases where the tire volume is not exactly estimated, the deviations could be caused by incorrect model inputs (as is the case for the Model S) or because the manufacturer opted for an oversizing of the tires (which would explain the deviations of Opel Ampera and Tesla Model X). Further inaccuracies may also be contained in the measurements of the A2mac1 database [163].

In this validation step, the rim diameter was inserted as model input. Theoretically, it is an optional input, since the architecture tool can estimate the minimum required rim size from the brake disc diameter (Subsection 3.4.1). However, the sizing of rims and tires is not based only on the package and load specifications, but also on design requirements [103]: vehicles with similar mass and tire loads may mount, depending on the applied design strategy, different rims and therefore require different tire widths. In conclusion, for a precise estimation of tire dimensions, the manufacturer design strategy (i.e. the rim dimensions) must be considered.

4.2.2 Battery

This section is divided into a verification and a validation step. The first step ensures that the battery filling algorithm (Subsection 3.4.6) is implemented correctly while the validation assesses the precision of the model. To test the battery model alone, only the modules shown in Figure 3.14 are used, while all the other parts of the vehicle architecture tool are deactivated.

Nevertheless, since the results of package modeling and LDS are also required to model the battery, it is necessary to assign more inputs (such as the battery size, which would otherwise be calculated in the interior and exterior modules) for a standalone run of the battery model.

In the verification step, a selected group of batteries contained in the battery dataset is simulated. Since the volumetric models for interior and exterior are deactivated, the battery size cannot be estimated and needs to be assigned as an input. Therefore, the real battery and cell dimensions are retrieved from the battery dataset (Subsection 3.4.5) and assigned as inputs. The cell dimensions are not varied and only the real cell size is used to fill the battery space. The package factors are retrieved from the battery dataset and assigned as inputs as well. Finally, for the dimensional chain in Equation (D.12), instead of using the constant values in Table D.4, the real values of each chain component (lower protection, cooling, etc.) are retrieved for each vehicle of the battery dataset. With this approach, the algorithm receives an input that is an almost perfect replica of the battery volume, fills it using the real cell dimensions, and derives the installable battery energy (orange bars in Figure 4.4).

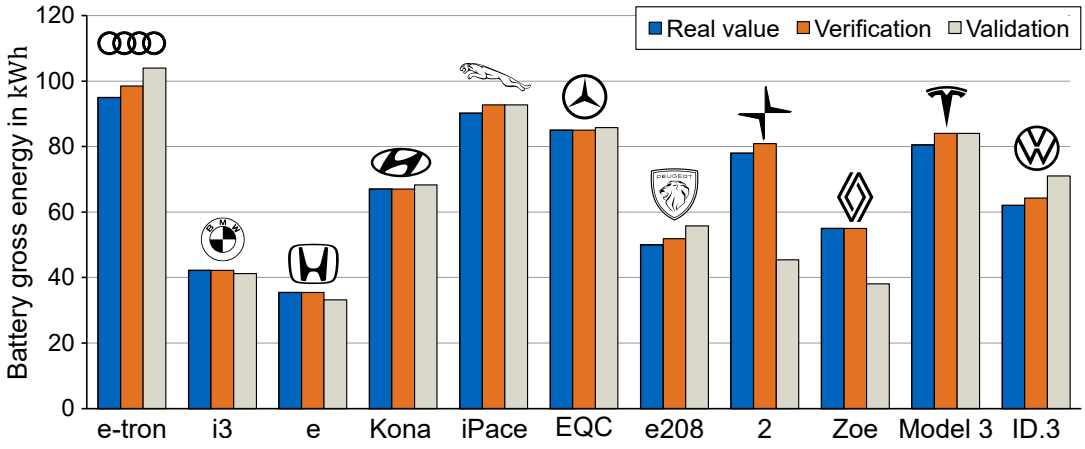

Figure 4.4: Comparison between real battery energy (blue bar) and battery energies calculated in the verification (orange bar) and validation steps (gray bar).

For batteries equipped with a drop shape (such as the Audi e-tron or the Jaguar I-Pace), there are deviations between real and calculated energy. These deviations are not caused by an implementation error, but rather by the modeling of the frontal part of the battery. As visible in Section B.2, the dimensions and shape of the frontal part vary within the drop shape batteries (compare for example the Audi e-tron and the Jaguar I-Pace batteries). It is not possible to derive a generalized method to precisely describe all drop shape variants. The MAE of the battery energies in Figure 4.4 is $1.51\,\mathrm{kWh}$ while the corresponding nMAE is $2.23\,\%$. Although the low MAE and nMAE confirm that the filling algorithms and the package factors are implemented correctly, a validation of the entire battery model is still required.

The validation step follows the same approach used for verification but has a lower number of inputs. For modeling the dimensional chain in Equation (D.12), the constant values in Table D.4 are used. Furthermore, instead of imposing a fixed cell size, the cell dimensions are left to vary within a given range (Section F.3). The calculated battery energy is represented as a gray bar in Figure 4.4. The validation step uses the chain values listed in Table D.4 (and not the real values of the validation vehicles), thus leading to different installable cell heights. Since Table D.4 summarizes the average values of the battery dataset, the installable cell height is overestimated in some cases, while in other cases it is underestimated. For the Polestar 2 and the Renault Zoe, the deviation between calculated and real energy is particularly high. The

Polestar 2 has one of the most complicated battery shapes (Figure B.3b) with a simultaneous filling of the underbody, tunnel, and second level. The algorithm underestimates the available cell height in the underbody and, since the estimated value is lower than the minimum allowed cell height, the underbody remains empty, leading to a considerable (almost $42\,\%$) energy deviation. A similar problem occurs also in the Renault Zoe. In this case, the underbody space is estimated correctly, but the vehicle is equipped with an above-average cell height (which is not included in the allowable dimension range). Therefore, the underbody is filled with smaller cells resulting in an underestimation of the battery energy.

Although there are some cases (Polestar 2 and Renault Zoe), where great deviations between calculated and real values occur, these deviations are mostly caused by the simplification introduced by the dimensional chain. Considering the current volumetric energy densities at the cell level, an under- (or over-) estimation of $1\,\mathrm{mm}$ in battery height leads to energy deviations in the order of $1\,\mathrm{kW\,h}$. The same estimation error in the available battery width or length leads to deviations in the order of $100\,\mathrm{W\,h}$. Therefore, this validation step identifies the predominant role of the z-direction on the installable battery energy.

In most cases, it is possible to obtain a good approximation of the installed energy if the package factors and the cell energy densities are known. It would also be possible to implement an average package factor for different cell types (e.g. for pouch, cylindrical, and prismatic cells). The author advises against this strategy since the empirical analysis of the package factors shows a great, mostly manufacturer-dependent, variability (Figure D.7). The same problem also applies to the volumetric and gravimetric energy densities. They also show a high variability depending on cell type, size, manufacturer, manufacturing year, and chemistry.

4.2.3 Gearbox

The analysis of the gearbox model is divided into two steps. First, the model is verified by comparing its results with the outputs of another gearbox sizing software. Second, the model is validated with a series of existing BEV gearboxes. For a standalone run of the gearbox model, it is necessary to collect further inputs that would normally be calculated by the other tool modules. Examples are the machine's maximum torque and rotational speed (calculated by the LDS) as well as machine diameter.

In the first step, the model is verified with the gearbox sizing software GAP [218, 179], developed by the Chair of Machine Elements of the Technical University of Munich. GAP enables a first design of gears and can also be used for sizing BEV gearboxes. However, it only sizes gears, shafts, and bearings without deriving the gearbox housing dimensions. A sensitivity analysis is conducted with both GAP and the model developed in this thesis to assess the influence of transmission ratio and maximum gearbox torque on the gear dimensions (Figure 4.5)

Figure 4.5a shows the change in diameter of the first wheel of the first stage. The slightly higher values in comparison to GAP are caused by different calculation methods. While the model sizes D_1 using an empirical estimation of the axle distance $d_{\mathrm{gb,shafts,12}}$ (Figure D.3), GAP's estimation uses a larger set of parameters [179, p. 57]. Figure 4.5c shows the calculated diameters of the first wheel of the second stage. The deviations between GAP and the model are caused by the different methods applied for the calculation of the transmission ratio of the second stage, which consequently lead to slightly different diameters. Although the diameter surfaces do not perfectly match, they show a similar trend. The MAE between the models is below $4\,\mathrm{mm}$ for both D_1 and D_3.

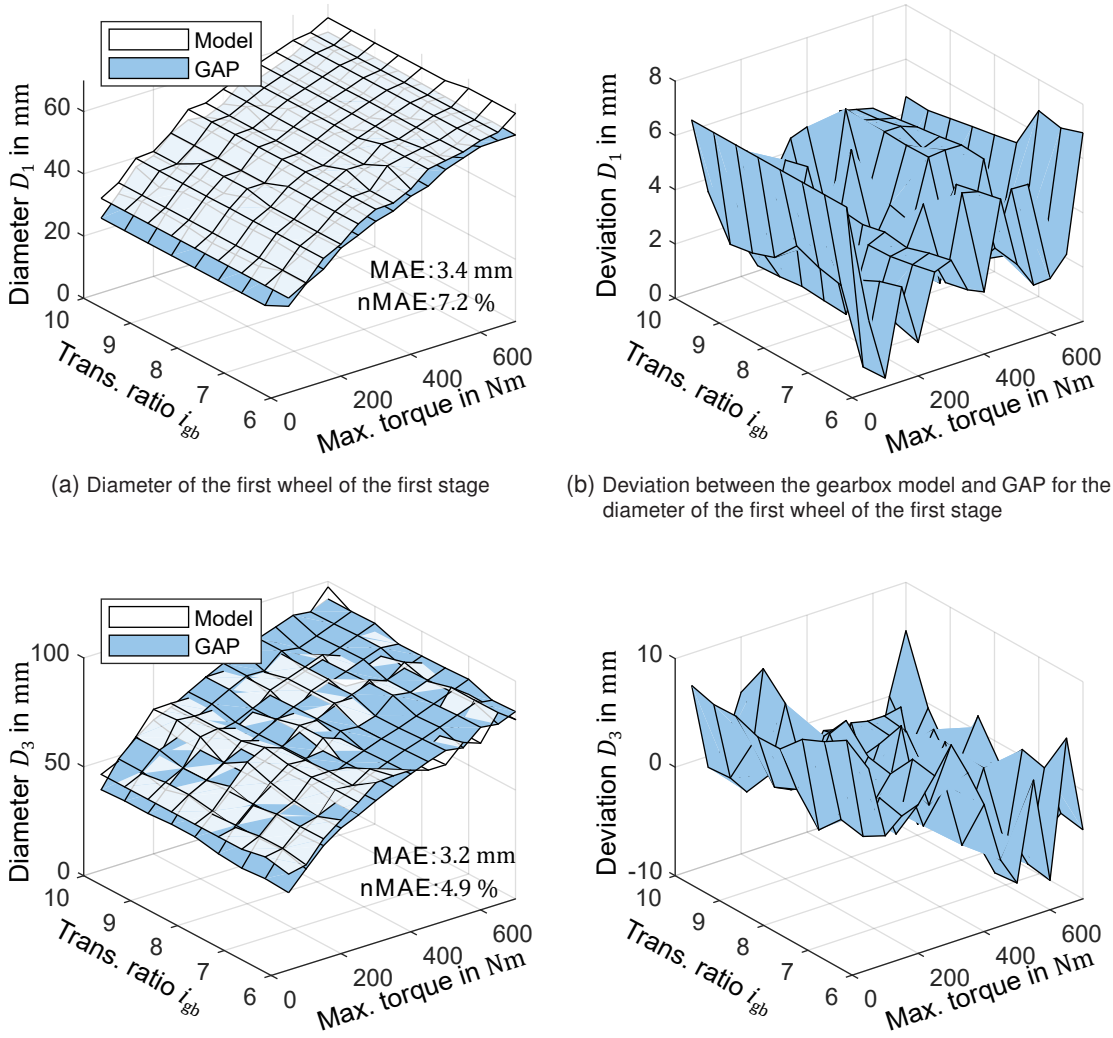

(a) Diameter of the first wheel of the first stage

(b) Deviation between the gearbox model and GAP for the diameter of the first wheel of the first stage

(c) Diameter of the first wheel of the second stage

(d) Deviation between the gearbox model and GAP for the diameter of the first wheel of the second stage

Figure 4.5: Comparison between the calculated gears dimensions of the two models for a parallel axle gearbox with two reduction stages. Based on [101, 27].

In the second step, the model is validated with a set of existing BEV gearboxes. This step is required to validate the dimensional chain-based housing model presented in Section D.3. GAP cannot be used for this purpose since it does not estimate housing dimensions. Therefore, the gearbox dataset introduced in Subsection 3.4.4 is used. For each gearbox contained in the gearbox dataset, the required inputs (machine torque, rotational speed, etc.) are collected. Subsequently, the gearboxes are simulated and the calculated housing dimensions are compared with the real ones (Table 4.1).

The deviations in Table 4.1 are mostly caused by the dimensional chains described in Section D.3. For example, the gearbox flanges (modeled with a constant value, Table D.2) cause deviations between calculated and real housing length and height. Further inaccuracies are caused by particular designs such as in the case of the BMW i3, where the differential cage is partially integrated into the differential wheel leading to a narrow gear width. Consequently, the tool overestimates the gearbox width for this vehicle.

Table 4.1: Calculated vs. real dimensions for a set of parallel axle gearboxes [101, p. 86]. The values are expressed as percentual deviations since the real housing dimensions are confidential.

Vehicle (model year)	Gearbox length $s_{\mathrm{gb,x}}$ Figure D.3	Gearbox width $s_{\mathrm{gb,y}}$ Figure D.3	Gearbox height $s_{\mathrm{gb,z}}$ Equation (D.5)
BMW i3 (2019)	2.94 %	22.96 %	0.69 %
Nissan Leaf (2011)	13.60 %	−4.18 %	−3.49 %
Renault Twizy (2014)	−0.15 %	9.56 %	−12.16 %
VW e-Golf (2014)	7.64 %	11.32 %	−2.89 %
VW e-Up! (2017)	9.95 %	7.05 %	−12.20 %

4.3 Gravimetric Component Modeling Validation

This section validates the gravimetric component modeling (step 5, Figure 3.1) using the dataset in Table F.2. The mass estimation presented in this section relies solely on the empirical models listed in Appendix E. The LDS and the volumetric component models are deactivated to allow for an in-depth validation of the mass model. However, for a standalone run of the gravimetric component modeling, it is necessary to collect additional inputs. For example, the battery mass is calculated from the installable energy (Equation (3.37)), which would normally be estimated by the volumetric component modeling and the LDS. These missing inputs are collected from the ADAC [149] and the A2mac1 database [163].

Once the inputs are collected, the vehicles in Table F.2 are simulated and their module masses calculated. Subsequently, the real module masses are retrieved from A2mac1 [163] and compared with the calculated ones. The results are represented as a whole model plot in Figure 4.6. Since the real module mass is confidential, the axis values are hidden. To further impede an extrapolation of the original data, the origin of the axes is not positioned at $0\,\mathrm{kg}$, and only a maximum of two vehicles per plot are labeled. Figure 4.6 also lists the average module deviations, expressed as MAE and nMAE.

Figure 4.6a shows the whole model plot of the frame module. The high deviations of the BMW i3 are caused by the fact that its frame does not have a unibody construction and combines carbon fibers (not considered in the vehicle architecture tool, Subsection 3.5.1) and aluminum [219, 220]. The BMW i3 is simulated assuming a unibody construction made entirely of aluminum. This assumption yields a good approximation of the BIW mass but leads to an underestimation of the mass of the other frame components. Another remarkable deviation (an overestimation in this case) occurs for the Jaguar I-Pace. The reason for such an overestimation lies in the lightweight design of this vehicle, which is equipped with a full aluminum frame [221] and has, despite its large size, an incredibly low frame mass. For the chassis module (Figure 4.6b), the BMW i3 has the highest deviation since its chassis is made entirely of aluminum [222] and is therefore particularly light.

Regarding the powertrain module (Figure 4.6c), the Mercedes EQC shows one of the highest deviations. A consistent portion of the EQC battery width is occupied by side crash reinforcements (Figure B.4b). Since the reinforcements are positioned on the outer sides of the battery, they do not constrain the module dimensions along the driving direction, which enables building large modules. However, this strategy results in an above-average battery housing mass. The powertrain module has the highest MAE since it is the heaviest module of the vehicle in most

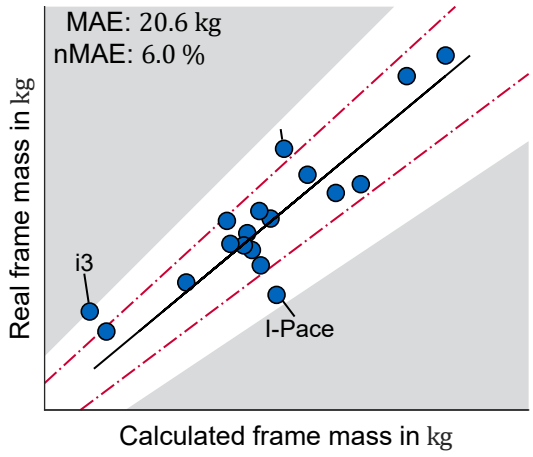

(a) Whole model plot for the frame module

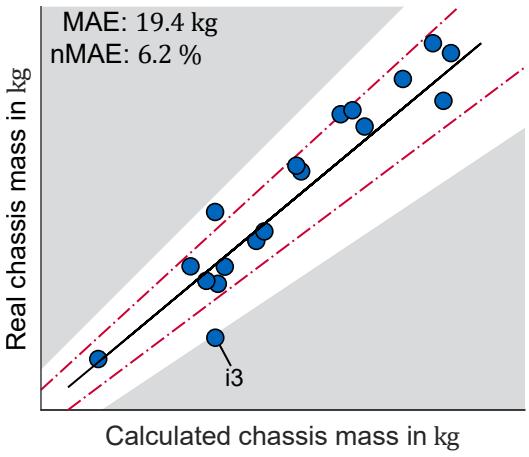

(b) Whole model plot for the chassis module

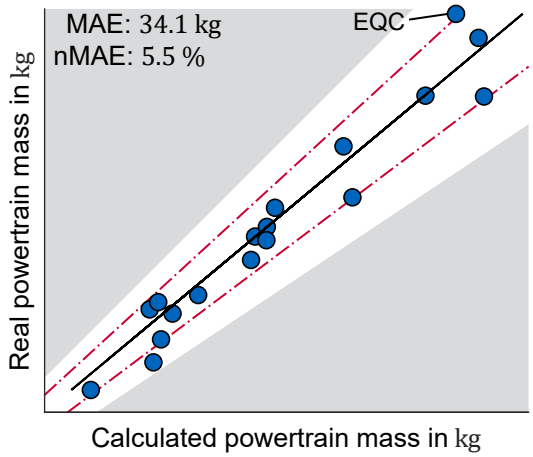

(c) Whole model plot for the powertrain module

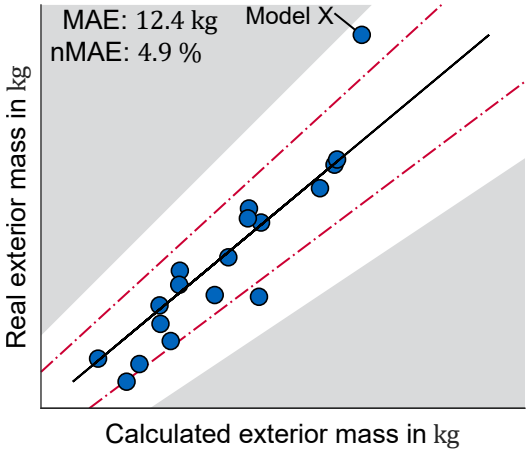

(d) Whole model plot for the exterior module

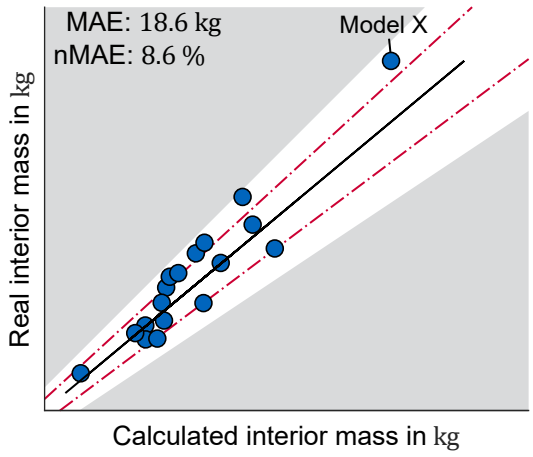

(e) Whole model plot for the interior module

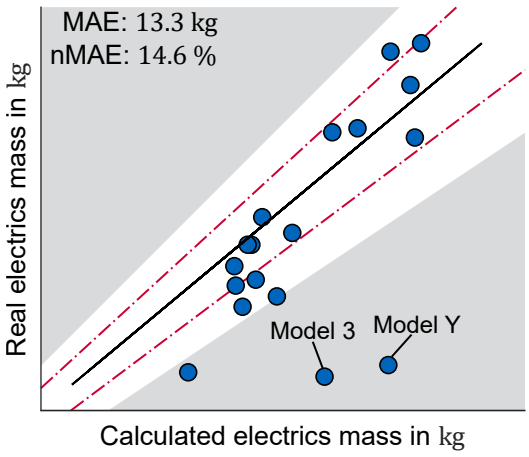

(f) Whole model plot for the electrics module

Figure 4.6: Calculated vs. real module masses for the vehicles listed in Table F.2. If the blue marker lies between the dashed red lines, deviation is smaller than 10 %. If it is located in the white areas comprised between the red dashed lines and the gray surfaces, deviation is greater than 10 % but smaller than 20 %. Finally, the gray areas mark the cases where deviation is greater than 20 %.

cases. Therefore, although the nMAE is similar to other modules (such as frame and exterior), the corresponding absolute error is higher.

For the exterior module (Figure 4.6d), the Tesla Model X has the highest deviation due to its heavy dual-hinged doors, which are not considered in the vehicle architecture tool (Subsection 3.5.3). Regarding the interior module (Figure 4.6e), the Model X is once again the vehicle with the highest deviation. This is due to its single-seat layout (while all other vehicles have bench seats) in the second seat row.

The mass of the electrics module is overestimated for the Tesla Model 3 and Model Y (Figure 4.6f). For these two vehicles, the DC-DC converter and the HV charger are integrated directly into the battery, while for the gravimetric component modeling they are considered as part of the module electronics. To correct this inaccuracy, it would be necessary to know the real masses of the DC-DC converter and HV charger to include them in the real electric module mass. However, the exact mass of these components cannot be estimated since an internal battery teardown is not available.

Finally, the sum of the simulated module masses is compared with the real empty vehicle mass (Figure 4.7). For the vehicles in Table F.2, the model yields an MAE of $54.5\,\mathrm{kg}$ and an nMAE of $2.9\,\%$. These values are similar to the deviations estimated by S. Fuchs [107, pp. 63-80] with his mass model. In addition, these deviations are not necessarily caused by errors in the tool, but rather by the unique characteristics (such as the battery housing of the Mercedes EQC) of some vehicles, which cannot be considered in the model.

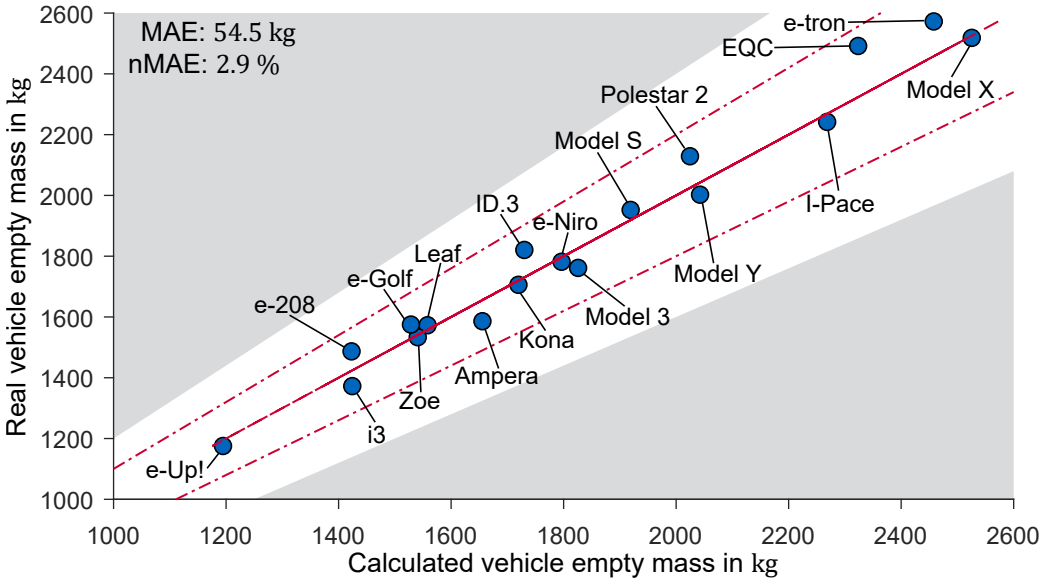

Figure 4.7: Calculated vs. real empty vehicle masses for the vehicles listed in Table F.2.

4.4 Vehicle Architecture Tool Validation

This chapter assesses the accuracy of the entire vehicle architecture tool, testing the interaction of all presented models: LDS (Section 3.3), volumetric (Section 3.4), and gravimetric (Section 3.5) component modeling. A validation for vehicles of all segments and derivatives is not possible due to the low number of existing BEVs. However, it is possible to validate the tool by simulating a set of current BEVs, which will be denoted as *validation dataset*. The dataset contains eight

top-selling BEVs: BMW i3s [223], VW ID.3 Max [213], VW ID.3 Pro S [224], Jaguar I-Pace [225], Tesla Model 3 Standard Range (SR) [226], Tesla Model 3 Long Range (LR), Tesla Model Y [227], and Audi e-tron [228]. These vehicles span different segments, body types, performance requirements, and are all documented in the A2mac1 database [163], meaning that precise mass and component data is available. A detailed description of the simulation setup for the validation dataset is given in Section F.4.

The validation follows the approach shown in Figure 4.8. First, the input set required by the architecture tool (Table 3.2) is collected for each validation vehicle (①, Figure 4.8). These inputs are listed in Table F.4 - F.6. The tables document a portion of the required input set since some design parameters (like the H30-1 and H30-2) are retrieved from the A2mac1 database [163] and cannot be disclosed. Furthermore, as already noted in Subsection 4.2.2, to accurately model the traction battery, the corresponding package factor and cell energy densities are required. Once again, these parameters are for internal use and cannot be disclosed.

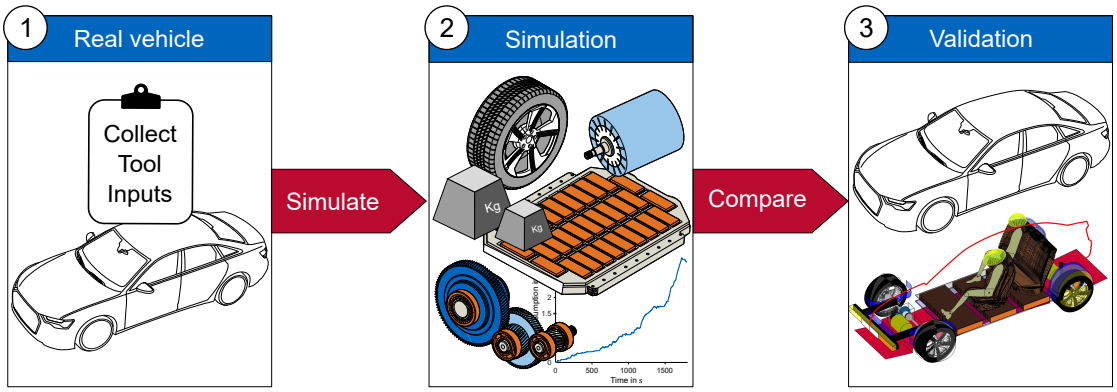

Figure 4.8: Structure of the vehicle architecture tool validation.

In the following step (②, Figure 4.8), the validation dataset is simulated. The architecture tool iterates according to the procedure depicted in Figure 3.1 until each validation vehicle converges. The result is a simulated vehicle with an estimate of both mass and package. The simulated vehicle also documents the estimated consumption. In the last step (③, Figure 4.8), the validation and the simulated vehicles are compared.

Table 4.2 shows the simulation results (including the percentual deviation from the real values) for four main categories: range, consumption, mass, and installed battery energy. These four categories are interdependent. For example, the simulated range depends on the available battery space (volumetric modeling) and vehicle consumption calculated by the LDS. The resulting consumption is in turn influenced by the mass estimated by the gravimetric component modeling. Finally, the installable battery energy is defined by the dimensions of wheels and drive units, which are in turn influenced by the vehicle mass. In most cases, deviations below $5\,\%$ are achieved. The highest deviations are between $5\,\%$ and $13\,\%$.

Range is simultaneously an input and an output. Although the architecture tool will fill the battery with cells to attain the input range, it is almost impossible to exactly match the required value. This is because each newly added cell provides a discrete increase in battery energy and accordingly a discrete increase in range. Further discontinuities are introduced by battery voltage requirements (Figure 3.17). For these reasons, certain ranges are infeasible. To counter this problem, there is no imposed cell size, but a range of feasible cell lengths, heights, and widths (Table F.3). Depending on the chosen type (pouch, cylindrical, or prismatic), the architecture tool can choose among several cell dimensions. Furthermore, as described in Subsection 3.4.6,

the feasible battery voltage is set between 350 V and 450 V. Due to these implementations, range discontinuities are drastically reduced, and in most cases, the deviation between real and simulated range is below 1 %. The tool confirms that the real range is achievable in terms of mass and package for all validation vehicles.

The second category listed in Table 4.2 is vehicle energy consumption. The losses of the gearbox, power electronics, and battery are modeled as described in Section 3.3. The PMSM losses are described with the efficiency map of Motor XP while the IM losses are modeled with the maps of the efficiency map database. Based on the acceleration times and maximum speeds listed in Table F.4 - F.6, the LDS identifies the maximum torque and machine speed, scales the efficiency map accordingly, and uses it to estimate the machine losses in the cycle. The resulting WLTP consumption shows deviations between −6.2 % and 6.3 %. The BMW i3s has one of the highest deviations: although the mass is overestimated, the simulated consumption is underestimated by 6.2 %. For this particular vehicle, the efficiency map of Motor XP largely overestimates the machine efficiency. A reason for this deviation could be the BMW i3s machine, which is a hybrid PMSM [229] and is probably not modeled correctly by the Motor XP map. Another vehicle with a high deviation is the Tesla Model 3 SR, where consumption is overestimated by 6.3 %. This is partly caused by overestimating the empty mass of the vehicle. Further causes are the lack of official data regarding the exact net energy density of the Tesla Model 3 SR documented in the A2mac1 database [163]. Additionally, there are several Tesla Model 3 variants equipped with cells from different manufacturers [230]. Depending on the cell manufacturer, the vehicle range and the net battery energy vary. Since Tesla does not publish an official overview of the existing Model 3 SR models and their ranges, it cannot be guaranteed that the values used in (Table F.5) for calculating the real vehicle consumption are correct.

Table 4.2: Simulated range, consumption, mass, and battery energy for the validation dataset. The percentages in parentheses denote the deviation from the real values.

Vehicle	Range in WLTP	Consumption in WLTP (no charging losses)	Vehicle empty mass (no driver)	Installed battery net energy
BMW i3s	283.3 km (0.1 %)	12.6 kWh/100km (−6.2 %)	1450.0 kg (12.4 %)	35.6 kW h (−6.1 %)
VW ID.3 Max	425.3 km (0.5 %)	13.5 kWh/100km (−1.4 %)	1726.2 kg (−0.6 %)	57.5 kW h (−0.9 %)
VW ID.3 Pro S	556.5 km (1.0 %)	14.3 kWh/100km (2.4 %)	1874.7 kg (1.3 %)	79.6 kW h (3.4 %)
Jaguar I-Pace	473.4 km (0.7 %)	17.7 kWh/100km (−3.7 %)	2265.8 kg (2.6 %)	84.0 kW h (−3.0 %)
Tesla Model 3 SR	412.3 km (0.8 %)	13.0 kWh/100km (6.3 %)	1680.8 kg (4.3 %)	53.6 kW h (7.1 %)
Tesla Model 3 LR	559.7 km (−0.1 %)	13.9 kWh/100km (0.1 %)	1841.7 kg (6.7 %)	77.9 kW h (0.1 %)
Tesla Model Y	480.1 km (0.0 %)	15.6 kWh/100km (0.1 %)	2194.6 kg (6.2 %)	75.1 kW h (0.1 %)
Audi e-tron	407.1 km (0.5 %)	21.7 kWh/100km (2.0 %)	2469.7 kg (−2.0 %)	88.2 kW h (2.5 %)

The fourth column in Table 4.2 lists the simulated empty vehicle mass (the value does not include the driver). In this case, the mean absolute deviation of the validation dataset is higher than the value derived in Section 4.3. In fact, the resulting mass is, in contrast to Section 4.3, derived from the vehicle architecture iterative process. Inaccuracies in the estimation of the component volumes and the vehicle consumption impact the simulated mass, leading to a higher deviation. Despite the interaction between volumetric models, LDS, and gravimetric models, the deviation in mass estimation is always below 13 %. The vehicle with the highest error is the BMW i3s. Following the same method applied in Section 4.3, the BIW of the i3s is assumed to be entirely made of aluminum, which leads to a good approximation of the frame mass. However, the tool is

not capable of modeling the lightweight measures applied on the i3s axles and battery housing and overestimates the masses of chassis and powertrain.

The last column of Table 4.2 compares simulated and real battery net energy. For each vehicle, the empirical package factors and cell energy densities are estimated and used as inputs. This leads to deviations usually below $3\,\%$. A higher deviation occurs for the Tesla Model 3 SR. As already discussed, this deviation may be caused by an error in the estimation of the real net energy, which is assumed to be $50\,\mathrm{kWh}$ [230]. The net energy underestimation by the BMW i3s is caused by vehicle consumption, which is underestimated as well. Consequently, the required range can be reached (at least in the simulation) with less battery energy.

Finally, inaccuracies in the consumption, mass, or battery energy estimation are also caused by the fact that some vehicles are simply designed better than others and act as outliners. Since the architecture tool is also based on empirical data, particularly well-designed vehicles (for example in terms of mass) will inevitably be overestimated.

4.5 Main Findings

The scope of the previous sections was the validation and verification of the vehicle architecture tool modules. Finally, Section 4.4 assessed the accuracy of the entire tool with a dataset of existing BEVs. With these steps, it was possible to assess the performance capabilities of the tool. This chapter summarizes the main insights of the validation.

In Section 4.1, it was observed that machine losses, and consequently machine efficiency maps, have a great influence on vehicle consumption. The PMSM maps implemented in the efficiency map database appear to be outdated and are therefore substituted with the machine map of the software Motor XP [216, 217]. A similar analysis for IMs maps could not be conducted. Nevertheless, IMs are not as relevant as PMSM since they are used less often in current BEVs (vehicles in Table F.4 - F.6). For robust results, it has to be ensured that the machine efficiency maps used are always up-to-date. The Motor XP map appears to correctly model the current electric machine efficiencies. Therefore, for the simulations in Chapter 5, the PMSMs will be described with the Motor XP map.

The validation of the wheel model (Subsection 4.2.1) showed that correct wheel sizing requires tire and rim diameters as simulation inputs. Only with these inputs is it possible to reproduce the diverse design strategies of the manufacturers. In the upcoming years, due to ongoing research and development, the maximum tire loads will further increase and new tire dimensions will be available. These changes have to be integrated into the tire dataset to avoid sizing tires based on outdated data. This can be achieved by monitoring the updates of the ETRTO, which publishes an overview of the existing tire dimensions and their corresponding maximum loads every few years.

The main insight from Subsection 4.2.2 is that for a correct estimation of the battery energy, both package factors and energy densities are required. It should also be considered cell energy densities have drastically improved over the last years [21]. Therefore, when simulating a new vehicle concept, the densities should be tuned according to the expected vehicle model year. König et. al [21] give an overview of cell energy density development until 2030.

The validation of the mass model (Section 4.3) yielded an nMAE of $2.9\,\%$. It has to be noted that the mass model can recreate the average tendency of the vehicles contained in the mass

dataset. On the one hand, the vehicle masses of manufacturers such as Tesla or BMW (which are characterized by lightweight measures on powertrain, chassis, and frame) are usually slightly overestimated. On the other hand, the masses of heavy SUVs that are not based on a pure purpose design strategy (e.g. Mercedes EQC and Audi e-tron) are underestimated.

The validation in Section 4.4 confirmed that the mass iteration loop always converges and can replicate the validation dataset correctly in most cases. However, there are still deviations in vehicle consumption. This is due to the fact that the PMSMs are modeled with one single efficiency map (the Motor XP map). A single map cannot represent all possible PMSM variants, which is particularly critical in the case of the BMW i3s. Furthermore, to apply the Motor XP map to the validation dataset, the map is scaled based on the required machine torque and rotational speed of each validation vehicle (following the procedure shown in Figure 3.3). However, scaling the efficiency map is a simplification and may lead to errors. Usually, a corresponding efficiency map should be calculated for each combination of torque and rotational speed. The efficiency map database was originally created to solve this problem: with its high number of maps with different torques and rotational speeds, scaling the map is not required anymore. However, the validation step in Section 4.1 showed that the database maps are unreliable. To solve this problem, it is required to update the efficiency map database or to integrate a reliable machine map calculator directly into the tool.

The validation step in Section 4.4 also highlights the relevance of mass estimation for vehicle architecture sizing. If the mass is under- (or over-) estimated, vehicle consumption will consequently also be under- (or over-) estimated. These errors are further propagated to the powertrain sizing and are amplified during the iteration loop of the tool. To ensure reliable results, the empirical models implemented in the gravimetric component modeling must always be up-to-date. This can be achieved by integrating the newer component data into the SQL database as soon as new BEVs enter the market.

In conclusion, the validation showed that the tool can model exiting BEVs precisely. For unconventional vehicle concepts, such as the BMW i3s, there are considerable deviations. To improve the modeling of the BMW i3s, carbon fiber BIWs should be integrated into the architecture tool. In the next chapter, some of the vehicles of the validation dataset will be used in a series of parametric studies.

5 Results

This chapter applies the tool to quantify the impact of different electrification strategies on future BEV architectures while considering both secondary mass and volume effects. First, the impact of different cell types is analyzed (Section 5.1). Subsequently, the potential of a novel integration principle is estimated (Section 5.2). Finally, Section 5.3 performs an optimization to determine which cell types and integration principles have the highest potential.

5.1 Cell Type Impact

An important decision at the project start of a new BEV is selecting a cell type. As shown in Section B.2, there are no clear guidelines in this regard and each manufacturer follows a different strategy. The Tesla electrification strategy uses cylindrical cells and is often considered as one of the reasons for Tesla's success. What if this strategy was applied to a vehicle of another manufacturer? What volume and mass effects are induced by this strategy and how do they impact vehicle range and its consumption?

To answer these questions, a VW ID.3 is chosen as the reference vehicle for a parametric study. The input set of the VW ID.3 Pro S is taken from Table F.4 and the vehicle is simulated twice: first with its original cell type (pouch cells) and then with 21700 cylindrical cells (like the Tesla Model 3). In the following sections, the first case will be denoted as *pouch variant*, while the second case will be denoted as *cylindrical variant*. Since this parametric study simulates an ID.3 to be launched in 2025, the cell energy densities are adjusted (Table 5.1). Moreover, the differences in terms of package factors and energy densities between the pouch and cylindrical cells have to be considered (Table 5.1).

To replicate the exact comfort requirements of the ID.3, the interior model (Subsection 3.4.3) is deactivated and the internal dimensions are retrieved from the A2mac1 database [163]. The simulated pouch and cylindrical variants have the same passenger compartment dimensions. However, cylindrical cells have a smaller height and do not have a cooling plate along the z-direction. The dimensional chain described in Section D.5 estimates a battery height reduction of $39\,\mathrm{mm}$. Therefore, for the cylindrical variant, the vehicle height (H100) is corrected and the passenger compartment shifted by $39\,\mathrm{mm}$ towards the road surface (Table 5.1).

The lower H100 leads, on the one hand, to a mass reduction and, on the other hand, to a reduction in the vehicle frontal area and drag coefficient. The mass reduction is accounted for gravimetric component modeling while the drag loss reduction induced by the smaller frontal area is considered in the LDS. The possible improvement in drag coefficient is (for the moment) neglected and both variants are simulated with the ID.3 drag coefficient, which is 0.26 [231]. No target range is assigned, meaning that the architecture tool derives the maximum achievable range for both variants. The results are shown in Figure 5.1.

Table 5.1: Comparison between the pouch and the cylindrical variants. The gross battery energy is estimated based on the gross cell volumetric energy density. The usable (or net) battery energy is estimated with the $K_{\text{gross2net}}$ factor (Section 3.3). The remaining inputs required for the reference vehicle simulation are taken from Table F.4 and are identical for both variants.

Design parameter	Pouch variant	Cylindrical variant
Gross volumetric cell energy density $E_{\text{cell,vol}}$ (2025)	$800\,\text{W h l}^{-1}$ [232]	$950\,\text{W h l}^{-1}$ [207]
Gross gravimetric cell energy density $E_{\text{cell,grav}}$ (2025)	$350\,\text{W h kg}^{-1}$ [232]	$350\,\text{W h kg}^{-1}$ [207]
Maximum cell height $s_{\text{cell,z}}$ (Table F.3)	100 mm	70 mm
Package factor K_{x} / Package factor K_{y}	0.821[1] / 0.821[1]	0.892[2] / 0.881[2]
Resulting vehicle height (H100)	1550 mm	1511 mm

[1] Estimated from VW ID.3 Pro S battery in A2mac1 [2] Estimated from Tesla Model 3 LR in A2mac1

While the pouch variant reaches a range above 700 km, the cylindrical variant's range remains below 580 km. Cylindrical cells have better filling capabilities along the x- and y-directions as well as a higher volumetric energy density, but they also are 30 mm lower than the pouch cells. This 30 mm difference causes a battery energy drop of 24.9 kW h. The lower battery energy leads to savings in terms of mass and consumption, which are nevertheless not sufficient to reach the same range as the pouch variant. In conclusion, for a vehicle with the characteristics of an ID.3, it is not purposeful to apply a cylindrical cell strategy. However, a change in external dimensions may overturn this trend.

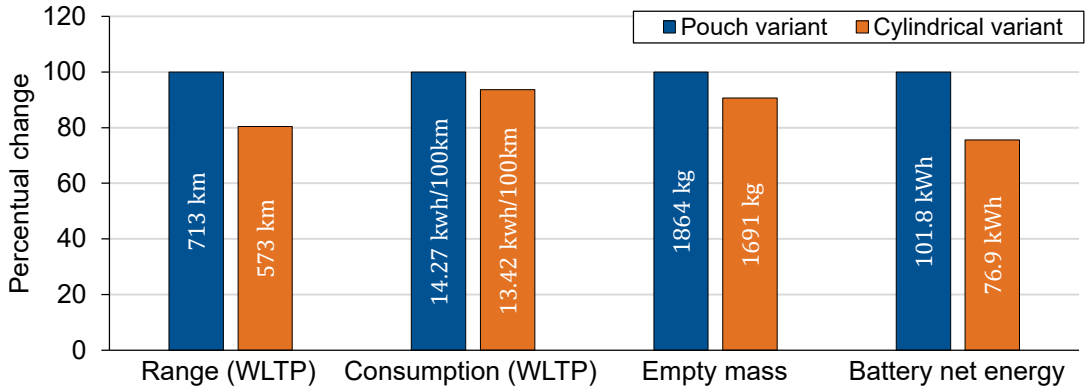

Figure 5.1: Resulting ranges, consumptions, masses, and battery energies for the pouch and the cylindrical variants. Both variants have the same external (except for H100) and internal dimensions, performance requirements, and battery footprint (i.e. battery width and length). For better readability, the results are scaled using the values of the pouch variant.

To quantify the impact of the external dimensions, a new parametric study is conducted (Figure 5.2). The two variants are simulated by iteratively adjusting total width (W103), wheelbase (L101), and height (H100). The starting values for L101 and W103 are the same for both variants. Regarding the H100, the pouch variant starts at 1550 mm, while the cylindrical variant starts at 1511 mm (according to Table 5.1). At every external dimension change, the architecture tool recalculates the available battery space and fills it with cells. The reference wheelbase and width are changed within a range of ±100 mm. For H100, the change is only comprised of ±20 mm. This range is intentionally set lower since an increase in H100 is only purposeful if the cell height can be increased accordingly. However, the empirical analysis in Table F.3 shows that current BEV cells have a limited range in terms of height. For this study, it is assumed that by 2025 the feasible cell height range is 80 mm–120 mm for pouch and 50 mm–90 mm for cylindrical cells.

By increasing L101, the battery length can be raised and more cells installed. With an increase of $100\,\mathrm{mm}$, the pouch variant obtains a range improvement of $35\,\mathrm{km}$ (Figure 5.2a). The average battery energy increase is $59\,\mathrm{Wh}$ for each additional mm. The cylindrical variant reaches a range slightly below $600\,\mathrm{km}$ and its battery energy gain is $42\,\mathrm{Wh\,mm^{-1}}$. Although the range changes only slightly for both variants, an L101 adjustment barely impacts vehicle consumption (Figure 5.2b) and mass (Figure 5.2c).

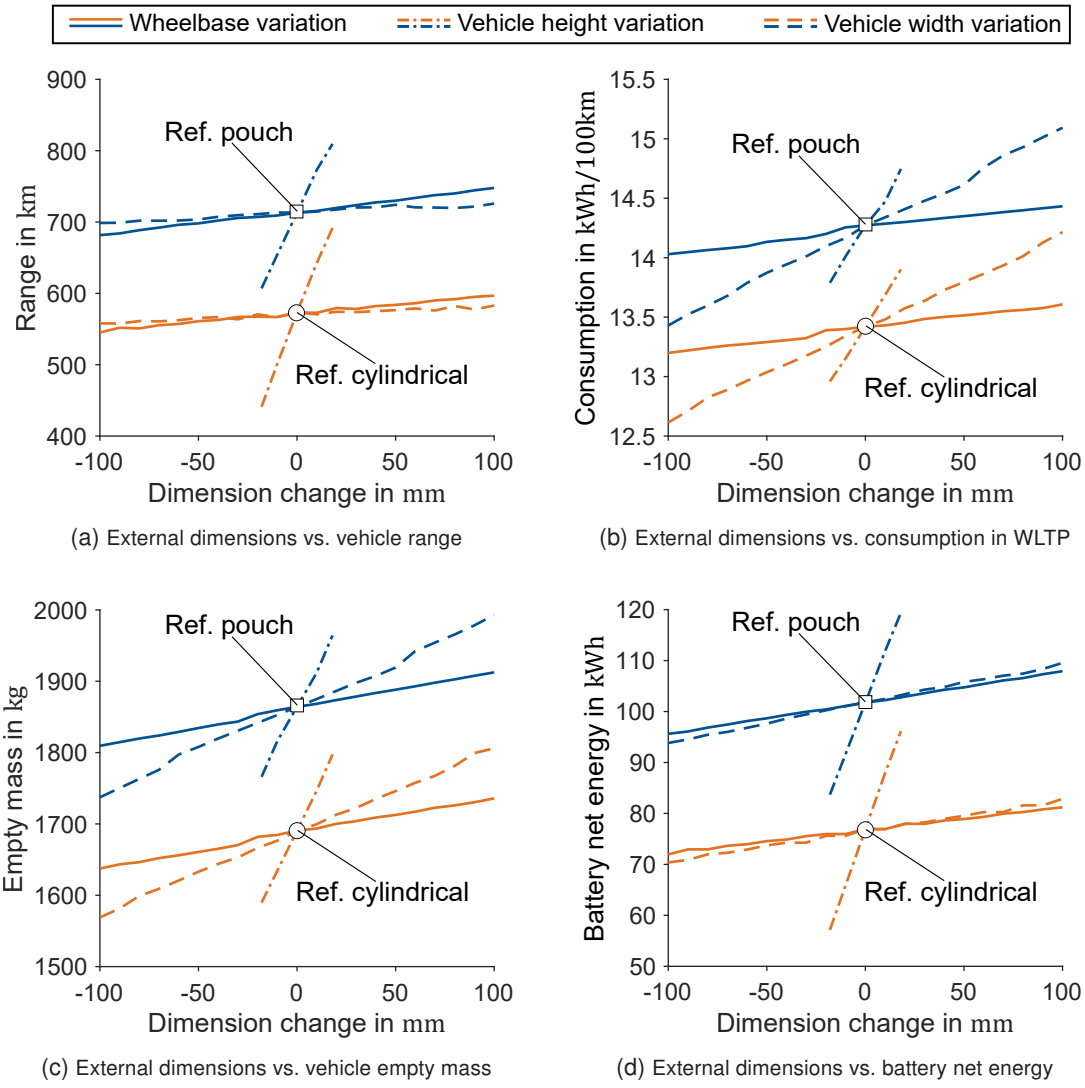

(a) External dimensions vs. vehicle range

(b) External dimensions vs. consumption in WLTP

(c) External dimensions vs. vehicle empty mass

(d) External dimensions vs. battery net energy

Figure 5.2: Impact of the external dimensions. The x-axis shows the change in external dimensions while the y-axis shows the corresponding impact on vehicle range, consumption, empty mass, and battery energy. The two variants shown in Figure 5.1 are positioned at the zero point of the x-axis. Both variants are simulated with a c_d of 0.26.

An adjustment in W103 influences battery width. W103 has a greater impact on battery energy than an equal change in L101 (Figure 5.2d). The reason for this trend is that the battery is shaped like a rectangle with its longest dimension oriented parallel to the driving direction (Section B.2). Therefore, the additional volume gained by a $1\,\mathrm{mm}$ increase of battery width is greater than the one obtained with a $1\,\mathrm{mm}$ increase of battery length. However, an increase in W103 has a high impact on vehicle mass (Figure 5.2c). Furthermore, W103 influences the frontal area and drag losses, thus affecting vehicle consumption (Figure 5.2b). In conclusion, although an increase in W103 offers a higher battery energy gain compared to an equal increase in L101, it also has a

higher impact on vehicle consumption. The resulting range improvement by a width increase of $100\,\mathrm{mm}$ is below $13\,\mathrm{km}$ for both variants.

H100 has the highest impact on vehicle consumption (Figure 5.2b) and empty mass (Figure 5.2c). Nevertheless, with every additional mm along the z-direction, battery net energy increases by over $1\,\mathrm{kWh}$ for both variants. The cylindrical variant has a higher increase since its cells have a better volumetric energy density. With a $20\,\mathrm{mm}$ H100 increase, taller cylindrical cells ($90\,\mathrm{mm}$ height) can be fitted into the vehicle. With this adjustment, the cylindrical variant reaches a range of $692\,\mathrm{km}$, which is close to the reference pouch variant.

To ensure that the trend in Figure 5.2 is not caused by neglecting the more favorable aerodynamics of the cylindrical variant, this variant is simulated again by adjusting the drag coefficient c_d. Initially, a c_d 0.23 is selected, which is then further decreased to 0.20. The first value corresponds to the Tesla Model 3 [233], while the second is so far the best existing drag coefficient for series BEVs [234]. Table 5.2 and Section G.1 present the results.

Table 5.2: Parametric study with different c_d values. The column *Ref* depicts the reference variants with the ID.3 external dimensions. The other columns show the impact of a change in external dimensions. For the cylindrical variants with c_d=0.23 and 0.20, the empty mass and battery energy have the same values as the cylindrical variant with c_d=0.26.

			Ref	**Wheelbase (L101)**		**Width (W103)**		**Height (H100)**	
				−100 mm	+100 mm	−100 mm	+100 mm	−20 mm	+20 mm
Pouch variant	c_d=0.26	Range in km	713	682	748	699	726	607	810
		Cons. in kWh/100km	14.27	14.03	14.43	13.43	15.09	13.79	14.75
		Empty mass in kg	1864	1809	1912	1737	1993	1766	1964
		Batt. net energy in kWh	101.8	95.6	107.9	93.8	109.5	83.7	119.4
Cylindrical variant	c_d=0.26	Range in km	573	545	597	558	583	441	692
		Cons. in kWh/100km	13.42	13.20	13.61	12.61	14.21	12.96	13.90
		Empty mass in kg	1691	1637	1736	1569	1806	1590	1797
		Batt. net energy in kWh	76.9	72.0	81.2	70.4	82.9	57.1	96.2
	c_d=0.23	Range in km	601	572	626	585	611	463	724
		Cons. in kWh/100km	12.80	12.58	12.98	12.03	13.57	12.35	13.28
	c_d=0.20	Range in km	631	601	657	614	641	488	759
		Cons. in kWh/100km	12.19	11.97	12.37	11.46	12.92	11.71	12.66

The improved c_d decreases consumption and leads to a range increase of approx. $28\,\mathrm{km}$ for the c_d=0.23 variant and of $58\,\mathrm{km}$ for the c_d=0.20 variant (Table 5.2). These gains are obtainable with a sole improvement of the drag coefficient. Based on this second study, it can be summarized that a c_d improvement of 0.01 leads to an average range increase of approx. $10\,\mathrm{km}$. Despite the c_d improvement, the pouch variant still remains better in terms of range.

5.2 Cell to Body Integration Principle

The study in Section 5.1 showed that increasing the current cylindrical cell height by $20\,\mathrm{mm}$ allows ranges comparable with pouch cells. In 2020, the Tesla chief executive officer, Mr. Musk,

presented a new integration principle that indeed goes in this direction [235]. In this thesis, this principle will be denoted as Cell to Body (C2B) integration (Figure G.2b), and this chapter assesses its impact on future BEVs in terms of mass, consumption, and range.

The current models of Tesla Model 3 and Model Y have a highfloor integration principle (Figure 2.7a) with cylindrical cells. The battery has a drop shape without a second level and the cells (21700 format) are grouped into four large modules (Figure B.3a). The future Tesla models with C2B principle will use the 4680 format (cylindrical cells with a diameter of $46\,\mathrm{mm}$ and a height of $80\,\mathrm{mm}$). Inside the battery, there will be no modules or internal crash structures, which will allow the cells to be packed more densely. Furthermore, as Mr. Musk said, "The battery for the first time will have dual-use [...] as energy device and as structure" [235]. The battery is integrated directly into the BIW and becomes part of the frame. The cells are glued together with a filler, which can also transfer shear stress so that the battery acts as a honeycomb structure increasing BIW stiffness. With these adjustments, Tesla claims that the mass of the BIW can be reduced by $10\,\%$ [235].

What is the range potential of the C2B principle in comparison to the highfloor? To answer this question, three vehicles are simulated. The first vehicle is the VW ID.3 with cylindrical cells (and c_d=0.26) described in Section 5.1. The second vehicle is a Tesla Model 3 LR (performance requirements and dimensions are taken from Table F.5) and the third is the Tesla Model Y listed in Table F.6. To simulate a C2B principle on these vehicles, some assumptions are required. First, the battery dimensional chain has to be corrected, since components such as the module housing and the battery cover are eliminated. Second, the cell energy densities and package factors have to be modified due to the different cell format. Finally, the mass savings generated by the C2B strategy have to be estimated. Section G.2 documents the assumptions while the simulation results are shown in Table 5.3.

Table 5.3: Comparison between highfloor and C2B integration principle.

		Highfloor (21700 format)	**C2B (4680 format)**
ID.3 cyl.	Range in km	573	696
	Cons. in $\mathrm{kWh/100km}$	13.42	13.43
	Empty mass in kg	1691	1694
	Battery net energy in kWh	76.9	93.5
Model 3	Range in km	667	799
	Cons. in $\mathrm{kWh/100km}$	13.75	13.76
	Empty mass in kg	1805	1810
	Battery net energy in kWh	91.7	109.9
Model Y	Range in km	602	727
	Cons. in $\mathrm{kWh/100km}$	15.28	15.30
	Empty mass in kg	2116	2123
	Battery net energy in kWh	92.0	111.2

By upgrading from a highfloor to a C2B integration principle, the vehicles obtain a battery energy increase between $16.6\,\mathrm{kWh}$ and $19.2\,\mathrm{kWh}$. This increase depends on the battery footprint. On the one hand, the Tesla Model Y has the largest footprint and obtains the highest energy increase if the 21700 cell format is substituted with the 4680 format. On the other hand, the Model Y also has the highest mass and consumption. Therefore, the resulting range increase is almost

identical to the VW ID.3, which has a smaller footprint but also lower consumption. All vehicles obtain a range increase above $120\,\mathrm{km}$.

Despite the considerable battery energy increase, the vehicle masses remain almost unchanged, since the mass savings generated by the C2B principle compensate for the mass increase caused by the larger cell format. Furthermore, despite being $10\,\mathrm{mm}$ higher, 4680 cells require the same installation space as 21700 cells along the vertical direction (Figure G.3). By combining these effects, an upgrade from highfloor to C2B principle barely impacts vehicle consumption (Table 5.3). In the next section, the C2B principle is further analyzed.

5.3 Integration Principle Optimization

Section 5.1 studied the impact of a shift from pouch to cylindrical cells, while Section 5.2 assessed the potential of the C2B principle. This section applies an optimization to identify which combination between cell type and integration principle yields the highest range. First, a set of reference vehicles is defined. Subsequently, a set of design variables and optimization objectives is selected (Subsection 5.3.1). Finally, the reference vehicles are optimized and the results presented (Subsection 5.3.2).

The set of reference vehicles includes three current BEVs: the VW ID.3, the Tesla Model 3, and the Audi e-tron (Table 5.4). These BEVs differ in their external dimensions, have different powertrain requirements, drive typologies, and body types. Each reference vehicle will be optimized with two cell types (pouch and cylindrical) while applying three different integration principles (mixedfloor, highfloor, and C2B). Simulating both pouch and cylindrical cells on the reference vehicles follows the same procedure as in Section 5.1. For the Tesla Model 3, the vehicle height is increased until there is enough space to fit a $100\,\mathrm{mm}$ tall pouch cell, thus deriving a pouch variant of the Tesla Model 3. For the Audi e-tron and the VW ID.3, the vehicle height is decreased until a 21700 cell format perfectly fits into the battery.

Table 5.4: Differences between the pouch and cylindrical variants of the reference vehicles. Besides the values listed in this table, the other simulation inputs are taken from Table F.4 - F.6.

	VW ID.3 ID.3 77 kWh in Table F.4		**Tesla Model 3** Model 3 LR in Table F.5		**Audi e-tron** e-tron in Table F.6	
Variant	Pouch	Cylindrical	Pouch	Cylindrical	Pouch	Cylindrical
Cell height	$100\,\mathrm{mm}$	$70\,\mathrm{mm}$	$100\,\mathrm{mm}$	$70\,\mathrm{mm}$	$100\,\mathrm{mm}$	$70\,\mathrm{mm}$
Vehicle height (H100)	$1550\,\mathrm{mm}$	$1511\,\mathrm{mm}$	$1482\,\mathrm{mm}$	$1443\,\mathrm{mm}$	$1636\,\mathrm{mm}$	$1597\,\mathrm{mm}$
$K_{\mathrm{pack,x}}$ / $K_{\mathrm{pack,y}}$	0.821/0.821	0.892/0.881[1]	0.821/0.821	0.892/0.881[1]	0.821/0.821	0.892/0.881[1]
$E_{\mathrm{cell,vol}}$ for 2025	$800\,\mathrm{W\,h\,l^{-1}}$	$950\,\mathrm{W\,h\,l^{-1}}$	$800\,\mathrm{W\,h\,l^{-1}}$	$950\,\mathrm{W\,h\,l^{-1}}$	$800\,\mathrm{W\,h\,l^{-1}}$	$950\,\mathrm{W\,h\,l^{-1}}$
$E_{\mathrm{cell,grav}}$ for 2025	$350\,\mathrm{W\,h\,kg^{-1}}$					

[1] When simulating a C2B strategy, the package factors and mass savings derived in Section G.2 are used.

The resulting vehicle heights for the six variants are listed in Table 5.4. When deriving a cylindrical variant from a pouch variant (and vice versa), the external dimensions (with the sole exception of the H100) and performance requirements of the original vehicle are not changed. The internal dimensions (which are retrieved from A2mac1) remain unchanged so that the pouch and cylindrical variant have the same comfort requirements for each vehicle. The pouch variants will be optimized with a highfloor and a mixedfloor integration principle. The cylindrical variants

will be optimized with a highfloor and a C2B principle. The mixedfloor principle is excluded for cylindrical cells since it has never been applied for this cell format.

5.3.1 Design Variables and Objective Selection

For the optimization, the author selected the NSGA II genetic algorithm, because it has already been used several times for vehicle concept design applications (Section 2.5) and has been proven suitable also for the use in this thesis. For the implementation in this thesis, the open-source code of Song [236] is modified to be used for the vehicle architecture tool. The optimizer parameters are set according to the values proposed by Angerer [75, p. xxv].

Once the NSGA II is coupled with the vehicle architecture tool, it can be used to optimize the reference vehicles in Table 5.4. The NSGA II can vary a selected set of vehicle architecture tool inputs to minimize (or maximize) a selected set of vehicle architecture tool outputs. The inputs of the tool that NSGA II can vary are denoted as design variables, while the outputs of the tool that it optimizes are denoted as objectives.

The author chooses vehicle range and battery net energy as objectives. The NSGA II will try to maximize range while minimizing required battery energy. In this way, it is possible to identify the vehicles that achieve the longest possible range with the least amount of battery energy. As design variables, the author chooses the following inputs of the architecture tool:

- **External dimensions**: The wheelbase (L101) and vehicle width (W103) of each reference vehicle can be varied within a range of $\pm 100\,\mathrm{mm}$.
- **Internal dimensions**: The passengers' seating position (expressed as H30-1, H30-2, H5-1, and H5-2, Figure 2.4) of each reference vehicle can be varied within a range of $\pm 20\,\mathrm{mm}$.
- **Cell dimensions**: The allowable pouch cell height range is $80\,\mathrm{mm}{-}120\,\mathrm{mm}$. The ranges for width and thickness are set according to Table F.3. The allowable cylindrical cell height is set between $50\,\mathrm{mm}{-}90\,\mathrm{mm}$. The cell diameter is varied according to Table F.3. If a C2B strategy is applied, the allowable cell diameter is set between $44\,\mathrm{mm}{-}48\,\mathrm{mm}$.
- **Number of machines**: For the Tesla Model 3 and the Audi e-tron (which are also equipped with an AWD variant), the algorithm also tests whether a front or rear-wheel drive topology is more advantageous.

The width and wheelbase were already identified in Section 5.1 as influential parameters on vehicle range. They are therefore chosen as design variables. Among the interior concept measures, the H30-1, H30-2, H5-1, and H5-2 are selected as design variables as they have a direct influence on the available battery space. By varying H5-1 and H5-2, the NSGA II can shift the entire passenger compartment vertically, while it can adjust the seating height of the passengers by varying H30-1 and H30-2. The allowed variation of these design variables is limited to $\pm 20\,\mathrm{mm}$ to not drastically impact the legroom. The remaining internal dimensions (such as the headroom H61-2) are blocked and taken from the original interior concept of the reference vehicles. The H100 is not chosen as a design variable, since it can be directly derived from the H5-1 and H5-2 and the fixed headroom.

The NSGA II also uses the cell dimensions as design variables. For each calculated vehicle architecture, the NSGA II selects the cell size within the allowable ranges that optimally fills

out the battery space. Finally, for vehicles equipped with two machines, the NSGA II also tests whether a topology with one machine yields better results.

5.3.2 Optimization Results

To present the results, four outputs of the vehicle architecture tool are used: vehicle mass, vehicle consumption, range, and battery net energy (the latter two are also the optimization objectives of the NSGA II). Further plots documenting the distribution of the design variables and other outputs of the tool are provided in Section G.3.

Figure 5.3 shows the resulting consumption and vehicle mass as a function of the two optimization objectives (range and battery energy) for the VW ID.3. Additional plots are documented in Figure G.4 and G.5.

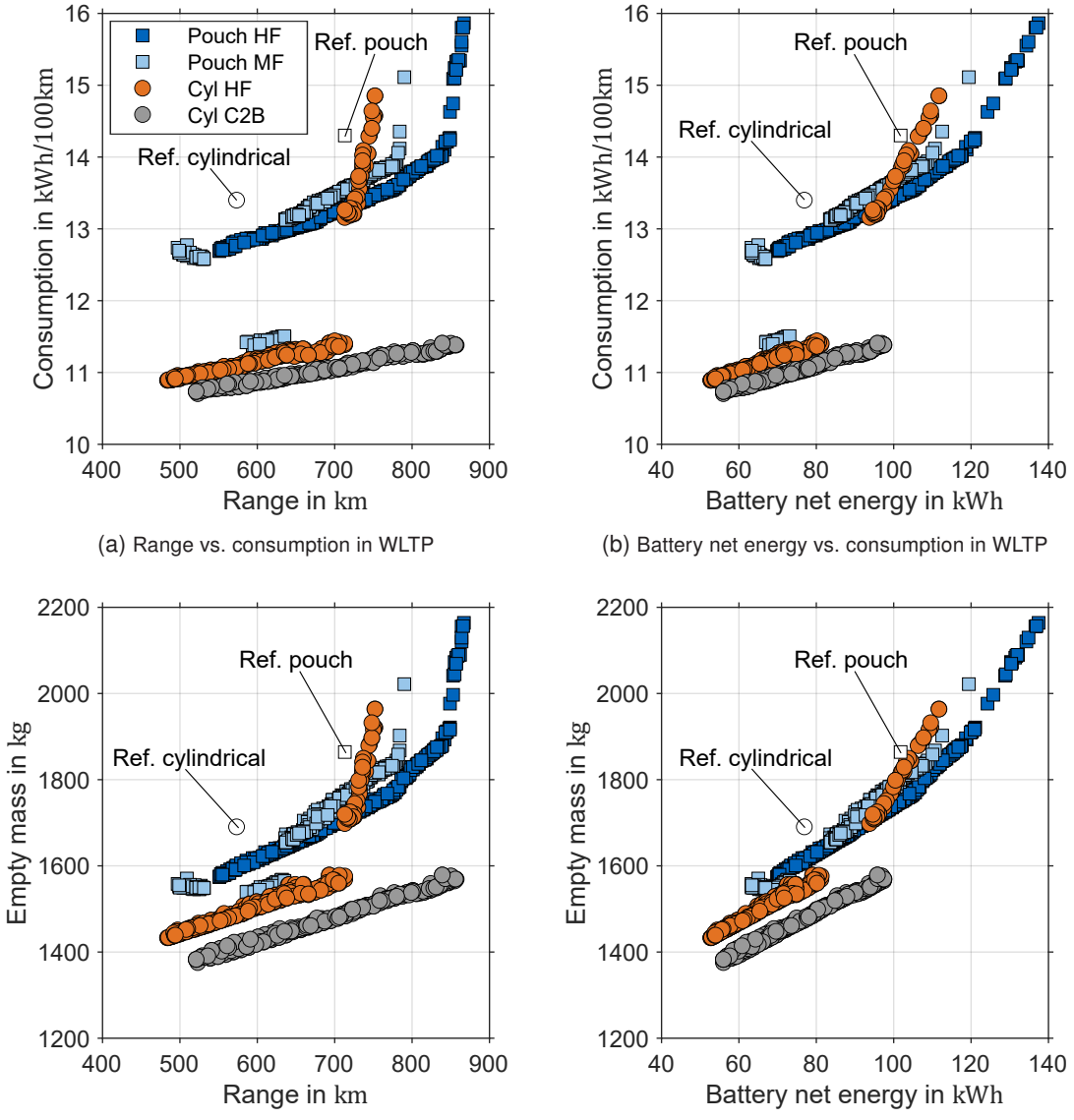

(a) Range vs. consumption in WLTP

(b) Battery net energy vs. consumption in WLTP

(c) Range vs. empty vehicle mass

(d) Battery net energy vs. empty vehicle mass

Figure 5.3: Resulting optimal architectures for the VW ID.3. These results are obtained with a population size of 300 over 30 generations.

The pouch variant with mixedfloor principle loses a part of the battery installation space due to the footwell at the first row of seats (Figure 2.7b). This loss is balanced by installing additional

cells underneath the second row of seats. There is a group of mixedfloor vehicles with a consumption below $12\,\mathrm{kWh/100km}$ and ranges between $600\,\mathrm{km}$ and $650\,\mathrm{km}$ (Figure 5.3a). These vehicles are equipped with cell heights below $90\,\mathrm{mm}$ (Figure G.4d) and have an H100 below $1540\,\mathrm{mm}$ (Figure G.4b). If the range has to be further increased, the cell height needs to be increased as well. This requires a simultaneous increase of underbody thickness and H30-2 (the latter adjustment is required to install taller cells underneath the second row of seats). These adjustments increase the H100 and yield a second front with higher consumption starting from $650\,\mathrm{km}$ range.

The pouch variant with highfloor principle builds a compact front extending from $550\,\mathrm{km}$ to $870\,\mathrm{km}$. First, the NSGA II gradually reduces the seating heights of the passengers (H30-1 and H30-2, Figure G.5c). This adjustment decreases the height of the passenger compartment and allows installing taller cells without affecting H100. Once it is no longer possible to decrease H30-1 and H30-2, the NSGA II raises H100 to further increase cell height. This strategy is followed until a range of approx. $750\,\mathrm{km}$. At this range value, the maximum allowable cell height has been reached (Figure G.4d). Consequently, the NSGA II raises L101, which yields a range increase of almost $80\,\mathrm{km}$ (Figure G.5a). Once L101 also reaches its maximum value, the NSGA II raises the vehicle width (which was so far kept to the minimum allowable value, Figure G.5e). As a result, the battery energy (Figure G.5e), the vehicle mass, and the consumption increase. The range improvement obtained with this measure is limited to only $20\,\mathrm{km}$.

The ID.3 highfloor cylindrical variant has two distinct fronts. The first extends between $480\,\mathrm{km}$ and $710\,\mathrm{km}$ and is characterized by a consumption below $12\,\mathrm{kWh/100km}$ (Figure 5.3a) and masses below $1600\,\mathrm{kg}$ (Figure 5.3c). The vehicles contained in this front require approx. $10\,\mathrm{kWh}$ less than the pouch variants (Figure G.4a). At approx. $710\,\mathrm{km}$, the vehicles reach a critical mass that requires a resizing of the wheels. This leads to wider tires that reduce available battery space. Consequently, the NSGA II tries to compensate for the space loss by increasing both vehicle width (Figure G.5e) and cell height (Figure G.4d). The resulting range improvement is below $50\,\mathrm{km}$ and each additional km requires on average $0.46\,\mathrm{kWh}$ (for the first front the cost is only $0.12\,\mathrm{kWh\,km^{-1}}$).

For the ID.3 reference vehicle, the C2B strategy is by far the best integration principle. This strategy enables ranges of up to $850\,\mathrm{km}$ with a vehicle consumption below $12\,\mathrm{kWh/100km}$ and masses lower than any other integration principle (Figure 5.3).

The second reference vehicle is the Tesla Model 3. Figure 5.4 shows the resulting consumption and vehicle mass as a function of the two optimization objectives (range and battery energy). Additional plots are documented in Figure G.6 and G.7. For this reference vehicle, the NSGA II can also choose whether to install one (as front or rear-wheel drive) or two machines (as AWD). The AWD option may reduce vehicle consumption, but also decreases the allowable battery length (as the battery must maintain a minimum clearance from both machines, Figure 3.10). The NSGA II in most cases opts for the AWD option since the energy savings that can be obtained with two machines compensate for the reduction of battery space.

The highfloor pouch variant is better than the mixedfloor variant in terms of consumption and mass (Figure 5.4). It almost reaches a range of $1000\,\mathrm{km}$ with battery net energies below $150\,\mathrm{kWh}$ (Figure G.6a). The highfloor cylindrical variant builds a compact front, which generally has lower consumption and mass than the pouch variants. Once again, the NSGA II first adjusts H30-1 and H30-2 to increase cell height. Once these design parameters cannot be used anymore, L101 is adjusted to further increase range. Finally, starting from a range of $900\,\mathrm{km}$, the NSGA II begins increasing W103 (Figure G.7f) since there is no remaining design variable that can be

used. The vehicles with larger W103 are on the rightmost edge of the cylindrical front and have worse values than the pouch variants in terms of mass and consumption.

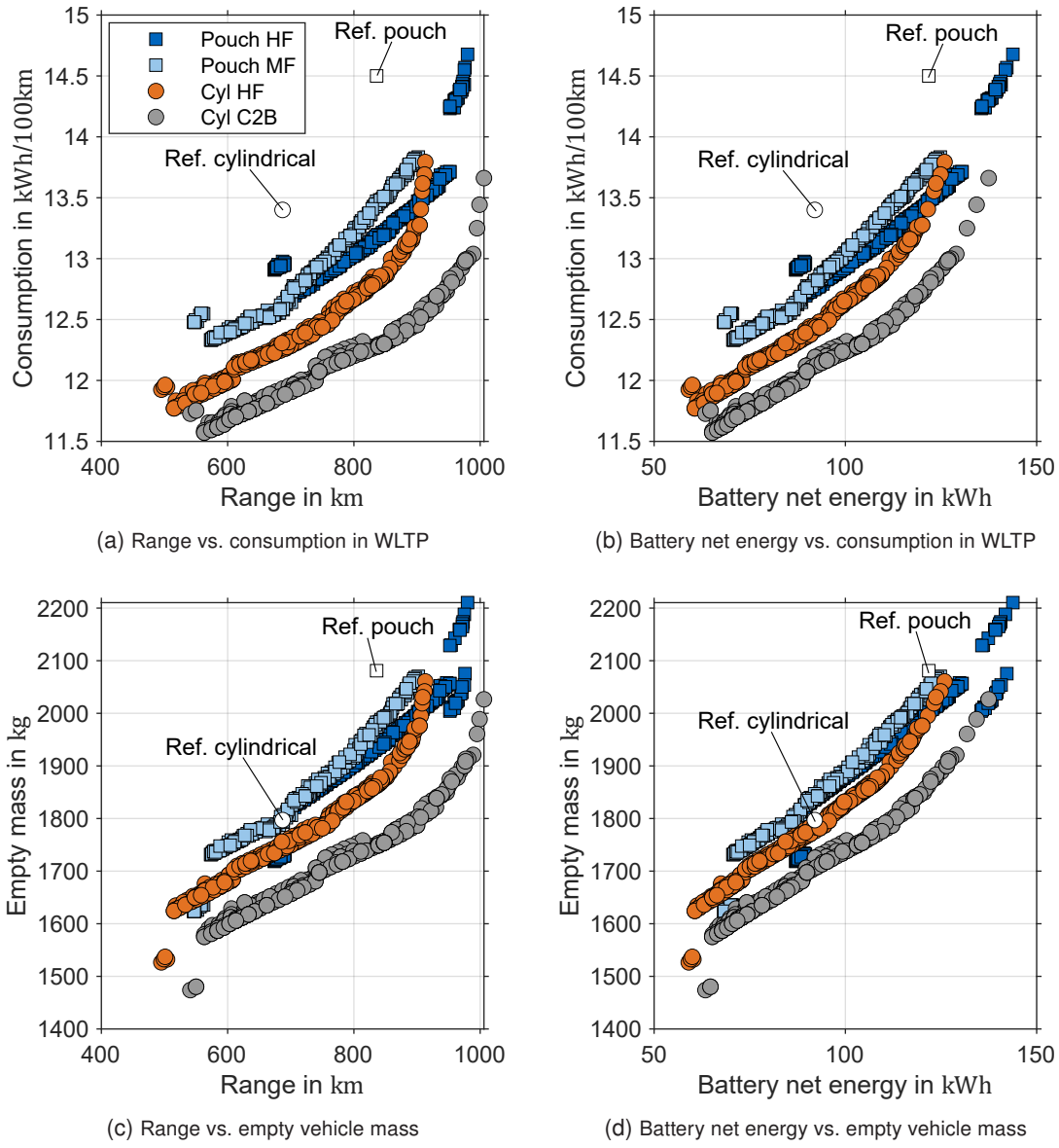

(a) Range vs. consumption in WLTP

(b) Battery net energy vs. consumption in WLTP

(c) Range vs. empty vehicle mass

(d) Battery net energy vs. empty vehicle mass

Figure 5.4: Resulting optimal architectures for the Tesla Model 3. These results are obtained with a population size of 300 over 30 generations.

As observed for the VW ID.3, the C2B principle is always better than the other principles in terms of mass and consumption. Assuming that the cells used can have a maximum height of $90\,\mathrm{mm}$, this integration principle can yield ranges above $1000\,\mathrm{km}$.

Figure 5.5 shows the resulting consumption and mass for the Audi e-tron. Additional plots are documented in Figure G.8 and G.9. Unlike the previously simulated vehicles, the Audi e-tron has a second level of cells underneath the second row of seats (Figure B.2a). Despite this difference, the resulting fronts are disposed similarly to the other two reference vehicles.

The NSGA II in most cases opts for an AWD topology since this decreases vehicle consumption. The resulting vehicle architectures have masses between $2000\,\mathrm{kg}$ and $2800\,\mathrm{kg}$. These high masses lead to a higher consumption (Figure 5.5a) than ID.3 (Figure 5.3a) and Model 3 (Figure 5.4a). Due to its large external dimensions, the Audi e-tron has a larger battery footprint

than the Model 3, and its second level of cells further increases the installable battery energy. However, its high consumption also impacts the required battery energy (and therefore costs): the e-tron requires a battery net energy between 105 kW h and 205 kW h for ranges between 600 km and 950 km (Figure G.8a). For the same ranges, the Tesla Model 3 requires only between 60 kW h and 145 kW h (Figure G.6a).

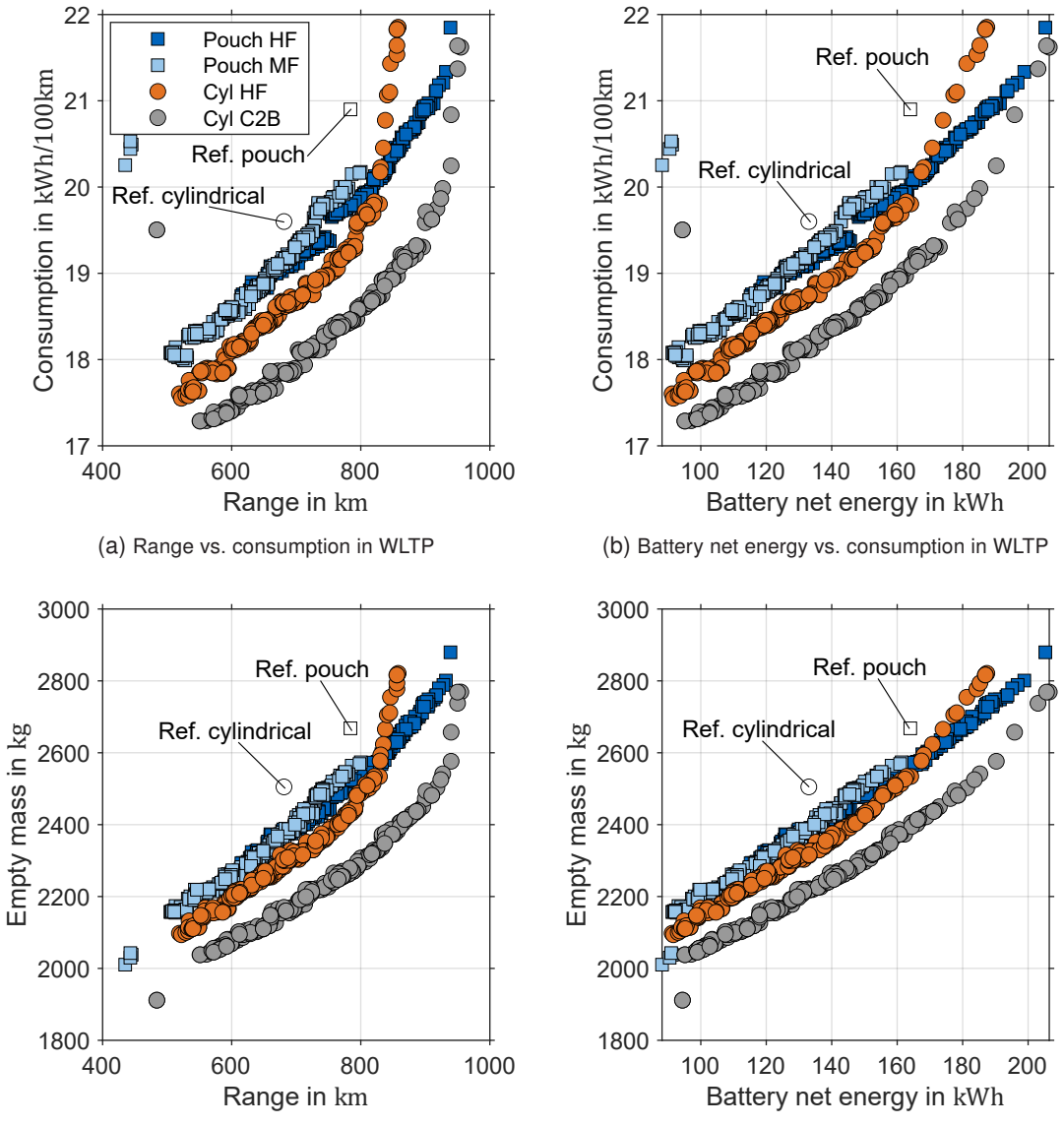

(a) Range vs. consumption in WLTP

(b) Battery net energy vs. consumption in WLTP

(c) Range vs. empty vehicle mass

(d) Battery net energy vs. empty vehicle mass

Figure 5.5: Resulting optimal architectures for the Audi e-tron. These results are obtained with a population size of 300 over 30 generations.

5.4 Main Findings

This section summarizes the main findings of the thesis. First, the impact of the integration principle is discussed in Subsection 5.4.1. Second, the influence of external and internal dimensions is described (Subsection 5.4.2). Finally, the impact of the components is discussed (Subsection 5.4.3). The findings presented in this chapter are based on the assumed cell sizes (Subsection 5.3.1) and energy densities (Table 5.1).

5.4.1 Impact of Integration Principle

The mixedfloor principle with pouch cells in most cases yields the highest consumptions and masses (Subsection 5.3.2). This strategy has a lower potential compared to the highfloor and C2B principles and it should not be used for future BEVs.

The highfloor principle with pouch cells allows ranges above $800\,\mathrm{km}$ for both Model 3 and ID.3. For the e-tron, the highfloor principle is simulated with a second level of cells. Without this additional level, the e-tron range would drop below $800\,\mathrm{km}$ regardless of the integration principle applied. A second level of cells may appear as an efficient integration strategy for the ID.3 and the Model 3. However, the presence of a second level creates a coupling between underbody height ($s_{\mathrm{ub,z}}$, Figure 3.13) and H30-2: if taller cells are installed in the underbody, H30-2 must also be raised to fit the cells into the second level. This leads to a further increase in vehicle height and consumption. For these reasons, a second level is simple to integrate into large SUVs due to their high H30-2 and H100, but becomes problematic for sedans and hatchbacks.

The highfloor principle with cylindrical cells generally has a lower consumption than a highfloor principle with pouch cells. Furthermore, if the difference in production costs between the pouch and cylindrical cells is neglected, the battery energy savings generated by the cylindrical highfloor principle are directly associated with lower costs. According to the estimation of König et al. [21], production cost savings between 100€ to 200€ are obtainable for each saved $\mathrm{kW\,h}$ by 2025.

This C2B principle can integrate up to $19\,\mathrm{kW\,h}$ more energy than a comparable highfloor principle without impacting the vehicle mass, its external dimensions, and its consumption (Section 5.2). This renders the C2B strategy the most promising integration principle for future BEVs. The optimization performed in Subsection 5.3.2 further highlights the potential of the C2B principle: for all three reference vehicles, this principle yields the highest ranges and the lowest battery energies.

In conclusion, a highfloor strategy coupled with pouch or cylindrical cells allows ranges of at least $800\,\mathrm{km}$ by 2025. In the case of large SUVs, it is advisable to extend the highfloor battery with a second level to compensate for the higher vehicle consumption. When a C2B strategy is applied, the same ranges can be obtained with lower battery energies. These results confirm that BEVs will be competitive with ICEVs in terms of range by 2025, regardless of the vehicle segment.

5.4.2 Impact of External Dimensions and Interior Concept

Section 5.1 quantified the influence of the external dimensions on a reference ID.3. On average (regardless of cell type), the increase in mass caused by larger external dimensions is $0.5\,\mathrm{kg\,mm^{-1}}$ for L101, $1.1\,\mathrm{kg\,mm^{-1}}$ for W103, and $5.5\,\mathrm{kg\,mm^{-1}}$ for H100. These values are for the case that the external dimension increase is used to install more cells. H100 has the highest mass increase since a greater amount of battery energy can be installed with additional space along the z-direction compared to an equal adjustment of W103 and L101.

During vehicle optimization, the NSGA II raises H100 to install taller cells in the vehicle, thus reaching higher ranges. On the one hand, a larger H100 increases the vehicle frontal area, its mass, and ultimately its consumption. On the other hand, taller cells can be installed and the resulting increase in energy compensates for the higher consumption.

The NSGA II also uses L101 as a design variable because it has a minor effect on the vehicle's mass and consumption. There is however a case, where L101 is an unsuitable design variable to

increase range. The reference vehicles were simulated with a constant ground clearance at the underbody $d_{\mathrm{clear,ub,z}}$ (for ID.3 and Model 3, the requirements were similar to the Korea standard, while the Audi e-tron was simulated with the LDT class described in Table 3.3). However, if the ground clearance at the underbody is influenced by the ramp angle (similar to the example shown in Figure 3.6), an increase in L101 would require a higher $d_{\mathrm{clear,ub,z}}$ (and consequently a decrease in battery height) to maintain the same ramp angle. In conclusion, in cases where the manufacturer wants to offer a particularly high ramp angle, L101 is not suitable to increase the battery energy.

On the contrary, W103 is rarely changed by the NSGA II. The optimizer tries to keep the W103 as small as possible and increases it only when it is not possible to use any other design variable. The reason for this trend is that increasing W103 yields a higher battery energy improvement than L101, but also has a higher impact on the vehicle mass. The higher resulting masses may require resizing the tires, which in turn decreases the available battery space along the y-direction. In many cases, the increase in battery width achieved by a wider W103 is canceled out by the increase in tire width. This effect, combined with the fact that W103 also impacts the frontal area and drag losses of the vehicle, renders W103 an unsuitable design variable to increase range.

Reducing W103 appears to be an efficient way to improve range. The vehicle architecture tool ensures that within the given W103 ranges, the electric machine remains installable. However, it must also be considered that apart from the package of machines and gearboxes, the passenger's comfort also plays a major role when defining the W103.

The NSGA II also adjusts the seating height of both rows of seats (H30-1 and H30-2) to increase battery energy. By lowering the seating position of the passengers, it is possible to reduce the effective height of the passenger compartment and to install taller cells, while keeping the frontal area and H100 unchanged. The same effect could also be obtained by reducing the passenger headroom or vehicle ground clearance. On the one hand, a reduction of headroom negatively affects the passengers' comfort and should therefore be avoided. On the other hand, ground clearance requirements (such as LDT and M1G) are an important selling point for SUVs. A solution to this problem is to equip large SUVs with air springs at the front and rear axle. In this way, the ground clearance can be actively adjusted depending on vehicle speed. For example, the Audi e-tron is equipped with air springs that yield a height range adjustment of $76\,\mathrm{mm}$ [237].

The optimization also highlights how large external dimensions are not always suitable for the range. This is exemplarily shown by the Audi e-tron that has larger reference external dimensions and a larger footprint than the Tesla Model 3. Furthermore, the e-tron is equipped with a second level of cells that yield a higher installed energy than the Model 3 but not higher ranges. The causes for the lower ranges are the large external dimensions of the e-tron (which lead to a large frontal area), its high drag coefficient (Table F.6), and its high mass. The combination of these effects yields a higher consumption and lower ranges in comparison to the Tesla Model 3.

In conclusion, it appears that L101 is an efficient design variable to increase range. Future BEVs should therefore have different proportions than ICEVs with comparable external dimensions: they should be equipped with larger wheelbases, shorter overhangs, low ground clearance, and low ramp angles. Furthermore, an increase in L101 can also be used to increase the passenger compartment length and the legroom for the passengers. H100 is the most powerful design variable to increase range, however, a reduction of the seating height yields the same effect without affecting the vehicle height and is, if possible, to be preferred. Finally, W103 should be kept as small as possible while considering the comfort requirements for the passengers.

5.4.3 Impact of Components

Regarding cell type, current pouch cells are $30\,\mathrm{mm}$ taller than current cylindrical cells and can therefore install a greater amount of energy in the same battery footprint. For example, for a battery footprint similar to the ID.3, the energy difference between pouch and 21700 cylindrical cells is $24.9\,\mathrm{kW\,h}$ (Figure 5.1). For every additional mm along the z-direction, the battery energy increases by $990\,\mathrm{W\,h\,mm^{-1}}$ for pouch and by $1080\,\mathrm{W\,h\,mm^{-1}}$ for cylindrical cells. An equal adjustment along the x-direction yields an increase of $40\,\mathrm{W\,h\,mm^{-1}}$ for cylindrical and $60\,\mathrm{W\,h\,mm^{-1}}$ for pouch cells. Finally, along the y-direction, the gain for cylindrical and pouch cells is $47\,\mathrm{W\,h\,mm^{-1}}$ and $76\,\mathrm{W\,h\,mm^{-1}}$ respectively. These results highlight the predominant impact of the z-direction on battery energy.

The tires have a great impact on the achievable range due to their geometrical interdependency with the battery (Figure 3.11 and 3.12). Due to a higher mass with respect to ICEVs, BEVs are equipped with extra load tires (Table F.4 - F.6). This strategy reduces the tire dimensions but also increases their costs. Another efficient way to decrease the tire dimensions is to reduce the rim diameter. By decreasing the rim diameter (for example from $20''$ to $19''$), it is possible to fit thinner tires while keeping a similar (or identical) outer tire diameter. This adjustment decreases the wheel arch width, which increases the available battery width: for example, with a tire width reduction from $235\,\mathrm{mm}$ to $225\,\mathrm{mm}$, the battery width could be increased (provided that an acceptable level of safety in case of a crash is ensured) by approx. $20\,\mathrm{mm}$. As already discussed at the beginning of this section, each additional mm along the y-direction yields an energy gain comprised between $47\,\mathrm{W\,h}$ and $76\,\mathrm{W\,h}$. However, from a design point of view, bigger rim diameters are more appealing. In conclusion, when choosing the tire and rim size, a compromise between small tire sizes and design has to be found.

The electric machines impact the battery footprint and constrain the available battery length. However, in the optimization step, the NSGA II mostly opts for two (instead of one) machines since the decrease of the battery length is compensated by the lower consumption of the AWD topology. Regarding the machine topology (Figure B.1), it would be ideal to position the machines "outside from the wheelbase" so that they take up as little space as possible from the battery. However, other requirements have to be taken into account when considering the machine position. For example, for the Tesla Model 3 and Model Y, the front machine is positioned behind the axle (Figure B.1a) to increase the available space at the front overhang and to install a large front trunk. The front trunk is a feature that appears in most current BEVs and may become an important selling point in the future. Regarding the rear machine topology, a positioning behind the axle (Figure B.1a) would yield additional space for the battery but also impact the available trunk height. During the optimization process, the machine topology was not changed, so that the resulting vehicles still ensure the same spaces for the front and rear trunks as the reference vehicles.

6 Discussion and Outlook

This chapter questions the methodological procedure and results, and provides an outlook for future research. First, the tool's limitations are presented. Second, the validity of the results is discussed.

The architecture tool is developed for the vehicle concept design and must therefore rely on a limited set of inputs. This requirement is only achievable with empirical models. The disadvantage of data aging, which is one of the main weaknesses of empirical models, is solved by an updatable database. With this implementation, the tool yields reliable results already at the start of the vehicle concept design. However, in further development steps, the architectures calculated by the tool need to be detailed with more sophisticated physical and semi-physical models.

One weakness of the tool are the maps contained in the efficiency map database and calculated with the tool of Kalt [238, 239]. As noted in Section 4.1, these maps can be unreliable, especially when modeling new BEVs. One solution to this problem is to integrate commercial efficiency map tools, such as Motor XP [216], into the vehicle architecture tool. Another possibility is to develop a machine loss model from scratch. However, such a model needs to be verified, and currently, there are, to the author's knowledge, no open-source machine efficiency maps that could be used for verification. There is also room for improvement for the electric machine volumetric model. This component is modeled empirically following the approach of Felgenhauer [39, p. cxxviii]. The machine sizing applies an empirical relationship between maximum power and stator volume (Equation (D.6)). Automotive manufacturers do not usually publish the maximum power of their machines, which complicates the creation of a machine database. For this reason, reliable machine data could only be collected for a limited number of machines. Future work should consider detailing the volumetric machine model.

The volumetric model of the gearbox was validated with a set of existing gearboxes that cover a transmission ratio range of 6–12 and a maximum torque range of $50\,\mathrm{N\,m}$–$600\,\mathrm{N\,m}$. Currently, the existing BEV gearboxes are within these ranges. However, future technology leaps, such as high rotational speed machines [240], may lead to different transmission ratios and require an adaptation of the model.

Regarding the interior concept model, the tool only considers conventional seat layouts, i.e. configurations where all passengers face towards the driving direction. Over the next years, especially due to the growing interest towards autonomous driving, new interior and seat layout concepts will gain importance [35]. An extension of the current tool to also consider innovative seat layouts is currently being carried out by König [35]. König will also model and consider the influence of trunk spaces on the vehicle architecture.

Regarding the battery model, the results in Subsection 5.3.2 show that, for future scenarios, a simple rectangular shape with highfloor principle yields ranges above $800\,\mathrm{km}$. A shift towards rectangular batteries (like the VW ID.3, Figure B.3c) will likely be observable in future years. This

shift would lead to a reduction of existing battery shapes and integration principles, allowing for a deeper dive into modeling a rectangular shape.

One of the main requirements for the vehicle architecture tool was to allow an automatic update of the implemented models. This requirement is fulfilled by coupling the tool with a database (Section 3.2). For the method to work, the database has to be kept up-to-date by gradually adding new component and vehicle data and filtering out older data.

After presenting the limitations of the vehicle architecture tool, the following paragraphs briefly discuss the parametric studies presented in Chapter 5. First of all, the results obtained from the parametric studies are valid for vehicles that are similar to the simulated reference vehicles. An extrapolation of the results to different segments is not possible and, if it is desired, requires a new simulation with the tool. The parametric studies in Chapter 5 predict the range improvement achievable by 2025 with different electrification strategies. The hereby generated secondary volumetric effects (for example on the battery dimensions) and the secondary mass effects (on the components and vehicle mass) are considered. Without modeling secondary effects, it would not be possible to predict the impact of electrification strategies on external dimensions, mass, consumption, and range.

The package factors used for the parametric studies are (with the only exception of the C2B integration principle) taken from current BEVs. The reason for this choice is that the package factors have high variability, which hinders an estimation of their improvement in the next years. A similar problem occurs for the electric machines: the tool models the machine losses with efficiency maps of current BEVs. However, an improvement in both package factors and machine efficiency is to be expected and will further increase the ranges predicted in Chapter 5.

During the optimization in Section 5.3, c_d is kept constant. There are empirical approaches that correlate c_d with the external dimensions of the vehicle [241]. However, c_d is not exclusively influenced by the external dimensions: for example, the c_d of the Audi e-tron is improved from 0.28 to 0.27 by substituting the conventional rearview mirrors with virtual rearview mirrors [242]. For the VW ID.3, the c_d varies in a range of 0.002 depending on the mounted rim design and size [231]. Finally, the external dimensions are not necessarily significant when it comes to c_d: in 2012, the truck manufacturer MAN developed a truck concept with optimized aerodynamics, thus obtaining a c_d of 0.3 [243]. In conclusion, for precise modeling of the drag coefficient, detailed knowledge of the optional extras (which is not available during the early development phase) as well as computational fluid dynamic models are required. An extension of the model with a computational fluid dynamic simulation is not purposeful, since it highly increases computation time.

A further remark is required for the C2B principle. The assumptions used to model this principle are based on the limited information available at the moment. In future works, as new insights are available, modeling the C2B principle should be further detailed, and the simulations presented in Subsection 5.3.2 repeated.

Finally, the optimization results shown in Subsection 5.3.1 are only valid for the selected reference vehicles and design variable ranges. The design variables and their ranges are chosen considering the tool limitations. The simulations are repeated multiple times with different numbers of generations and population sizes. A convergence of the pareto fronts is ensured with a generation number of 30 and a population size of 300. However, the NSGA II is sensitive to the selected optimization parameters: adding new design variables or changing their ranges may impact the shape and position of the pareto fronts and lead to different results.

7 Summary

Chapter 1 presented the motivation for the development of a vehicle architecture tool. The shift towards BEVs requires new components, such as the traction battery, which in turn cause secondary effects. The current development process is not capable of estimating the secondary effects that occur during the early development phase. The lack of knowledge on secondary effects gives rise to the probability of estimation errors during vehicle sizing. These errors may in turn render the vehicle package infeasible or result in a range below the desired value.

In Chapter 2, the four architectural features were presented. A literature review revealed that existing methods focus on one or two architectural features while neglecting the others. Furthermore, none of the methods fully consider secondary effects. Consequently, there is no methodology capable of supporting the early development phase of BEVs, while considering secondary volume and mass effects. To solve this problem, a novel vehicle architecture tool had to be developed. The chapter closed by identifying the requirements that such a tool should have.

Based on the requirements derived in Chapter 2, Chapter 3 outlined a vehicle architecture tool for BEV sizing. The tool inputs were identified through extensive literature research. For machine sizing and to estimate vehicle consumption, an LDS was implemented. For modeling the component volumes and the available installation spaces, a set of dimensional chains, semi-physical models, and empirical models was derived. Empirical models were also employed to estimate the mass of the vehicle modules and ultimately the total vehicle mass. The empirical data that was gathered during the development of the tool is stored in an SQL database. The database can be extended with new empirical data and enables an automatic update of the empirical models used in the tool. Finally, to consider the secondary volume and mass effects, the tool is nested in an iterative loop.

Chapter 4 validated the functionality of the tool by comparing the generated results with the consumption, component volumes, and component masses of existing vehicles. In such cases where the tool could not model the components or masses correctly, the reason for these deviations was identified and discussed. The validation step identified and solved the tool's weak points.

Following the validation, the tool was applied to estimate the potential of BEVs in 2025 (Chapter 5). Several cell types and integration strategies were simulated on vehicles belonging to different segments. Interdependencies between vehicle dimensions, mass, and attainable range were identified and discussed. Finally, optimization was conducted to identify the maximum range potential for different cell types and integration principles.

Finally, Chapter 6 discussed the limitations of the tool and provided an outlook for future research.

List of Figures

List of Tables

Bibliography

[1] European Commission, Secretariat-General. „*The Road from Paris: assessing the implications of the Paris Agreement and accompanying the proposal for a Council decision on the signing, on behalf of the European Union, of the Paris agreement adopted under the United Nations Framework Convention on Climate Change: COM/2016/0110*," 2016. Available: https://eur-lex.europa.eu/legal-content/EN/ALL/?uri=CELEX:52016DC0110 [visited on 05/25/2021].

[2] European Commission. „*International climate policy post-Copenhagen: Acting now to reinvigorate global action on climate change: COM(2010) 86*," 2010. Available: https://eur-lex.europa.eu/legal-content/EN/TXT/?uri=CELEX%3A52010DC0086 [visited on 01/05/2021].

[3] L. Nicoletti et al., „Review of Trends and Potentials in the Vehicle Concept Development Process," in *15th International Conference on Ecological Vehicles and Renewable Energies*, Monaco, 2020, pp. 1–15, DOI: 10.1109/EVER48776.2020.9243115.

[4] European Parliament, Council of the European Union. „*Setting CO2 emission performance standards for new passenger cars and for new light commercial vehicles, and repealing Regulations (EC) No 443/2009 and (EU) No 510/2011: EC 2019/631*," 2019. Available: https://eur-lex.europa.eu/legal-content/EN/TXT/?uri=CELEX%3A32019R0631 [visited on 06/13/2020].

[5] ICCT, „CO2 emission standards for passenger cars and light-commercial vehicles in the European Union," 2019. Available: https://theicct.org/publications/ldv-co2-stds-eu-2030-update-jan2019 [visited on 02/12/2020].

[6] L. Nicoletti et al., „Topology analysis of electric vehicles, with a focus on the traction battery," *Forschung im Ingenieurwesen*, vol. 85, no. 2, pp. 457–467, 2020, DOI: 10.1007/s10010-020-00422-1.

[7] A. Achleitner et al., „Formen und neue Konzepte," in *Vieweg Handbuch Kraftfahrzeugtechnik*, S. Pischinger and U. Seiffert, ed. Wiesbaden: Springer Fachmedien Wiesbaden, 2016, pp. 131–251, ISBN: 978-3-658-09527-7.

[8] C. Hongyang and H. Hui, „China announced 2020–2022 subsidies for new energy vehicles," The international council of clean transportation, 2020. Available: https://theicct.org/publications/china-2020-22-subsidies-new-energy-vehicles-jul2020 [visited on 01/23/2021].

[9] Y. Sun et al., „China wants new energy vehicle sales in 2025 to be 25% of all car sales," *Reuters Media*, 2019. Available: https://www.reuters.com/article/us-china-autos-electric/china-wants-new-energy-vehicle-sales-in-2025-to-be-25-of-all-car-sales-idUSKBN1Y70BN [visited on 01/05/2021].

[10] Y. Sun et al., „China to cut new energy vehicle subsidies by 10% this year," *Reuters Media*, 2020. Available: https://www.reuters.com/article/us-china-autos-electric-subsidies/china-to-cut-new-energy-vehicle-subsidies-by-10-this-year-idUSKCN225177 [visited on 01/05/2021].

[11] L. Nicoletti, W. Schmid and M. Lienkamp, „Databased Architecture Modeling for Battery Electric Vehicles," in *15th International Conference on Ecological Vehicles and Renewable Energies*, Monaco, 2020, pp. 1–9, DOI: 10.1109/EVER48776.2020.9242995.

[12] G. Scherelis and M. Langendorf. „*Volkswagen Konzern auf Kurs zur Senkung der CO2-Emissionen*," Wolfsburg, 2019. Available: https://www.volkswagen-newsroom.com/de/pressemitteilungen/volkswagen-konzern-auf-kurs-zur-senkung-der-co2-emissionen-5454 [visited on 01/04/2021].

[13] Groupe PSA. „Electric vehicles, Plug-In Hybrid : Groupe PSA Technologies," 2020. [Online]. Available: https://www.groupe-psa.com/en/automotive-group/innovation/groupe-psa-lelectrification-en-marche/ [visited on 12/21/2020].

[14] Tesla Investor Relations. „*Tesla Q4 2020 Vehicle Production & Deliveries | Tesla Investor Relations*," Palo Alto, 2021. Available: https://ir.tesla.com/press-release/tesla-q4-2020-vehicle-production-deliveries [visited on 01/05/2021].

[15] H. Löbberding et al., „From Cell to Battery System in BEVs: Analysis of System Packing Efficiency and Cell Types," *World Electric Vehicle Journal*, vol. 11, no. 4, p. 77, 2020, DOI: 10.3390/wevj11040077.

[16] Statista. „Argumente gegen den Kauf von Elektrofahrzeugen in Deutschland 2018 | Statista," 2021. [Online]. Available: https://de.statista.com/prognosen/856966/umfrage-in-deutschland-zu-argumenten-gegen-den-kauf-von-elektrofahrzeugen [visited on 01/05/2021].

[17] Duden. „Reichweitenangst," 2021. [Online]. Available: https://www.duden.de/rechtschreibung/Reichweitenangst [visited on 01/04/2021].

[18] P. L. Peters, R. Demuth and D. Schramm, „Ableitung von objektivierten Auslegungsprämissen zukünftiger Fahrzeugkonzepte auf der Basis von Prognosen zum Mobilitätsverhalten in Deutschland im Jahr 2035," in *Mobilität in Zeiten der Veränderung*, H. Proff, ed. Wiesbaden: Springer Fachmedien Wiesbaden, 2019, pp. 157–179, ISBN: 978-3-658-26106-1.

[19] T. Mersch, „Mobilitätsforschung: „Wir wissen nicht, ob die Lithium-Ionen-Batterien nicht doch ein Problem haben"," *Handelsblatt*, 2020. Available: https://www.handelsblatt.com/unternehmen/flottenmanagement/mobilitaetsforschung-wir-wissen-nicht-ob-die-lithium-ionen-batterien-nicht-doch-ein-problem-haben/26706132.html?ticket=ST-17234438-FDfWpLb4tbrWtb6ETnXS-ap4 [visited on 12/23/2020].

[20] W. Bernhart et al., „E-mobility Index 2018: Roland Berger – Automotive Competence Center & Forschungsgesellschaft Kraftfahrwesen mbH Aachen," Roland Berger, 2018. Available: https://www.rolandberger.com/de/Insights/Publications/E-mobility-Automakers-in-need-of-battery-strategy.html [visited on 01/02/2021].

[21] A. König et al., „An Overview of Parameter and Cost for Battery Electric Vehicles," *World Electric Vehicle Journal*, vol. 12, no. 1, p. 21, 2021, DOI: 10.3390/wevj12010021.

[22] B. Frieske et al., „Strukturstudie BWe mobil 2019: Transformation durch Elektromobilität und Perspektiven der Digitalisierung," 2019. Available: https://www.e-mobilbw.de/service/meldungen-detail/strukturstudie-bwe-mobil-2019 [visited on 10/26/2020].

[23] H. Naunheimer et al., *Fahrzeuggetriebe: Grundlagen, Auswahl, Auslegung und Konstruktion*, 3rd Edition, Springer, 2019, ISBN: 978-3-662-58883-3.

[24] M. Hilgers, *Dieselmotor*, Wiesbaden, Springer Fachmedien Wiesbaden GmbH, 2017, ISBN: 978-3-658-14641-2.

[25] O. A. Hjelkrem et al., „Estimation of tank-to-wheel efficiency functions based on type approval data," *Applied Energy*, vol. 276, p. 115463, 2020, DOI: 10.1016/j.apenergy.2020.115463.

[26] L. Nicoletti et al., „Design Parameters for the Early Development Phase of Battery Electric Vehicles," *World Electric Vehicle Journal*, vol. 11, no. 3, p. 47, 2020, DOI: 10.3390/wevj11030047.

[27] L. Nicoletti et al., „Parametric Modeling of Weight and Volume Effects on Battery Electric Vehicles, with Focus on the Gearbox," in *Proceedings of the Design Society*, Gothenburg, Sweden, 2021, pp. 2389–2398, DOI: 10.1017/pds.2021.500.

[28] L. Nicoletti et al., „An Estimation of the Lightweight Potential of Battery Electric Vehicles," *Energies*, vol. 14, no. 15, p. 4655, 2021, DOI: 10.3390/en14154655.

[29] A. König, *Methodik zur Auslegung von autonomen Fahrzeugkonzepten*, in review, Ph.D. Thesis, Institute of Automotive Technology, Technical University of Munich, Munich, 2022.

[30] A. Koch, *Energieeffizientes Fahren und Antriebskonzept-Optimierung elektrischer Fahrzeuge*, in review, Ph.D. Thesis, Institute of Automotive Technology, Technical University of Munich, Munich, 2022.

[31] F. Schockenhoff, *Fahrzeugkonzeptentwicklung für autonome, geteilte und elektrische Mobilität*, in review, Ph.D. Thesis, Institute of Automotive Technology, Technical University of Munich, Munich, 2022.

[32] SAE J3016 Taxonomy and Definitions for Terms Related to Driving Automation Systems for On-Road Motor Vehicles, 2021.

[33] F. Schockenhoff et al. „*Workshop: Group vehicle concepts*," Garching, Munich, 2021.

[34] A. König et al., „Concept Design Optimization of Autonomous and Electric Vehicles," in *8th International Conference on Power Science and Engineering*, Dublin, Ireland, 2019, pp. 44–49, DOI: 10.1109/ICPSE49633.2019.9041175.

[35] A. König et al., „Package Planning of Autonomous Vehicle Concepts," in *Proceedings of the Design Society*, Gothenburg, Sweden, 2021, pp. 2369–2378, DOI: 10.1017/pds.2021.498.

[36] A. König et al., „The Impact of HVAC on the Development of Autonomous and Electric Vehicle Concepts," *Energies*, vol. 15, no. 2, p. 441, 2022, DOI: 10.3390/en15020441.

[37] A. Koch et al., „Eco-Driving for Different Electric Powertrain Topologies Considering Motor Efficiency," *World Electric Vehicle Journal*, vol. 12, no. 1, 2021, DOI: 10.3390/wevj12010006.

[38] A. Koch et al., „Eco-Driving Algorithm for Electric Powertrains using Detailed Loss Models," *in review process, Journal of eTransportation*, 2022.

[39] M. Felgenhauer, *Automated Development of Modular Systems for the Vehicle Front of Passenger Cars*, Ph.D. Thesis, Institute of Automotive Technology, Technical University of Munich, Munich, 2019.

[40] M. Lienkamp. „*Fahrzeugkonzepte: Entwicklung und Simulation*," Technical University of Munich, Munich, Lecture notes, Winter term 2021.

[41] S. Matz, *Nutzorientierte Fahrzeugkonzeptoptimierung in einer multimodalen Verkehrsumgebung*, Ph.D. Thesis, Institute of Automotive Technology, Technical University of Munich, Munich, Verlag Dr. Hut, 2015, ISBN: 978-3-8439-2140-4.

[42] E. Wiedemann, *Ableitung von Elektrofahrzeugkonzepten aus Eigenschaftszielen*, Ph.D. Thesis, Institute of Automotive Technology, Technical University of Munich, Munich, Cuvillier Verlag, 2014, ISBN: 978-3-95404-789-5.

[43] H.-H. Braess et al., „Produktentstehungsprozess," in *Vieweg Handbuch Kraftfahrzeugtechnik*, S. Pischinger and U. Seiffert, ed. Wiesbaden: Springer Fachmedien Wiesbaden, 2016, pp. 1257–1369, ISBN: 978-3-658-09527-7.

[44] J. Fuchs, *Analyse der Wechselwirkungen und Entwicklungspotentiale in der Auslegung elektrifizierter Fahrzeugkonzepte*, Ph.D. Thesis, Institute of Automotive Technology, Technical University of Munich, Munich, Cuvillier Verlag, 2014, ISBN: 978-3-95404-874-8.

[45] J. Hahn, *Eigenschaftsbasierte Fahrzeugkonzeption: Eine Methodik in der frühen Konzeptphase*, Ph.D. Thesis, Otto-von-Guericke University, Magdeburg, Springer, 2017, ISBN: 978-3-658-20100-5.

[46] U. Lindemann, *Methodische Entwicklung technischer Produkte*, Berlin, Springer, 2009, ISBN: 978-3-642-01422-2.

[47] K. Kuchenbuch, *Methodik zur Identifikation und zum Entwurf packageoptimierter Elektrofahrzeuge*, Ph.D. Thesis, Technical University Carolo-Wilhelmina, Braunschweig, Logos Verlag Berlin, 2012, ISBN: 978-3-8325-3262-8.

[48] P. Rossbacher and M. Hirz, „Flexible parameterization strategies in automotive 3D vehicle layout," *Computer-Aided Design and Applications*, vol. 14, no. 5, pp. 549–562, 2017, DOI: 10.1080/16864360.2016.1273575.

[49] M. Ried et al., „Parametrische Geometriemodelle für die Konzeptgestaltung elektrifizierter Fahrzeuge," in *Schritte in die künftige Mobilität*, H. Proff et al., ed. Wiesbaden: Springer Fachmedien Wiesbaden, 2013, pp. 19–33, ISBN: 978-3-8349-4307-1.

[50] A. Müller, *Systematische und nutzerzentrierte Generierung des Pkw-Maßkonzepts als Grundlage des Interior- und Exteriordesign*, Ph.D. Thesis, Institute for Engineering Design and Industrial Design, University of Stuttgart, Stuttgart, 2010, ISBN: 978-3-922823-77-3.

[51] SAE J1100 Motor Vehicle Dimensions, 2019.

[52] European Parliament, Council of the European Union. „*DIRECTIVE 2007/46/EC OF THE EUROPEAN PARLIAMENT AND OF THE COUNCIL of 5 September 2007 establishing a framework for the approval of motor vehicles and their trailers, and of systems, components and separate technical units intended for such vehicles: 2007/46/EC*," 2007. Available: http://data.europa.eu/eli/dir/2007/46/oj [visited on 08/18/2021].

[53] 49 CFR 523.5 - Light truck. Regulatory Information 1998.

[54] 40 CFR 600.315-08 - Classes of comparable automobiles, Regulatory Information 2008.

[55] European Parliament, Council of the European Union. „*Commission Regulation (EU) No 1230/2012 of 12 December 2012: implementing Regulation (EC) No 661/2009 of the European Parliament and of the Council with regard to type-approval requirements for masses and dimensions of motor vehicles and their trailers and amending Directive 2007/46/EC of the European Parliament and of the CouncilText with EEA relevance*," 2012. Available: http://data.europa.eu/eli/reg/2012/1230/oj [visited on 05/19/2020].

[56] ISO 3833: Road Vehicles - Types - Terms and Definitions Second Edition, 1977.

[57] R. E. Grünen, F. Günzkofer and H. Bubb, „Anatomische und anthropometrische Eigenschaften des Fahrers," in *Automobilergonomie*. vol. 1, H. Bubb et al., ed. Wiesbaden: Springer Fachmedien Wiesbaden, 2015, pp. 163–219, ISBN: 978-3-8348-1890-4.

[58] L. Nicoletti et al., „Derivation of Geometrical Interdependencies between the Passenger Compartment and the Traction Battery Using Dimensional Chains," *World Electric Vehicle Journal*, vol. 11, no. 2, p. 39, 2020, DOI: 10.3390/wevj11020039.

[59] SAE J4002 - H-Point Machine (HPM-II) Specifications and Procedure for H-Point Determination - Auditing Vehicle Seats, 2010.

[60] SAE J826 - Devices for Use in Defining and Measuring Vehicle Seating Accommodation, 2015.

[61] SAE J1516 Accommodation Tool Reference Point for Class B Vehicles, 2011.

[62] SAE J1517 Driver Selected Seat Position for Class B Vehicles - Seat Track Length and SgRP, 2011.

[63] SAE J4004 Positioning the H-Point Design Tool - Seating Reference Point and Seat Track Length, 2008.

[64] SAE J1052 - Motor Vehicle Driver and Passenger Head Position, 2010.

[65] W. Remlinger, *Analyse von Sichteinschränkungen im Fahrzeug*, Ph.D. Thesis, Chair of Ergonomics, Technical University of Munich, Munich, Cuvillier Verlag, 2013, ISBN: 978-3-7369-4417-6.

[66] SAE J941 - Motor Vehicle Drivers' Eye Locations, 2010.

[67] Economic Commission for Europe of the United Nations. „*Uniform provisions concerning the approval of motor vehicles with regard to the forward field of vision of the motor vehicle driver: ECE R125*," 2010. Available: http://data.europa.eu/eli/reg/2010/125(2)/oj.

[68] T. Tzivanopoulos, „Methodik zur technischen Detaillierung variantenreicher Fahrzeugkonzepte in der frühen Phase," Thesis, Technical University of Graz, Graz, 2012.

[69] F. Schockenhoff et al., „Customer-Oriented Concept Assessment," in *Researchgate* 2020. Available: https://www.researchgate.net/publication/345242497 [visited on 12/13/2020].

[70] L. Nicoletti, F. Schockenhoff and M. Bayerlein. „COCA Tool - Customer-Oriented Concept Assessment Tool," 2021. [Online]. Available: https://github.com/TUMFTM/Customer-Oriented-Concept-Assessment-COCA-Tool [visited on 12/02/2021].

[71] E. Elagamy, „Creation of a Parametric Model for the Derivation of the Conceptual Dimensions for Battery Electric Vehicles," Master thesis, Institute for Automotive Engineering, RWTH Aachen University, Aachen, 2020.

[72] ISO 3832: Passenger cars - Luggage compartments - Method of measuring reference volume, 2002.

[73] H. Wallentowitz and A. Freialdenhoven, *Strategien zur Elektrifizierung des Antriebsstranges*, 2nd Edition, Wiesbaden, Vieweg+Teubner Verlag, 2011, ISBN: 978-3-8348-1412-8.

[74] M. Felgenhauer and M. Lienkamp, „Automated Generation of Vehicle Architectures and Derivation of Modular Systems within the Vehicle Front," in *Proceedings of NordDesign*, Linköping, Sweden, 2018, ISBN: 978-91-7685-185-2.

[75] C. Angerer, *Antriebskonzept-Optimierung für batterieelektrische Allradfahrzeuge*, Ph.D. Thesis, Institute of Automotive Technology, Technical University of Munich, Munich, Verlag Dr. Hut, 2020, ISBN: 978-3-8439-4388-8.

[76] A. Perner and J. Vetter, „Lithium-ion batteries for hybrid electric vehicles and battery electric vehicles," in *Advances in battery technologies for electric vehicles*. vol. 80, B. Scrosati, J. Garche and W. Tillmetz, ed. Cambridge, UK: Woodhead Publishing an imprint of Elsevier, 2015, pp. 173–190, ISBN: 978-1-78242-377-5.

[77] A. Kampker, D. Vallée and A. Schnettler, *Elektromobilität*, Berlin, Springer, 2018, ISBN: 978-3-662-53136-5.

[78] F. Chang, *Improving the Partial Load Efficiency of Electric Powertrains by Silicon MOSFET Multilevel Inverters*, Ph.D. Thesis, Institute of Automotive Technology, Technical University of Munich, Munich, 2020.

[79] I. Busche, *Ein Beitrag zur optimierten Konzeptauslegung von Fahrzeugen im Bereich der Elektromobilität*, Ph.D. Thesis, Otto-von-Guericke University, Magdeburg, 2014, ISBN: 978-3-941016-08-8.

[80] A. Karle, *Elektromobilität: Grundlagen und Praxis*, 3rd Edition, München, Fachbuchverlag Leipzig im Carl Hanser Verlag, 2018, ISBN: 978-3-446-45668-6.

[81] H. Jelden et al., „The Electric Powertrain Matrix from Volkswagen," *MTZ worldwide*, vol. 75, no. 2, pp. 4–9, 2014, DOI: 10.1007/s38313-014-0015-1.

[82] S. Fuchss et al., „The Propulsion System of the New Jaguar I-Pace," *MTZ worldwide*, vol. 80, no. 1, pp. 18–25, 2019, DOI: 10.1007/s38313-018-0123-4.

[83] J. Doerr et al., „The new full electric drivetrain of the Audi e-tron," in *Der Antrieb von morgen 2019*, 2019, pp. 13–37, DOI: 10.1007/978-3-658-26056-9_2.

[84] B. Frieske, M. Kloetzke and F. Mauser, „Trends in vehicle concept and key technology development for hybrid and battery electric vehicles," in *World Electric Vehicle Symposium and Exhibition (EVS27)*, Barcelona, Spain, 2013, pp. 1–12, DOI: 10.1109/EVS.2013.6914783.

[85] J. Doerr et al., „The Electric Drivetrain with Three-motor Layout of the Audi E-tron S," *MTZ worldwide*, vol. 81, no. 7-8, pp. 16–25, 2020, DOI: 10.1007/s38313-020-0254-2.

[86] R. Kasper and M. Schünemann, „5. Elektrische Fahrantriebe Topologien Und Wirkungsgrad," *MTZ - Motortechnische Zeitschrift*, vol. 73, no. 10, pp. 802–807, 2012, DOI: 10.1007/s35146-012-0484-1.

[87] B. Gombert, „X-by-wire im Automobil: Von der Electronic Wedge Brake zum e Corner," in *Chassis-tech 2007*, Munich, 2007.

[88] B. Gombert, R. Fischer and W. Heinrich, „Wheel-hub motors," *ATZelektronik worldwide*, vol. 5, no. 1, pp. 4–10, 2010, DOI: 10.1007/bf03242249.

[89] M. Sato et al., „Development of Wireless In-Wheel Motor Using Magnetic Resonance Coupling," *IEEE Transactions on Power Electronics*, vol. 31, no. 7, pp. 5270–5278, 2016, DOI: 10.1109/TPEL.2015.2481182.

[90] H. Fujimoto et al., „Development of Wireless In-wheel Motors for Dynamic Charging: From 2nd to 3rd generation," in *IEEE PELS Workshop on Emerging Technologies: Wireless Power Transfer*, Seoul, Korea, 2020, pp. 56–61, DOI: 10.1109/WoW47795.2020.9291287.

[91] M. Kraus, C. Harkort and B. Wuebbolt-Gorbatenko, „A solution for future urban mobility: the Schaeffler mover – the fusion of chassis and drive," in *10th International Munich Chassis Symposium*, P. Pfeffer, ed. Wiesbaden: Springer Fachmedien Wiesbaden, 2020, pp. 47–55, DOI: 10.1007/978-3-658-26435-2_8.

[92] J. Warner, „Lithium-Ion Battery Packs for EVs," in *Lithium-ion batteries: Advances and applications*, G. Pistoia, ed. Amsterdam: Elsevier, 2014, pp. 127–150, ISBN: 978-0-444-59513-3.

[93] B. Erler and C. Zorn, „Karosseriestruktur des Volkswagen e-up!," in *Karosseriebautage Hamburg: 13. ATZ-Fachtagung*, G. Tecklenburg, ed. Wiesbaden: Springer Fachmedien Wiesbaden GmbH, 2014, pp. 35–41, DOI: 10.1007/978-3-658-05980-4_5.

[94] M. Reichenecker and B. Schweizer, „Porsche Taycan - recuperative brake system for combined braking," in *11th International Munich Chassis Symposium*, P. Pfeffer, ed. Berlin: Springer, 2021, pp. 59–72, DOI: 10.1007/978-3-662-63193-5_5.

[95] Audi MediaCenter. „Audi e-tron GT," 2021. [Online]. Available: https://www.audi-mediacenter.com/de/audi-e-tron-gt-13716 [visited on 09/08/2021].

[96] J. Baxter et al., „UltraCapacitor Power for a Drag Racecar," in *SAE Technical Paper Series*, 2004, DOI: 10.4271/2004-01-3500.

[97] D. Hauck and M. Kurrat, „Overdischarging Lithium-Ion Batteries," in *Recycling of Lithium-Ion Batteries*, A. Kwade, ed. Springer International Publishing, 2018, pp. 53–81, ISBN: 978-3-319-70571-2.

[98] P. Ramminger and H.-G. Schade, „The Propulsion, Energy Storage and Charging System of the New Opel Corsa-e," in *CTI SYMPOSIUM* Berlin: Springer, 2021, pp. 422–436, DOI: 10.1007/978-3-662-61515-7_38.

[99] M. Schorn, „Modelle zur Beschreibung des Fahrzeugverhaltens," in *Fahrdynamik-Regelung*, R. Isermann, ed. Wiesbaden: Vieweg, 2006, pp. 27–46, ISBN: 978-3-8348-0109-8.

[100] P. Köhler, „Semi-physikalische Modellierung von Antriebsstrangkomponenten für Elektrofahrzeuge," Semester thesis, Institute of Automotive Technology, Technical University of Munich, Munich, 2020.

[101] P. Köhler, „Semi-physikalische Modellierung von Antriebsstrangkomponenten für Elektrofahrzeuge," Master thesis, Institute of Automotive Technology, Technical University of Munich, Munich, 2021.

[102] M. Felgenhauer et al., „Geometric substitute models for efficient scaling of dimensions during vehicle architecture design," in *15th International Design Conference*, Dubrovnik, Croatia, 2018, pp. 261–272, DOI: 10.21278/idc.2018.0176.

[103] L. Nicoletti et al., „Parametric Modeling of Mass and Volume Effects for Battery Electric Vehicles, with Focus on the Wheel Components," *World Electric Vehicle Journal*, vol. 11, no. 4, p. 63, 2020, DOI: 10.3390/wevj11040063.

[104] L. Nicoletti, „Erweiterung eines Baukasten-Architektur-Auslegungstools durch Modellierung von Abmessungen und Gewichten," Master thesis, Institute of Automotive Technology, Technical University of Munich, Munich, 2018.

[105] T. Dirr et al., „Konzeptmethodik für die Topologie von Elektrofahrzeugen," *ATZ - Automobiltechnische Zeitschrift*, vol. 123, no. 5-6, pp. 38–43, 2021, DOI: 10.1007/s35148-021-0690-6.

[106] E. Wiedemann, J. Meurle and M. Lienkamp, „Optimization of Electric Vehicle Concepts Based on Customer-Relevant Characteristics," in *SAE Technical Paper Series*, Detroit, Michigan, United States of America, 2012, DOI: 10.4271/2012-01-0815.

[107] S. Fuchs, *Verfahren zur parameterbasierten Gewichtsabschätzung neuer Fahrzeugkonzepte*, Ph.D. Thesis, Institute of Automotive Technology, Technical University of Munich, Munich, 2014.

[108] T. Gänsicke, M. Goede and J. Sandiano, „Die Technische Motivation," in *Leichtbau in der Fahrzeugtechnik*, H. E. Friedrich, ed. Wiesbaden: Springer Vieweg, 2017, pp. 33–44, ISBN: 978-3-658-12294-2.

[109] D. Malen and K. Reddy, „Preliminary Vehicle Mass Estimation Using Empirical Subsystem Influence Coefficients," 2007. Available: https://www.semanticscholar.org/paper/Preliminary-Vehicle-Mass-Estimation-Using-Empirical-Malen-Reddy/77b94cb8fac8916a0f46919ea7159e4830da239f [visited on 12/02/2021].

[110] R. Gobbels et al., „Analyse der sekundären Gewichtseinsparung," Verband deutscher Automobilindustrie, rep. 230, 2011. Available: https://www.vda.de/de/services/Publikationen/analyse-der-sekund-ren-gewichtseinsparung.html [visited on 01/24/2021].

[111] E. Alonso et al., „Evaluating the potential for secondary mass savings in vehicle lightweighting," *Environmental science & technology*, vol. 46, no. 5, pp. 2893–2901, 2012, DOI: 10.1021/es202938m.

[112] S. Fuchs and M. Lienkamp, „Parametric Modelling of Mass and Efficiency of New Vehicle Concepts," *ATZ worldwide*, vol. 115, no. 3, pp. 60–67, 2013, DOI: 10.1007/s38311-013-0034-6.

[113] S. Mayer, „Literaturrecherche: Packagemodellierung," Semester thesis, Institute of Automotive Technology, Technical University of Munich, Munich, 2020.

[114] S. Biereder, „Literaturrecherche Packagemodellierung," Semester thesis, Institute of Automotive Technology, Technical University of Munich, Munich, 2020.

[115] M. Felgenhauer et al., „Empiric Weight Model for the Early Phase of Vehicle Architecture Design," in *14th International Conference on Ecological Vehicles and Renewable Energies*, Monaco, 2019, DOI: 10.1109/EVER.2019.8813530.

[116] K. Deb et al., „A fast and elitist multiobjective genetic algorithm: NSGA-II," *IEEE Transactions on Evolutionary Computation*, vol. 6, no. 2, pp. 182–197, 2002, DOI: 10.1109/4235.996017.

[117] T. Yanni and P. J. T. Venhovens, „Impact and Sensitivity of Vehicle Design Parameters on Fuel Economy Estimates," in *SAE Technical Paper Series*, 2010, DOI: 10.4271/2010-01-0734.

[118] R. Raabe, *Ein rechnergestütztes Werkzeug zur Generierung konsistenter Pkw-Maßkonzepte und parametrischer Designvorgabe*, Ph.D. Thesis, Institute for Engineering Design and Industrial Design, University of Stuttgart, Stuttgart, 2013, ISBN: 978-3-922823-86-5.

[119] M. Ried, *Lösungsraumanalyse für Plug-In-Hybridfahrzeuge hinsichtlich Wirtschaftlichkeit und Bauraumkonzept*, Ph.D. Thesis, University Duisburg-Essen, Duisburg-Essen, 2016, ISBN: 978-3-944339-10-8.

[120] T. Stefaniak and D. Maiwald, „Ermittlung nutzbarer Bauräume für Energiespeicher auf Hochvoltebene in Elektrofahrzeugen mit dezentralisierten Antriebssträngen," in *13. Magdeburger Maschinenbau-Tage*, Magdeburg, Germany, 2017, ISBN: 978-3-944722-54-2.

[121] T. Stefaniak, D. Maiwald and G. Püschel, „Durch Maßkonzept und Algorithmen zur optimierten Fahrzeugbatterie," *Konstruktion: Zeitschrift für Produktentwicklung und Ingenieur-Werkstoffe*, no. 4, 2018, DOI: 10.37544/0720-5953-2018-04-67.

[122] MathWorks. „*MATLAB*," 2020. Available: https://de.mathworks.com/products/matlab.html [visited on 02/24/2020].

[123] C. Angerer et al., „Parameter-adaption for a vehicle dynamics model for the evaluation of powertrain concept designs," in *International Conference on New Energy Vehicle and Vehicle Engineering*, Seoul, Korea, 2018, DOI: 10.1051/matecconf/201927201022.

[124] V. Bhise et al., „Development of a Parametric Model for Advanced Vehicle Design," in *SAE Technical Paper Series*, Detroit, Michigan, USA, 2004, DOI: 10.4271/2004-01-0381.

[125] G. Domingues, A. Reinap and M. Alakula, „Design and cost optimization of electrified automotive powertrain," in *International Conference on Electrical Systems for Aircraft, Railway, Ship Propulsion and Road Vehicles & International Transportation Electrification Conference*, Toulouse, France, 2016, pp. 1–6, DOI: 10.1109/ESARS-ITEC.2016.7841350.

[126] G. Domingues et al., „Scalable performance, efficiency and thermal models for electric drive components used in powertrain simulation and optimization," in *IEEE Transportation and Electrification Conference and Expo*, Chicago, IL, USA, 2017, pp. 644–649, DOI: 10.1109/ITEC.2017.7993345.

[127] J. Hasenpusch, *Methodik zur Beurteilung eigenschaftsoptimierter Karosseriekonzepte in Mischbauweise*, Ph.D. Thesis, Technical University Carolo-Wilhelmina, Braunschweig, Springer Fachmedien Wiesbaden, 2018, ISBN: 978-3-658-22227-7.

[128] T. Nemeth et al., „A Simulation Platform for Optimization of Electric Vehicles With Modular Drivetrain Topologies," *IEEE Transactions on Transportation Electrification*, vol. 4, no. 4, pp. 888–900, 2018, DOI: 10.1109/TTE.2018.2869371.

[129] T. Pesce, *Ein Werkzeug zur Spezifikation von effizienten Antriebstopologien für Elektrofahrzeuge*, Ph.D. Thesis, Institute of Automotive Technology, Technical University of Munich, Munich, Verlag Dr. Hut, 2014, ISBN: 978-3-8439-1624-0.

[130] A. Prinz, *Struktur und Ablaufmodell für das parametrische Entwerfen von Fahrzeugkonzepten*, Ph.D. Thesis, Technical University Carolo-Wilhelmina, Braunschweig, Logos Verlag Berlin, 2011, ISBN: 978-3-8325-2869-0.

[131] G. N. Reddy, „An EV-simulator for Electric Vehicle Education," in *International Conference on Engineering Education*, Kuala Lumpur, Malaysia, 2009, pp. 131–137, DOI: 10.1109/ICEED.2009.5490597.

[132] G. N. Reddy and M. Ademola, „A Visual C++ based modeling & simulation package for electric vehicle design," in *IEEE Vehicle Power and Propulsion Conference*, Chicago, IL, USA, 2011, pp. 1–5, DOI: 10.1109/VPPC.2011.6043210.

[133] K. Kuchenbuch, T. Vietor and J. Stieg, „Optimierungsalgorithmen für den Entwurf von Elektrofahrzeugen," *ATZ - Automobiltechnische Zeitschrift*, vol. 113, no. 7-8, pp. 548–551, 2011, DOI: 10.1365/s35148-011-0128-7.

[134] M. Orner, *Nutzungsorientierte Auslegung des Antriebsstrangs und der Reichweite von Elektrofahrzeugen*, Ph.D. Thesis, University of Stuttgart, Stuttgart, Springer Fachmedien Wiesbaden, 2018, ISBN: 978-3-658-21724-2.

[135] P. Rossbacher, *Beitrag integrierter Konzeptmodelle zur virtuellen Gesamtfahrzeugentwicklung in der frühen Entwurfsphase*, Ph.D. Thesis, Technical University of Graz, Graz, Verlag der Technischen Universität Graz, 2018, ISBN: 978-3-85125-730-4.

[136] C. Schmidt et al., „System Design Model for Parallel Hybrid Powertrains using Design of Experiments," in *SAE Technical Paper Series*, 2018, DOI: 10.4271/2018-01-0417.

[137] R. Raabe, T. Maier and J. Meyer-Eberling, „Methodische Gestaltung von abgesicherten Maßkonzepten und parametrischen Package-Vorgabemodellen in der frühen Phase der Fahrzeugkonzeptauslegung," in *4. Grazer Symposium Virtuelles Fahrzeug*, 2011.

[138] H. Yim and K. Lee, „Preliminary Modular Design for Electric Personal Mobility with Design-Engineering Collaboration," *World Electric Vehicle Journal*, vol. 7, no. 3, pp. 426–435, 2015, DOI: 10.3390/wevj7030426.

[139] M. Luccarelli et al., „Purpose Design for Electric Cars: Parameters Defining Exterior Vehicle Proportions," in *3rd Conference on Future Automotive Technology*, Garching, Munich, Germany, 2014, pp. 1–7, DOI: 10.13140/2.1.3077.4727.

[140] V. Bhise and A. Pillai, „A Parametric Model for Automotive Packaging and Ergonomics Design," in *International Conference on Computer Graphics & Virtual Reality*, Las Vegas, NV, USA, 2006, pp. 161–167, ISBN: 1-932415-85-8.

[141] G. Ranocchia, „Creation of a database concept for expandable parametric vehicle architectures," Master thesis, Politecnico di Torino, Torino, 2020.

[142] M. Unterstein and G. Matthiessen, *Relationale Datenbanken und SQL in Theorie und Praxis*, Berlin, Springer, 2012, ISBN: 978-3-642-28985-9.

[143] Information technology - Database languages - SQL - Part 1: Framework (SQL/Framework), ISO/IEC 9075-1:2016-12, 2016.

[144] Oracle Corporation. „MySQL: Die populärste Open-Source-Datenbank der Welt," 2021. [Online]. Available: https://www.mysql.com/de/ [visited on 01/14/2021].

[145] The PostgreSQL Global Development Group. „PostgreSQL: The World's Most Advanced Open Source Relational Database," 2021. [Online]. Available: https://www.postgresql.org/ [visited on 01/14/2021].

[146] SQLite Consortium. „SQLite Home Page: Small. Fast. Reliable. Choose any three." 2021. [Online]. Available: https://www.sqlite.org/index.html [visited on 01/14/2021].

[147] Microsoft. „Perfektionieren Sie Ihre Daten Eigene Datenbankanwendungen in Formaten, die perfekt auf Ihr Unternehmen abgestimmt sind – nur für den PC," 2021. [Online]. Available: https://www.microsoft.com/de-de/microsoft-365/access [visited on 01/14/2021].

[148] MathWorks. „Database Toolbox: Datenaustausch mit relationalen und nicht relationalen Datenbanken," 2021. [Online]. Available: https://de.mathworks.com/products/database.html [visited on 01/14/2021].

[149] ADAC. „Automarken- und Modelle im ADAC Autokatalog," 2021. [Online]. Available: https://www.adac.de/rund-ums-fahrzeug/autokatalog/marken-modelle/ [visited on 01/14/2021].

[150] R. Marksteiner, „Ableitung von Korrelationen für den Bauraumbedarf von Antriebskomponenten," Master thesis, Institute of Automotive Technology, Technical University of Munich, Munich, 2017.

[151] F. Schneider, „Erstellung empirischer Ersatzmodelle für Wärmetauscher, Bremsen, Felgen und Reifen im KFZ-Vorderwagen," Master thesis, Institute of Automotive Technology, Technical University of Munich, Munich, 2017.

[152] L. Guzzella and A. Sciarretta, *Vehicle Propulsion Systems: Introduction to Modeling and Optimization*, 3rd ed. 2013, Berlin, Springer, 2013, ISBN: 978-3-642-35912-5.

[153] M. Tschochner, *Comparative Assessment of Vehicle Powertrain Concepts in the Early Development Phase*, Ph.D. Thesis, Institute of Automotive Technology, Technical University of Munich, Munich, Shaker, 2019, ISBN: 978-3-8440-6461-2.

[154] A. König et al., „An Open-Source Modular Quasi-Static Longitudinal Simulation for Full Electric Vehicles," in *15th International Conference on Ecological Vehicles and Renewable Energies*, Monaco, 2020, pp. 1–9, DOI: 10.1109/EVER48776.2020.9242981.

[155] K. Moller, „Validierung einer MATLAB Längsdynamiksimulation für die Auslegung von Elektrofahrzeugen," Bachelor thesis, Institute of Automotive Technology, Technical University of Munich, Munich, 2020.

[156] R. Hefele, „Implementierung einer MATLAB Längsdynamiksimulation für Elektrofahrzeuge," Semester thesis, Institute of Automotive Technology, Technical University of Munich, Munich, 2019.

[157] A. König, L. Nicoletti and K. Moller. „Modular Quasi-Static Longitudinal Simulation for BEV," 2020. [Online]. Available: https://github.com/TUMFTM/Modular-Quasi-Static-Longitudinal-Simulation-for-BEV [visited on 01/07/2020].

[158] European Commission, Directorate-General for Internal Market, Industry, Entrepreneurship and SMEs. „*Supplementing Regulation (EC) No 715/2007 of the European Parliament and of the Council on type-approval of motor vehicles with respect to emissions from light passenger and commercial vehicles (Euro 5 and Euro 6) and on access to vehicle repair and maintenance information, amending Directive 2007/46/EC of the European Parliament and of the Council, Commission Regulation (EC) No 692/2008 and Commission Regulation (EU) No 1230/2012 and repealing Commission Regulation (EC) No 692/2008: (EU) 2017/1151*," 2017. Available: https://eur-lex.europa.eu/legal-content/EN/ALL/?uri=CELEX:32017R1151 [visited on 04/07/2020].

[159] S. Kalt, J. Erhard and M. Lienkamp, „Electric Machine Design Tool for Permanent Magnet Synchronous Machines and Induction Machines," *Machines*, vol. 8, no. 1, p. 15, 2020, DOI: 10.3390/machines8010015.

[160] K. Moller, „Antriebsstrangmodellierung zur Optimierung autonomer Elektrofahrzeuge," Semester thesis, Institute of Automotive Technology, Technical University of Munich, Munich, 2021.

[161] E. A. Grunditz and T. Thiringer, „Performance Analysis of Current BEVs Based on a Comprehensive Review of Specifications," *IEEE Transactions on Transportation Electrification*, vol. 2, no. 3, pp. 270–289, 2016, DOI: 10.1109/TTE.2016.2571783.

[162] A. Romano, „Data-based Analysis for Parametric Weight Estimation of new BEV Concepts," Master thesis, Institute of Automotive Technology, Technical University of Munich, Munich, 2021.

[163] A2MAC1 EUL. „A2mac1: Automotive Benchmarking," 2021. [Online]. Available: a2mac1.com/ [visited on 05/25/2021].

[164] A. Romano, „Datenbasierte Analyse zur geometrischen Modellierung von Reifen und Felgen," Semester thesis, Institute of Automotive Technology, Technical University of Munich, Munich, 2020.

[165] K. Reif, *Bremsen und Bremsregelsysteme*, Wiesbaden, Vieweg+Teubner Verlag / GWV Fachverlage GmbH Wiesbaden, 2010, ISBN: 978-3-8348-1311-4.

[166] D. Wagner, J. Hoffmann and M. Lienkamp, „Downsizing potential of wheel brakes in electric vehicles," in *8th International Munich Chassis Symposium*, P. Pfeffer, ed. Wiesbaden: Springer Fachmedien Wiesbaden, 2017, pp. 661–691, DOI: 10.1007/978-3-658-18459-9_47.

[167] B. Breuer and K. H. Bill, *Bremsenhandbuch: Grundlagen, Komponenten, Systeme, Fahrdynamik*, 2nd Edition, Wiesbaden, Vieweg+Teubner Verlag, 2004, ISBN: 978-3-322-99535-3.

[168] The European Tyre and Rim Technical Organization, „Standards Manual 2014," The European Tyre and Rim Technical Organization, 2014. Available: http://www.etrto.org/Home [visited on 12/02/2021].

[169] M. Luccarelli et al., „Automotive Design Quantification: Parameters Defining Exterior Proportions According to Car Segment," in *SAE Technical Paper Series*, 2014, DOI: 10.4271/2014-01-0357.

[170] Korea Motor Vehicle Safety Standards (KMVSS), Ministry of Land, Infrastructure and Transport (MOLIT), Regulations for Performance and Safety Standards of Motor Vehicle and Vehicle Parts, Ordinance number 577, 2017.

[171] Vehicle Safety Standards, Department of Infrastructure and Regional Development, Vehicle Configuration and Dimensions, Australian Design Rule 43/04, 2006.

[172] SAE J689 - Curbstone Clearance, Approach, Departure, and Ramp Breakover Angles–Passenger Car and Light Truck, 2009.

[173] S. Mirti, „Erstellung eines parametrischen Modells zur Herleitung von Maßkonzepten für Elektrofahrzeuge," Bachelor thesis, Institute of Automotive Technology, Technical University of Munich, Munich, 2019.

[174] R. J. Mau and P. J. Venhovens, „Development of a consistent continuum of the dimensional parameters of a vehicle for optimization and simulation," *Proceedings of the Institution of Mechanical Engineers, Part D: Journal of Automobile Engineering*, vol. 228, no. 6, pp. 591–603, 2014, DOI: 10.1177/0954407013497195.

[175] Porsche AG. „*Weltpremiere des Porsche Taycan: Sportwagen, nachhaltig neu gedacht - Dr. Ing. h.c. F. Porsche AG Presse-Datenbank*," 2019. Available: https://presse.porsche.de/prod/presse_pag/PressResources.nsf/Content?ReadForm&languageversionid=1019499 [visited on 05/15/2021].

[176] Rimac Automobili C Two hypercar. „Rimac Automobili C Two hypercar - A car alive with technology," 2021. [Online]. Available: https://ctwo.rimac-automobili.com/ [visited on 06/01/2021].

[177] F. Bottiglione et al., „Energy Consumption of a Battery Electric Vehicle with Infinitely Variable Transmission," *Energies*, vol. 7, no. 12, pp. 8317–8337, 2014, DOI: 10.3390/en7128317.

[178] J. Ruan, P. Walker and N. Zhang, „A comparative study energy consumption and costs of battery electric vehicle transmissions," *Applied Energy*, vol. 165, pp. 119–134, 2016, DOI: 10.1016/j.apenergy.2015.12.081.

[179] J. C. Parlow, *Entwicklung einer Methode zum anforderungsgerechten Entwurf von Stirnradgetrieben*, Ph.D. Thesis, Institute of Machine Elements, Technical University of Munich, Munich, 2016, ISBN: 978-3-00-053444-7.

[180] Schaeffler Technologies AG & Co. KG. „Rolling bearings: Ball bearings, Roller bearings, Needle roller bearings, Track rollers, Bearings for screw drives, Insert bearings/housing units, Bearing housings, Accessories," 2021. [Online]. Available: https://www.schaeffler.de/content.schaeffler.de/de/news_medien/mediathek/publikationen/downloadcenter-global-pages/downloadcenter-language-list-publications.jsp?pubid=246581&ppubid=246579&tab=mediathek-pub&uid=386195&subfilter=app:dc [visited on 02/06/2021].

[181] Insurance Institute for Highway Safety, Side Impact Crashworthiness Evaluation – Crash Test Protocol (Version X), 2017.

[182] B. Frieß et al., „Herausforderungen in der Batterieentwicklung Grundlagen und Vorschläge zur Kostenoptimierung," *ATZ - Automobiltechnische Zeitschrift*, vol. 120, no. 2, pp. 52–57, 2018, DOI: 10.1007/s35148-017-0213-7.

[183] EURO NCAP: European new car assessment programme: Full width frontal impact testing protocol, Consumer test 2015.

[184] Insurance Institute for Highway Safety, Small Overlap Frontal Crashworthiness Evaluation - Crash Test Protocol (Version VI), 2017.

[185] A. Obermüller, „Dynamic All-wheel steering (DAS)," in *8th International Munich Chassis Symposium*, P. Pfeffer, ed. Wiesbaden: Springer Fachmedien Wiesbaden, 2017, pp. 487–498, DOI: 10.1007/978-3-658-18459-9_31.

[186] Audi Technology Portal. „Audi Technology Portal - Audi A8 – Dynamic all-wheel steering," 2021. [Online]. Available: https://www.audi-technology-portal.de/en/chassis/wheel-suspension-steering/audi-a8-dynamic-all-wheel-steering [visited on 09/10/2021].

[187] M. Spreng, „Maßkettenanalyse am Hinterwagen zur Erstellung von Ersatzmodellen," Bachelor thesis, Faculty of Mechanical Engineering, Ostbayerische Technische Hochschule Regensburg, Regensburg, 2020.

[188] C. Gordon et al., „2012 Anthropometric survey of U.S. army personnel: methods and summary statistics," U.S. Army Natick Soldier Research, Development and Engineering Center, Natick, Massachusetts, 2014. Available: https://apps.dtic.mil/dtic/tr/fulltext/u2/a611869.pdf [visited on 02/26/2021].

[189] P. Fischer and S. Neunteufel, „Elektrifizierte Antriebssysteme," in *Grundlagen Verbrennungsmotoren*. vol. 5, G. P. Merker and R. Teichmann, ed. Wiesbaden: Springer Fachmedien Wiesbaden, 2019, pp. 313–363, DOI: 10.1007/978-3-658-23557-4_14.

[190] T. Woehrle, „Lithium-ion cell," in *Lithium-Ion Batteries: Basics and Applications*, R. Korthauer, ed. Berlin: Springer, 2018, pp. 101–111, ISBN: 978-3-662-53069-6.

[191] R. Schmuch et al., „Performance and cost of materials for lithium-based rechargeable automotive batteries," *Nature Energy*, vol. 3, no. 4, pp. 267–278, 2018, DOI: 10.1038/s41560-018-0107-2.

[192] Elektrische Straßenfahrzeuge - Batteriesysteme - Anforderungen an die Gestaltung von Lithium-Ionen-Batteriezellen; DIN 91252:2016-11, 2016.

[193] American National Standard For Portable Lithium Primary Cells and Batteries: General and Specifications, ANSI C18.3M, Part 1, 2005.

[194] M. Kerler and M. Lienkamp, „A method to find a thermal optimum cell size," in *4th Conference on Future Automotive Technology*, 2015. Available: https://www.researchgate.net/publication/283052180_A_method_to_find_a_thermal_optimum_cell_size/citations [visited on 05/25/2021].

[195] D. Deng, „Li-ion batteries: basics, progress, and challenges," *Energy Science & Engineering*, vol. 3, no. 5, pp. 385–418, 2015, DOI: 10.1002/ese3.95.

[196] G. Zubi et al., „The lithium-ion battery: State of the art and future perspectives," *Renewable and Sustainable Energy Reviews*, vol. 89, pp. 292–308, 2018, DOI: 10.1016/j.rser.2018.03.002.

[197] J. van Mierlo et al., „Beyond the State of the Art of Electric Vehicles: A Fact-Based Paper of the Current and Prospective Electric Vehicle Technologies," *World Electric Vehicle Journal*, vol. 12, no. 1, p. 20, 2021, DOI: 10.3390/wevj12010020.

[198] R. Roth, J. Clark and A. Kelkar, „Automobile bodies: Can aluminum be an economical alternative to steel?," *JOM*, vol. 53, no. 8, pp. 28–32, 2001, DOI: 10.1007/s11837-001-0131-7.

[199] L. Eckstein, F. Schmitt and B. Hartmann, „Leichtbau bei Elektrofahrzeugen," *ATZ - Automobiltechnische Zeitschrift*, vol. 112, no. 11, pp. 788–795, 2010, DOI: 10.1007/BF03222207.

[200] M. Hirz and P. Rossbacher, „Enhanced knowledge-based 3D-CAD methods supporting automotive body-in-white production engineering," *Acta Technica Corviniensis - Bulletin of Engineering*, vol. 10, no. 2, 2017. Available: http://acta.fih.upt.ro/pdf/2017-2/ACTA-2017-2-20.pdf.

[201] M. Ahlers, „Carbon Core – die neue BMW 7er Karosserie," in *Karosseriebautage Hamburg*, G. Tecklenburg, ed. Wiesbaden: Springer Vieweg, 2016, pp. 125–135, DOI: 10.1007/978-3-658-14144-8_9.

[202] T. Evertz et al., „Die Leichtbauwerkstoffe für den Fahrzeugbau," in *Leichtbau in der Fahrzeugtechnik*. vol. 4, H. E. Friedrich, ed. Wiesbaden: Springer Vieweg, 2017, pp. 205–449, ISBN: 978-3-658-12294-2.

[203] T. Kersten and S. Fiebig, „Challenges and benefits for lightweight chassis components focusing on rear axle development," in *10th International Munich Chassis Symposium*, P. Pfeffer, ed. Wiesbaden: Springer Fachmedien Wiesbaden, 2020, pp. 231–247, DOI: 10.1007/978-3-658-26435-2_18.

[204] M. L. Brown et al., „Dual hinged vehicle door," United States Patent US8511738B2, 2013.

[205] D. Lieske, D. Landes and J. Fischer, „Optimization of the Powertrain Noise for the Electric Vehicle Mercedes-Benz EQC," *ATZ worldwide*, vol. 122, no. 3, pp. 56–61, 2020, DOI: 10.1007/s38311-020-0200-6.

[206] G. Lepoittevin, J. Horak and D. Caprioli, „The New Challenges of NVH Package for BEVs," in *SAE Technical Paper Series*, 2019, DOI: 10.4271/2019-01-1452.

[207] A. Thielmann et al., „Energiespeicher-Roadmap (Update 2017). Hochenergie-Batterien 2030+ und Perspektiven zukünftiger Batterietechnologien," Karlsruhe, 2017. Available: https://www.isi.fraunhofer.de/content/dam/isi/dokumente/cct/lib/Energiespeicher-Roadmap-Dezember-2017.pdf [visited on 12/02/2021].

[208] A. Thielmann, A. Sauer and M. Wietschel, „Gesamt-Roadmap Energiespeicher für die Elektromobilität 2030," Karlsruhe, 2015. Available: https://www.isi.fraunhofer.de/content/dam/isi/dokumente/cct/lib/GRM-ESEM.pdf [visited on 12/02/2021].

[209] P. Hofmann, *Hybridfahrzeuge: Ein alternatives Antriebssystem für die Zukunft*, 2nd Edition, Wien, Springer, 2014, ISBN: 9783709117804.

[210] K. Vuorilehto, „Materials and function," in *Lithium-Ion Batteries: Basics and Applications*, R. Korthauer, ed. Berlin: Springer, 2018, pp. 21–28, ISBN: 978-3-662-53069-6.

[211] 2nd Institute of Physics RWTH. „Phyphox: Your smartphone is a mobile lab," 2021. [Online]. Available: https://phyphox.org/ [visited on 06/08/2021].

[212] Argonne national Laboratory. „Electric Vehicle Testing | Argonne National Laboratory," 2019. [Online]. Available: https://www.anl.gov/es/electric-vehicle-testing [visited on 09/01/2019].

[213] ADAC. „VW ID.3 Pro Performance (58 kWh) 1st Max (09/20 - 11/20)," 2021. [Online]. Available: https://www.adac.de/rund-ums-fahrzeug/autokatalog/marken-modelle/vw/id3/1generation/299587 [visited on 09/06/2021].

[214] N. Wassiliadis et al., „Quantifying the state of the art of electric powertrains in battery electric vehicles: Range, Power and lifetime from component to system level of the VW ID.3," *in review process, Journal of eTransportation*, 2022.

[215] B. Danquah et al., „Statistical Validation Framework for Automotive Vehicle Simulations Using Uncertainty Learning," *Applied Sciences*, vol. 11, no. 5, p. 1983, 2021, DOI: 10.3390/app11051983.

[216] VEPCO TECHNOLOGIES INC. „MotorXP – Electric Machine Design and Analysis Software," 2021. [Online]. Available: https://motorxp.com/#motorim [visited on 07/15/2021].

[217] V. Kuptsov et al., „Electromagnetic Analysis and Design Methodology for Permanent Magnet Motors Using MotorAnalysis-PM Software," *Machines*, vol. 7, no. 4, p. 75, 2019, DOI: 10.3390/machines7040075.

[218] Chair of Machine Elements. „Simulation and Computer Programs - Department of Mechanical Engineering," 2021. [Online]. Available: https://www.mw.tum.de/en/fzg/research/simulation-and-computer-programs/ [visited on 08/10/2021].

[219] K. Pudenz, „BMW i3: Automobilbau mit CFK," *springerprofessional.de*, 2013. Available: https://www.springerprofessional.de/automobil---motoren/werkstoffe/bmw-i3-automobilbau-mit-cfk/6559150 [visited on 05/25/2021].

[220] P. Bubna and M. Wiseman, „Impact of Light-Weight Design on Manufacturing Cost - A Review of BMW i3 and Toyota Corolla Body Components," in *SAE Technical Paper Series*, 2016, DOI: 10.4271/2016-01-1339.

[221] P. Rucker, „Lackieren ohne Limit," *Journal für Oberflächentechnik*, vol. 60, no. 5-6, pp. 28–30, 2020, DOI: 10.1007/s35144-020-0540-4.

[222] A. Jacob, „Carbon fibre and cars – 2013 in review," *Reinforced Plastics*, vol. 58, no. 1, pp. 18–19, 2014, DOI: 10.1016/S0034-3617(14)70036-0.

[223] ADAC. „BMW i3s (120 Ah) (ab 11/18)," 2021. [Online]. Available: https://www.adac.de/rund-ums-fahrzeug/autokatalog/marken-modelle/bmw/i3/i01-facelift/294685/ [visited on 10/19/2021].

[224] ADAC. „VW ID.3 Pro S (77 kWh) Tour (5-Sitzer) (03/21 - 05/21)," 2021. [Online]. Available: https://www.adac.de/rund-ums-fahrzeug/autokatalog/marken-modelle/vw/id3/1generation/319804/ [visited on 04/22/2021].

[225] Jaguar. „Jaguar I-Pace EV400 S AWD (10/18 - 06/20),“ 2021. [Online]. Available: https://www.adac.de/rund-ums-fahrzeug/autokatalog/marken-modelle/jaguar/i-pace/x590/288009/ [visited on 10/22/2021].

[226] ADAC. „Tesla Model 3 Standard Range Plus (11/19 - 11/20),“ 2021. [Online]. Available: https://www.adac.de/rund-ums-fahrzeug/autokatalog/marken-modelle/tesla/model-3/1generation/308033/ [visited on 10/20/2021].

[227] ADAC. „Tesla Model Y Performance AWD (ab 09/21),“ 2021. [Online]. Available: https://www.adac.de/rund-ums-fahrzeug/autokatalog/marken-modelle/tesla/model-y/1generation/297991/ [visited on 10/20/2021].

[228] ADAC. „Audi e-tron 55 quattro (03/19 - 11/19),“ 2021. [Online]. Available: https://www.adac.de/rund-ums-fahrzeug/autokatalog/marken-modelle/audi/e-tron/ge/309075/ [visited on 01/04/2021].

[229] BMW Group PressClub. „Technical specifications of the new BMW i3 and the new BMW i3s,“ 2021. [Online]. Available: https://www.press.bmwgroup.com/global/article/detail/T0280411EN/technical-specifications-of-the-new-bmw-i3-and-the-new-bmw-i3s-valid-from-11/2017 [visited on 10/29/2021].

[230] TFF Forum - Tesla Fahrer & Freunde. „Model 3 / Model Y - Batteriewiki [W.I.P.] - Essentials - TFF Forum - Tesla Fahrer & Freunde,“ 2021. [Online]. Available: https://tff-forum.de/t/model-3-model-y-batteriewiki-w-i-p/107641 [visited on 10/28/2021].

[231] T. Barth et al., „The Aerodynamics of the VW ID.3 Electric Car,“ *ATZ worldwide*, vol. 122, no. 9, pp. 48–53, 2020, DOI: 10.1007/s38311-020-0270-5.

[232] Volkswagen AG. „*Powerful and scalable: the new ID. Battery system*,“ 2018. Available: https://www.volkswagenag.com/en/news/stories/2018/10/powerful-and-scalable-the-new-id-battery-system.html.

[233] M. Steinstraeter, T. Heinrich and M. Lienkamp, „Effect of Low Temperature on Electric Vehicle Range,“ *World Electric Vehicle Journal*, vol. 12, no. 3, p. 115, 2021, DOI: 10.3390/wevj12030115.

[234] H. Wittich, „Facelift für Tesla Model S (2021),“ 2021. Available: https://www.auto-motor-und-sport.de/neuheiten/facelift-tesla-model-s-2021-plaid-antrieb/ [visited on 10/29/2021].

[235] Future Lab. „Tesla Battery Day: entire Event in 16 minutes (Supercut),“ 2021. [Online]. Available: https://www.youtube.com/watch?app=desktop&v=HK79ioBW8Mg&t=830s [visited on 11/17/2021].

[236] L. Song, „NGPM – A NSGA-II Program in Matlab: Version 1.4,“ 2011. Available: https://usermanual.wiki/Pdf/NGPM20manual20v14.1073441263/view [visited on 02/12/2020].

[237] O. Röder and M. Wein, „Chassis development for a fully electric vehicle with quattro drivetrain,“ in *9th International Munich Chassis Symposium*, P. Pfeffer, ed. Wiesbaden and Heidelberg: Springer Vieweg, 2019, pp. 77–88, ISBN: 978-3-658-22049-5.

[238] S. Kalt, L. Brenner and M. Lienkamp, „Requirements for Electric Machine Design based on Operating Points from Real Driving Data in Cities,“ *World Electric Vehicle Journal*, vol. 10, no. 4, p. 60, 2019, DOI: 10.3390/wevj10040060.

[239] S. Kalt et al., „Electric Machine Design Tool for Permanent Magnet Synchronous Machines,“ in *14th International Conference on Ecological Vehicles and Renewable Energies*, Monaco, 2019, pp. 1–7, DOI: 10.1109/EVER.2019.8813601.

[240] D. Schweigert et al., „On the Impact of Maximum Speed on the Power Density of Electromechanical Powertrains," *Vehicles*, vol. 2, no. 2, pp. 365–397, 2020, DOI: 10.3390/vehicles2020020.

[241] S. Matz et al., „Beschreibung der Modellierungsart sowie der Modellierungsparameter von Elektrofahrzeugen in der Konzeptphase," 2014. Available: https://www.researchgate.net/publication/261174335_Beschreibung_der_Modellierungsart_sowie_der_Modellierungsparameter_von_Elektrofahrzeugen_in_der_Konzeptphase [visited on 11/25/2019].

[242] Audi MediaCenter. „How aerodynamics influence an electric car's range," 2021. [Online]. Available: https://www.audi.com/de/experience-audi/mobility-and-trends/e-mobility/e-tron-aerodynamic.html [visited on 09/13/2021].

[243] MAN Truck & Bus. „MAN presents the aerodynamically optimised road train of the future | MAN Truck Northern Africa," 2021. [Online]. Available: https://www.truck.man.eu/naf/en/man-world/man-in-north-africa/press-and-media/MAN-presents-the-aerodynamically-optimised-road-train-of-the-future-20800.html [visited on 12/01/2021].

[245] Jaguar Media. „JAGUAR I-PACE: THE ART OF ELECTRIC PERFORMANCE," 2021. [Online]. Available: https://media.jaguar.com/2018/jaguar-i-pace-art-electric-performance [visited on 05/13/2021].

[246] F. Lambert, „Elon Musk makes incredible claims about Tesla Model 3 longevity, will offer battery module replacement," *Electrek.co*, 2019. Available: https://electrek.co/2019/04/13/tesla-model-3-longevity-claims-elon-musk/ [visited on 07/24/2020].

[247] F. Lambert, „Tesla Model 3: Exclusive first look at Tesla's new battery pack architecture," *Electrek.co*, 2017. Available: https://electrek.co/2017/08/24/tesla-model-3-exclusive-battery-pack-architecture/ [visited on 05/13/2021].

[248] Polestar. „Polestar 2 Reveal | 100% electric | full presentation 40 min | - YouTube," 2021. [Online]. Available: https://www.youtube.com/watch?v=kVg5ycWTAhQ [visited on 05/13/2021].

[249] Volkswagen AG. „*In brief: Key components for a new era – the battery system*," Wolfsburg, 2019. Available: https://www.volkswagen-newsroom.com/en/press-releases/in-brief-key-components-for-a-new-era-the-battery-system-5645 [visited on 11/23/2020].

[250] A. Saathoff and T. Kersten, „The new chassis of Volkswagen ID.3 within MEB platform," in *11th International Munich Chassis Symposium*, P. Pfeffer, ed. Berlin: Springer, 2021, pp. 1–17, DOI: 10.1007/978-3-662-63193-5_1.

[251] Green Car Congress. „BMW boosts i3 and i3s batteries to 120Ah; 42.2 kWh pack almost doubles original range," 2021. [Online]. Available: https://www.greencarcongress.com/2018/09/20180928-bmw.html [visited on 05/12/2021].

[252] F. Schoewel and E. Hockgeiger. „*The high voltage batteries of the BMW i3 and BMW i8*," Presentation, Atalanta, February 2014.

[253] W. Wolfgang and G. Koert. „Fakten zur Entwicklung und Erprobung des neuen Mercedes-Benz EQC: Wir geben Strom: Der EQC voll im Plan auf dem Weg zur Serienreife," 2021. [Online]. Available: https://media.daimler.com/marsMediaSite/de/instance/ko.xhtml?oid=40367883&relId=1001&resultInfoTypeId=172#toRelation [visited on 05/10/2021].

[254] NISSAN MOTOR. „Electric vehicle lithium-ion battery," 2021. [Online]. Available: https://www.nissan-global.com/EN/TECHNOLOGY/OVERVIEW/li_ion_ev.html [visited on 05/13/2021].

[255] J. Pavlovic et al., „How much difference in type-approval CO2 emissions from passenger cars in Europe can be expected from changing to the new test procedure (NEDC vs. WLTP)?," *Transportation Research Part A: Policy and Practice*, vol. 111, no. 3, pp. 136–147, 2018, DOI: 10.1016/j.tra.2018.02.002.

[256] European Commission, Directorate-General for Internal Market, Industry, Entrepreneurship and SMEs. „*Consolidated text: Supplementing Regulation (EC) No 715/2007 of the European Parliament and of the Council on type-approval of motor vehicles with respect to emissions from light passenger and commercial vehicles (Euro 5 and Euro 6) and on access to vehicle repair and maintenance information, amending Directive 2007/46/EC of the European Parliament and of the Council, Commission Regulation (EC) No 692/2008 and Commission Regulation (EU) No 1230/2012 and repealing Commission Regulation (EC) No 692/2008: (EU) 2017/1151*," 2020. Available: https://eur-lex.europa.eu/legal-content/EN/TXT/?uri=CELEX:02017R1151-20200125 [visited on 04/30/2021].

[257] X. Liu et al., „From NEDC to WLTP: Effect on the Energy Consumption, NEV Credits, and Subsidies Policies of PHEV in the Chinese Market," *Sustainability*, vol. 12, no. 14, p. 5747, 2020, DOI: 10.3390/su12145747.

[258] Stecker, Steckdosen, Fahrzeugkupplungen und Fahrzeugstecker - Konduktives Laden von Elektrofahrzeugen - Teil 2: Anforderungen und Hauptmaße für die Kompatibilität und Austauschbarkeit von Stift- und Buchsensteckvorrichtungen für Wechselstrom, DIN 62196-2: 2017-11, 2017.

[259] Stecker, Steckdosen und Fahrzeugsteckvorrichtungen - Konduktives Laden von Elektrofahrzeugen - Teil 3: Anforderungen an und Hauptmaße für Stifte und Buchsen für die Austauschbarkeit von Fahrzeugsteckvorrichtungen zum dedizierten Laden mit Gleichstrom und als kombinierte Ausführung zum Laden mit Wechselstrom/Gleichstrom, DIN 62196-3:2015-05, 2015.

[260] Weston Arthur Hermann, „Liquid cooling manifold with multi-function thermal interface," United States Patent US20100104938A1, April 29, 2010.

[261] BMW Group. „BMW i3 (I01): Motoren & technische Daten | BMW.de," 2021. [Online]. Available: https://www.bmw.de/de/neufahrzeuge/bmw-i/i3/2021/bmw-i3-technische-daten.bmw-i3s--120-ah.html [visited on 10/19/2021].

[262] Volkswagen AG. „Der neue ID.3," 2021. [Online]. Available: https://www.volkswagen-newsroom.com/de/der-neue-id3-6240 [visited on 10/19/2021].

[263] Volkswagen AG. „VW ID.3 Infomaterial," 2021. [Online]. Available: https://www.volkswagen.at/id3/infomaterial [visited on 10/21/2021].

[264] Jaguar. „Jaguar Deutschland | The Art of Performance | Broschüren," 2021. [Online]. Available: https://www.jaguar.de/broschuere-anfragen/index.html [visited on 10/21/2021].

[265] Car Manuals. „Download 2019 Tesla Model 3 - Owner's Manual (Europe) PDF (179 Pages)," 2021. [Online]. Available: https://carmanuals2.com/get/tesla-model-3-2020-owner-s-manual-115116 [visited on 10/20/2021].

[266] Tesla. „Model Y Owner's Manual | Tesla," 2021. [Online]. Available: https://www.tesla.com/ownersmanual/modely/en_eu/ [visited on 10/20/2021].

[267] AUDI AG. „Audi e-tron: Der Elektro-SUV von Audi | Audi.de," 2021. [Online]. Available: https://www.audi.de/de/brand/de/neuwagen/tron/audi-e-tron.html# [visited on 10/20/2021].

List of Pre-publications

During the writing of this thesis, publications and student research projects were published, in which partial aspects of this work are presented.

Journals; Scopus/Web of Science listed (peer-reviewed)

[6] L. Nicoletti, F. Ostermann, M. Heinrich, A. Stauber, X. Lin and M. Lienkamp, „Topology analysis of electric vehicles, with a focus on the traction battery," *Forschung im Ingenieurwesen*, vol. 85, no. 2, pp. 457–467, 2020, DOI: 10.1007/s10010-020-00422-1.

[21] A. König, L. Nicoletti, D. Schröder, S. Wolff, A. Waclaw and M. Lienkamp, „An Overview of Parameter and Cost for Battery Electric Vehicles," *World Electric Vehicle Journal*, vol. 12, no. 1, p. 21, 2021, DOI: 10.3390/wevj12010021.

[26] L. Nicoletti, S. Mayer, M. Brönner, F. Schockenhoff and M. Lienkamp, „Design Parameters for the Early Development Phase of Battery Electric Vehicles," *World Electric Vehicle Journal*, vol. 11, no. 3, p. 47, 2020, DOI: 10.3390/wevj11030047.

[28] L. Nicoletti, A. Romano, A. König, P. Köhler, M. Heinrich and M. Lienkamp, „An Estimation of the Lightweight Potential of Battery Electric Vehicles," *Energies*, vol. 14, no. 15, p. 4655, 2021, DOI: 10.3390/en14154655.

[36] A. König, S. Mayer, L. Nicoletti, S. Trumphart and M. Lienkamp, „The Impact of HVAC on the Development of Autonomous and Electric Vehicle Concepts," *Energies*, vol. 15, no. 2, p. 441, 2022, DOI: 10.3390/en15020441.

[38] A. Koch, L. Nicoletti, T. Herrmann and M. Lienkamp, „Eco-Driving Algorithm for Electric Powertrains using Detailed Loss Models," *in review process, Journal of eTransportation*, 2022.

[58] L. Nicoletti, S. Mirti, F. Schockenhoff, A. König and M. Lienkamp, „Derivation of Geometrical Interdependencies between the Passenger Compartment and the Traction Battery Using Dimensional Chains," *World Electric Vehicle Journal*, vol. 11, no. 2, p. 39, 2020, DOI: 10.3390/wevj11020039.

[103] L. Nicoletti, A. Romano, A. König, F. Schockenhoff and M. Lienkamp, „Parametric Modeling of Mass and Volume Effects for Battery Electric Vehicles, with Focus on the Wheel Components," *World Electric Vehicle Journal*, vol. 11, no. 4, p. 63, 2020, DOI: 10.3390/wevj11040063.

Conferences, Periodicals; Scopus/Web of Science listed (peer-reviewed)

[3] L. Nicoletti, M. Bronner, B. Danquah, A. Koch, A. König, S. Krapf, A. Pathak, F. Schockenhoff, G. Sethuraman, S. Wolff and M. Lienkamp, „Review of Trends and Potentials in the Vehicle Concept Development Process," in *15th International Conference on Ecological Vehicles and Renewable Energies*, Monaco, 2020, pp. 1–15, DOI: 10.1109/EVER48776.2020.9243115.

[11] L. Nicoletti, W. Schmid and M. Lienkamp, „Databased Architecture Modeling for Battery Electric Vehicles," in *15th International Conference on Ecological Vehicles and Renewable Energies*, Monaco, 2020, pp. 1–9, DOI: 10.1109/EVER48776.2020.9242995.

[27] L. Nicoletti, P. Köhler, A. König, M. Heinrich and M. Lienkamp, „Parametric Modeling of Weight and Volume Effects on Battery Electric Vehicles, with Focus on the Gearbox," in *Proceedings of the Design Society*, Gothenburg, Sweden, 2021, pp. 2389–2398, DOI: 10.1017/pds.2021.500.

[35] A. König, D. Telschow, L. Nicoletti and M. Lienkamp, „Package Planning of Autonomous Vehicle Concepts," in *Proceedings of the Design Society*, Gothenburg, Sweden, 2021, pp. 2369–2378, DOI: 10.1017/pds.2021.498.

[115] M. Felgenhauer, L. Nicoletti, F. Schockenhoff, C. Angerer and M. Lienkamp, „Empiric Weight Model for the Early Phase of Vehicle Architecture Design," in *14th International Conference on Ecological Vehicles and Renewable Energies*, Monaco, 2019, DOI: 10.1109/EVER.2019.8813530.

[154] A. König, L. Nicoletti, S. Kalt, K. Moller, A. Koch and M. Lienkamp, „An Open-Source Modular Quasi-Static Longitudinal Simulation for Full Electric Vehicles," in *15th International Conference on Ecological Vehicles and Renewable Energies*, Monaco, 2020, pp. 1–9, DOI: 10.1109/EVER48776.2020.9242981.

Journals, Conferences, Periodicals, Reports, Conference Proceedings and Poster, etc.; not Scopus/Web of Science listed

[69] F. Schockenhoff, L. Nicoletti, M. Bayerlein, S. Krapf and M. Lienkamp, „Customer-Oriented Concept Assessment," in *Researchgate* 2020. Available: https://www.researchgate.net/publication/345242497 [visited on 12/13/2020].

Thesis-relevant open-source software

[70] L. Nicoletti, F. Schockenhoff and M. Bayerlein. „COCA Tool - Customer-Oriented Concept Assessment Tool," 2021. [Online]. Available: https://github.com/TUMFTM/Customer-Oriented-Concept-Assessment-COCA-Tool [visited on 12/02/2021].

[157] A. König, L. Nicoletti and K. Moller. „Modular Quasi-Static Longitudinal Simulation for BEV," 2020. [Online]. Available: https://github.com/TUMFTM/Modular-Quasi-Static-Longitudinal-Simulation-for-BEV [visited on 01/07/2020].

Supervised Student's Thesis

The following student research projects were developed within the framework of the thesis under the author's supervision in terms of content, subject matter, and scientific research, as well as under his author's authoritative guidance. In the following, the bachelor, semester, and master theses related to this dissertation are listed. Many thanks to the authors for their extensive support within the scope of this research project.

[71] E. Elagamy, „Creation of a Parametric Model for the Derivation of the Conceptual Dimensions for Battery Electric Vehicles," Master thesis, Institute for Automotive Engineering, RWTH Aachen University, Aachen, 2020.

[100] P. Köhler, „Semi-physikalische Modellierung von Antriebsstrangkomponenten für Elektrofahrzeuge," Semester thesis, Institute of Automotive Technology, Technical University of Munich, Munich, 2020.

[101] P. Köhler, „Semi-physikalische Modellierung von Antriebsstrangkomponenten für Elektrofahrzeuge," Master thesis, Institute of Automotive Technology, Technical University of Munich, Munich, 2021.

[113] S. Mayer, „Literaturrecherche: Packagemodellierung," Semester thesis, Institute of Automotive Technology, Technical University of Munich, Munich, 2020.

[114] S. Biereder, „Literaturrecherche Packagemodellierung," Semester thesis, Institute of Automotive Technology, Technical University of Munich, Munich, 2020.

[141] G. Ranocchia, „Creation of a database concept for expandable parametric vehicle architectures," Master thesis, Politecnico di Torino, Torino, 2020.

[156] R. Hefele, „Implementierung einer MATLAB Längsdynamiksimulation für Elektrofahrzeuge," Semester thesis, Institute of Automotive Technology, Technical University of Munich, Munich, 2019.

[162] A. Romano, „Data-based Analysis for Parametric Weight Estimation of new BEV Concepts," Master thesis, Institute of Automotive Technology, Technical University of Munich, Munich, 2021.

[164] A. Romano, „Datenbasierte Analyse zur geometrischen Modellierung von Reifen und Felgen," Semester thesis, Institute of Automotive Technology, Technical University of Munich, Munich, 2020.

[173] S. Mirti, „Erstellung eines parametrischen Modells zur Herleitung von Maßkonzepten für Elektrofahrzeuge," Bachelor thesis, Institute of Automotive Technology, Technical University of Munich, Munich, 2019.

[187] M. Spreng, „Maßkettenanalyse am Hinterwagen zur Erstellung von Ersatzmodellen," Bachelor thesis, Faculty of Mechanical Engineering, Ostbayerische Technische Hochschule Regensburg, Regensburg, 2020.

S. Hottner, „Data based Volumetric Modeling of Traction Batteries for Electric Vehicles," Master thesis, Institute of Automotive Technology, Technical University of Munich, Munich, 2020.

Appendix

A Exterior and Interior Concept

The exterior and interior concept dimensions considered in this work are listed in Table A.1 and A.2. A detailed description of these dimensions is documented in the SAE J1100 [51]. It is possible to skip the dimensional concept calculation and assign an already existing dimensional concept. This feature is preferable if the BEV has to be derived based on an already existing reference vehicle. To assign an existing dimensional concept, a set of optional inputs (marked with * in Table A.1 and A.2) is required.

Table A.1: Exterior concept dimensions considered in this thesis. Based on [51].

Code	Definition according to the SAE
A106-1	Angle of approach: Smallest angle in side view formed by the ground and the line tangent to the front tire static-loaded radius arc and the underside of the vehicle, including all flexible components
A106-2	Angle of departure: Smallest angle in side view formed by the ground and the line tangent to the rear tire static-loaded radius arc and the underside of the vehicle, including all flexible components
A117	Ramp breakover angle at maximum load: Supplement of an angle between two lines tangential to the front and rear tire static laden radii at the gross vehicle mass and intersecting at a point on the underside of the vehicle which defines the largest ramp over which the vehicle can roll
L101*	Wheelbase: Longitudinal distance from the front wheel centerline to the rear wheel centerline
L103	Vehicle length: Maximum longitudinal distance between the foremost point and the rearmost point on the vehicle
L104*	Vehicle front overhang: Longitudinal distance from the centerline of the front wheels to the foremost point on the vehicle
L105*	Vehicle rear overhang: Longitudinal distance from the centerline of the rear wheels to the rearmost point on the vehicle
L113*	Longitudinal distance between the front wheel centerline and the driver's BOF
L114	Longitudinal distance between the front wheel centerline and the driver's SgRP
L115-2	Longitudinal distance from the SgRP-2 to the centerline of the rear wheels
H100*	Vehicle height: Maximum distance on the BIW normal to the ground excluding hardware and trim (such as roof racks, antennas, spoilers, etc.)
H101	Vehicle height: Maximum distance on the BIW normal to the ground including hardware and trim (such as roof racks, antennas, spoilers, etc.)
H156	Ground clearance: Minimum distance from the underside of the vehicle (i.e. sprung mass) to the ground. Unsprung parts and assemblies are typically excluded
W103*	Vehicle width: Maximum lateral distance between the widest points on the vehicle (side mirrors excluded)
W117	Body width at the SgRP: Maximum lateral distance between the natural shape of the vehicle through the SgRP

Table A.2: Interior concept dimensions considered in this thesis. Based on [51].

Code	Definition according to the SAE
A40	Angle of the manikin torso from the vertical
A44	Angle between the thigh line and the (lower) leg line
A46	Angle between the (lower) leg line and the bare foot flesh line
A47-1*	Acute angle of the driver's shoe plane from horizontal
A47-2*	Acute angle of the passenger (second row of seats) shoe plane from horizontal
A57	Angle of the thigh line from horizontal
L50-2	Longitudinal distance between the SgRPs of the first and second row of seats
L53-1*	Longitudinal distance between SgRP and AHP
L53-2*	Longitudinal distance between SgRP-2 and FRP
L99-1	Longitudinal distance between the driver's BOF and SgRP
L99-2*	Longitudinal distance between the driver's BOF and SgRP-2
H5-1	Minimum distance between SgRP and ground
H5-2	Minimum distance between SgRP-2 and ground
H30-1*	Vertical distance from SgRP to the AHP
H30-2*	Vertical distance from SgRP to the FRP
H61-1*	Distance along a line $8°$ rear of vertical from the SgRP to the first limiting surface plus $102\,\mathrm{mm}$
H61-2*	Distance along a line $8°$ rear of vertical from the SgRP-2 to the first limiting surface plus $102\,\mathrm{mm}$
SL14	Maximum seat thickness measured through the seatback
SW16-1	Maximum lateral distance across the trimmed width of the driver's seat cushion
W3	Minimum lateral distance between the trimmed door surfaces within the measurement zone defined by the SAE J1100
W5	Minimum lateral distance between the trimmed door surfaces within the measurement zone defined by the SAE J1100
W9	Maximum diameter of the steering wheel
W20-1*	Lateral distance between SgRP and vehicle center
W20-2*	Lateral distance between SgRP-2 and vehicle center
W27	Diagonal head clearance, defined using the side view top contour defined by the SAE J1052
W31-1	Lateral distance between the trimmed door surfaces within the measurement zone defined by the SAE J1100
W35	Lateral head clearance, defined using the side view top contour defined by the SAE J1100

B Drive Topology

This section outlines the electric machine (Section B.1) and battery topologies (Section B.2) considered in this work.

B.1 Electric Machine Topology

Figure B.1 shows the drive unit configurations resulting from the combination between the electric machine topologies (Figure 2.6) and gearbox types (Subsection 3.4.4). The red arrow in Figure B.1 points toward the driving direction.

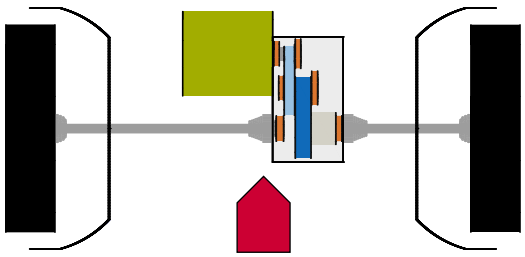

(a) Central machine (in front of the axle) with a parallel axles gearbox. Example: VW e-Up.

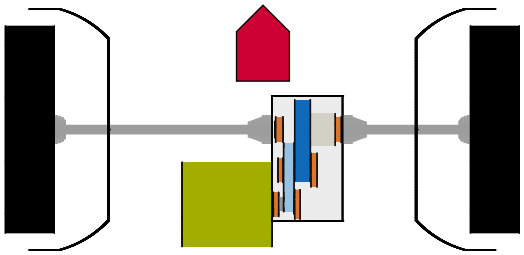

(b) Central machine (behind the axle) with a parallel axles gearbox. Example: Tesla Model Y.

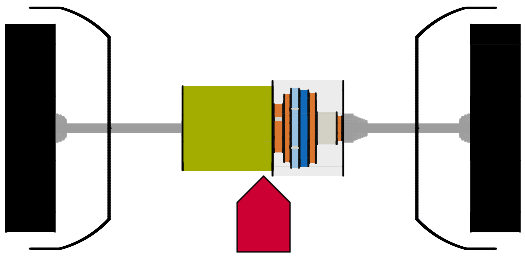

(c) Central machine in coaxial design with a planetary gearbox. Example: Jaguar I-Pace.

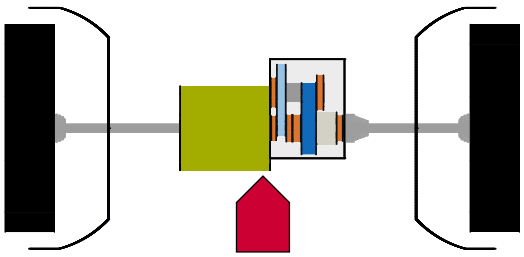

(d) Central machine in coaxial design with a coaxial gearbox. Example: Opel Ampera.

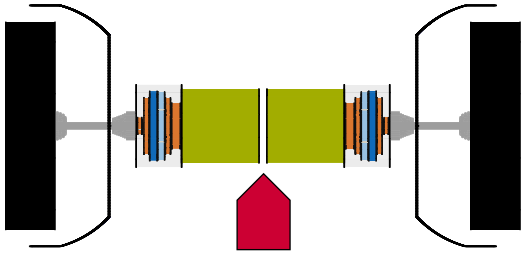

(e) Machine near to the wheel in coaxial design with a planetary gearbox. Example: Audi e-tron S.

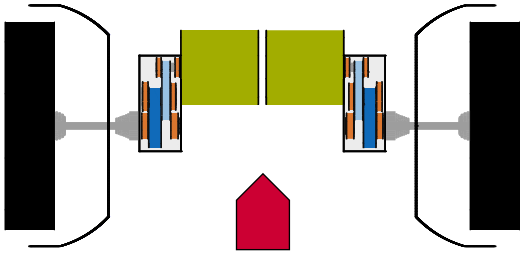

(f) Machine near to the wheel with a parallel axles gearbox. Example: Rimac Concept 2.

Figure B.1: Existing electric machine topologies and gearbox types.

B.2 Traction Battery Topology

This section presents the battery shapes and cell layouts of some of the vehicles used for characterizing the battery topology. Information regarding cell layout and battery shapes is obtained from open-source publications, the manufacturer's sites, and internet documents. The white arrow in Figure B.2 - B.4 points toward the driving direction.

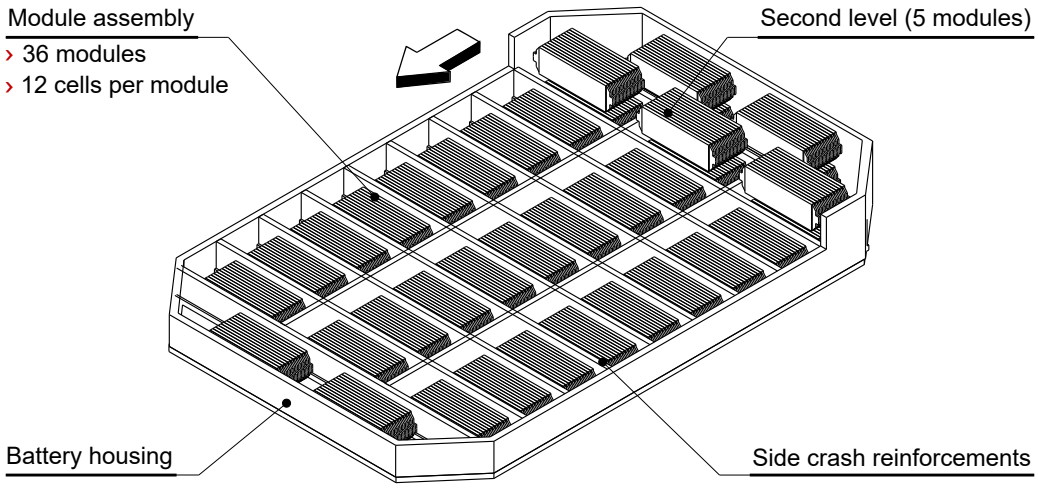

(a) Audi e-tron (2019): highfloor battery, drop shape with second level. Based on [83].

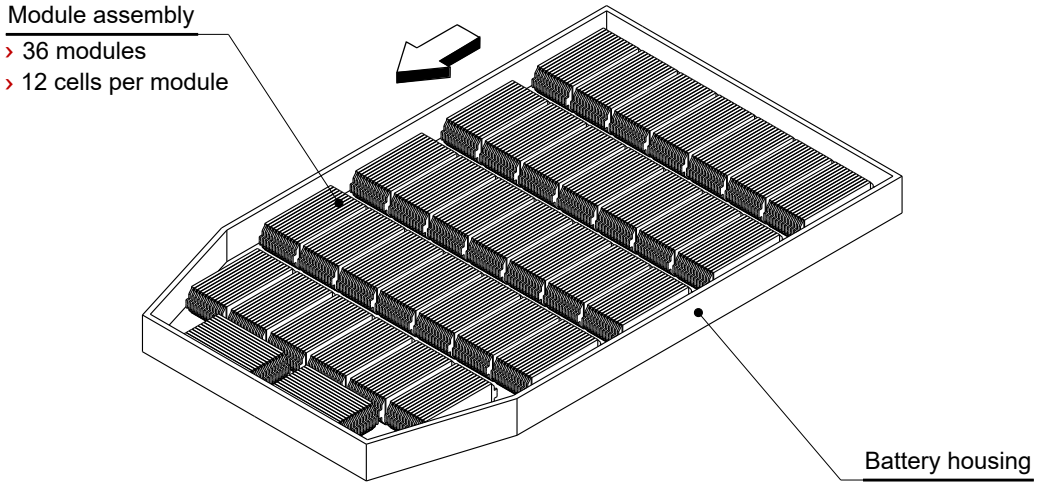

(b) Jaguar I-pace (2018): highfloor battery, drop shape. Based on [245].

Figure B.2: Existing battery designs (Part 1/3).

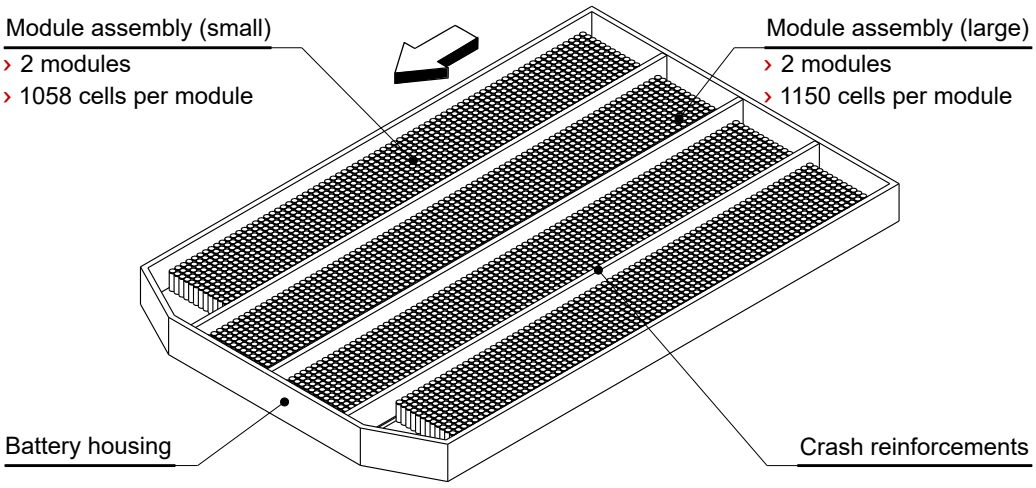

(a) Tesla Model 3 (2017): highfloor battery, drop shape. Based on [246, 247].

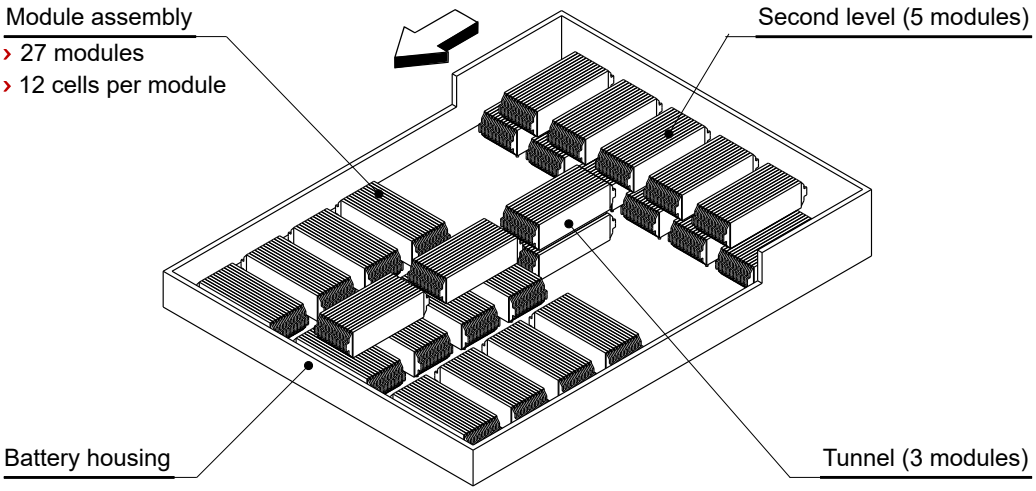

(b) Polestar 2 (2020): highfloor battery, rectangular shape with second level and tunnel. Based on [248].

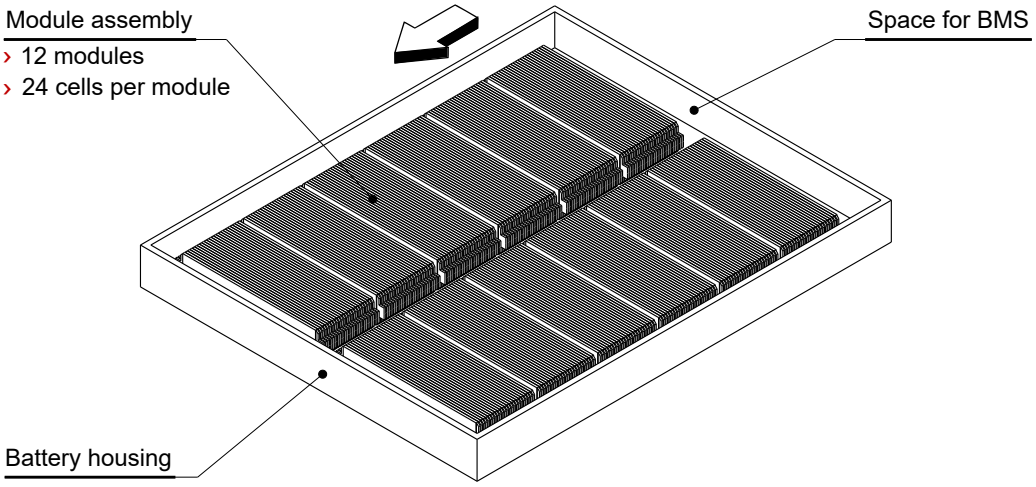

(c) VVW ID.3 Pro S (2020): highfloor battery, rectangular shape. Based on [249, 250].

Figure B.3: Existing battery designs (Part 2/3).

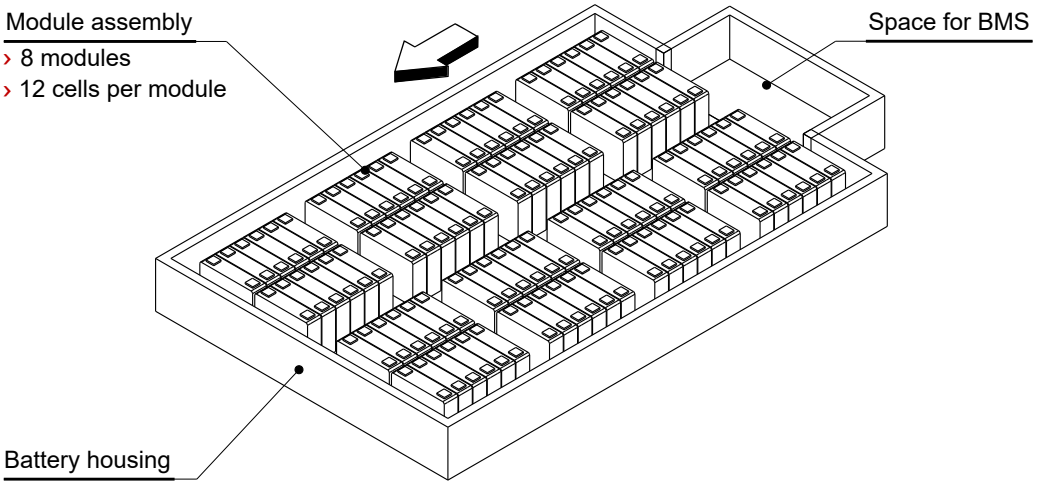

(a) BMW i3 (2017): highfloor battery, rectangular shape. Based on [251, 252].

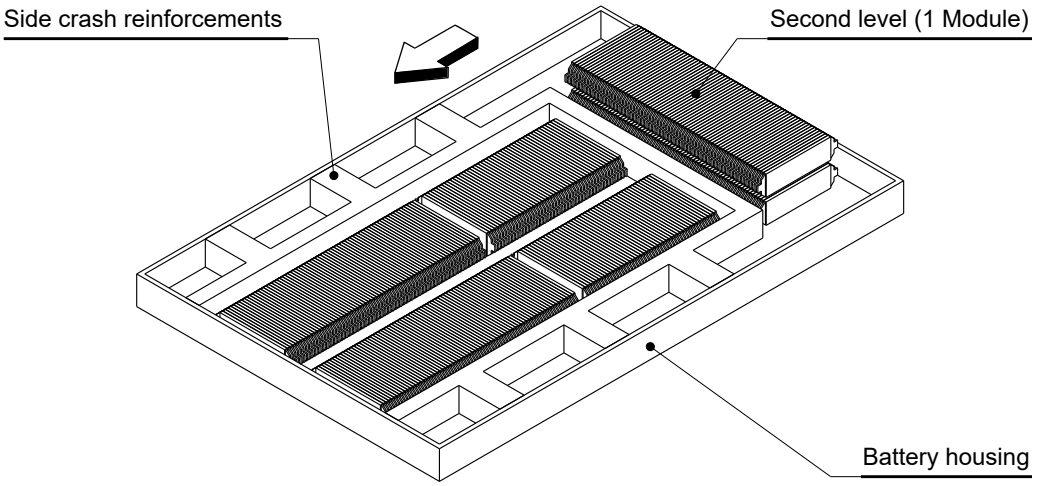

(b) Mercedes EQC (2020): highfloor battery, rectangular basic shape, with second level. Based on [253].

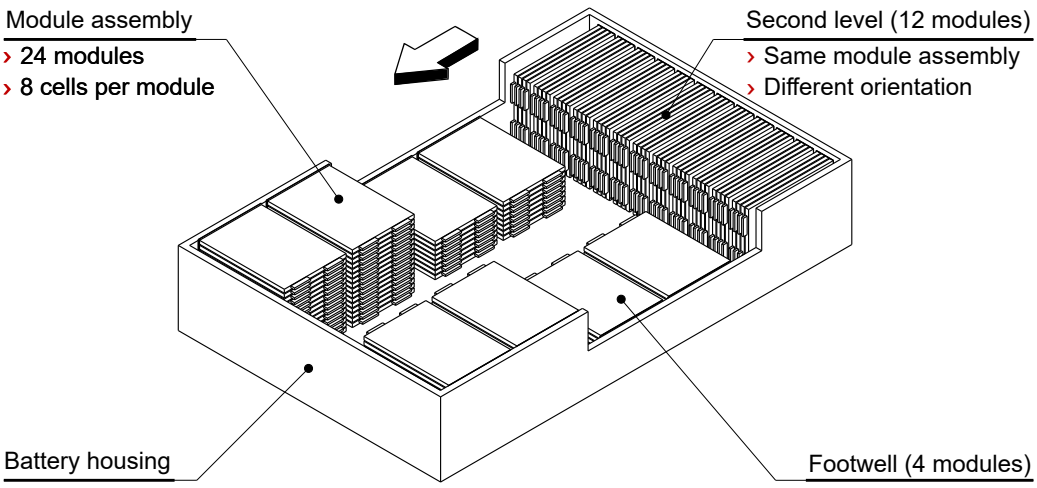

(c) Nissan Leaf (2018): mixedfloor battery, rectangular shape with second level and footwell at the second row of seats. Based on [92, p. 146, 254].

Figure B.4: Existing battery designs (Part 3/3).

C Longitudinal Simulation, the WLTP

The procedure for calculating vehicle consumption and emission in Europe is documented in the WLTP [255]. The first step of the WLTP is the definition of a test cycle, i.e. the WLTC. For this purpose, the vehicles are divided into classes according to their power-to-mass ratios and speed [256, pp. 494-495]. Each class corresponds to a different WLTC. Most BEVs belong to class 3b, which is therefore further considered in this section. A class 3b cycle (Figure C.1) consists of a low, a medium, a high, and an extra high phase [256, p. 495].

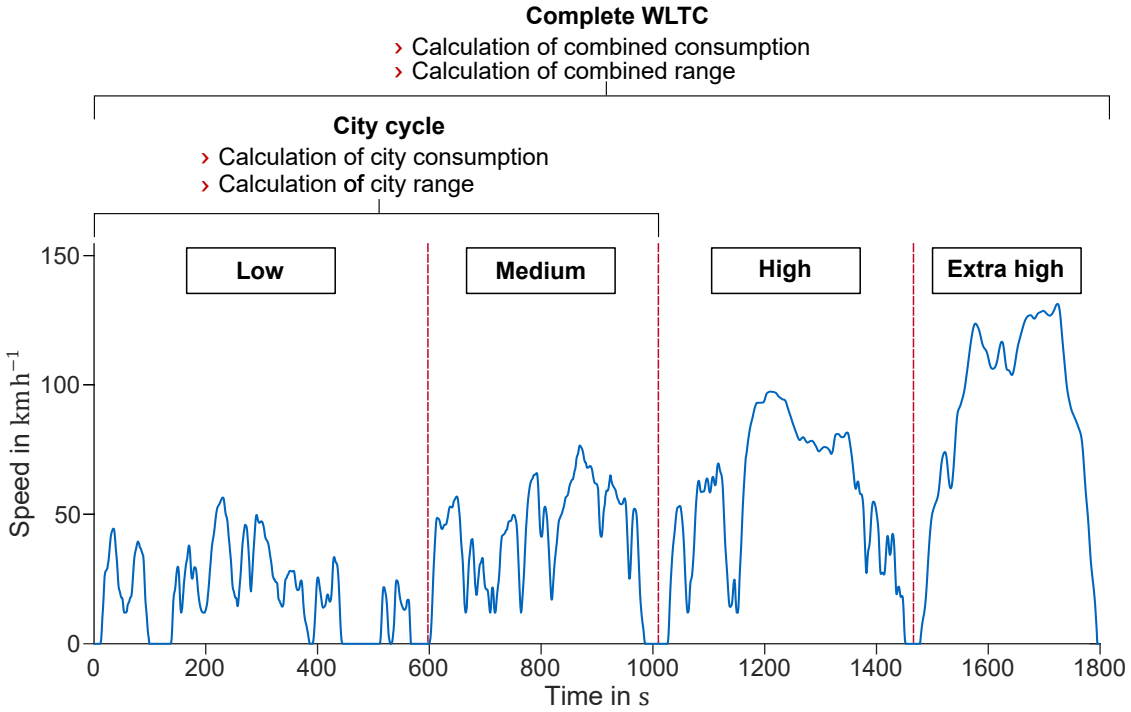

Figure C.1: Speed profile of a class 3b WLTC. The cycle covers a distance of $23.3\,\mathrm{km}$ and has a duration of $1800\,\mathrm{s}$, with an average speed of $46.5\,\mathrm{km\,h^{-1}}$ and a maximum speed of $131\,\mathrm{km\,h^{-1}}$ [257] . Data from [256, pp. 522-540].

The first two phases (low and medium) simulate an urban trip and are referred to as *city cycle*. The high and extra high phases simulate a high-speed road and highway profile. While the city cycle is used to calculate the city consumption, all four phases are used for the estimation of the combined consumption. The combined consumption is further considered since the vehicles simulated by the architecture tool are not sized exclusively for urban trips. For calculating combined consumption, there are two possible procedures [256, p. 743-745]: Consecutive Test Procedure and Shortened Test Procedure (STP). As the name suggests, the consecutive test procedure consists of a maximum of three consecutive WLTCs. Nevertheless, this procedure is only applicable to BEVs with a range below $70\,\mathrm{km}$ [256, p. 743-745]. Since most BEVs have greater ranges, the STP (Figure C.2) is used to reduce the test duration.

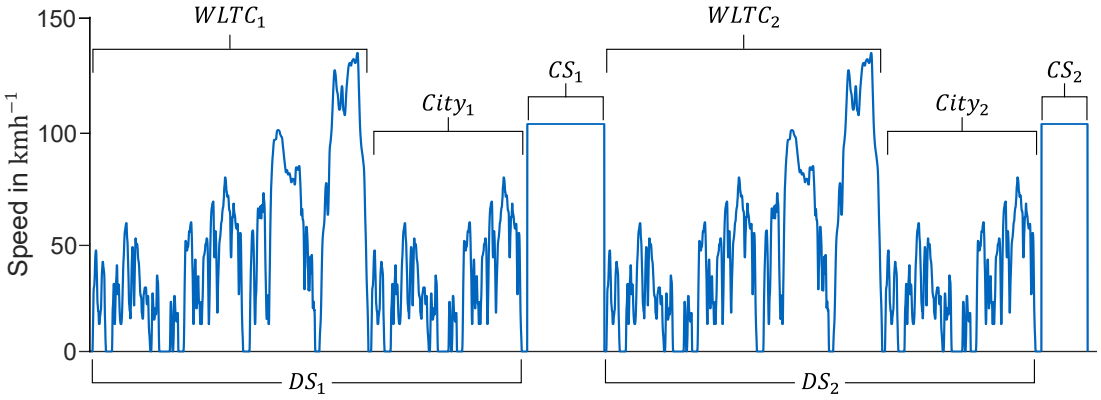

Figure C.2: STP with two dynamic segments (DS_1 and DS_2) and two constant speed segments with a velocity of $100\,\mathrm{km\,h^{-1}}$ (CS_1 and CS_2). Each dynamic segment is composed of a standard WLTP ($WLTC_1$ and $WLTC_2$) and city cycle ($City_1$ and $City_2$). Based on [256, p. 745].

The STP is composed of two dynamic and two constant speed segments. The dynamic segments (DS_1 and DS_2, Figure C.2) include a complete WLTC and an additional city cycle. The constant speed segments (CS_1 and CS_2, Figure C.2) are not relevant for estimating consumption and are only used to deploy the battery, thus shortening the test duration. Their length is not fixed, but rather depends on the battery energy of the vehicle. The combined range $R_{\mathrm{WLTP,comb}}$ is calculated according to Equation (C.1).

$$R_{\mathrm{WLTP,comb}} = \frac{E_{\mathrm{STP}}}{C_{\mathrm{DS,WLTC}}} = \frac{E_{\mathrm{STP}}}{C_{\mathrm{WLTC1}}\,K_1 + C_{\mathrm{WLTC2}}\,K_2} \tag{C.1}$$

Where E_{STP} is the usable battery energy during the entire procedure (which corresponds to the net battery energy), and $C_{\mathrm{DS,WLTC}}$ is the energy consumption of the WLTC parts ($WLTC_1$ and $WLTC_2$ in Figure C.2) of the dynamic segments [256, p. 768]. The $C_{\mathrm{DS,WLTC}}$ is expressed as the weighted sum of the consumption in the WLTC parts (C_{WLTC1} and C_{WLTC2}). The weighting factors K_1 and K_2 are calculated according to [256, p. 768]. With the combined range from Equation (C.1), the combined consumption $C_{\mathrm{WLTP,comb}}$ is derived according to:

$$C_{\mathrm{WLTP,comb}} = \frac{E_{\mathrm{AC}}}{R_{\mathrm{WLTP,comb}}} \tag{C.2}$$

Where E_{AC} is the energy required to fully recharge the battery after the STP. E_{AC} is measured at the vehicle charger [256, p. 747] and includes the losses occurring in the charger, cables, and battery during the charging process. The manufacturers usually publish the combined consumption $C_{\mathrm{WLTP,comb}}$ and the combined range $R_{\mathrm{WLTP,comb}}$. However, the combined consumption does not correspond to the combined range: $C_{\mathrm{WLTP,comb}}$ includes charging losses (Equation (C.2)), while $R_{\mathrm{WLTP,comb}}$ is derived from the actual measured consumption in the cycle $C_{\mathrm{DS,WLTC}}$ and does not include charging losses (Equation (C.1)).

The LDS implemented in this work does not consider charging losses since the high variability of existing charging plugs and strategies complicates modeling this feature [258, 259]. Therefore, the main output of the LDS is $C_{\mathrm{DS,WLTC}}$, which is not comparable with the $C_{\mathrm{WLTP,comb}}$ values given by the manufacturers. One way to filter out charging losses from the manufacturer values (thus estimating $C_{\mathrm{DS,WLTC}}$), is by inverting Equation (C.1), with the assumption that the usable energy during the test procedure E_{STP} is equal to the net battery energy. The net battery energy is usually documented in the ADAC database [149]. This method will be used during the vehicle architecture tool validation in Section 4.4.

D Volumetric Component Modeling

This section provides additional information for the models developed for the tires (Section D.1), interior (Section D.2), gearbox (Section D.3), electric machine (Section D.4), and battery (Section D.5).

D.1 Tires

For estimating the tire volume, the vehicle architecture tool performs a sizing based on the maximum occurring axle loads. The axle loads are derived from the momentum and force balance of the weight forces of the passengers, luggage, and vehicle. Figure D.1 shows the modeling approach used to describe the position of the Center of Gravity (COG) of these components.

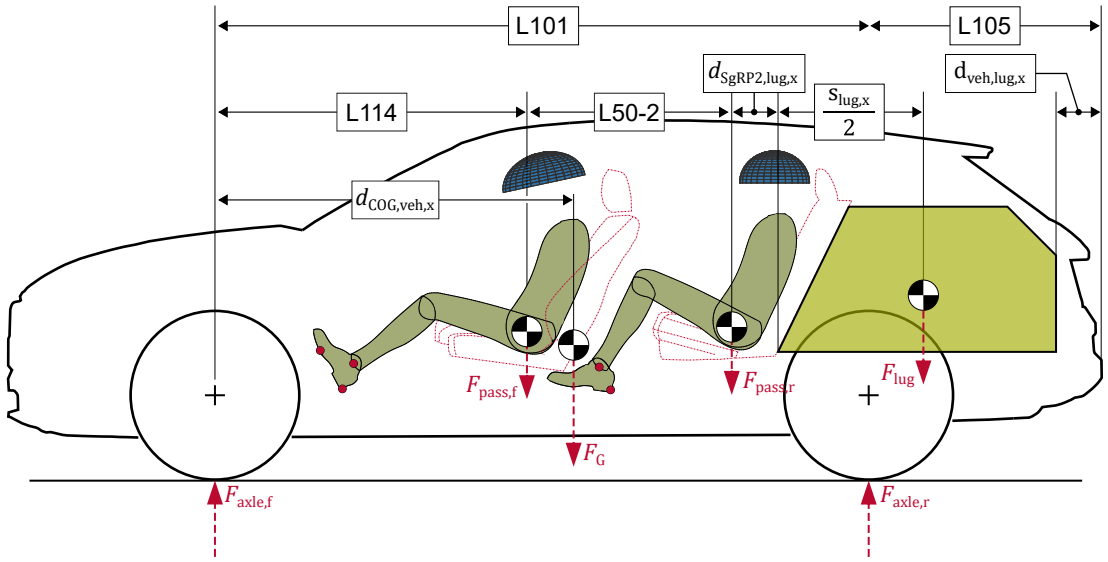

Figure D.1: Dimensional chain for positioning the forces of a fully-loaded vehicle.

The empty vehicle weight force F_G (in N) is derived from the empty mass of the current iteration in m_n. Subsequently, F_G is positioned at the vehicle COG $d_{COG,veh,x}$, which is calculated with the vehicle's mass distribution at the rear axle $K_{rep,r}$ (in %, typical values in Subsection 3.5.2) according to Equation (D.1).

$$d_{COG,veh,x} = L101 \frac{K_{rep,r}}{100} \tag{D.1}$$

In accordance with [55, p. 4], the driver is modeled with a mass of 75 kg. The same value is also used for the other passengers. The passenger's weight forces $F_{pass,f/r}$ are positioned at the

seating reference points, which are in turn calculated by the interior model (Subsection 3.4.3). The interior model also estimates the available luggage length $s_{\mathrm{lug,x}}$ using the dimensional chain shown in Equation (D.2).

$$s_{\mathrm{lug,x}} = L101 + L105 - L114 - L50\text{-}2 - d_{\mathrm{SgRP2,lug,x}} - d_{\mathrm{veh,lug,x}} \tag{D.2}$$

Where $d_{\mathrm{SgRP2,lug,x}}$ is the minimum longitudinal distance between SgRP-2 and the luggage compartment. This element of the dimensional chain models the space requirements for the passenger torso and the seat thickness. $d_{\mathrm{veh,lug,x}}$ models the loss of available luggage compartment length caused by trunk frame and bumpers. These two chain elements are modeled empirically with constant values. By combining Equation (D.2) with the other interior concept dimensions, the tool derives the luggage compartment COG (which is assumed to be half the luggage length, Figure D.1). Estimating the luggage load F_{lug} requires the payload given by the vehicle manufacturer. Since it usually includes the mass of the passengers, F_{lug} is calculated from the difference between payload and passenger weight forces.

Once all occurring forces are calculated, the axle loads are estimated. The vehicle architecture tool simulates the axle loads at each iteration to check whether a resizing of the tires is required.

D.2 Interior

For the sizing of the second row of seats, the internal dimension H61-2 is used (Subsection 3.4.3). H61-2 depends on the design and shape of the vehicle's rear-end. For this reason, it is not possible to derive an empirical regression between the H61-2 and other internal dimensions. For the calculation in the vehicle architecture tool, three body-type-dependent H61-2 values are derived from the interior dataset (Table D.1). Since the H61-2 values are derived from existing vehicles, they can be varied within the limits specified by the corresponding standard deviations, while ensuring that sufficient headroom is available for the passengers.

Table D.1: Typical H61-2 values derived from the interior dataset. The H61-2 given in this table does not include the 102 mm prescribed by the SAE J1100 (compare Table A.2).

Body type	Mean value	Standard deviation	Number of evaluated vehicles
SUV	877.4 mm	17.9 mm	64
Hatchback	846.4 mm	23.1 mm	57
Sedan	845.8 mm	22.8 mm	18

D.3 Gearbox

For modeling the gearbox, the gears, shafts, and bearings are considered separately. The semi-physical gearbox model is documented in the theses of Köhler [100, 101] and a previous publication [27], and will not be further detailed in this thesis. This section only presents the dimensional chains (derived from the gearbox dataset) used for sizing the housing.

Figure D.3 shows the dimensional chains describing the gearbox length $s_{\mathrm{gb,x}}$ and its height $s_{\mathrm{gb,z}}$. Based on the calculated gear diameters, the axle distance between the first and second shaft

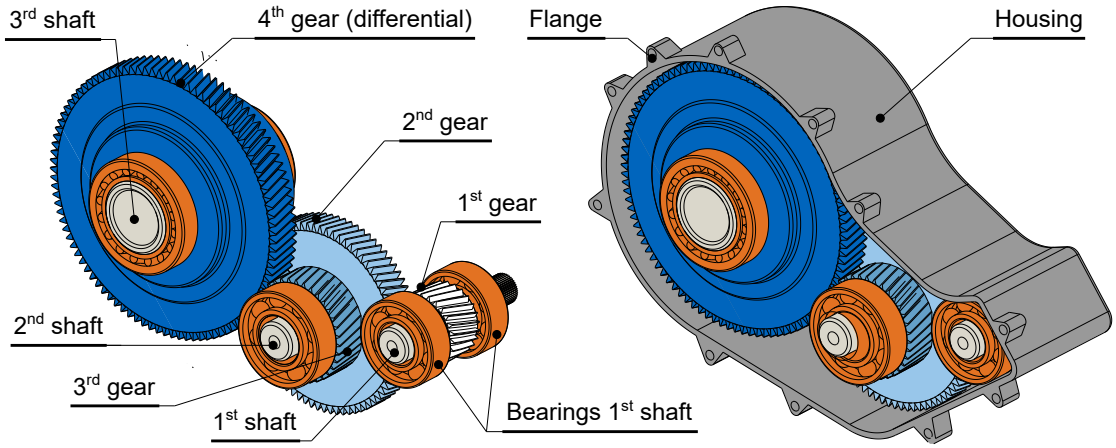

Figure D.2: Typical layout of a parallel axles gearbox with two reduction stages.

($d_{\text{gb,shafts,12}}$) and between the second and third shaft ($d_{\text{gb,shafts,23}}$) are derived. In some vehicles, such as the Renault Twizy, the centers of the three shafts are collinear. However, in most cases, they are not arranged on a straight line and, to describe their relative position, the angles α_{12} and α_{23} are introduced (Figure D.3). An analysis of the gearbox dataset identifies an empirical range between 20° and 40° for α_{12} and α_{23}, respectively.

In the gearbox model, the shafts are arranged based on the chosen sizing options. It is possible to choose between an arrangement that minimizes the gearbox length or one that minimizes its height. Consequently, the angles are tuned within the empirical range to minimize the selected option.

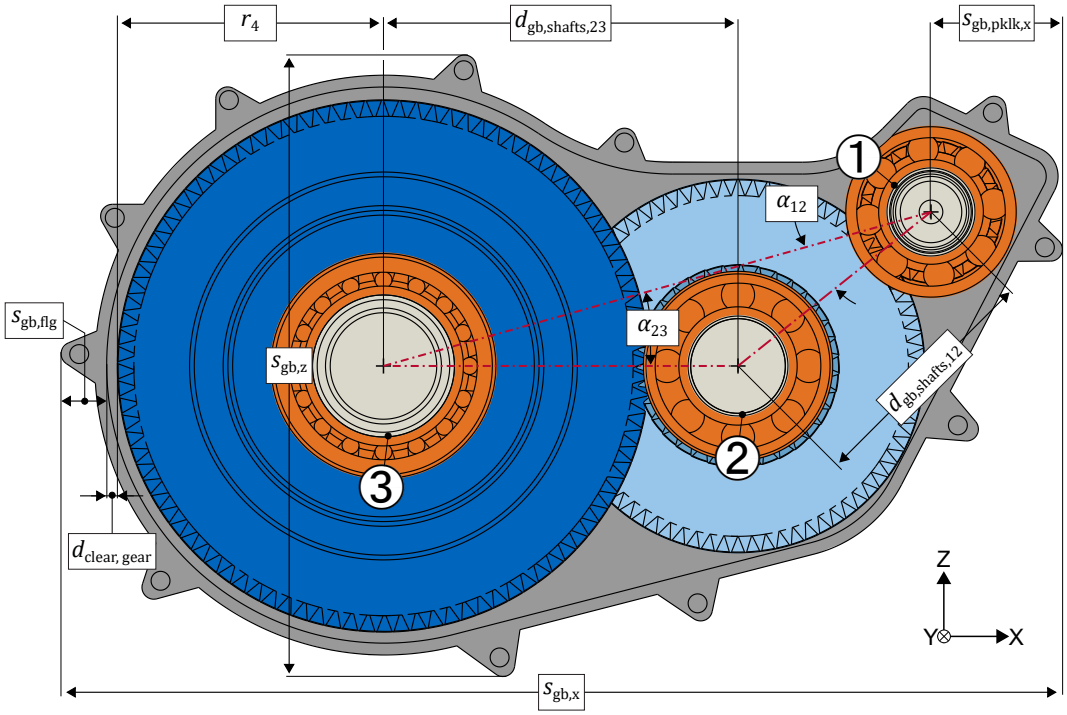

Figure D.3: Typical arrangement of a parallel axle gearbox. The figure shows the first shaft ① (which is directly connected with the electric machine), the middle shaft ②, and the differential (or output) shaft ③.

Based on the calculated angles, the dimensional chain in Equation (D.3) is applied to estimate the total gearbox length $s_{\mathrm{gb,x}}$.

$$s_{\mathrm{gb,x}} = s_{\mathrm{gb,flg}} + d_{\mathrm{clear,gear}} + r_4 + [d_{\mathrm{gb,shafts,23}}\, cos(\alpha_{23}) + d_{\mathrm{gb,shafts,12}}\, cos(\alpha_{12})]\, cos(\alpha_{23}) + s_{\mathrm{gb,pklk,x}} \quad \text{(D.3)}$$

In Equation (D.3), $s_{\mathrm{gb,flg}}$ includes the housing thickness and flanges, while $d_{\mathrm{clear,gear}}$ is the clearance between the differential wheel and the inner side of the gearbox housing. On the side of the first shaft (①, Figure D.3), the critical component is the parking lock wheel. In most cases, the parking lock wheel is placed on the first shaft and has a greater diameter than the first gear. To consider its influence on the housing dimensions, the term $s_{\mathrm{gb,pklk,x}}$ is introduced. This element is derived from the gearbox database as well. As shown in Figure D.3 and in Equation (D.3), the differential wheel has a great influence on the gearbox length $s_{\mathrm{gb,x}}$. Since it is usually the biggest wheel in the gearbox, the differential wheel also determines the gearbox height $s_{\mathrm{gb,z}}$, which is calculated in Equation (D.4).

$$s_{\mathrm{gb,z}} = 2\,[r_4 + d_{\mathrm{clear,gear}} + s_{\mathrm{gb,flg}}] \quad \text{(D.4)}$$

The gearbox width $s_{\mathrm{gb,y}}$ (not represented in Figure D.3) is derived with the last dimensional chain. For this scope, the width of the gears $s_{\mathrm{gb,gears,y}}$ (which represents the width of the components on the left-hand side of Figure D.2) is calculated by the gearbox model and inserted into Equation (D.5).

$$s_{\mathrm{gb,y}} = s_{\mathrm{gb,gears,y}} + 2\, s_{\mathrm{gb,seal,y}} \quad \text{(D.5)}$$

In addition, the term $s_{\mathrm{gb,seal,y}}$ considers the housing thickness and the installation space for the sealing rings placed on the first and third shaft. Table D.2 summarizes the chain elements discussed in this section.

Table D.2: Dimensional chain elements for the gearbox model. Based on [101, p. 60].

Chain element	Mean value	Description
$s_{\mathrm{gb,pklk,x}}$	100 mm	Required space by the parking lock wheel, and housing
$d_{\mathrm{clear,gear}}$	5.5 mm	Clearance between differential and housing
$s_{\mathrm{gb,flg}}$	25 mm	Thickness of flange and housing thickness
$s_{\mathrm{gb,seal,y}}$	12 mm	Required installation space for the gearbox sealing ring

D.4 Electric Machine

Apart from the machine technology (such as IM or PMSM, Subsection 2.2.2), another possible categorization for electric machines is based on the rotor-stator layout. Electric machines can be divided into inrunners (the rotor is placed inside the stator) and outrunners (the stator is placed inside the rotor). Outrunner machines are normally used for wheel-hub motors or in mild hybrid vehicles [189, p. 344]. Since these two cases are not covered in this thesis, the developed volumetric models exclusively consider the inrunner layout (Figure D.4). For modeling, a benchmark analysis is conducted on the machine dataset. More information regarding this analysis is documented in the thesis of Köhler [101, pp. 41-47]. In the following paragraphs, the workflow of the machine sizing model is briefly explained.

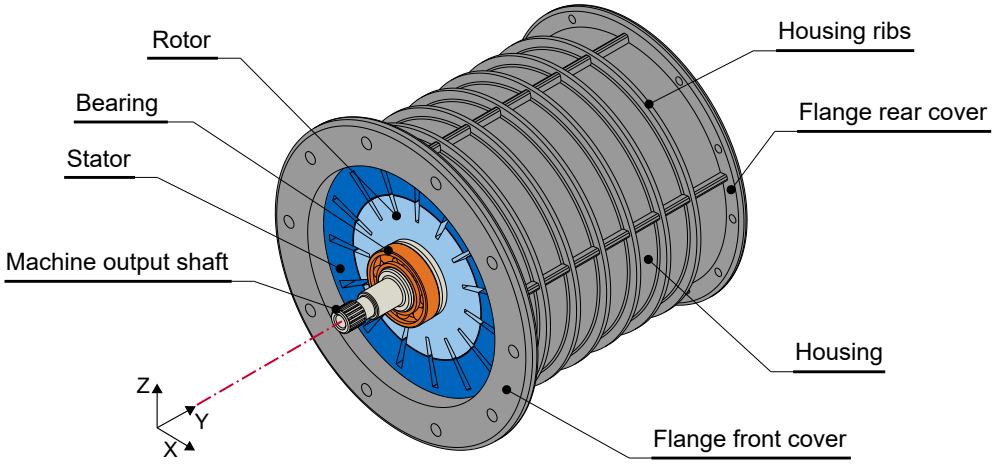

Figure D.4: Typical structure of an electric machine with its sub-components.

In the first step, the stator (marked as dark blue in Figure D.4) is dimensioned. Its sizing is based on the empirical regression in Equation (D.6), which estimates the stator volume $V_{\mathrm{mach,stat}}$ from the maximum machine power $P_{\mathrm{mach,max}}$ (in kW).

$$V_{\mathrm{mach,stat}} = -2.7930\,\mathrm{l} + (0.0948\,\mathrm{l\,kW^{-1}})\,P_{\mathrm{mach,max}} \tag{D.6}$$

Given the stator volume $V_{\mathrm{mach,stat}}$, the corresponding diameter $D_{\mathrm{mach,stat}}$ (expressed in mm and shown in Figure D.5) is derived according to Equation (D.7).

$$D_{\mathrm{mach,stat}} = \left(\frac{4\,V_{\mathrm{mach,stat}}\,10^{6}}{\pi\,K_{\mathrm{stat}}} \right)^{\frac{1}{3}} \quad \text{where} \quad K_{\mathrm{stat}} = \frac{s_{\mathrm{mach,stat,y}}}{D_{\mathrm{mach,stat}}} \tag{D.7}$$

K_{stat} is the stator's length to diameter ratio. Köhler [101, p. 46] estimates a K_{stat} of 0.986 for PMSMs and of 0.865 for IMs. With Equation (D.6) and (D.7), the dimensions of the stator are fully defined. Nevertheless, to estimate the machine dimensions, a consideration of the housing is also required. For this scope, the dimensional chains shown in Equation (D.8) and (D.9) are used.

$$D_{\mathrm{mach}} = D_{\mathrm{mach,stat}} + 2\,s_{\mathrm{mach,rib,x}} + 2\,s_{\mathrm{mach,hous,x}} \tag{D.8}$$

$$s_{\mathrm{mach,y}} = s_{\mathrm{mach,stat,y}} + d_{\mathrm{mach,stat,y}} \tag{D.9}$$

Equation (D.8) yields the outer diameter of the machine housing D_{mach}, which considers, besides the stator diameter, also the thickness of the housing $s_{\mathrm{mach,hous,x}}$ and of its ribs $s_{\mathrm{mach,rib,x}}$ (Figure D.5). The flanges for the front and rear cover (which usually have a wider diameter to accommodate the bolts fixing the covers) are neglected for the calculation of D_{mach}.

Equation (D.9) yields the machine length $s_{\mathrm{mach,y}}$, which also includes the space requirements of the housing covers (not shown in Figure D.5). For this scope, the empirical factor $d_{\mathrm{mach,stat,y}}$ is derived from the difference between stator length and housing length. Table D.3 summarizes the terms required for the dimensional chains in Equation (D.7) - (D.9).

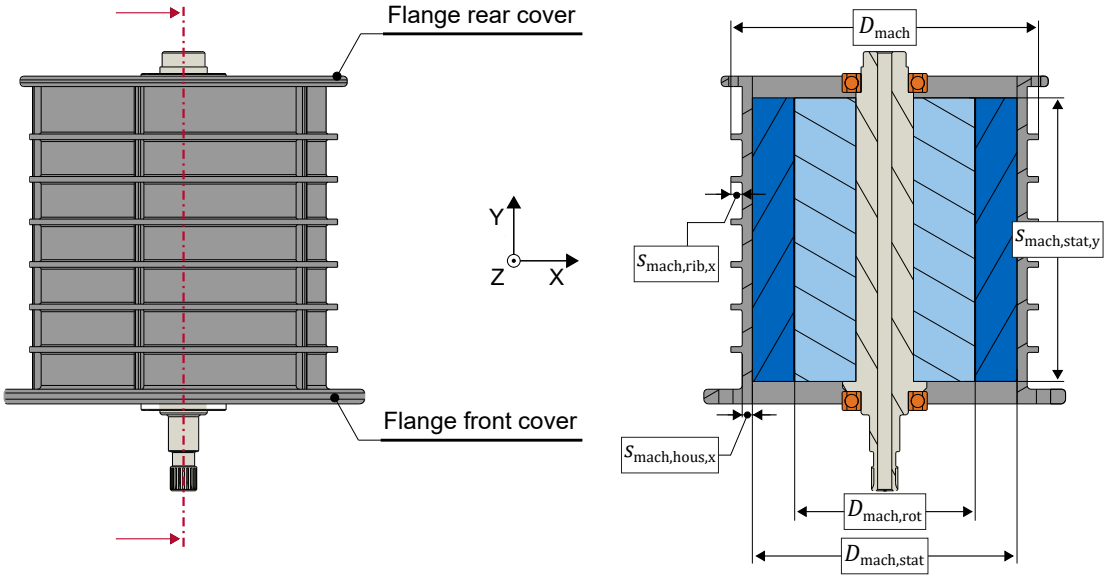

Figure D.5: Section view of an electric machine with its sub-components.

Table D.3: Dimensional chain elements for the electric machine model. Based on [101, p. 46].

Chain element	Mean value	Description
$K_{stat,PMSM}$	0.986	Stator length to stator diameter ratio for PMSMs
$K_{stat,IM}$	0.865	Stator length to stator diameter ratio for IMs
$s_{mach,rib,x}$	13.4 mm	Machine housing thickness
$s_{mach,hous,x}$	12.44 mm	Height of the rims of the machine housing
$d_{mach,stat,y}$	74.00 mm	Difference between stator and machine length

D.5 Traction Battery

For filling the available battery space, package factors and dimensional chains are derived from the battery dataset. To understand how the package factors are derived, Figure D.6 shows a simplified battery pack.

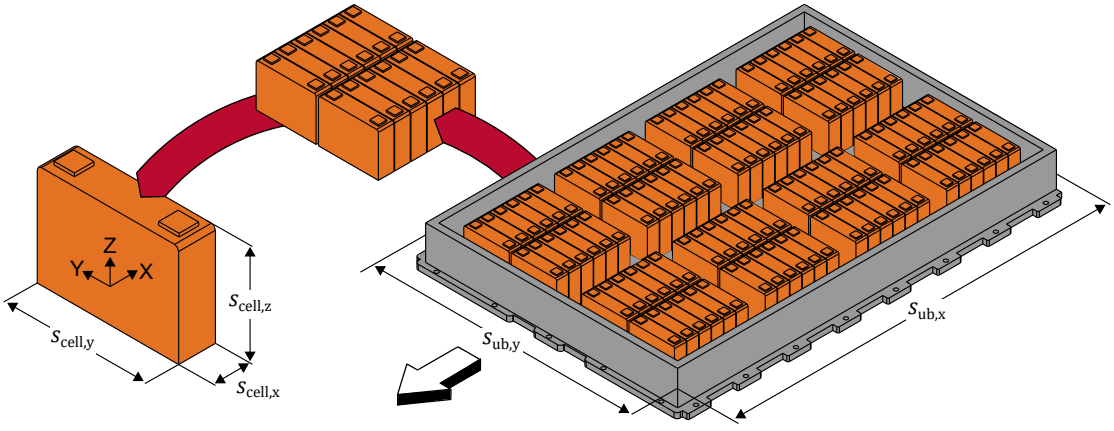

Figure D.6: A rectangular shape with prismatic cells. The white arrow points towards the driving direction.

For the calculation, a coordinate system is defined, where the x-direction is parallel to the driving direction. The package factor along x $K_{\text{pack,x}}$ is derived according to Equation (D.10).

$$K_{\text{pack,x}} = \frac{N_{\text{cell,x}}\, s_{\text{cell,x}}}{s_{\text{ub,x}}} \tag{D.10}$$

Where $N_{\text{cell-x}}$ is the number of cells along the x-direction. In the case shown in Figure D.6, it is equal to 24. The same procedure is applied for the y-direction (Equation (D.11)).

$$K_{\text{pack,y}} = \frac{N_{\text{cell,y}}\, s_{\text{cell,y}}}{s_{\text{ub,y}}} \tag{D.11}$$

Where the number of cells $N_{\text{cell,y}}$ is equal to four. The battery in Figure D.6 is one of the simplest layouts possible. As shown in Section B.2, some vehicles have cells in the second level or in the tunnel and not necessarily with the same orientation as in the underbody. In these cases, separate $K_{\text{pack,x}}$ and $K_{\text{pack,y}}$ are derived for each installation space. Figure D.7 gives an overview of underbody batteries. More information is specified in the thesis of Köhler [101, p. xxiii].

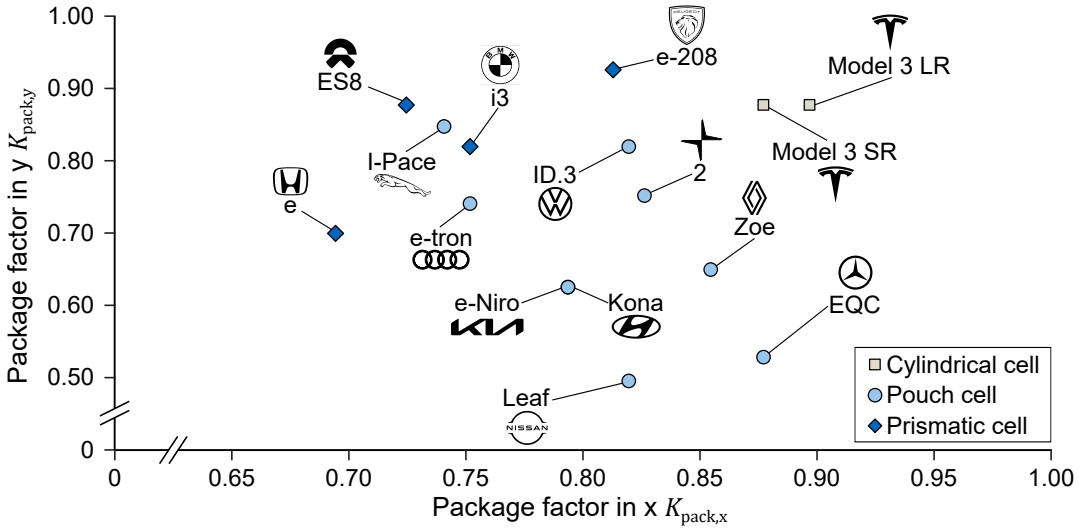

Figure D.7: Typical package factors for underbody batteries. Based on [101]

In contrast to the x- and y-directions, the z-direction shows less variability between manufacturers and is therefore modeled with a dimensional chain. Figure D.8 shows the main components of the chain. Starting from the underbody height $s_{\text{ub,z}}$, the chain derives the available cell space along the z-direction $s_{\text{cell,av,z,ub}}$ according to Equation (D.12).

$$s_{\text{cell,av,z,ub}} = s_{\text{ub,z}} - s_{\text{batt,lowp,z}} - s_{\text{batt,cool,z}} - d_{\text{cell,mod,z}} - d_{\text{clear,batt,z}} - s_{\text{batt,cover,z}} \tag{D.12}$$

Where $s_{\text{batt,lowp,z}}$ represents the thickness of the lower protection and $s_{\text{batt,cool,z}}$ the thickness of the cooling system. The latter is normally composed of a cooling plate installed underneath the cell modules (Figure D.8). An exception is the manufacturer Tesla, which cools the battery with water pipes running within the modules [260]. This solution reduces the battery height (since $s_{\text{batt,cool,z}}$ is equal to 0) at the cost of a loss of space along the y-direction (where the cooling pipes are installed).

The factor $d_{\text{cell,mod,z}}$ considers the space required by the housing components of the module. Köhler derives three different values depending on cell type [101, p. 76]. Furthermore, $d_{\text{clear,batt,z}}$

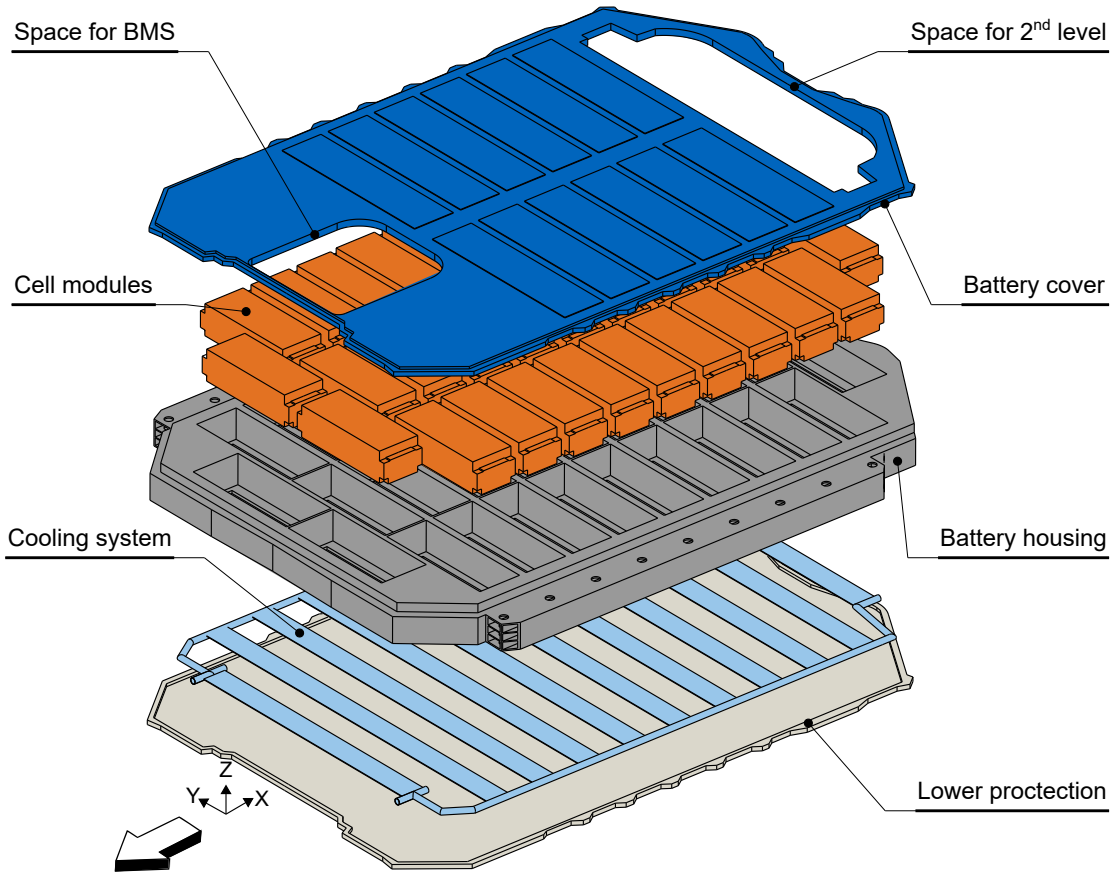

Figure D.8: An Audi e-tron battery (second level and BMS are not shown) with its main components. The white arrow points towards the driving direction.

describes the vertical clearance between module and battery cover. This space is normally left empty or occasionally used to lead the module cables. Finally, $s_{\text{batt,cover,z}}$ describes the thickness of the battery top cover. The dimensional chain shown in Equation (D.12) is valid for the battery underbody, but can also be adapted for the second level and the tunnel. Table D.4 summarizes the dimensional chain elements required for Equation (D.12).

Table D.4: Dimensional chain elements for the battery model. The terms in brackets have to be used in case there is no cooling along the z-direction (e.g. Tesla). Based on [101, p. 76].

Chain element	Mean value	Description
$s_{\text{batt,lowp,z}}$	11.63 mm (15.07 mm)	Lower protection thickness
$s_{\text{batt,cool,z}}$	12.59 mm (0 mm)	Cooling plate thickness
$d_{\text{cell,mod,z,pouch}}$	7.29 mm	Difference between cell and module height for pouch cells
$d_{\text{cell,mod,z,cyl}}$	7.50 mm	Difference between cell and module height for cylindrical cells
$d_{\text{cell,mod,z,prism}}$	12.18 mm	Difference between cell and module height for prismatic cells
$d_{\text{clear,batt,z}}$	7.75 mm	Vertical clearance between module and battery cover
$s_{\text{batt,cover,z}}$	4.21 mm	Battery cover thickness

E Gravimetric Component Modeling

This section provides additional information for the mass models presented in Section 3.5. If more detailed information about the simulated architecture is available, it is possible to increase the precision of the mass model by initializing the set of optional inputs shown in Table E.1. If the inputs in Table E.1 are not assigned, the model runs the simulation with a set of default values.

In the following pages, the complete list of the empirical mass model is specified. These models have first been developed in the thesis of Romano [162] and further detailed in a previous publication [28]. The models are grouped in Table E.3 - E.9 according to the module they belong to. To make the list more compact, a set of formula symbols (Table E.2) is introduced.

The single components are described with constant values or linear regressions. In the former case, Table E.3 - E.9 report the average component mass derived from the mass dataset. In the second case, the tables report the calculated empirical regression. Equation (E.1) shows the general structure of a linear regression for modeling the mass of a component $m_{\text{component}}$ based on the inputs X_1 and X_2.

$$m_{\text{component}} = A + B X_1 + C X_2 \tag{E.1}$$

Where A is the empirically derived intercept (always expressed in kg) and B and C are the empirical coefficients multiplying X_1 and X_2. Their units depend on X_1 and X_2. For example, if X_1 represents a length (in mm), then B is expressed in $\mathrm{kg\,mm^{-1}}$.

Table E.1: Optional Inputs for the gravimetric component modeling. Based on [28].

Frame, Chassis, and Powertrain options	**Interior options**
Aluminum percentage in the frame	Cluster type (Digital/Analog)
Air suspensions (Yes/No)	Head-up display (Yes/No)
All-wheel steering (Yes/No)	Sliding rear seats (Yes/No)
Gravimetric cell energy density in $\mathrm{W\,h\,kg^{-1}}$	Rear seat type (Bench/individual)
Rear axle type (Multilink/Torsion beam)	Subwoofer (Yes/No)
Exterior options	**Accessories options**
Door material (steel/aluminum)	Phone connectivity (Yes/No)
Hood material (steel/aluminum)	Active cruise control (Yes/No)
Hatch material (steel/aluminum)	Lane-keeping support (Yes/No))
Fenders material (steel/aluminum)	Park assistant (Yes/No)
Headlights type (LED/Xenon/Halogen)	Spare tire (Yes/No)
Panorama roof (Yes/No)	Tow Hitch (Yes/No)
Sliding roof (Yes/No)	
Number of doors (2/4)	

Table E.2: List of symbols employed in Table E.3 - E.9.

Symbol	Unit	Description
$D_{\mathrm{rim,inch}}$	inch	Diameter of the rim
D_{tire}	mm	Outer diameter of the tire
$E_{\mathrm{batt,is}}$	kW h	Installed battery gross energy
$E_{\mathrm{cell,grav}}$	W h kg^{-1}	Gravimetric energy density at the cell level
$H100$	mm	Vehicle height (compare Table A.1)
$L101$	mm	Vehicle wheelbase (compare Table A.1)
$L103$	mm	Vehicle length (compare Table A.1)
$L104$	mm	Vehicle front overhang (compare Table A.1)
$L105$	mm	Vehicle rear overhang (compare Table A.1)
$L_{\mathrm{axle,f}}$	kg	Occurring maximum load at the front axle
$L_{\mathrm{axle,r}}$	kg	Occurring maximum load at the rear axle
$m_{\mathrm{brakes,f}}$	kg	Mass of the front brake system
$m_{\mathrm{gross,n}}$	kg	Calculated vehicle gross mass at the n_{th} iteration
m_{wheel}	kg	Mass of one wheel (includes both tire and rim mass)
$P_{\mathrm{machs,max}}$	kW	Total installed machine maximum power
$s_{\mathrm{tire,y}}$	mm	Tire width
$T_{\mathrm{mach,max}}$	N m	Maximum torque of the electric machine
$U_{\mathrm{batt,nom}}$	V	Nominal voltage of the battery
V_{batt}	l	Battery volume (not including the sills)
$V_{\mathrm{veh,s}}$	m^3	Vehicle substitute volume
$W103$	mm	Vehicle width (compare Table A.1)
ρ_{Alu}	%	Percentage of aluminum in the BIW

Table E.3: Mass models for the frame module. Based on [28].

Component	Equation or constant value	R^2
BIW	$4.5748 + 5.9108\,V_{\mathrm{veh,s}}\,\rho_{\mathrm{Alu}} + 13.2029\,V_{\mathrm{veh,s}}(1-\rho_{\mathrm{Alu}}) + 0.0797\,m_{\mathrm{gross,n}}$	0.86 %
Other frame components	$-18.2704 + 4.0904\,V_{\mathrm{veh,s}}$	0.49 %

Table E.4: Mass models for the chassis module. Based on [28].

Component	Equation or constant value	R^2
Anti-lock braking system	$2.71\,\mathrm{kg}$	-
Brake disc covers	$0.81\,\mathrm{kg}$	-
Brake fluid	$0.58\,\mathrm{kg}$	-
Brake hoses	$0.57\,\mathrm{kg}$	-
Brake lines system	$1.41\,\mathrm{kg}$	-
Front axle active spring-damper assembly[1]	$16.68\,\mathrm{kg}$	-
Front axle links	$-83.2618 + 0.0281\,L_{\mathrm{axle,f}} + 0.0526\,W103$	58 %
Front axle passive spring-damper assembly[2]	$2.6178 + 0.0099\,L_{\mathrm{axle,f}}$	48 %
Front brake system	$-4.857 + 0.0154\,m_{\mathrm{gross,n}}$	68 %
Further components air springs[3]	$8.97\,\mathrm{kg}$	-
Master cylinder	$4.59\,\mathrm{kg}$	-
Parking brake actuators	$1.12\,\mathrm{kg}$	-
Rear axle links (multi link axle)	$-65.9170 + 0.0088\,m_{\mathrm{gross,n}} + 0.0539\,W103$	43 %
Rear axle links (torsion beam axle)	$-0.7229 + 0.0219\,m_{\mathrm{gross,n}}$	56 %
Rear axle passive spring-damper assembly[1]	$1.6343 + 0.0087\,L_{\mathrm{axle,r}}$	53 %
Rear axle active spring-damper assembly[2]	$14.55\,\mathrm{kg}$	-
Rear axle steering system[4]	$11.46\,\mathrm{kg}$	-
Rear brake system	$2.0549 + 0.5855\,m_{\mathrm{brakes,f}}$	64 %
Rim mass (one rim)	$-13.0632 + 1.4047\,D_{\mathrm{rim,inch}}$	88 %
Steering system	$-10.8485 + 0.0024\,m_{\mathrm{gross,n}} + 0.0099\,L101$	79 %
Tire mass (one tire)	$-16.8902 + 0.0541\,s_{\mathrm{tire,y}} + 0.0234\,D_{\mathrm{tire}}$	86 %

[1] Air suspension mass at the front/rear axle. Use only when the "Air suspensions" option is set to "Yes"
[2] Passive suspensions system. Use only when the "Air suspensions" option is set to "No"
[3] Includes the masses of the air bottles and compressor. Use only when the "Air suspensions" option is set to "Yes"
[4] Includes the masses of the rear actuation motor and tie rods. Use only when the "All-wheel steering" option is set to "No"

Table E.5: Mass models for the exterior module. Based on [28].

Component	Equation or constant value	R^2
Fenders: steel /aluminum	5.44 kg / 5.12 kg	-
Fog lights	1.22 kg	-
Front bumper	$-36.8280 + 0.0308\,W103$	46 %
Front doors (material: aluminum)[1]	$-41.2364 + 0.0238\,H100 + 0.0129\,L101$	69 %
Front doors (material: steel)[1]	$-23.6024 + 0.0110\,H100 + 0.0150\,L101$	72 %
Front doors (two-door vehicles)[2]	$62.6775 + 0.0338\,H100 + 0.0206\,L101$	78 %
Halogen headlights	$-18.2866 + 0.0138\,W103$	46 %
Hood (material: aluminum)	$-72.4132 + 0.0473\,W103$	52 %
Hood (material: steel)	$-78.9009 + 0.0537\,W103$	62 %
LED headlights	$-24.5286 + 0.0179\,W103$	41 %
Rear bumper	$-38.4403 + 0.0288\,W103$	35 %
Rear doors (material: aluminum)[1]	$-84.4604 + 0.0223\,H100 + 0.0268\,L101$	60 %
Rear doors (material: steel)[1]	$-46.0006 + 0.0155\,H100 + 0.0179\,L101$	73 %
Rear quarter glass (SUVs and hatchbacks)	$-2.4013 + 0.0052\,L105$	34 %
Rear quarter glass (sedans)	1.91 kg	-
Rear window (only for sedans)	8.37 kg	-
Roof glass: glass fixed[3] / sliding glass[4]	21.44 kg / 30.87 kg	-
Stop lights	0.24 kg	-
Taillights	$-11.7713 + 0.0061\,W103 + 0.0027\,H100$	38 %
Trunk (material: aluminum)	$-85.0098 + 0.0531\,W103 + 0.0091\,H100$	71 %
Trunk (material: steel)	$-103.0405 + 0.0559\,W103 + 0.0192\,H100$	75 %
Trunk lid: steel/aluminum	19.95 kg / 18.16 kg	-
Windshield (L101 $\leq$ 2493 mm)	12.4 kg	-
Windshield (2493 mm $<$ L101 $\leq$ 2640 mm)	12.51 kg	-
Windshield (2640 mm $<$ L101 $\leq$ 2750 mm)	13.68 kg	-
Windshield (2750 mm $<$ L101 $\leq$ 2927 mm)	12.71 kg	-
Windshield (L101 $>$ 2927 mm)	13.66 kg	-
Wiper system with reservoir and fluids	4.86 kg	-
Wipers	3.6 kg	-
Xenon headlights	$-22.3259 + 0.0119\,W103 + 0.0053\,H100$	33 %

[1] The regression yields the mass of one door. Use only when the "Number of doors" option is set to 4
[2] The regression yields the mass of one door. Use only when the "Number of doors" option is set to 2
[3] Includes the masses of the additional components for the panorama roof. Use only when the "Panorama roof" option is set to "Yes"
[4] Includes the masses of the additional components for the sliding roof. Use only when the "Sliding roof" option is set to "Yes"

Table E.6: Mass models for the interior module. Based on [28].

Component	Equation or constant value	R^2
A/C system with refrigerant	16.73 kg	-
Airbag sensors and control unit	0.44 kg	-
Brake pedal	1.58 kg	-
Center console	$-25.4609 + 0.0120\,L101$	50 %
Cross-car beam	6.25 kg	-
Curtain airbag / Driver airbag / Knee airbag	2.48 kg / 1.07 kg / 1.42 kg	-
Dashboard	7.82 kg	-
Drive pedal	0.38 kg	-
Front seat (one seat)	$-44.0809 + 0.0257\,W103 + 0.0073\,L101$	57 %
Glove box	2.38 kg	-
Head-up display	1.49 kg	-
Heating system passenger compartment	$-19.5455 + 0.0196\,W103$	52 %
Horn system	0.51 kg	-
Infotainment	1.11 kg	-
Instrument cluster: analog/digital	1.26 kg / 1.66 kg	-
Interior trim parts	$-261.2804 + 0.1394\,W103 + 0.0089\,L103$	83 %
Noise insulation (L101 $\leq$ 2750 mm)	6.42 kg	-
Noise insulation (L101 $>$ 2750 mm)	12.76 kg	-
Passenger airbags: front rear	1.66 kg / 0.79 kg	
Rear seats (entire rear seat bench)[1]	$-97.1243 + 0.0955\,W103 + 0.0181\,L101$	47 %
Rear seats sliding mechanism[2]	9.90 kg	47 %
Seatbelt (one) front/rear	2.29 kg / 1.73 kg	-

[1] If the "Individual" option is selected, the mass of the rear seats is obtained by multiplying the mass of the front seat by the number of passengers in the second (and if present) third row
[2] Rear sliding mechanism mass. Use only when the "Sliding rear seats" option is set to "Yes"

Table E.7: Mass models for the powertrain module. Based on [28].

Component	Equation or constant value	R^2
Battery electrics[1]: AWD / non AWD vehicles	20.65 kg / 9.67 kg	-
Battery housing	$1.7900 + 0.0330\,V_{\text{batt}}$	54 %
Cells with module casing[2]	$K_{\text{cell2mod}}\left(\frac{E_{\text{batt,is}}}{E_{\text{cell,grav}}}\right)$	-
Coolant fluid: AWD / non AWD vehicles	10.17 kg / 7.39 kg	-
Electric machine mounts (one machine)	11.52 kg	-
Gearbox, differential, driveshafts	See [100, 101, 27]	-
IM (one machine with housing)	$29.3478 + 0.1305\,T_{\text{mach,max}}$	70 %
Noise insulation (one machine)	1.42 kg	-
PMSM (one machine with housing)	$23.1450 + 0.0884\,T_{\text{mach,max}}$	34 %
Powertrain cooling system	$11.1957 + 0.0433\,P_{\text{mach,max}}$	39 %
Transmission fluid (one gearbox)	1.1 kg	-

[1] Includes BMS, electric connectors, cables, and battery junction box
[2] K_{cell2mod} is 1.23 for pouch cells, 1.14 for cylindrical cells, and 1.12 for prismatic cells

Table E.8: Mass models for the electrics module. Based on [28].

Component	Equation or constant value	R^2
12 V battery	19.96 kg	-
12 V battery cables	0.33 kg	-
AC home charging cable	2.33 kg	-
AC public charging cable	2.16 kg	-
Additional charging plug components	1.47 kg	-
Charging plug	3.42 kg	-
DC-DC converter	$1.8787 + 0.0070\, U_{\text{batt,nom}}$	75 %
DC-DC converter supports	0.65 kg	-
Fuse box	1.11 kg	-
HV cables: AWD / non AWD vehicles	9.30 kg / 4.13 kg	-
HV charger	$5.3459 + 0.1097\, E_{\text{batt,is}}$	62 %
Inverter	9.13 kg	-
Inverter supports	2.74 kg	-
LV wiring	$-71.1687 + 0.0345\, L101$	62 %
Other LV components	4.22 kg	-

Table E.9: Mass models for the accessories module. Based on [28].

Component	Equation or constant value	R^2
Advanced driver assistance systems	1.03 kg	-
Adaptive cruise control (if present)	0.37 kg	-
Blind spot monitoring (if present)	0.5 kg	-
Key-less entry (if present)	0.25 kg	-
Lane-keeping support (if present)	0.18 kg	-
Night vision camera (if present)	1.02 kg	-
Park assist (if present)	0.43 kg	-
Pedestrian warning	0.79 kg	-
Phone connectivity (if present)	0.4 kg	-
Spare tire (if present)	$-0.0758 + 0.6628\, m_{\text{wheel}}$	78 %
Toolbox (if spare tire not present)	3.34 kg	-
Toolbox (if spare tire present)	5.25 kg	-
Tow hitch system (if present)	21.66 kg	-
Trunk opening assist (if present)	0.24 kg	-

F Verification and Validation

This chapter provides additional information about validating the LDS (Section F.1), tire model (Section F.2), battery model (Section F.3), and architecture tool (Section F.4).

F.1 Longitudinal Simulation Validation

To simulate the VW ID.3 in the LDS, the vehicle is parameterized. Table F.1 summarizes the most important values used for the parametrization.

Table F.1: LDS parameters for simulating the VW ID.3

Parameter	Value	Description
m	$1820\,\mathrm{kg}$	Empty mass (no driver), measured before the roller dynamometer analysis
t_{0-100}	$7.3\,\mathrm{s}$	Acceleration time from $0\,\mathrm{km\,h^{-1}}$ to $100\,\mathrm{km\,h^{-1}}$ [213]
$v_{\mathrm{veh,max}}$	$160\,\mathrm{km\,h^{-1}}$	Maximum vehicle speed [213]
c_{d}	0.26	Aerodynamic drag coefficient. Value set as described by [231]
c_{r}	0.0095	Rolling resistance coefficient; estimated with the model of Moller [160]
P_{aux}	$0.2\,\mathrm{kW}$	Auxiliaries power. Measured during the roller dynamometer analysis
i_{gb}	11.53	Transmission ratio [214].
Tires	215/45 R20	Mounted tire variant

The following additional information is required to perform the validation step:

- The coefficients c_{d} and c_{r} are used to model the driving resistances. More information is specified in [153, p. 10].
- Energy consumption was measured at the battery output and does not include internal battery losses. Therefore, in the simulation of the ID.3, the battery losses are set to zero.
- From the analysis of the ID.3 measurements, it appears that the vehicle does not activate recuperation mode (independent of the driving cycle) when the vehicle speed is below $4\,\mathrm{km\,h^{-1}}$. In the LDS, this limit is not considered. The error introduced by this simplification is negligible since the extra energy that can be recuperated in the cycle parts below $4\,\mathrm{km\,h^{-1}}$ is below $100\,\mathrm{W\,h}$.
- P_{aux} describes the onboard power system. It does not include air conditioning or passenger cabin heating power since these were deactivated during the cycle measurements.

F.2 Tire Validation

Table F.2 shows the vehicles used to validate the tire model (Subsection 4.2.1). The dataset is created from the A2mac1 database and contains only BEVs. When possible, the vehicle model series according to the ADAC nomenclature is given. For the Tesla Model 3 LR RWD and the BMW i3 120 Ah (RE), there are no ADAC model series since these particular models are not available on the European market. The same vehicles are also used in the gravimetric component modeling validation (Section 4.3).

Table F.2: Dataset used to validate the tire and vehicle mass modeling.

Manufacturer	ADAC model series	Model
Audi	e-tron (GE) (ab 03/19)	e-tron 55 quattro
BMW	n.a.	i3 120 Ah (RE)
Hyundai	Kona (OS) Elektro (ab 08/18)	Kona (64 kWh)
Jaguar	I-Pace (X590) (ab 10/18)	I-Pace EV400 AWD
Kia	e-Niro (DE) (ab 12/18)	e-Niro (64 kWh)
Mercedes	EQC (293) (ab 06/19)	EQC 400 4MATIC
Nissan	Leaf (ZE1) (ab 01/18)	Leaf (40 kWh) Tekna
Opel	Ampera-E (07/17-06/19)	Ampera-E
Peugeot	e-208 (II) (ab 01/20)	e-208 GT
Polestar	2 Launch Edition (06/20 - 07/20)	2
Renault	Zoe (ab 10/19)	Zoe R135
Tesla	n.a.	Model 3 LR RWD
Tesla	Model X (ab 06/16)	Model X P90D
Tesla	Model Y (ab 01/21)	Model Y Performance
Tesla	Model S (08/13 - 04/16)	Model S 60
VW	Golf (VII) e-Golf (04/17-05/20)	e-Golf VII (Facelift)
VW	up! e-up! (11/13 - 06/16)	e-Up!
VW	ID.3 Pro Performance (58 kWh) (09/20 - 11/20)	ID.3 Pro Performance

F.3 Traction Battery Validation

In the vehicle architecture tool, the user does not have to specify the cell dimensions and can let the filling algorithm identify them in dependency of the available battery space. To identify the optimal cell dimensions, the filling algorithm varies the cell size (Figure F.1) within given empirical ranges (Table F.3).

For the prismatic cells, the defined cell height $s_{\mathrm{cell,z}}$ does not consider the cell connections since their required installation space is already accounted for in the term $d_{\mathrm{cell,mod}}$ in Table D.4. For pouch cells, when considering cell length (denoted as $s_{\mathrm{cell,x}}$ in Figure F.1), the cell connections are excluded as well. In this case, the required installation space for the cell connections is considered by the package factors.

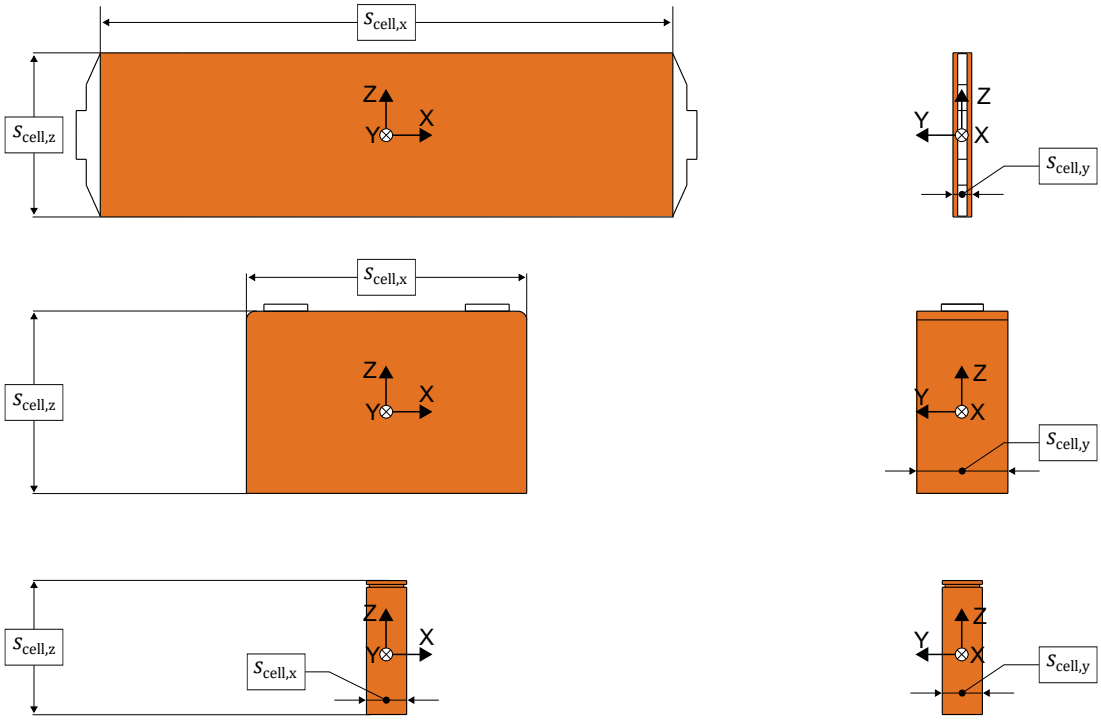

Figure F.1: Definition of cell width, height, and length. The x-axis points opposite to the driving direction.

Table F.3: Cell ranges for the vehicles contained in the battery dataset. Based on [101, pp. 88-89].

Cell type	$s_{cell,x}$	$s_{cell,y}$	$s_{cell,z}$
Pouch	266 mm-513 mm	9 mm-14 mm	97 mm-101 mm
Prismatic	148 mm-280 mm	28 mm-79 mm	82 mm-125 mm
Cylindrical	18 mm-21 mm	18 mm-21 mm	65 mm-70 mm

F.4 Vehicle Architecture Tool Validation

Table F.4 - F.6 list the inputs required to simulate the validation dataset (Section 4.4). Apart from the inputs, the tables list the empty vehicle mass, battery energy, tire dimensions, and WLTP consumption. These values are not required as inputs, but are used for validation purposes.

Regarding vehicle consumption, the values listed by the manufacturers cannot be directly used for validation. The LDS does not model charging losses, which are included in the official consumption values (Appendix C). For a comparison with the LDS results, a correction is required. This is achieved by inverting Equation (C.1) and imposing E_{STP} as the net battery energy given by the manufacturer and $R_{WLTP,comb}$ as the listed range in WLTP. This yields an estimation of the consumption that does not include charging losses and that is denoted as *Cons. in WLTP (calculated)* in Table F.4 - F.6.

The validation vehicles can be equipped with different tire and rim combinations. In most cases, different rim diameters are available with the same tire width. In this case, the base rim size is chosen. For some vehicles, the highest rim size can be represented only with wider tires. Since the tire width also influences battery space, the author selects the widest tire combination for these vehicles since it is the critical one for the definition of the battery space.

Table F.4: Main inputs of the validation dataset (Part 1/3).

Variable	BMW i3s	VW ID.3 62 kWh	VW ID.3 77 kWh
General			
Model series in ADAC	i3s (120 Ah) [223]	Pro Perf. 1st max [213]	Pro S 5 seats [224]
Model year	2019	2020	2020
Length (L103)	4006 mm [261]	4261 mm [262]	4261 mm [262]
Wheelbase (L101)	2570 mm [261]	2771 mm [262]	2771 mm [262]
Width (W103)	1791 mm [223]	1809 mm [262]	1809 mm [262]
Height (H100)	1570 mm [261]	1552 mm [262]	1552 mm [262]
Number of seats	4 [261]	5 [213]	5 [224]
Body type	Hatchback	Hatchback	Hatchback
Tire dimensions	195/55 R20[1]	215/45 R20 [213]	215/50 R19 [224]
Tire type	Extra load	Extra load	Extra load
Drag coefficient c_d	0.29 [229]	0.26 [231]	0.26 [231]
Mass and payload			
Empty mass (without driver)	1290 kg [261]	1737 kg [263]	1850 kg [263]
Payload (with passengers)	440 kg [261]	533 kg[2]	450 kg[2]
Performance requirements			
Acceleration time	6.9 s [261]	7.3 s [262]	7.9 s [262]
Maximum vehicle speed	160 km h^{-1} [261]	160 km h^{-1} [262]	160 km h^{-1} [262]
Range in WLTP	283 km [261]	423 km [263]	551 km [263]
Cons. in WLTP (calculated)	13.39 kWh/100km	13.71 kWh/100km	13.97 kWh/100km
Traction battery			
Integration principle	Highfloor	Highfloor	Highfloor
Battery shape	Rectangular	Rectangular	Rectangular
Net battery energy	37.9 kW h [261]	58.0 kW h [262]	77.0 kW h [262]
Cell type	Prismatic	Pouch	Pouch
Electric machine and gearbox (front axle / rear axle)			
Drive unit configuration	- / Figure B.1a	- / Figure B.1a	- / Figure B.1a
Number of machines	- / 1	- / 1	- / 1
Machine type	- / PMSM	- / PMSM	- / PMSM
Gearbox type	Parallel axles	Parallel axles	Parallel axles
Transmission ratio	- / 9.67 [240]	- / 11.53 [214]	- / 11.53 [214]
Further remarks			
Used for cell type study (Section 5.1)	No	No	Yes
Used for C2B study (Section 5.2)	No	No	Yes
Used for optimization study (Section 5.3)	No	No	Yes

[1] The table lists the tire size at the rear axle. At the front axle, smaller tires are used [261]
[2] Estimated from the difference between empty and gross mass given in [263]

Table F.5: Main inputs of the validation dataset (Part 2/3). The parameters marked with * are retrieved directly from A2mac1 and cannot be disclosed.

Variable	Jaguar I-Pace	Tesla Model 3	Tesla Model 3 LR
General			
Model series in ADAC	I-Pace EV 400 [225]	Model 3 SR Plus [226]	not available
Model year	2019	2020	2018
Length (L103)	4682 mm [264]	4694 mm [265]	4694 mm [265]
Wheelbase (L101)	2990 mm [264]	2875 mm [265]	2875 mm [265]
Width (W103)	2011 mm [264]	1849 mm [265]	1849 mm [265]
Height (H100)	1566 mm [264]	1443 mm [265]	1443 mm [265]
Number of seats	5 [264]	5 [265]	5 [265]
Body type	SUV	Sedan	Sedan
Tire dimensions	255/40 R22 [264]	235/45 R18 [265]	235/45 R18 [265]
Tire type	Extra load	Extra load	Extra load
Drag coefficient c_d	0.29 [82]	0.23 [233]	0.23 [233]
Mass and payload			
Empty mass (without driver)	2208 kg [264]	1611 kg [265]	1726 kg [265]
Payload (with passengers)	537 kg [264]	443 kg [265]	443 kg [265]
Performance requirements			
Acceleration time	4.8 s [225]	5.6 s [226]	5.1 s [226]
Maximum vehicle speed	200 km h^{-1} [225]	225 km h^{-1} [226]	225 km h^{-1}
Range in WLTP	470 km [264]	409 km [265]	560 km [230]
Cons. in WLTP (calculated)	18.42 kWh/100km	13.89 kWh/100km	13.89 kWh/100km
Traction battery			
Integration principle	Highfloor	Highfloor	Highfloor
Battery shape	Drop shape	Drop shape	Drop shape
Net battery energy	86.6 kW h [264]	50 kW h[1]	77.8 kW h [230]
Cell type	Pouch	Cylindrical	Cylindrical
Electric machine and gearbox (front axle / rear axle)			
Drive unit configuration	Figure B.1c / Figure B.1c	- / Figure B.1a	- / Figure B.1a
Number of machines	1 / 1	- / 1	- / 1
Machine type	PMSM / PMSM	- / PMSM	- / PMSM
Gearbox type	Planetary / Planetary	- / Parallel axles	- / Parallel axles
Transmission ratio	9.06 / 9.06 [82]	* / *	* / *
Further remarks			
Used for cell type study (Section 5.1)	No	No	No
Used for C2B study (Section 5.2)	No	No	Yes
Used for optimization study (Section 5.3)	No	No	Yes

[1] Own calculation. Estimated by scaling the net energy and the number of cells [247] of the Model 3 LR [230].

Table F.6: Main inputs of the validation dataset (Part 3/3). The parameters marked with * are retrieved directly from A2mac1 and cannot be disclosed.

Variable	Tesla Model Y	Audi e-tron
General		
Model series in ADAC	Model Y Perf. AWD [227]	e-tron 55 quattro [228]
Model year	2021	2019
Length (L103)	4751 mm [266]	4901 mm [228]
Wheelbase (L101)	2890 mm [266]	2928 mm [228]
Width (W103)	1921 mm [266]	1935 mm [228]
Height (H100)	1624 mm [266]	1629 mm [228]
Number of seats	5 [266]	5 [228]
Body type	SUV	SUV
Tire dimensions	275/35 R21[1]	265/45 R21 [267]
Tire type	Extra load	Extra load
Drag coefficient c_d	0.23	0.28 [242]
Mass and payload		
Empty mass (without driver)	2066 kg [266]	2520 kg [228]
Payload (with passengers)	340 kg[2]	575 kg [228]
Performance requirements		
Acceleration time	3.7 s [227]	5.7 s [228]
Maximum vehicle speed	241 km h^{-1} [266]	200 km h^{-1} [228]
Range in WLTP	480 km [227]	405 km [228]
Cons. in WLTP (calculated)	15.63 kWh/100km	21.23 kWh/100km
Traction battery		
Integration principle	Highfloor	Highfloor
Battery shape	Drop shape	Drop Shape + 2nd level
Net battery energy	75 kW h [227]	86 kW h [267]
Cell type	cylindrical	pouch
Electric machine and gearbox (front axle / rear axle)		
Drive unit configuration	Figure B.1a / Figure B.1c	Figure B.1b / Figure B.1a
Number of machines	1 / 1	1 / 1
Machine type	IM / PMSM	IM / IM
Gearbox type	Parallel axles / Parallel axles	Parallel axles / Planetary
Transmission ratio	* / *	9.0 / 9.2 [83]
Further remarks		
Used for cell type study (Section 5.1)	No	No
Used for C2B study (Section 5.2)	Yes	No
Used for optimization study (Section 5.3)	No	Yes

[1] The table lists the tire size at the rear axle. At the front axle, smaller tires are used [266]
[2] Estimated from the difference between empty and gross mass given in [266]

G Results

This chapter provides additional information for the interpretation of the results discussed in Chapter 5. Section G.1 provides the plots for the parametric study discussed in Section 5.1. Section G.2 documents the assumptions used for the C2B strategy simulation (Section 5.2). Finally, Section G.3 documents additional plots of the optimization described in Section 5.3.

G.1 Impact Assessment: Cell Type

In Section 5.1, a parametric study was performed to assess the impact of the external dimensions on a VW ID.3. The ID.3 is electrified using pouch and cylindrical cells as well as different drag coefficients. The results of the parametric study are summarized in Table 5.2. The table considers four different cases: pouch variant, cylindrical variant with c_d=0.26, cylindrical variant with c_d=0.23, and cylindrical variant with c_d=0.20. The first two variants are represented graphically in Figure 5.2. The remaining cylindrical variants with c_d=0.23 and c_d=0.20 are shown in Figure G.1. Since the pouch case was identified as the variant with the highest range, it is also represented as reference in Figure G.1.

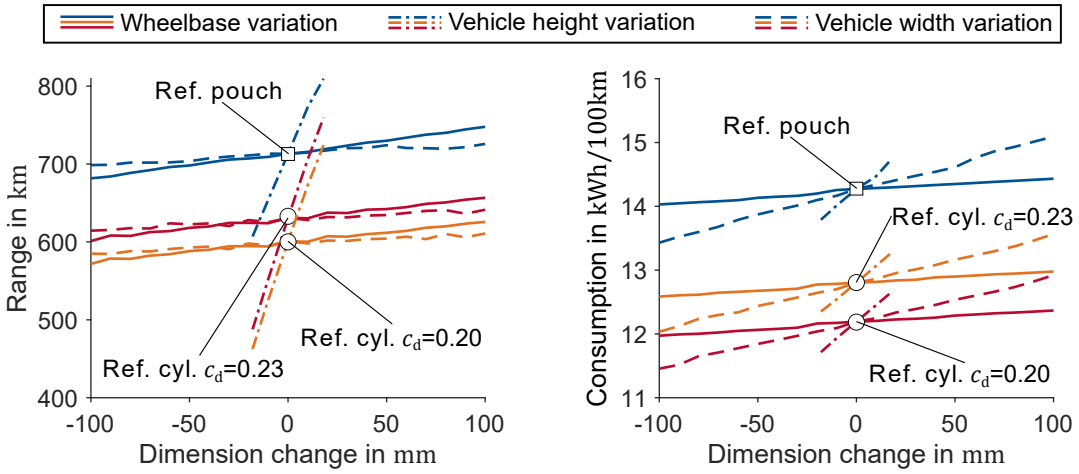

(a) External dimensions vs. vehicle range

(b) External dimensions vs. consumption in WLTP

Figure G.1: Impact of the external dimensions. The x-axis shows the change in external dimensions while the y-axis shows the corresponding impact on vehicle range and consumption.

The only difference between the two cylindrical variants in Figure G.1 is the c_d value. A change in c_d does not impact the vehicle architecture mass and the battery energy. The cylindrical variant with c_d=0.20 has a better range due to its lower consumption (Figure G.1b). However, the attainable range mostly remains below the values obtained by the pouch variant. The only exception, where the cylindrical variants outperform the pouch variant in terms of range, is when

H100 is increased by $20\,\mathrm{mm}$. In conclusion, a sole improvement of c_d is not sufficient to reach the same ranges as the pouch variant.

G.2 Assumptions for the C2B Strategy Simulation

There is little information regarding the C2B strategy since it is not available on the market yet. For the modeling in the tool, a set of assumptions regarding battery dimensional chains, package factors, mass savings, and energy density is required. Figure G.2 highlights the differences between the highfloor and the C2B principle.

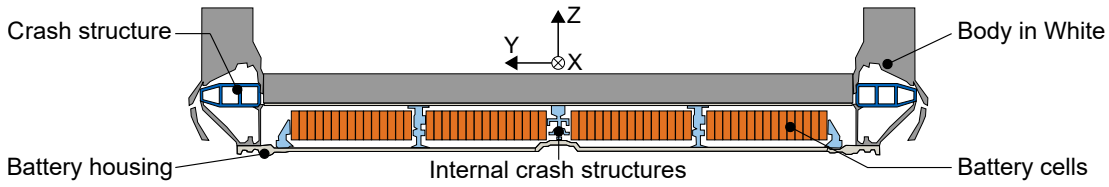

(a) Highfloor integration principle of the Tesla Model 3 and Model Y (21700 cell format).

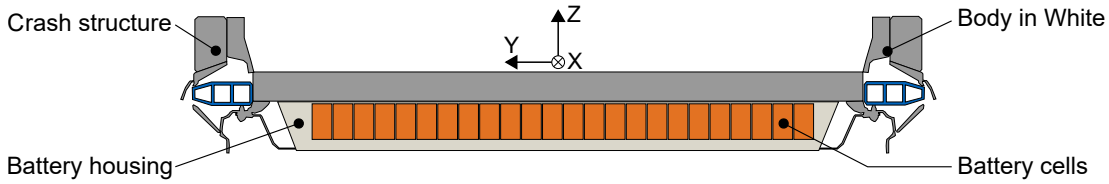

(b) C2B integration principle for future Tesla models (4680 cell format).

Figure G.2: Highfloor vs. C2B integration principle. The figure shows the BIW and the battery. The x-direction points opposite to the driving direction.

First of all, to model the C2B strategy, the battery dimensional chain components (Table D.4) are modified as shown in Figure G.3. The upper cover is no longer needed since the battery is integrated directly into the BIW. The module housings are eliminated, which further increases the usable space along the z-direction. Nevertheless, the dimensional chain element describing the module housing (denoted as *Module housing* in Figure G.3) is not set to zero, but to a value of $2\,\mathrm{mm}$, which considers the space required by the cell-to-cell interconnects. The component *Air* in Figure G.3 represents the clearance between the battery cover and the top of the module housing. In the case of the C2B strategy, this space is occupied with a filler. It is assumed that the height of this clearance remains unchanged. With these adjustments, it is possible to fit the 4680 cells in the same battery space as the 21700 cells.

Second, the C2B allows packing the cells more densely, meaning that the package factors have to be corrected. For this scope, the Tesla Model 3 battery is taken as reference. Along the driving direction, the inactive space is occupied by the cooling pipes and the electrical connections between the modules. The assumption is made that these components are also required for a C2B strategy and $K_\mathrm{pack,x}$ is set equal to the Tesla Model 3. Along the y-direction, consistent adjustments are required: the Tesla Model 3 has internal crash structures between the modules (Figure G.2a). However, with a C2B strategy, the internal crash structures are not required anymore (Figure G.2b) and the usable space along the y-direction increases. To calculate the $K_\mathrm{pack,y}$ improvement, the internal crash structures of the Tesla Model 3 are measured in A2mac1 and the package factor is corrected. This leads to an improvement of $K_\mathrm{pack,y}$ from 0.89 to 0.95.

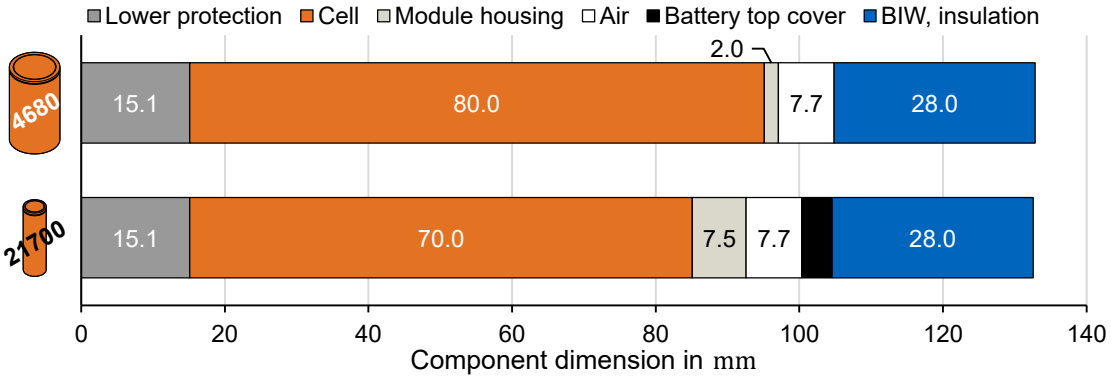

Figure G.3: Comparison between the dimensional chain of a Tesla Model 3 (with 21700 cells, values from Table D.4) and the dimensional chain used for the C2B simulation (with 4680 cells).

Third, the mass saving obtainable with a C2B strategy must be estimated. The savings resulting from the module's elimination are considered by adjusting the cell to module factor K_{cell2mod} (Table E.7). The K_{cell2mod} factor models the mass increase due to electrical connectors inside the modules, cooling plates, and module housings. A benchmark analysis of the Tesla Model 3 shows that, if the module housings are eliminated, K_{cell2mod} can be improved from 1.14 to 1.06. Furthermore, the $10\,\%$ saving on the frame, which was declared by Mr. Musk during the *Tesla Battery Days* [235], is estimated using the equations presented in Subsection 3.5.1. For the vehicles considered in the parametric study, the frame mass ranges between $300\,\text{kg}$ and $400\,\text{kg}$. Therefore, independent of the considered vehicle, a mass saving of $35\,\text{kg}$ ($10\,\%$ of the mean value of the frame mass range) is assumed.

Finally, the energy density improvement of the 4680 format has to be quantified. During the Tesla battery days, the energy of the 4680 cells in comparison to the 21700 was described with the following statement: "So when we put it all together and go to our new $80\,\text{mm}$ length [. . .] we get five times the energy and six times the power" [235]. According to this statement, 4680 cells should have five times the energy of the 21700. However, they also have approx. five times the volume. Therefore, it is assumed that the volumetric energy density does not change with the new cell format. The same assumption is also used for the gravimetric energy density. Consequently, the vehicles analyzed in the parametric study are simulated with the density values listed in Table 5.1.

G.3 Integration Principle Optimization

This section provides further plots of the optimization of the reference vehicles VW ID.3 (Figure G.4 and G.5), Tesla Model 3 (Figure G.6 and G.7), and Audi e-tron (Figure G.8 and G.9). The figures also show the original value of the reference pouch (denoted as a white square) and cylindrical (denoted as a white circle) variant. For the H30-2, the original values are retrieved from the A2mac1 database and cannot be disclosed.

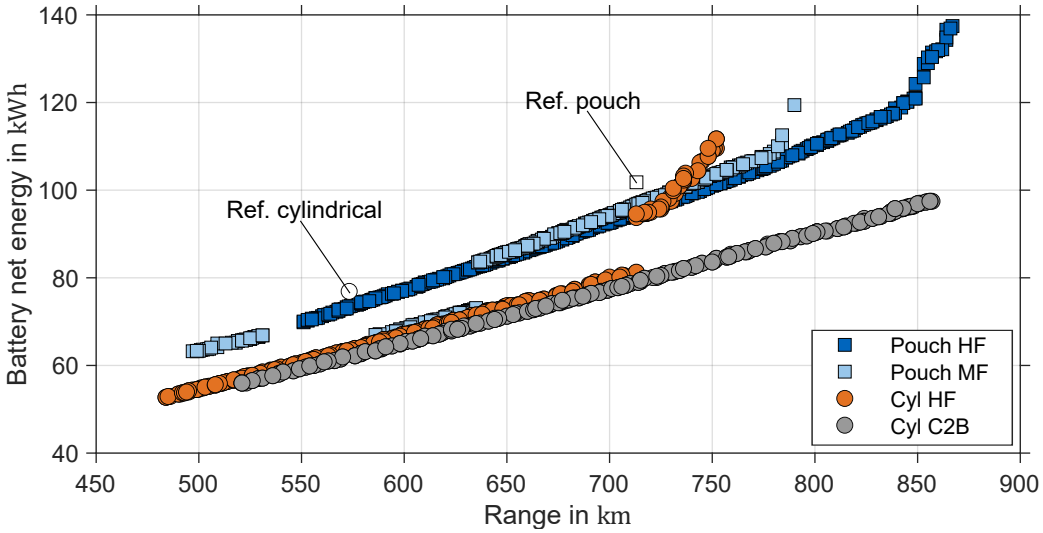

(a) Pareto fronts of the two optimization objectives (range and battery net energy)

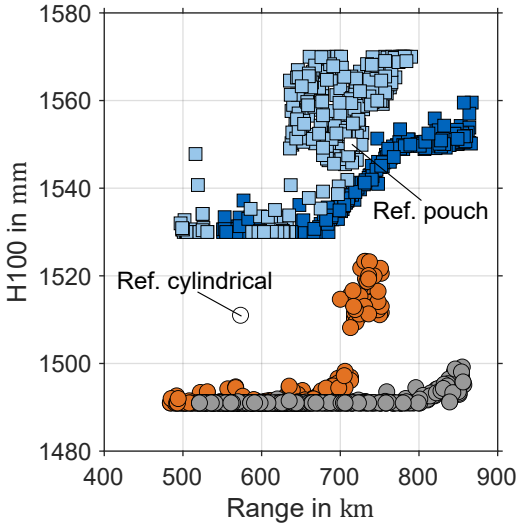

(b) Range vs. vehicle height

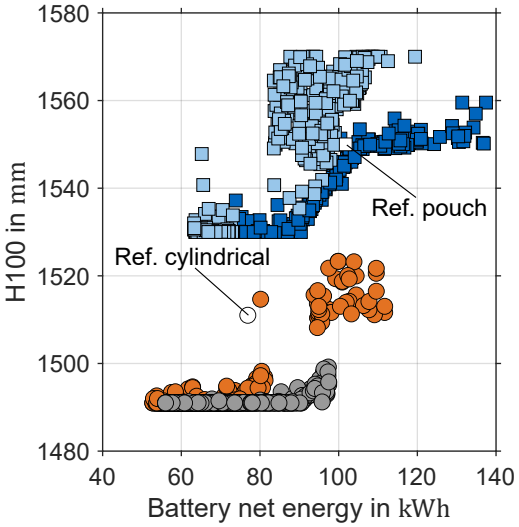

(c) Battery net energy vs. vehicle height

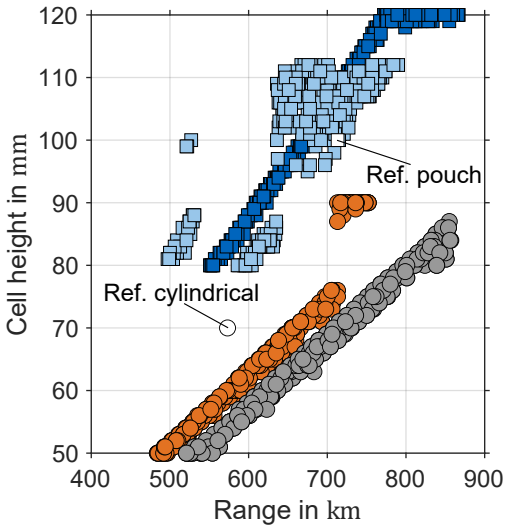

(d) Range vs. cell height

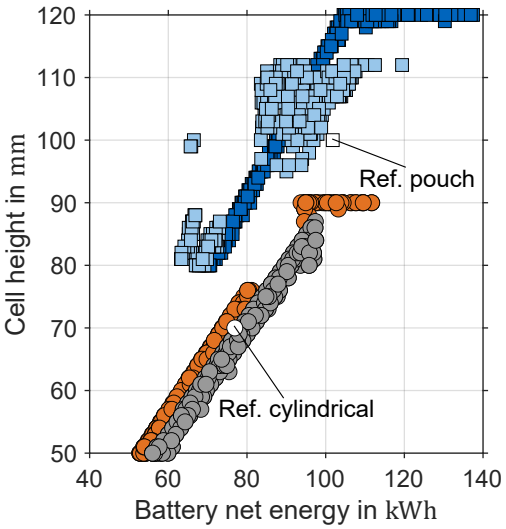

(e) Battery net energy vs. cell height

Figure G.4: Overview of the pareto fronts and some of the tool outputs for the VW ID.3. These results are obtained with a population size of 300 over 30 generations.

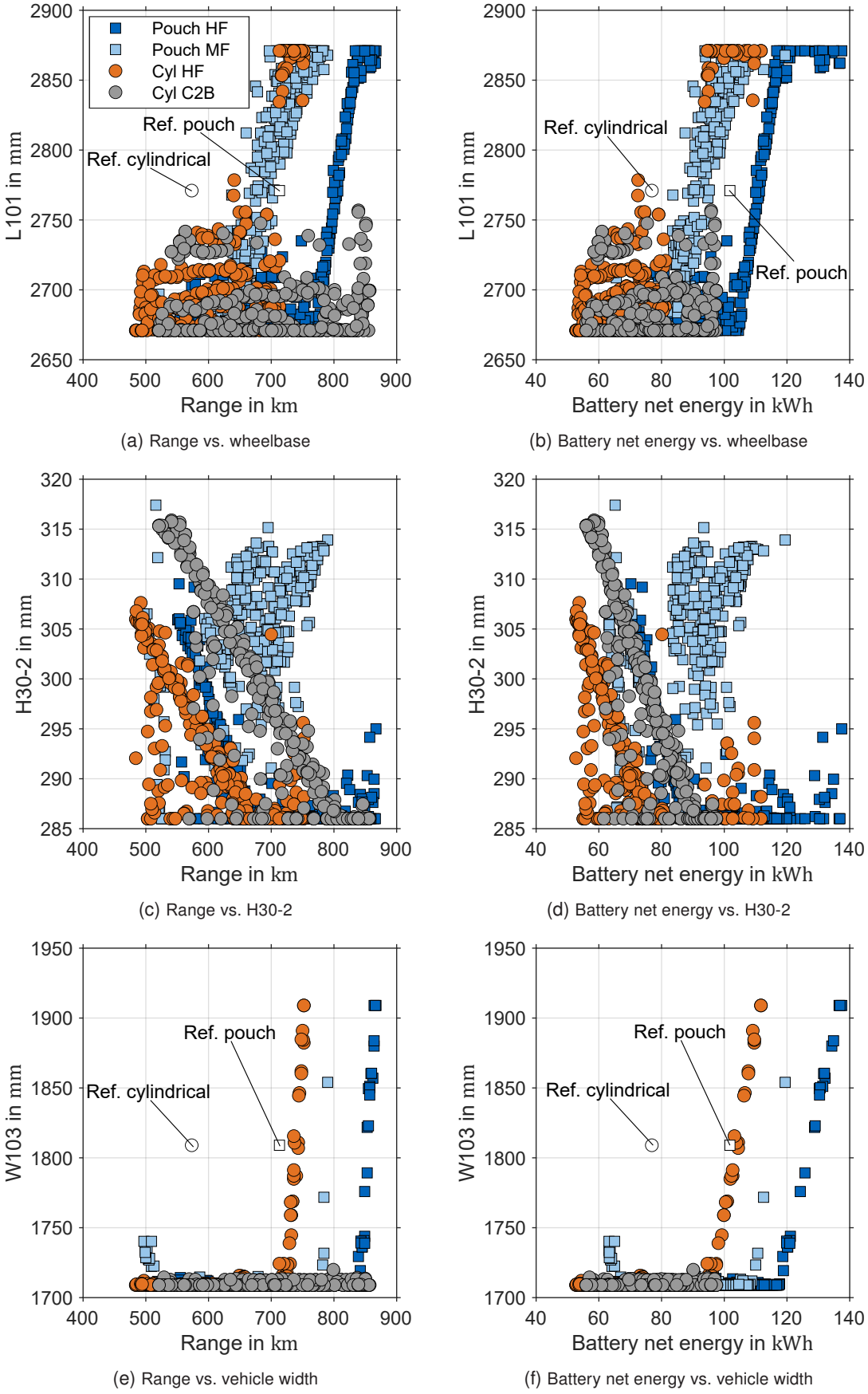

(a) Range vs. wheelbase

(b) Battery net energy vs. wheelbase

(c) Range vs. H30-2

(d) Battery net energy vs. H30-2

(e) Range vs. vehicle width

(f) Battery net energy vs. vehicle width

Figure G.5: Overview of the main design variables for the optimal configurations of the VW ID.3. These results are obtained with a population size of 300 over 30 generations.

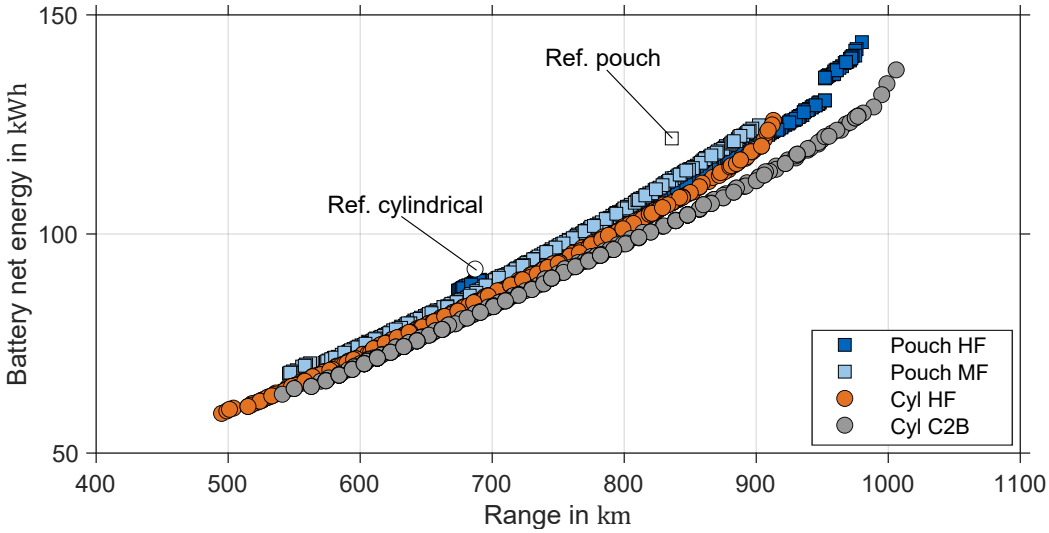

(a) Pareto fronts of the two optimization objectives (range and battery net energy)

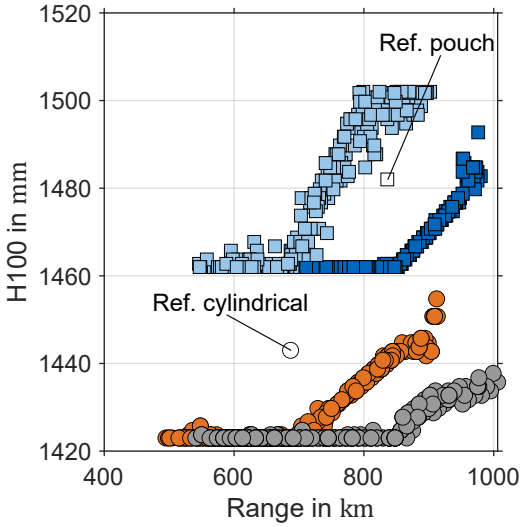

(b) Range vs. vehicle height

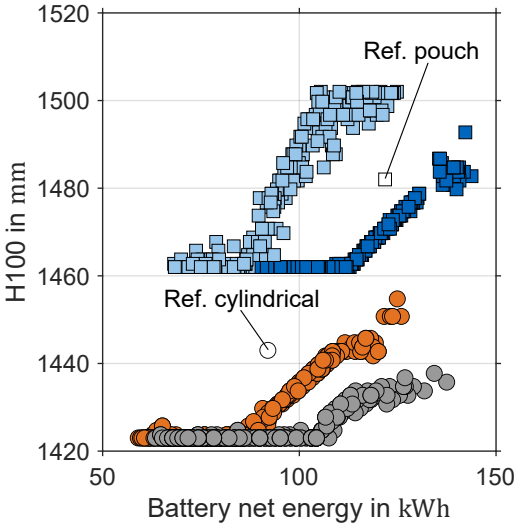

(c) Battery net energy vs. vehicle height

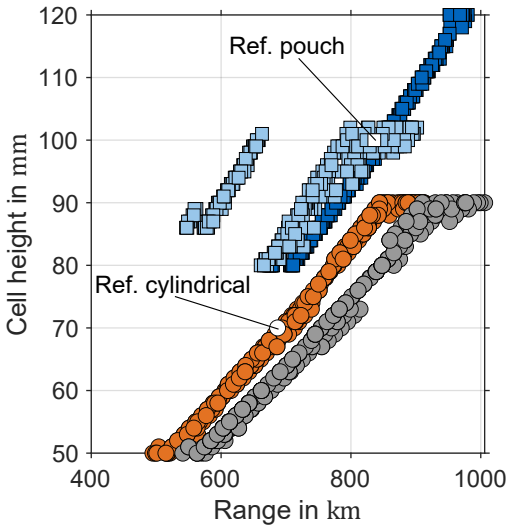

(d) Range vs. cell height

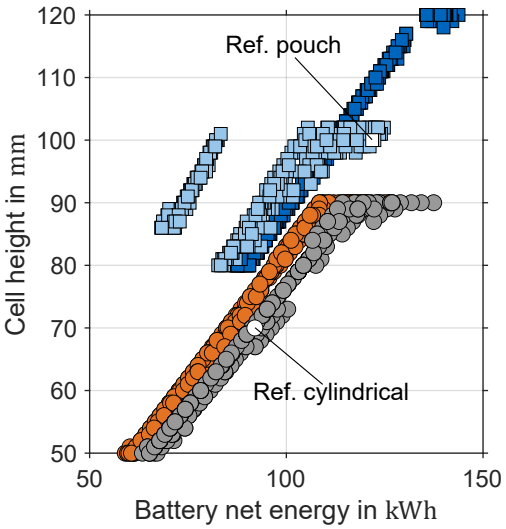

(e) Battery net energy vs. cell height

Figure G.6: Overview of the pareto fronts and some of the tool outputs for the Tesla Model 3. These results are obtained with a population size of 300 over 30 generations.

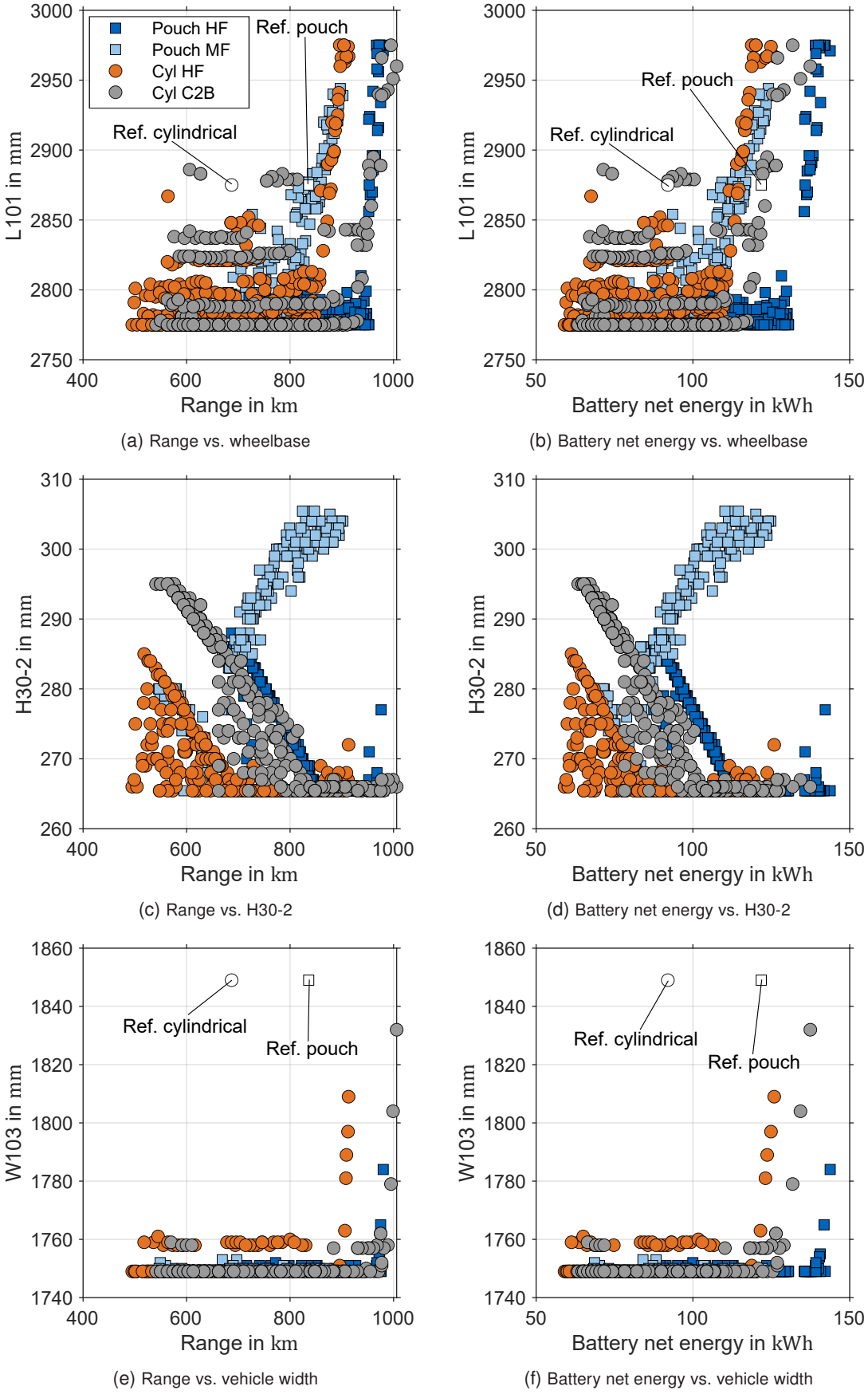

(a) Range vs. wheelbase

(b) Battery net energy vs. wheelbase

(c) Range vs. H30-2

(d) Battery net energy vs. H30-2

(e) Range vs. vehicle width

(f) Battery net energy vs. vehicle width

Figure G.7: Overview of the main design variables for the optimal configurations of the Tesla Model 3. These results are obtained with a population size of 300 over 30 generations.

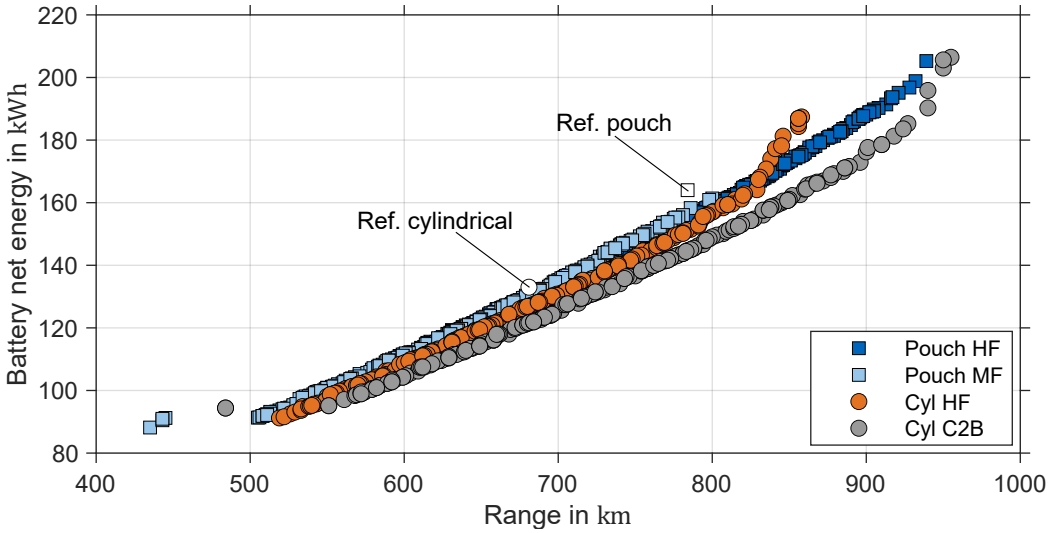

(a) Pareto fronts of the two optimization objectives (range and battery net energy)

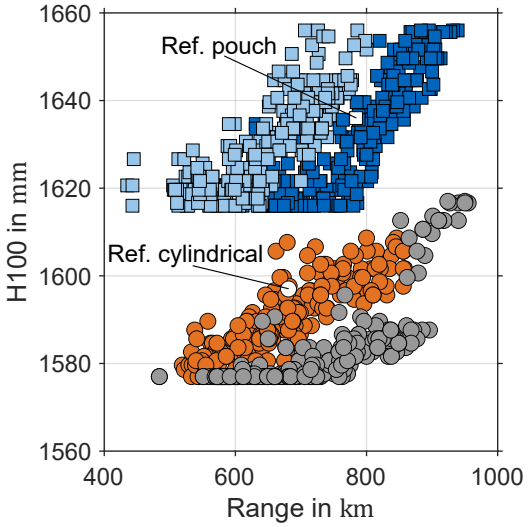

(b) Range vs. vehicle height

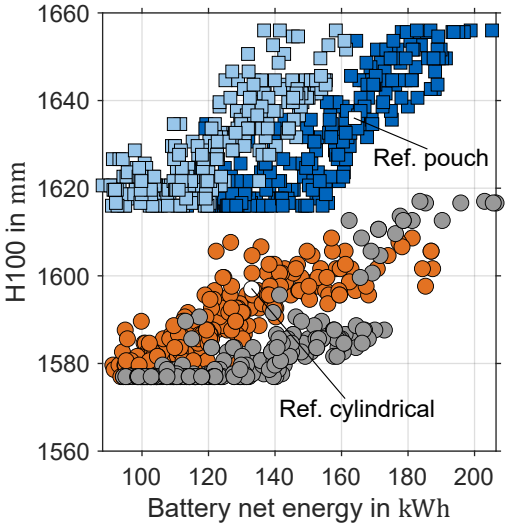

(c) Battery net energy vs. vehicle height

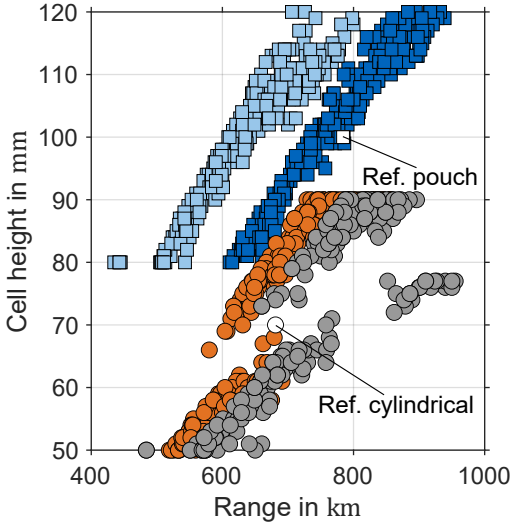

(d) Range vs. cell height

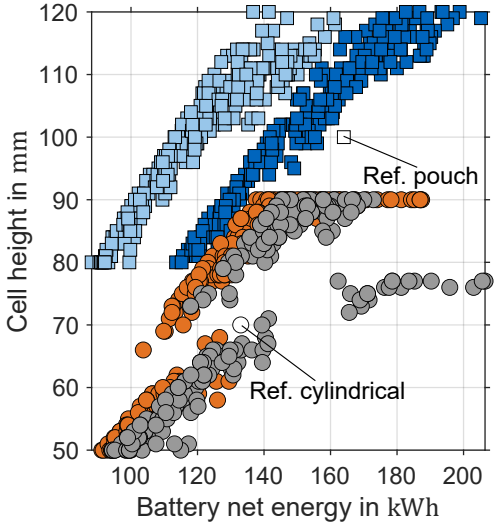

(e) Battery net energy vs. cell height

Figure G.8: Overview of the pareto fronts and some of the tool outputs for the Audi e-tron. These results are obtained with a population size of 300 over 30 generations.

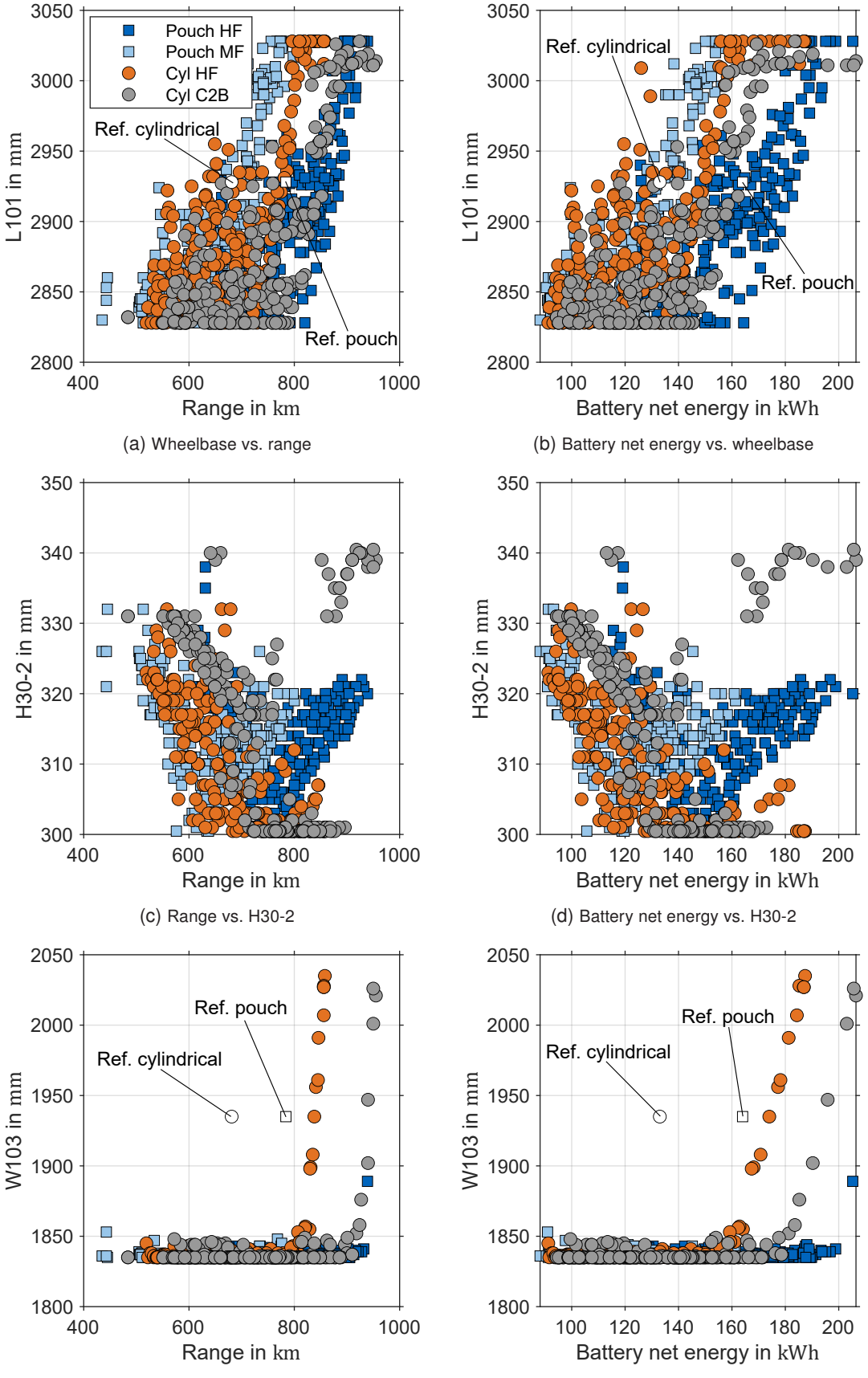

(a) Wheelbase vs. range

(b) Battery net energy vs. wheelbase

(c) Range vs. H30-2

(d) Battery net energy vs. H30-2

(e) Range vs. vehicle width

(f) Battery net energy vs. vehicle width

Figure G.9: Overview the main design variables for the optimal configurations of the Audi e-tron. These results are obtained with a population size of 300 over 30 generations.